

VERÖFFENTLICHUNGEN

des Fachgebietes Bodenmechanik und Grundbau
der Rheinland-Pfälzischen Technischen Universität

Herausgeber: Prof. Dr.-Ing. C. Vrettos

Heft 21

NUMERICAL STUDY ON THE KINEMATIC RESPONSE
OF PILED FOUNDATIONS TO A STATIONARY
OR MOVING LOAD

von

Georgia Efthymiou

KAISERSLAUTERN 2023

Vom Fachbereich Bauingenieurwesen
der Rheinland-Pfälzischen Technischen Universität

zur
Verleihung des akademischen Grades
DOKTOR-INGENIEUR (Dr.-Ing.)
genehmigte

DISSERTATION

D 386

Tag der Einreichung: 6. März 2023

Tag der mündlichen Prüfung: 30. Juni 2023

Dekan: Prof. Dr.-Ing. Karsten Körkemeyer

Berichterstatter: Prof. Dr.-Ing. habil. Christos Vrettos
Prof. Dr. Ioannis Anastasopoulos

Autorin dieses Heftes ist

Georgia Efthymiou

Wissenschaftliche Mitarbeiterin am Fachgebiet Bodenmechanik und
Grundbau der Rheinland-Pfälzischen Technischen Universität

To my family

Editor's Foreword

The dynamic soil–structure interaction is still one of the most challenging issues in soil dynamics. Most of the work published so far concerns foundations excited by impinging seismic waves or inertial forces. The response of foundations to remote harmonic surface loads has only been sporadically investigated. Even rarer are studies on the response of deep foundations to wave fields caused by moving loads. Analytical solutions for such boundary value problems are primarily based on modelling the dynamic interaction between the piles and the soil using discrete spring and damper elements. The solution using numerical continuum methods is significantly more difficult due to the large area to be considered in the analysis.

In addition to the dynamic system response, the shielding effect of piled foundations is also essential in practice. This influences the reduction of the vibration level within the affected structure and behind it. The associated wave phenomena are complex and strongly frequency-dependent. Since the vibration characteristic in the vicinity of railway traffic routes is mostly high-frequency, a fine discretisation of the soil continuum is required. This increases the computational effort and imposes limits on the modelling of the continuum.

The above points are the subject of the present dissertation, which comprises an extensive numerical investigation of the dynamic response of single piles, pile groups and piled rafts to the wave field emanating from stationary or moving loads at variable distances from the foundation. The outcome of the demanding and complex simulations provides valuable insight into the behaviour of piled foundations in the context of vibration protection. The methodology can be used as a starting point for investigating inhomogeneous soils or complex system geometries. In addition, solutions in the time domain allow the incorporation of non-linear material behaviour for the soil.

Christos Vrettos

Preface

The present doctoral dissertation was supported partly by a fellowship from Marie Skłodowska-Curie Actions (MSCA) under the program “Horizon 2020” of the European Union, and by a scholarship from the Division of Soil Mechanics and Foundation Engineering at the Technical University of Kaiserslautern.

First, I would like to genuinely thank my supervisor Prof. Christos Vrettos, not only for giving me the opportunity to conduct research on the highly interesting topic of dynamics, but also for his constant support and valuable guidance throughout this journey. Our interaction has influenced to a great extent my scientific mindset and motivated me to keep on progressing further.

For the review of my thesis, as well as for his remarks and suggestions, I would like to thank Prof. Ioannis Anastasopoulos.

Last but not least, I thank all my colleagues for their support and the pleasant atmosphere at the university all these years.

Georgia Efthymiou

Table of contents

Preface	iii
List of symbols	vii
Latin symbols	vii
Greek symbols	viii
Abbreviations.....	viii
Abstract	ix
1 Introduction	1
2 State of the art.....	5
2.1 Dynamic soil–structure interaction.....	5
2.1.1 Definition of dynamic impedances.....	6
2.1.2 Dynamic impedances of piles.....	9
2.2 Kinematic interaction	10
2.2.1 Dynamic interaction of pile groups	10
2.2.2 Moving load.....	14
3 Dynamic impedances of piled foundations and embedded footings.....	16
3.1 Dynamic impedances of piled foundations	16
3.1.1 Problem statement and finite-element modelling.....	16
3.1.2 Results	18
3.2 Dynamic impedances of an embedded footing	29
3.2.1 Problem statement and finite-element modelling.....	29
3.2.2 Results	31
3.3 Conclusions	38
4 Single piles and pile groups in the wave field of a moving load.....	41
4.1 Single pile in a Rayleigh wave field – Winkler model	41
4.2 Excitation due to a vertical harmonic point load – Finite-element method	44
4.2.1 Modelling of the near-field.....	44
4.2.2 Modelling of the far-field	49
4.2.3 Identification of the far-field	50

4.2.4	Verification of the free-field response.....	52
4.2.5	Results for single piles.....	53
4.2.6	Results for pile groups.....	58
4.3	Excitation due to a moving point load.....	60
4.3.1	Barber’s analytical solution.....	60
4.3.2	Finite-element modelling.....	61
4.3.3	Verification of the free-field response.....	63
4.3.4	Soil stratum: FE modelling.....	67
4.3.5	Results for single piles.....	68
4.3.6	Results for pile groups.....	75
4.3.7	Full 3D FE-model.....	80
4.5	Conclusions	83
5	Kinematic response of piles to a stationary harmonic load.....	86
5.1	Problem statement	86
5.2	Finite-element modelling.....	91
5.3	Frequency- vs. time-domain analysis.....	95
5.3.1	Verification of the free-field response.....	95
5.3.2	Results for a single pile and pile group.....	99
5.4	Additional validation: inertial loading of a single pile.....	104
5.5	Pile group vs. piled raft – Frequency-domain analysis	110
5.5.1	Pile array 2x3.....	110
5.5.2	Pile array 3x3.....	115
5.5.3	Pile array 4x3.....	119
5.5.4	Pile array 5x3.....	124
5.5.5	Comparison between 5x3 and 5x5 pile arrays	129
5.5.6	Comparison with a Winkler model solution	131
5.5.7	Influence of pile row number on vibration reduction	137
5.6	Conclusions	142
6	Summary & outlook.....	144
	Literature.....	148
	Appendix.....	157

List of symbols

Latin symbols

a_0	Dimensionless frequency
C_H	Horizontal dashpot coefficient
c_P	P-wave velocity in soil
C_R	Rocking dashpot coefficient
c_R	Rayleigh wave in soil
c_S	S-wave velocity in soil
C_V	Vertical dashpot coefficient
d	Pile diameter
E	Young's modulus of soil
E_p	Young's modulus of pile
f	Frequency
G	Shear modulus of soil
H	Thickness of soil stratum
K_H	Horizontal dynamic stiffness
K_{H0}	Horizontal static stiffness
K_{H0_1}	Horizontal static stiffness of single pile
K_R	Rocking dynamic stiffness
K_{R0}	Rocking static stiffness
K_V	Vertical dynamic stiffness
K_{V0}	Vertical static stiffness
K_{V0_1}	Vertical static stiffness of single pile
l	Pile length
L_f	Distance of model center from absorbing boundary
L_{FE}	Finite-element length
L_{inf}	Infinite-element length
n	Number of piles
Q	Vertical point load
R	Radius of foundation
r	Distance of point load to a surface point
s	Pile-to-pile distance
v_0	Moving load speed
w	Vertical displacement

w_B	Vertical displacement at point B behind a pile group/piled raft/raft
w_C	Vertical displacement at the center-point C of a pile group/piled raft/raft
w_p	Vertical displacement of pile
w_{ff}	Vertical displacement of free-field
$w_{ff,B}$	Vertical displacement of free-field corresponding to point B
$w_{ff,C}$	Vertical displacement of free-field corresponding to point C
x_0	Normal distance of point load to pile row
x_i	Normal distance of each pile to the rocking axis

Greek symbols

a_V	Vertical interaction factor
λ_R	Rayleigh wavelength
λ_S	S-wavelength
ν	Poisson's ratio of soil
ν_p	Poisson's ratio of pile
ξ	Hysteretic damping
ω	Circular frequency

Abbreviations

FEA	Finite-element analyses
FEA AX	Axisymmetric finite-element analyses
FEA 3D	Three-dimensional finite-element analyses
FEM	Finite-element method
TLM	Thin-layer method

Abstract

The present numerical study focuses on the problem of dynamic interaction of piled foundations under harmonic excitation at high frequencies relevant for the vibration protection practice. The finite-element programs Plaxis (2D & 3D) and Abaqus are employed for time- and frequency-domain analyses, respectively.

As a first step, dynamic impedances of pile groups, piled rafts and embedded footings are derived for all oscillation modes in order to gain insight into the problem of inertial loading.

Emphasis is placed on the kinematic response of single piles, pile groups and piled rafts to a wave field emanating from a distant stationary or moving harmonic vertical point load acting on the surface of the soil. Transfer functions, which are ratios relating the response of the foundation to that of the free-field, quantify the kinematic interaction. Only the vertical component of the response is assessed as mostly critical in the frame of the selected excitation. It is shown that a stationary harmonic load is a good approximation for a moving harmonic load; this is true for a travelling speed of the load that is relatively low in comparison with the Rayleigh wave velocity in the soil, which is quite common in engineering practice. Analogously, a static load is a good approximation of a moving load of constant magnitude. Moreover, analytical solutions are presented for single pile and pile group response under Rayleigh wave excitation, which can be also employed in the near-field, as shown herein.

The extension of piled foundations by additional rows against the wave propagation direction is examined under the scope of vibration protection. Indeed, for a considerable frequency range, the further addition of pile rows to a piled foundation has a favorable effect on the reduction of the vibration level calculated at the furthest-back pile row or at the free-field behind the foundation. This is, however, not valid, as the excitation frequency increases further, and the interplay between the piles becomes more complex. On the other hand, the extension of the piled foundation by additional pile columns parallel to the wave propagation direction has a positive effect at high frequencies.

The accuracy of the results is assessed by verification against rigorous solutions. The importance of key aspects in finite-element modelling is also highlighted.

1 Introduction

The issue of ground-borne vibrations and noise has been gaining increasing attention over the last years. Of particular importance for the engineering practice is the assessment and mitigation of vibrations due to their effect on people in buildings, and under circumstances on the structure itself.

One of the most common sources of ground-borne vibrations is railway traffic. Due to the train–track–soil interaction, the dynamic vibratory loading generated by trains is transmitted to the ground, subsequently affecting foundations and superstructures. The vast development of high-speed traffic in conjunction with limitations on the train speed enforced by the low stiffness of soft soils has led to a plethora of studies on the associated dynamic effects (Sheng et al., 1999; Grundmann et al., 1999; Madshus & Kaynia, 2000; Takemiya, 2003; Aubry et al., 2005; Auersch, 2005; Karlström & Boström, 2006; Lombaert et al., 2006, etc.). Ground-borne vibrations lie within a frequency range crudely between 1 and 100 Hz (Satis, 2017). According to ISO 14837-1 (“Mechanical vibration – Ground-borne noise and vibration arising from rail systems – Part 1, General Guidance”) railway noise is generated inside a building by ground-borne vibration due to the pass-by of a vehicle on rail. This type of noise has a frequency range between 20 and 250 Hz (Satis, 2017).

The basic aim of engineering design is to limit the induced vibration amplitudes to a level that will neither put into stake the satisfactory performance of structures nor disturb the people working in the immediate vicinity of rail tracks.

The problem of kinematic interaction of piles, which are vastly used for the foundation of a variety of structures, has been mostly investigated in the case of seismic excitation by vertically propagating S-waves (e.g. Kaynia & Kausel, 1982; Fan et al., 1991; Makris & Gazetas, 1992; Mylonakis & Crispin, 2022). Other types of wave have been considered in few studies (e.g. Kaynia & Novak, 1992; Makris & Badoni, 1995). A pertinent property of piled foundations subjected to a harmonic wave field is their shielding efficiency. Studies that focus on this aspect in case of a pile row include Kattis et al. (1999a), Lu et al. (2009), Auersch (2010), etc. This ability of piles to diffract surface waves and significantly reduce their amplitudes has inspired the concept of pile barriers

aimed to serve as a ground-borne vibration mitigation measure that can isolate nearby structures (Kattis et al., 1999b; Pu & Zhifei, 2018; Zhao et al., 2022).

Furthermore, the shielding efficiency of piles has recently found application in the field of metamaterials. These are natural or artificial materials, or structures in periodic patterns, able to control wave propagation (Brûlé et al., 2014; Palermo et al., 2016). Based on this definition, the piles embedded in the soil form a composite system with potential in wave shielding. The present study takes into account this aspect by employing a particular design concept, which will be elaborated in the sequel.

Regarding the source of excitation, in reality, a moving load has a dynamic as well as a static component representing the vehicle weight. The study of Takemiya & Bian (2005) has shown that the train weight could generate ground vibrations frequencies less than 10 Hz, which attenuate rapidly with increasing distance from the rail track. The findings in the work of Auersch (2006) confirm that a moving load of constant magnitude is of importance only in the close vicinity of the track due to its a quasi-static nature. Consequently, it is the dynamic component of the moving load that is of particular interest for the vibration protection practice.

The present work focuses on the kinematic response of piled foundations to a harmonic wave field. To analyse the problem, the finite-element method (FEM) is employed. The piles, modelled with volume elements, are embedded in a linear-elastic continuum with hysteretic damping. Either a half-space or a soil stratum resting on a rigid substratum is considered.

First, to shed light into the problem of inertial interaction, which along with kinematic interaction reproduce the complete dynamic problem, dynamic impedances of piled foundations and embedded footings are presented in Chapter 3 in specific examples. The pertinent analyses are conducted in the frequency domain with the FEM code Abaqus. The inertial response of pile groups is compared to that of corresponding piled rafts for a close and a wider pile spacing.

In Chapter 4, analyses are performed with the general purpose geotechnical FEM code Plaxis in the time domain considering as an excitation source a vertical point load of time-harmonic magnitude travelling with constant speed on the soil surface at a specific distance from a piled foundation. The kinematic interaction is quantified by transfer functions, which are ratios relating the vertical

displacement amplitude at characteristic points to that of the free-field. Moreover, the case of a stationary harmonic load is also examined as a lower-bound of a travelling speed equal to zero. It is then shown that is possible to employ the stationary solution as an approximation for the moving load for numerous cases relevant for the engineering practice.

Based on the above good agreement, as a next step, an extensive parametric study is presented in Chapter 5 on the response of pile groups with different layouts to a stationary harmonic point load. In addition, composite foundations comprising piles and raft in interaction through the soil, so-called piled rafts, are also considered. In specific, advantage is taken of the frequency-domain analysis tool provided by the FEM code Abaqus. Direct-solution steady-state analyses are performed in order to gain insight into the potential further vibration attenuation due to the periodicity of piled foundations under the scope of metamaterials. In specific, it is explored how the number of pile rows against the wave propagation direction influences the wave shielding of the pile group. The effect of additional pile columns is also examined by accordingly extending the pile group parallel to the wave propagation direction. For each case, the response of the pile group is contrasted to that of a corresponding piled raft accounting for a perfect contact between the underlying soil and the raft. Analyses considering the raft acting alone are also performed. Thus, the role of the latter is examined in the overall response. Characteristic points in the pile group/piled raft, as well as at the free-field behind them are chosen for the evaluation of the results.

Furthermore, a comparison with available analytical solutions on the kinematic response of single piles and pile groups to a Rayleigh wave field is presented in Chapters 4 and 5. Although these solutions consider far-field conditions, which in the cases examined herein are not fulfilled due to the vicinity of the piles to the source of excitation, the agreement is overall quite good. It is consequently shown, that the methodology can be employed in the frame of a preliminary design with an acceptable level of accuracy. In specific, in the case of a single pile, a closed-form expression is derived from the corresponding analytical solution.

The aim of this study is first to gain insight into the mechanics of the problem of kinematic response of pile foundations to the wave fields emanating from stationary or moving harmonic loads. Moreover, the influence of specific modelling aspects on the accuracy of the finite-element results is highlighted by

verification against rigorous solutions. Finally, it is shown, that the FEM can accurately reproduce the complex problem of wave propagation at high frequencies.

2 State of the art

2.1 Dynamic soil–structure interaction

Over the years, the topic of dynamic soil–structure interaction has been the subject of a plethora of studies. The dynamic loading of a superstructure may result either from direct external actions (e.g. traffic, ocean waves, operating machines) or from indirectly developing inertial forces (e.g. during seismic or any other type of ground shaking). Then, the forces and moments are transmitted through the foundation–soil interface into the underlying soil causing deformations. The dynamic response of foundations depends on: (a) the properties of the supporting soil, (b) the geometry and inertia of the foundation and superstructure, as well as on (c) the nature of the dynamic excitation. To predict the vibratory response of a foundation, a required input is the complex frequency-dependent *dynamic impedance* or, equivalently, the frequency-dependent “*spring*” and “*dashpot*” coefficients of the foundation (Gazetas, 1991; Vrettos, 2017). The estimation of these coefficients is key in dynamic response analyses, since the oscillation amplitude can be subsequently calculated. The basic aim of design is to limit these amplitudes to sufficiently low levels that do not put into stake the proper operation of the machine or the performance of the foundation, while at the same time ensure that people in the vicinity are not disturbed.

Typically, these displacement amplitudes are of the order of a hundredth of a centimeter, and, consequently, the resulting soil deformations are quasi-elastic, with minor non-linearities. Therefore, the analyses for the prediction of vibration amplitudes assume elastic soil behavior with hysteretic damping to account for the energy losses at these small-strain amplitudes. In specific, the internal energy dissipation characteristics of the soil are described through a frequency-independent hysteretic damping ratio ξ . Key parameter for the analyses is the small-strain shear modulus G_{\max} of the soil.

Tools to compute dynamic impedances include: (a) analytical solutions based on integral transforms, (b) semi-analytical formulations requiring the discretization of only the contact area, and (c) the finite-element method (FEM) employing special wave absorbing boundaries to minimize reflections. Details on these

techniques can be found e.g. in Roesset (1980), Luco (1982), Gazetas (1983, 1987, 1991), Kausel (2010), Vrettos (2014).

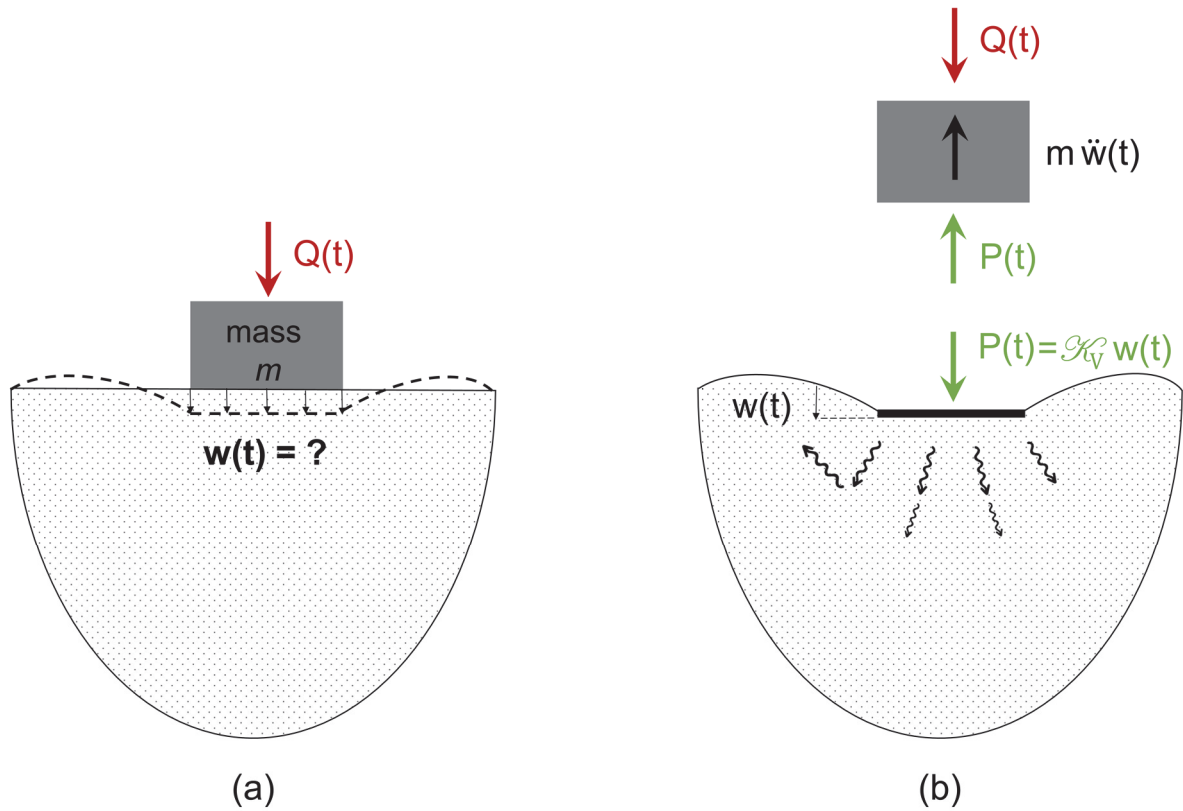


Figure 2.1: Schematic illustration of the dynamic equilibrium of a vertically oscillating foundation.

2.1.1 Definition of dynamic impedances

This section presents the general methodology to calculate dynamic displacements or rotations of foundations subjected to steady-state harmonic loading. A typical application involves machine foundations, which are usually rigid block foundations supporting machinery that produces this type of dynamic loading. Since machine foundations are rigid bodies, their response to the dynamic excitation is linked with the deformation of the supporting ground. In addition, this method can be used to determine the dynamic soil–foundation–superstructure interaction under any ground shaking, with the loading stemming in this case from inertial forces that develop in the oscillating superstructure.

The method can be generalized to any degree of freedom; herein the vertical mode of oscillation is exemplarily presented. A schematic illustration of the problem is given in Figure 2.1(a). Consider a rigid foundation of total mass m

being subjected to a vertical harmonic force $Q(t)$. The foundation responds by a vertical harmonic displacement $w(t)$ with the same circular frequency ω that rules the excitation. Given the external force $Q(t)$, the displacement $w(t)$ needs to be determined.

The motion of each body (foundation block and supporting ground) can be taken into account separately. Figure 2.1(b) includes the respective free-body diagrams along with the inertial forces. The foundation and the soil are always in contact, consequently, their displacements are identical and equal to the rigid body displacement $w(t)$. The dynamic equilibrium of the block is written as:

$$P(t) + m\ddot{w}(t) = Q(t) \quad (2.1)$$

and that of the supporting soil:

$$P(t) = \mathcal{K}_V w(t) \quad (2.2)$$

where \mathcal{K}_V is the dynamic vertical impedance for this system, defined as the dynamic force-over-displacement ratio.

By combining Equations (2.1) and (2.2):

$$\mathcal{K}_V w(t) + m\ddot{w}(t) = Q(t) \quad (2.3)$$

it is obvious that the solution of the problem requires the determination of \mathcal{K}_V . As known from structural dynamics, the steady-state solution $w(t)$ to Equation (2.3) for the harmonic excitation $Q(t) = Q \cdot e^{i\omega t}$ (i being the imaginary unit), is not only harmonic as well, but has also the same frequency ω as the excitation. However, due to radiation and material damping in the system, the harmonic action $Q(t)$ and the harmonic displacement $w(t)$ are out-of-phase. Consequently, the latter can be resolved into one in-phase and one 90°-out-of-phase component, $w_1 \cdot e^{i\omega t}$ and $w_2 \cdot e^{i(\omega t + \pi/2)}$, respectively. Thus, the dynamic impedance can be written in the form:

$$\mathcal{K}_V = \frac{Q}{w_1 + i w_2} = K_V + i\omega C_V \quad (2.4)$$

in which both K_V and C_V are frequency-dependent (Gazetas, 1991). The real component, K_V , is called “dynamic stiffness” and reflects the stiffness and inertia of the supporting soil; note that the dependence on frequency in this case is linked with inertia, since soil properties are frequency-independent. The imaginary component $\omega \cdot C_V$ involves the “dashpot coefficient” C_V , which reflects the two types of damping in the system: the radiation damping due to energy carried by

waves spreading away from the foundation, and the material or hysteretic damping due to energy dissipation in the soil through hysteretic action.

By substituting Equation (2.4) in Equation (2.1), and through straightforward operations, it is derived:

$$K_V w(t) + C_V \dot{w}(t) + m\ddot{w}(t) = Q(t) \quad (2.5)$$

and then

$$[(K_V - m\omega^2) + i\omega C_V] w(t) = Q(t) \quad (2.6)$$

Consistent with the physical interpretation above, Equation (2.5) describes the motion of a simple oscillator with mass m , spring K_V and dashpot C_V . Subsequently, an analogy is suggested by Equation (2.5) between the actual foundation–soil system and a system involving the same foundation supported on a “spring” and “dashpot” with moduli K_V and C_V , respectively, as portrayed in Figure 2.2. Having determined K_V and C_V for a frequency of interest, the vertical displacement can be calculated from Equation (2.7):

$$w(t) = \frac{Q}{(K_V - m\omega^2) + i\omega C_V} \quad (2.7)$$

and accordingly the oscillation amplitude:

$$|w| = \frac{Q}{\sqrt{(K_V - m\omega^2)^2 + \omega^2 C_V^2}} \quad (2.8)$$

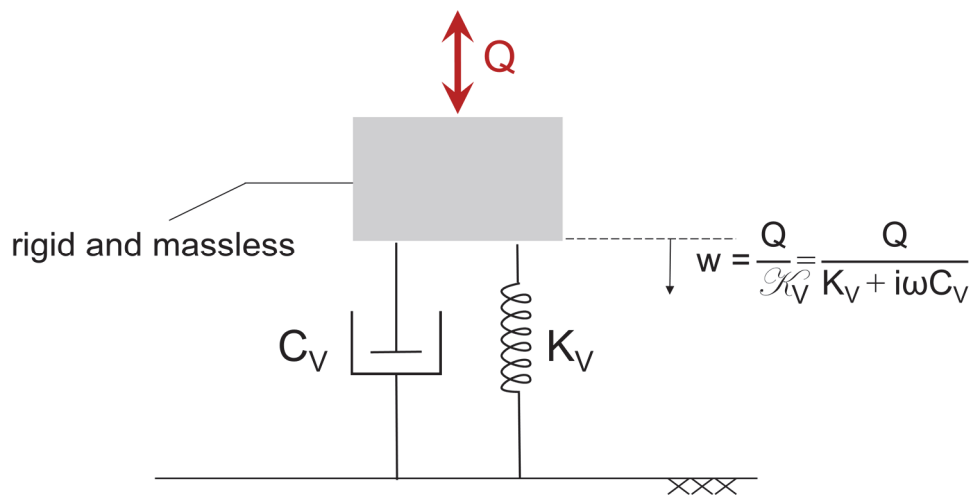


Figure 2.2: Physical interpretation of the dynamic stiffness K_V and the dashpot coefficient C_V for a vertically oscillating foundation.

2.1.2 Dynamic impedances of piles

The static stiffness of a pile group differs from the sum of stiffnesses of the individual piles; the ratio is defined as *static group efficiency* and remains always below unity. As illustrated in Figure 2.3, when a pile is located in the deformation field of a statically loaded neighbour pile, it will experience a displacement, which is a fraction α_v of the movement of the vertically loaded pile. This fraction is called interaction factor. The concept of pile-to-pile interaction factors in the form used today was introduced by Poulos (1968, 1971), who demonstrated that the assessment of pile group effects is possible by superimposing the effects between all possible pairs of piles in the group.

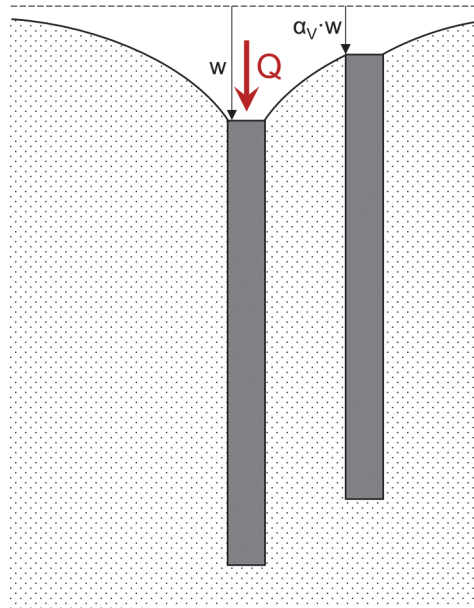


Figure 2.3: Definition of vertical pile-to-pile interaction factor α_v .

Under dynamic conditions, however, static interaction factors are proven insufficient. Numerical studies by Wolf & Von Arx (1978) and Nogami (1979) revealed that the *dynamic group efficiency* exhibits a strong oscillatory behavior, and can even (by far) exceed unity due to out-of-phase vibration of piles. Subsequent works including those by Nogami (1980, 1983), Kaynia (1982), Kaynia & Kausel (1982), Waas & Hartmann (1981, 1984) and Roesset (1984) confirmed this finding.

The superposition method by Poulos (1968, 1971) can be extended to dynamic problems. Kaynia & Kausel (1982, 1991), Sanchez-Salinero (1983), Roesset (1984), Padr3n (2008) and Padr3n et al. (2008) showed that this approximation is in good accord with rigorous solutions. Practically, it is assumed that intermediate piles do not influence the interplay between a source and a receiver

pile. As Dobry & Gazetas (1988) state, this assumption is valid for wavelengths greater than six times the diameter of the pile ($\lambda > 6d$).

Employing the above finding, Dobry & Gazetas (1988) developed a simple analytical method to compute the dynamic impedance functions of floating pile groups. The method is based on the following two assumptions:

- The simultaneous emanation of cylindrical waves from all points along the pile shaft.
- The pile is replaced by its axis, so the actual pile geometry is neglected.

In this frame, Dobry & Gazetas (1988) presented an approximate expression for the vertical dynamic interaction factor:

$$\alpha_v = (2s/d)^{-0.5} \exp(-\zeta\omega s/c_s) \exp(-i\omega s/c_s) \quad (2.9)$$

with s being the pile-to-pile distance, ζ the hysteretic damping ratio, and c_s the S-wave velocity in the soil.

It is underlined that the simultaneous emanation of waves from the pile shaft is deemed realistic in the case of soft soils in relation to the pile stiffness. Moreover, the replacement of the pile by its axis can be a problematic assumption for close pile spacings as well as high frequencies, where the dimensions of the pile are comparable to the corresponding wavelengths.

2.2 Kinematic interaction

2.2.1 Dynamic interaction of pile groups

While for dynamic impedances a plethora of results in the form of diagrams as well as simple methods are available in the literature, e.g. Gazetas (1991), the kinematic interaction of piles has been considered mostly for the case of seismic excitation by vertically propagating shear waves or compressional waves, e.g. Waas & Hartmann (1984), Fan et al. (1991), Gazetas & Mylonakis (1998), Nikolaou et al. (2001), Crispin & Mylonakis (2022), Mylonakis & Crispin (2022).

During dynamic excitation, the generated waves lead to free-field deformations, with the foundation–superstructure system being drifted too. The computation of the complete dynamic response of such a system, as exemplarily sketched in Figure 2.4 for the case of a single pile excited by vertically propagating S-waves, is possible through the superposition of the two following phenomena:

- *Kinematic interaction* (often referred to as ‘wave scattering’ effect) involving the response to base excitation of the system of Figure 2.4 with the mass of the superstructure being set to zero.
- *Inertial interaction*, referring to the response of the complete pile–soil–superstructure system to excitation by inertial forces from the acceleration of the superstructure due to the kinematic interaction.

The computational convenience constitutes the basic motive in order to decouple the complete problem into the above effects, which, in reality, take place simultaneously. The separation is exact for linear systems, if the analysis at both stages is performed rigorously. Yet, the extension of the superposition to moderately non-linear systems is also possible as an approximation under conditions.

The problem of kinematic interaction requires firstly the analysis of the free-field response to the considered dynamic excitation (in absence of the foundation), and then the analysis of the system consisting of the soil and the single pile or the pile group to account for the interplay between them.

In addition, for the inertial response, a two-step approach can be implemented, which is also depicted in Figure 2.4. This two-step analysis, originally suggested by Kausel & Roesset (1974), involves the derivation of the dynamic impedances at the pile head or the cap of the pile group for the relevant modes of motion, and subsequently, the analysis of the dynamic response of the superstructure supported on the corresponding springs and dashpots, while it is subjected to the pile-head motion calculated through the kinematic interaction problem. The latter is known as foundation input motion (FIM). This principle is elucidated, among others, by Mylonakis et al. (1997), Gazetas & Mylonakis (1998), Mylonakis & Gazetas (1999).

In the frame of the present study, particular emphasis is accorded to the kinematic response of piles to a stationary or moving harmonic load acting on the soil surface. The quantification of the kinematic interaction is possible by means of *kinematic interaction factors* also known as *transfer functions*, which are ratios that relate e.g. the amplitude of acceleration, displacement or rotation of the embedded foundation to that of the free-field (either at the same or at a different location). Due to radiation and material damping in the system, the acceleration, displacement or rotation components are generally out-of-phase with the excitation. Consequently, the kinematic interaction factors turn out to be complex functions of frequency. Herein, it is chosen to present the results mostly

in terms of displacement amplitudes (absolute values) with respect to the pile head or pile cap, when considering a piled foundation.

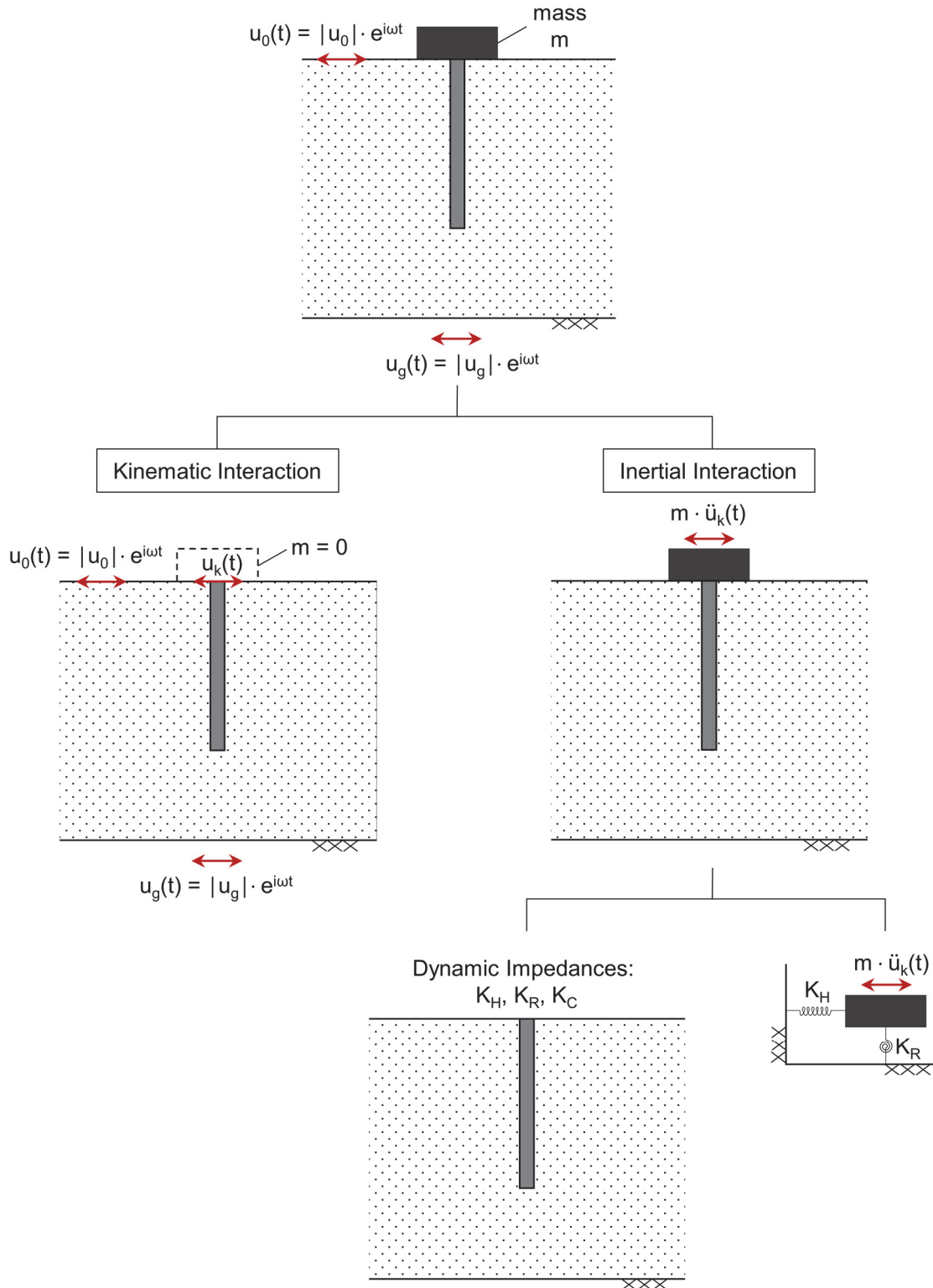


Figure 2.4: Decoupling of the problem of dynamic response of a soil–pile–superstructure system to seismic excitation with vertically propagating S-waves into kinematic and inertial interaction problems.

The solution of dynamic interaction problems is not a trivial process, since it almost exclusively requires sophisticated codes that are not generally accessible. Numerical continuum methods such as the finite-element method (FEM) are rarely used in engineering practice due to the complex modelling and the often prohibitive computation expenses. The latter are due to the fine discretization required in order to properly capture the small wavelengths (associated with high frequencies) in combination with the large dimensions of the investigated systems. Moreover, for practical applications, the size and economics of the project play a major role in the selection of an appropriate method.

For vibration protection tasks in practice, a two-step method is used: firstly, the free-field vibrations to be expected at the location of interest are either obtained directly by field measurements (on the surface of the site and/or in a borehole) or predicted using suitable analytical or numerical methods based on the source characteristics (Vrettos, 2009). The output is then applied as a stationary excitation on a finite-element model of the construction, with the foundation compliance being abstracted by suitable springs and dashpots. Alternatively, the foundation is embedded in a soil continuum. Depending on availability, two- or three-dimensional (2D or 3D) models are employed.

The knowledge gained so far from measurements (Appel et al., 2015) on the shielding efficiency of individual piles or pile groups does not yet allow a reliable quantification of the associated effects, with several questions remaining unanswered up to date. Regarding numerical methods, the work of Kaynia & Novak (1992) and Makris (1994) on the dynamic response of a single pile to the wave field of a Rayleigh wave should be mentioned. In the former, a versatile numerical continuum model for stratified soil is used. In the latter, a Winkler model with frequency-dependent springs and dashpots is employed for the calculation of the soil-pile interaction, and an explicit solution of the free-field – pile transfer function is derived. Makris & Badoni (1995) extended this methodology to pile groups under excitation by Rayleigh waves as well as oblique shear waves. The shielding efficiency of a row of piles has been also examined numerically (Avilés & Sánchez-Sesma, 1988; Kattis et al., 1999a,b; Lu et al., 2009; Tsai et al., 2008; Auersch, 2010).

2.2.2 Moving load

The type of excitation plays an important role on the kinematic response of embedded foundations. In the majority of the studies to date, stationary loads of variable frequency are assumed. Loads from railway traffic are, however, location-variable. As a result, the speed of a moving load constitutes a further parameter that needs to be considered (Auersch, 2008).

Special attention must be drawn to the nature of a moving load. A load of constant magnitude leads to a quasi-static response. By contrast, a time-varying magnitude is a governing factor in ground vibration (Katou et al., 2008), since it is associated with dynamic response. In railway traffic, both components are obviously present: the weight of the train is linked with the first one, while the vehicle-track interaction results in dynamic loading, with the sleeper distance determining the frequency. With the distance between the sleepers being typically equally to 50-60 cm, the observed vibrations lie in the frequency range between 5 and 40 Hz, with an offset of 10-20 m from the track (Katou et al., 2008).

The problem of waves induced in the soil by a surface time-dependent point load was first solved by Lamb (1904). In this work three types of waves were identified: P-waves, S-waves and Rayleigh waves, with wave velocities c_P , c_S and c_R , respectively. Eason (1965) derived the surface displacements due to a traction on a rectangular or circular surface moving at constant speed on the surface of an elastic half-space. The solution in terms of integrals had to be numerically evaluated. Payton (1964), and Gakenheimer & Miklowitz (1969) obtained soil surface and internal displacements, respectively, when a suddenly applied point load is travelling at a constant speed on an elastic half-space. Fryba (1972) derived the stationary solution for this problem, while De Barros & Luco (1994) for a layered half-space. The problem of a point load of constant magnitude travelling from infinity at a constant speed on the surface of a half-space was studied analytically by Barber (1996), who presented closed-form expressions for the surface deformations. Galvín & Domínguez (2007) presented a 3D time-domain formulation of the boundary element method (BEM) to investigate soil deformations induced by moving loads characterized by high speed. Using the software Plaxis 3D, Galavi & Bringreave (2014) shed light on aspects of finite-element modelling of a point load with constant magnitude travelling on the surface of the soil. Similar investigations were carried out by Kouroussis et al. (2013) utilizing a different numerical approach.

When an embedded foundation is considered in the vicinity of a moving load source, alternations in the induced wave field are to be expected as a result of kinematic interaction. Specifically, when assuming a moving vibrating source, both the excitation frequency, as well as the distance of the foundation from the load are significant parameters. Recently, by means of the FEM, Efthymiou & Vrettos (2022 a,b,c) presented results on the shielding efficiency of pile groups and single piles in the wave field of a moving point load with a magnitude varying harmonically with time. Since the focus was on the physics of the specific dynamic problem, numerical modelling of the track or the consideration of the load–track interaction were neglected. The simplified scenario examined in the above studies, where the static component corresponding to the weight of the train is ignored, is contrasted to the case of a stationary harmonic load. These findings are included in the present dissertation, and are enhanced by additional results and conclusions.

3 Dynamic impedances of piled foundations and embedded footings

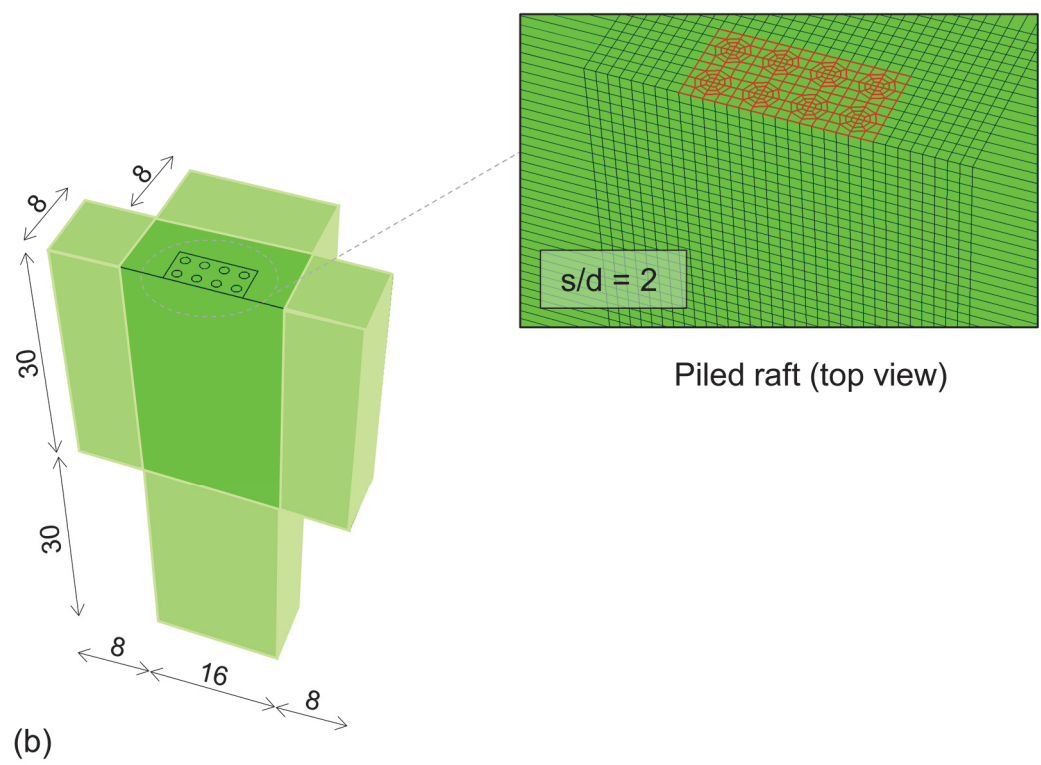
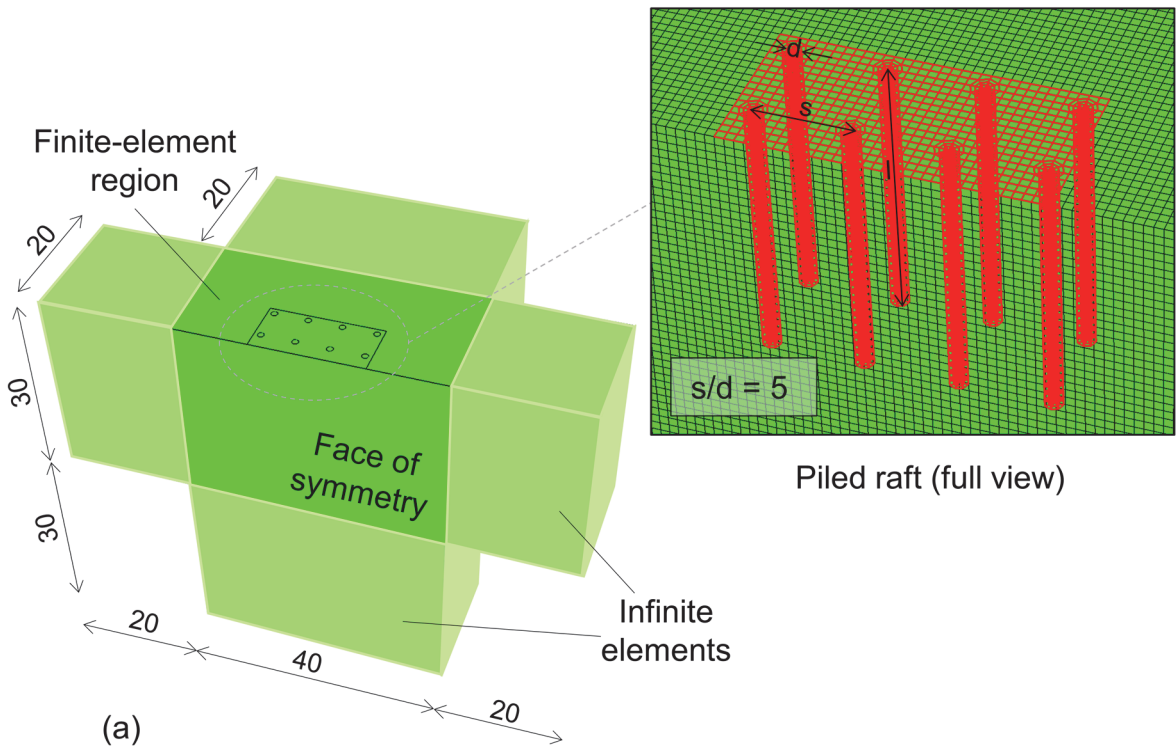
Before proceeding with the computation of the kinematic response of pile groups and piled rafts to a harmonic wave field, which constitutes the main objective of this work, a parametric study on the impedances of a variety of foundations including pile groups and piled rafts, as well as embedded footings is conducted. The finite-element software Abaqus (version 2019) is employed in the frequency domain to derive dynamic impedances for all modes of oscillation. The accuracy is assessed by comparison with available rigorous solutions. To shed light into modelling details, the influence of key aspects such as the mesh discretization and the distance from the region of interest of the infinite elements used herein as absorbing boundaries is examined in certain examples.

The goal is to demonstrate that the finite-element method (FEM) with proper implementation is capable of reproducing the essential features of dynamic soil–structure interaction phenomena over wide frequency ranges. The methodology can be used to solve problems of complex geometry and soil stratigraphy arising in engineering practice.

3.1 Dynamic impedances of piled foundations

3.1.1 Problem statement and finite-element modelling

The dynamic impedances (vertical, horizontal and rocking) of a 4x4 pile group and a corresponding piled raft in a homogeneous half-space are calculated with the finite-element software Abaqus. For this purpose, direct-solution steady-state dynamic analyses are conducted in the frequency domain. A relatively close and a wider pile spacing are considered, with the ratio of the pile-to-pile distance over the pile diameter being equal to $s/d = 2$ and 5, respectively. Accordingly, different models are created, which are portrayed in Figure 3.1 along with aspects of mesh discretization. Only half of the problem is modeled, since advantage of symmetry is taken. Built-in infinite elements (CIN3D8) serving as absorbing boundaries are placed peripherally as well as at the base of each model to simulate a half-space. Both piles and soil are modelled with first-order 8-node



Length unit: meter [m]

Figure 3.1: Finite-element models of a 4x4 pile group/piled raft with pile spacing $s/d = 5$ (a) and $s/d = 2$ (b) embedded in half-space.

continuum elements (C3D8). The pile–soil contact is fully bonded, implying an infinite tensile capacity, not allowing detachment, siding, or uplifting.

The corresponding piled rafts are examined by adding a rigid, massless raft atop of the piles, which is also in perfect contact with the underlying soil. Quadratic rafts with the dimensions [17 m x 17 m] and [8 m x 8 m] are chosen for the configurations with $s/d = 5$ and 2, respectively. Linear 4-node shell elements (S4) are used to model the raft. A fixed connection (no rotation) between the raft and the pile heads is considered.

The soil is linear-elastic with a hysteretic damping ratio $\xi = 5\%$. The Poisson ratio is taken as $\nu = 0.4$. With the Young's modulus of the soil being equal to $E = 30$ MPa and the density $\rho_s = 1.7$ Mg/m³, the resulting S-wave velocity is $c_s \approx 80$ m/s.

Assumed to represent concrete, a linear-elastic material with a Young's modulus $E_p = 30$ GPa and $\nu_p = 0.2$ is assigned to the piles. Consequently, the flexibility of the pile is equal to $E_p/E = 1000$. The ratio of the pile over soil density is $\rho_p/\rho_s = 0.68$. The pile length $l = 15$ m with the diameter $d = 2 \cdot R = 1$ m yield a slenderness $l/d = 15$.

For the derivation of the dynamic impedances of the pile group, uniform displacement/rotation is directly applied on the pile heads. This boundary condition is assumed to be enforced by a rigid, massless cap, which is not modeled. On the other hand, for the analyses including the piled rafts, the excitation is applied on the complete raft surface. In both cases, the reference point is taken at the center-point of the configuration at the soil surface level. The dynamic impedance is then calculated as the ratio of the reaction force/moment at the reference point over the applied displacement/rotation. For each oscillation mode examined, only the corresponding degree of freedom of interest is active, while the rest remain constrained. The harmonic excitation includes frequencies up to $f = 13$ Hz, which corresponds to a dimensionless frequency $a_0 = \omega \cdot d/c_s = 1$.

A homogeneous mesh was created with a finite-element size equal to 0.5 m. This essentially means that the shortest S-wavelength λ_s is captured by approximately 12 finite elements, which is sufficient for this type of problems.

3.1.2 Results

The vertical and horizontal static stiffnesses of the single pile, herein denoted as K_{V0_1} and K_{H0_1} , respectively, are used to normalize the dynamic impedances. For

this purpose, an additional finite-element model, which is depicted in Figure 3.2, was created to perform the required analyses. Apart from the significantly reduced computational time due to the coarser mesh allowed by the static analyses, the main reason behind the choice of this particular model is the lower accuracy ascertained in the analyses with the initial models comprising infinite elements (Figure 3.1) at static conditions. Note that according to the documentation of Abaqus (2019), the infinite-element formulation for static response is based on the work of Zienkiewicz et al. (1983), consequently differing from the one for dynamic response following the theory developed by Lysmer & Kuhlemeyer (1969). In the model portrayed in Figure 3.2, infinite elements are omitted; instead, conventional boundaries are placed at a sufficient distance from the single pile. The base of the model is fixed, thus corresponding to a rigid substratum, yet, since it is placed at a distance from the surface being equal to $4 \cdot l$, its influence on the response is expected to be negligible. This aspect is particularly important, since the target is to reproduce stiffnesses for piles embedded in a half-space.

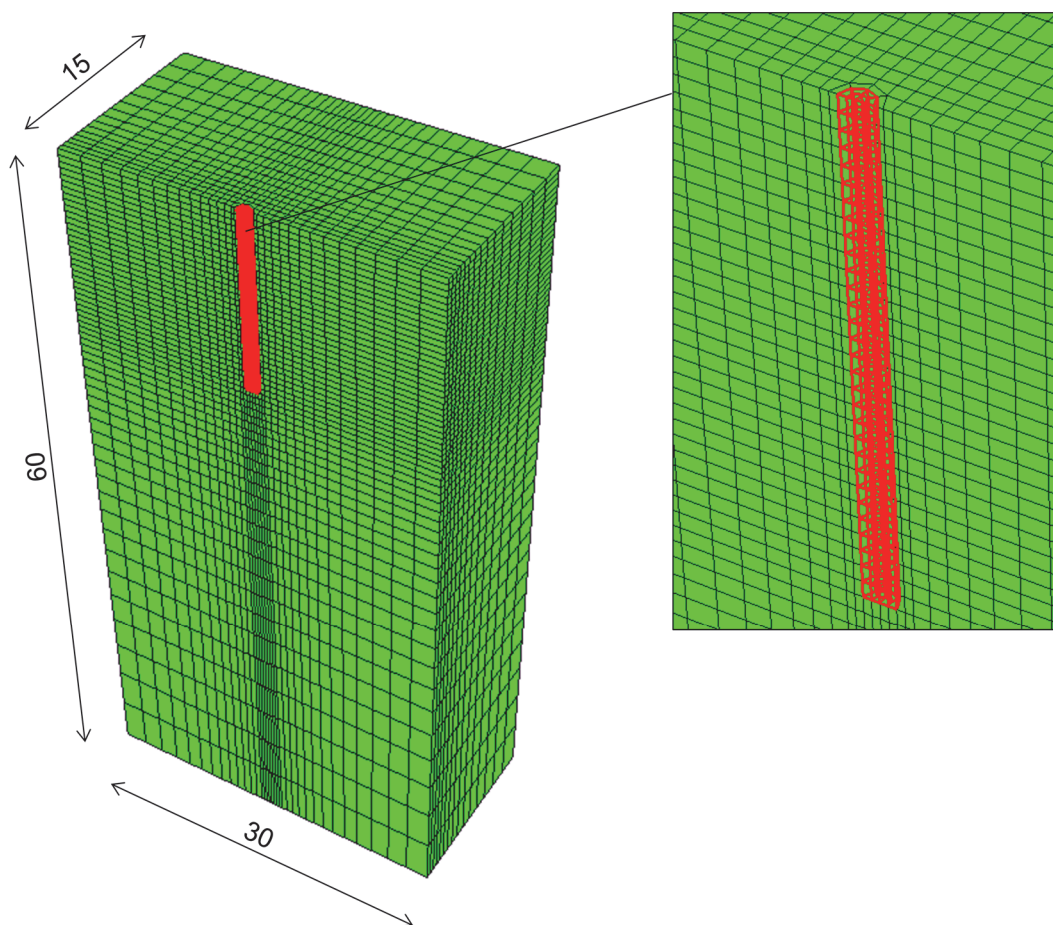


Figure 3.2: Finite-element model for the static analysis of a single pile.

In Table 3.1, the static stiffnesses of a single pile with $E_p/E = 1000$ and $l/d = 15$ from the finite-element analyses are compared to results in DGGT (2019) derived from Hartmann with the thin-layer method (TLM). The maximum discrepancy, observed in the case of the horizontal stiffness, is approximately equal to 10 %. Even though the influence of the rigid substratum is particularly critical for the vertical vibration mode, the remarkable agreement with the TLM solution confirms that the presence of a fixed base in the finite-element model does not affect the response, with the half-space solution being accurately reproduced.

Table 3.1: Comparison of static stiffnesses of a single pile in homogeneous half-space derived from finite-element analyses (FEA) with results from Hartmann with the thin-layer method (TLM); $E_p/E = 1000$, $l/d = 15$, $\nu = 0.4$.

	FEA	TLM
$\frac{K_{H0_1}}{E \cdot R}$	9.28	8.42
$\frac{K_{V0_1}}{E \cdot R}$	18.43	18.4

Figure 3.3 presents the vertical, horizontal and rocking impedances (\mathcal{K} , \mathcal{K}_H , \mathcal{K}_R) of the 4x4 pile group/piled raft for $s/d = 2$ and 5. The vertical and horizontal impedances are normalized by the number of piles n and the corresponding static stiffness of the single pile. The resulting ratio is also defined as *dynamic group efficiency*. The rocking impedance is divided by the sum of the pile distances (x_i) normal to the rocking axis times the vertical static stiffness of the single pile.

First of all, the peaks in the dynamic stiffness curves indicate that a larger force is required in order to impose the boundary condition of uniform displacement at the pile heads, since the piles are excited in an out-of-phase motion. In the simplified scenario of two piles, for example, while the one pile is being pushed down, the other is being forced up. Therefore, it is not uncommon for the resulting dynamic group efficiency to exceed unity, and in fact by far. In the

static case, on the other hand, the group efficiency always attains values below 1. In a similar manner, the valleys in the dynamic stiffness appear at frequencies associated with equiphase motion. The addition of a raft to the system significantly limits these peaks in the dynamic stiffnesses, leading to smoother curves.

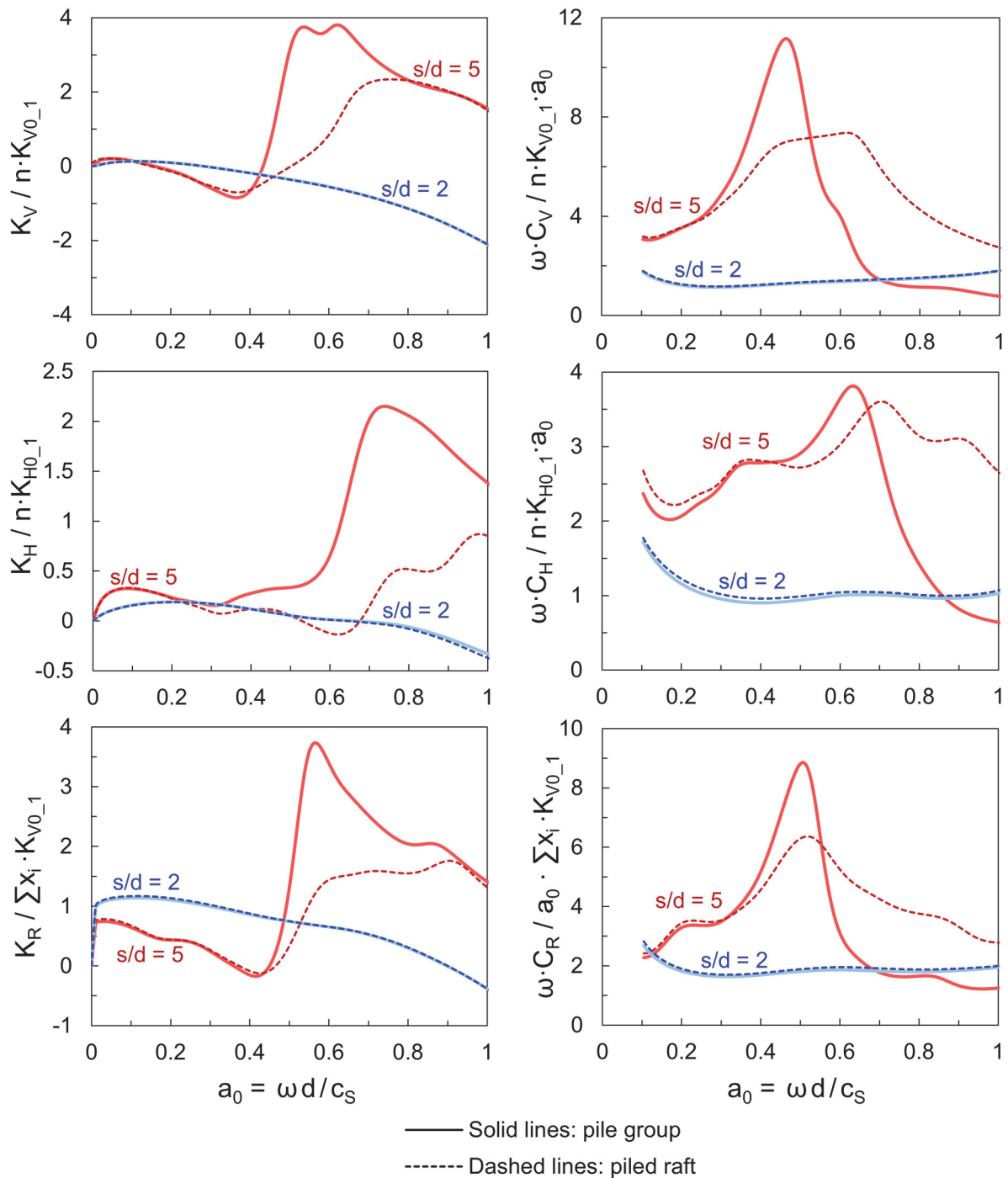


Figure 3.3: Dynamic impedances of a 4x4 pile group/piled raft in a homogeneous half-space; $E_p/E = 1000$, $l/d = 15$, $\nu = 0.4$.

Interestingly, for $s/d = 2$, the dynamic impedances of the pile group are almost identical to those of the piled raft for all vibration modes. Apparently, when the piles are closely spaced, the raft hardly affects the overall response. Instead, the inertial response is governed by the piles, the influence zones of which are overlapping, as revealed by the horizontal displacement contours due to horizontal loading at $a_0 = 1$ in Figure 3.4.

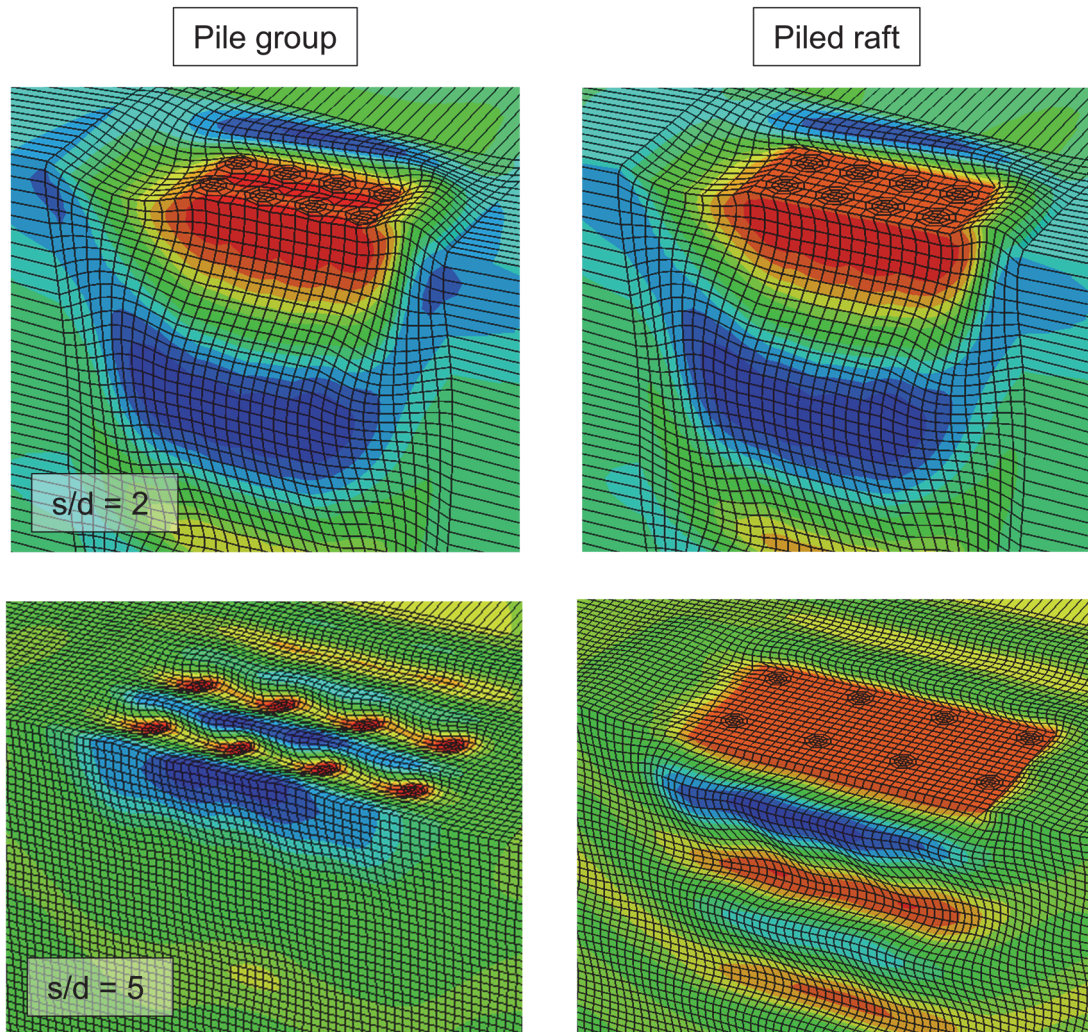


Figure 3.4: Contours of horizontal displacements (real part) due to horizontal loading at $a_0 = 1$ of the various systems.

A wider centre-to-centre pile distance ($s/d = 5$), on the other hand, leads to substantial differences between the pile group and the piled raft response at high frequencies. However, up to $a_0 \approx 0.4$, both foundation systems behave quite similarly for all cases due to the associated large wavelengths that expand the

influence zone of each pile. Certainly, differences at these low frequencies exist; however, due to the graph scale these are not visible. As portrayed in Figure 3.4 for the highest applied dimensionless frequency $a_0 = 1$, the larger distance between the piles does not permit an overlap of their influence zones, and subsequently, the contribution of the raft in the load distribution increases. This is manifested through a considerable shearing action in the supporting soil in the case of horizontal loading.

The results from the finite-element analyses are verified against the rigorous solutions from Kaynia & Kausel (1982) and Hartmann (2015) in Figures 3.5 - 3.7 in the case of the pile group for each vibration mode. The results from Hartmann (2015) were calculated in the frequency domain according to the approach by Hartmann (1986) which is based on the TLM developed by Waas et al. (1985).

For the calculation of the single pile impedance, the finite-element model (dimensions, mesh fineness) in Figure 3.1(b) was used after being appropriately modified to account for a single pile located at the center of the plane of symmetry.

The comparison with the rigorous results is overall satisfactory. The peaks in the response attain in the case of the finite-element analyses slightly lower values. The valleys are smoother as well. Some differences are detected mostly in the case of the pile group with $s/d = 2$; more specifically, for the dashpot coefficient in all types of loading at higher frequencies and the rocking dynamic stiffness. In addition, deviations can be observed at frequencies close to zero. These are attributed to the lower accuracy of the infinite elements used as “quiet” boundaries in the models as the static state is being approached. Instead of being properly absorbed from the infinite elements, the waves are rather partially reflected due to their large wavelengths associated with low frequencies. Subsequently, the extension of the finite-element region (and accordingly of the infinite-element size) is tested as a potential solution to the above issue, as shown next.

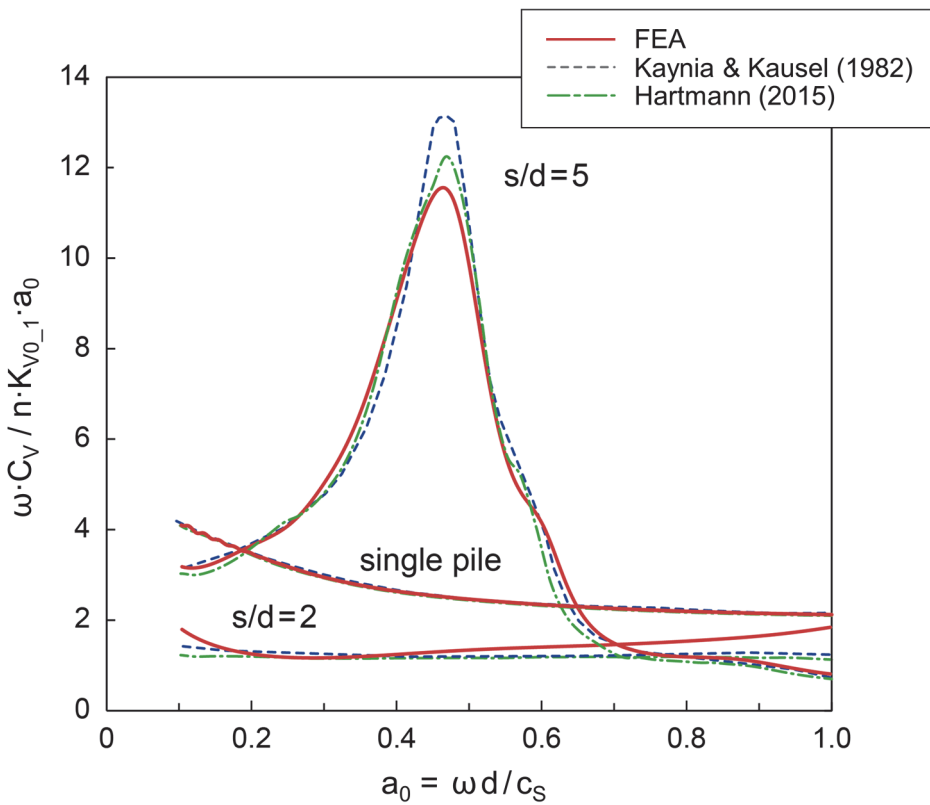
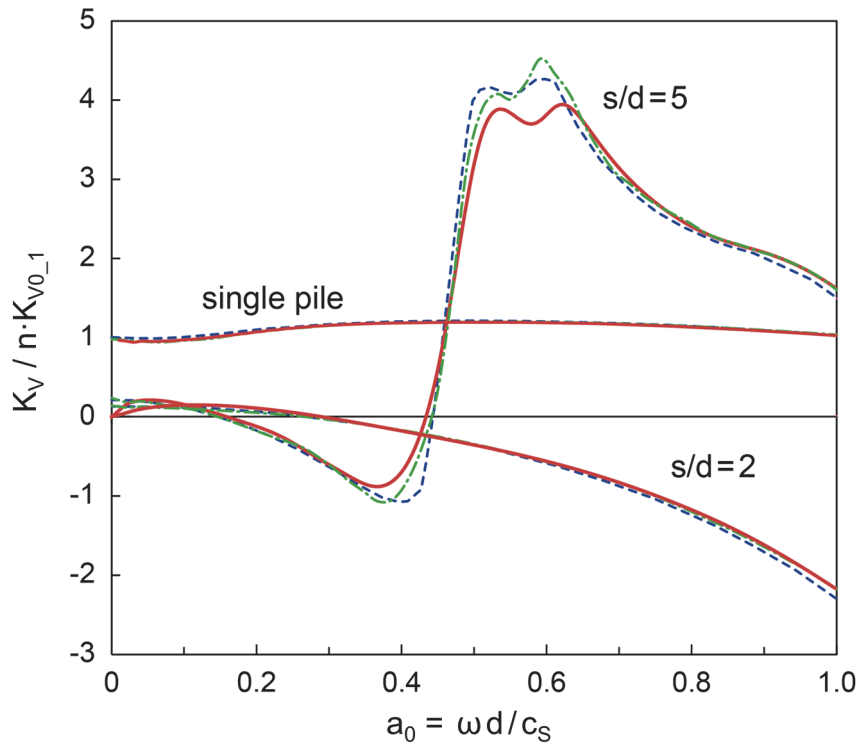


Figure 3.5: Comparison of the vertical dynamic impedances of a 4x4 pile group in a homogeneous half-space with the rigorous results from Kaynia & Kausel (1982) and Hartmann (2015); $E_p/E = 1000$, $l/d = 15$, $\nu = 0.4$.

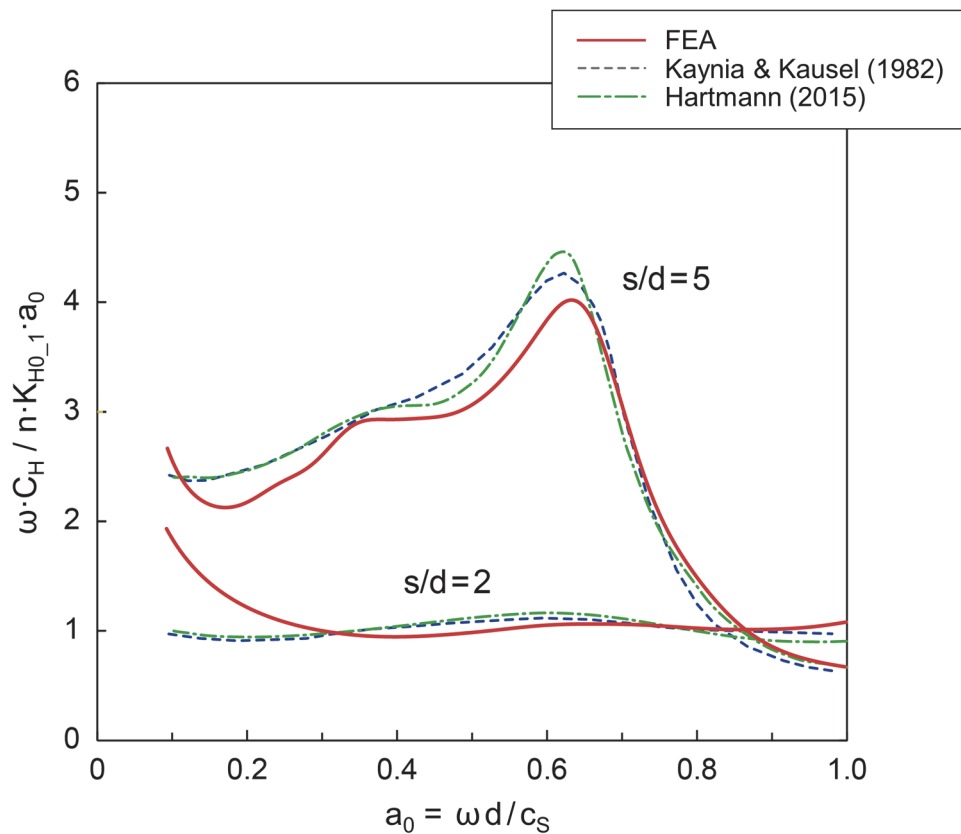
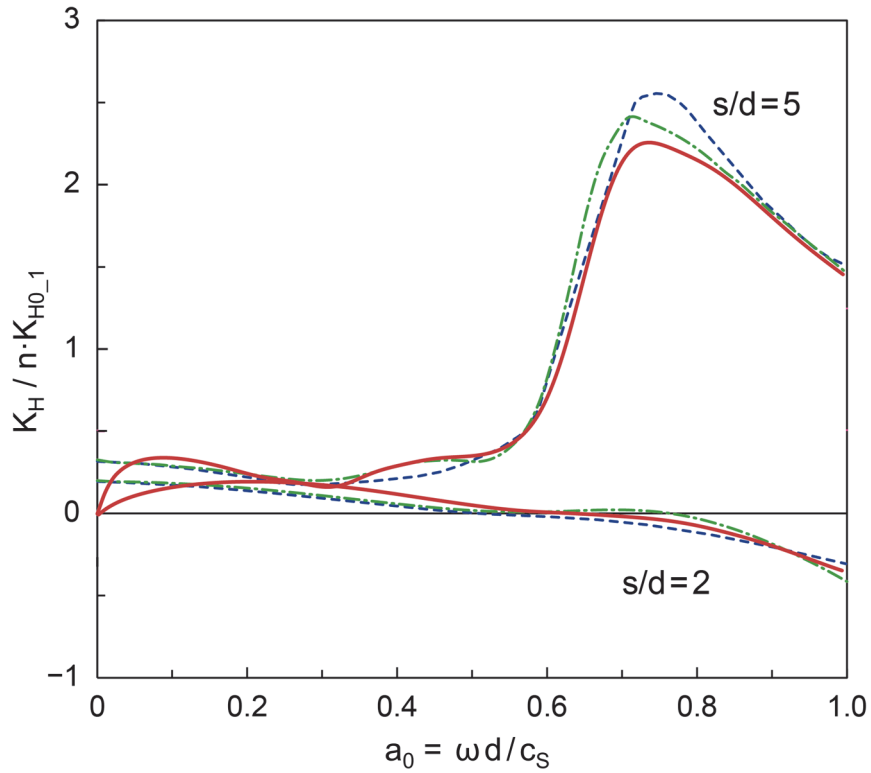


Figure 3.6: Comparison of the horizontal dynamic impedances of a 4x4 pile group in a homogeneous half-space with the rigorous results from Kaynia & Kausel (1982) and Hartmann (2015); $E_p/E = 1000$, $l/d = 15$, $\nu = 0.4$.

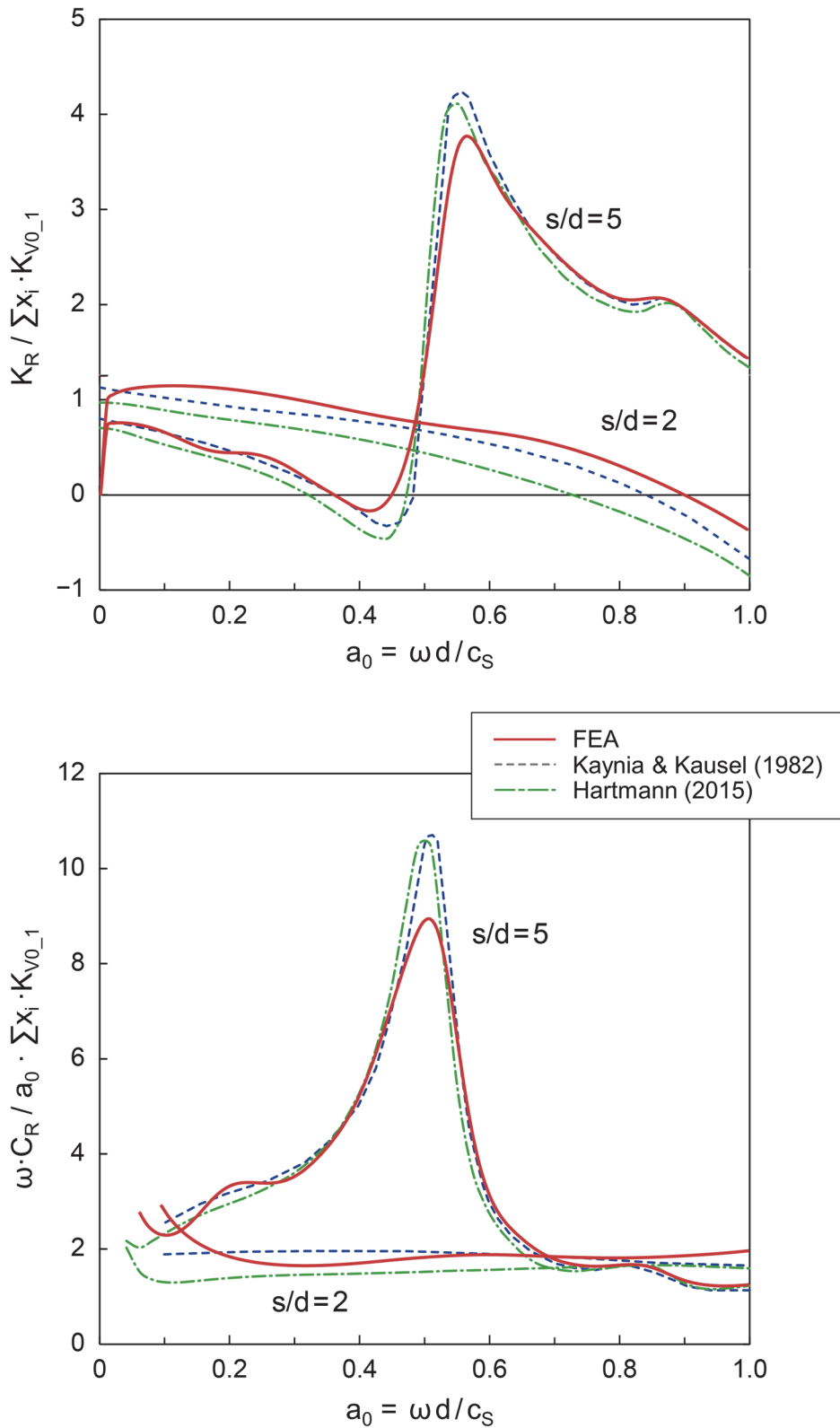


Figure 3.7: Comparison of the rocking dynamic impedances of a 4x4 pile group in a homogeneous half-space with the rigorous results from Kaynia & Kausel (1982) and Hartmann (2015); $E_p/E = 1000$, $l/d = 15$, $\nu = 0.4$.

Targeting an improved accuracy at low frequencies, two larger finite-element models were created for the closely spaced pile group, which are illustrated in Figure 3.8. To differentiate between the various models, the initial model (recall Figure 3.1 (b)) will be now referred to as Model I. Model II retains the same mesh fineness, with the finite-element region size being the sole parameter that differentiates it from the initial model. The size of the model is further extended in the case of Model III, but since the focus lies on the calculation of dynamic impedances at low frequencies, the initial fine mesh discretization is not deemed necessary, thus, a larger finite-element size of 3 m (instead of the previous 0.5 m) is selected. Only in the vicinity of the pile group a finer discretization is applied. The analyses with Model III consider frequencies up to $f = 1.77$ Hz, which corresponds to $a_0 = 0.07$. Subsequently, 15 finite elements reproduce the shortest shear wavelength λ_s .

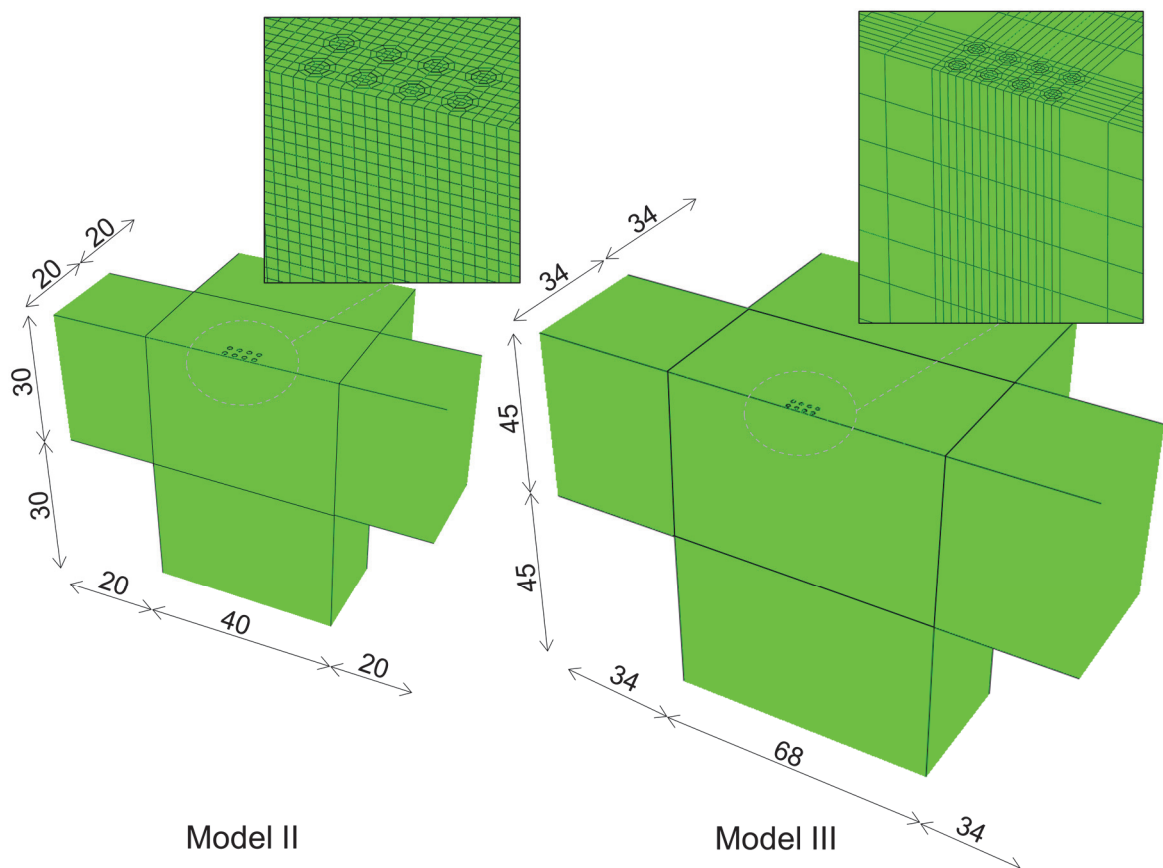


Figure 3.8: Models II and III of the 4x4 pile group with $s/d = 2$ embedded in half-space.

The comparison between the results from the different models is presented in Figure 3.9 along with the rigorous solution from Hartmann (2015). The vertical vibration mode is indicatively selected. Since emphasis is placed on the low-frequency response, only the dynamic stiffness is presented. The analyses with Model II involve the initial excitation frequency range up to $a_0 = 1$. At first glance, Models I & II yield practically the same results. This is to a great extent true, however, due to its larger size, Model II exhibits an improved performance as the static case is approached. The agreement with the rigorous results is even better in the case of the largest Model III, which due to its coarse mesh is only intended for low-frequency analyses. Despite the fact that all three dynamic stiffness curves obtained with the finite-element models tend inevitably to zero, it is clear that the accuracy at low frequencies can be significantly improved with the proper choice of model size. Based on these, when performing analyses over an extensive frequency range, employing different models for lower and higher frequencies, each accordingly adapted to the requirements of the corresponding frequency range, leads not only to considerable computational savings, but also to higher accuracy.

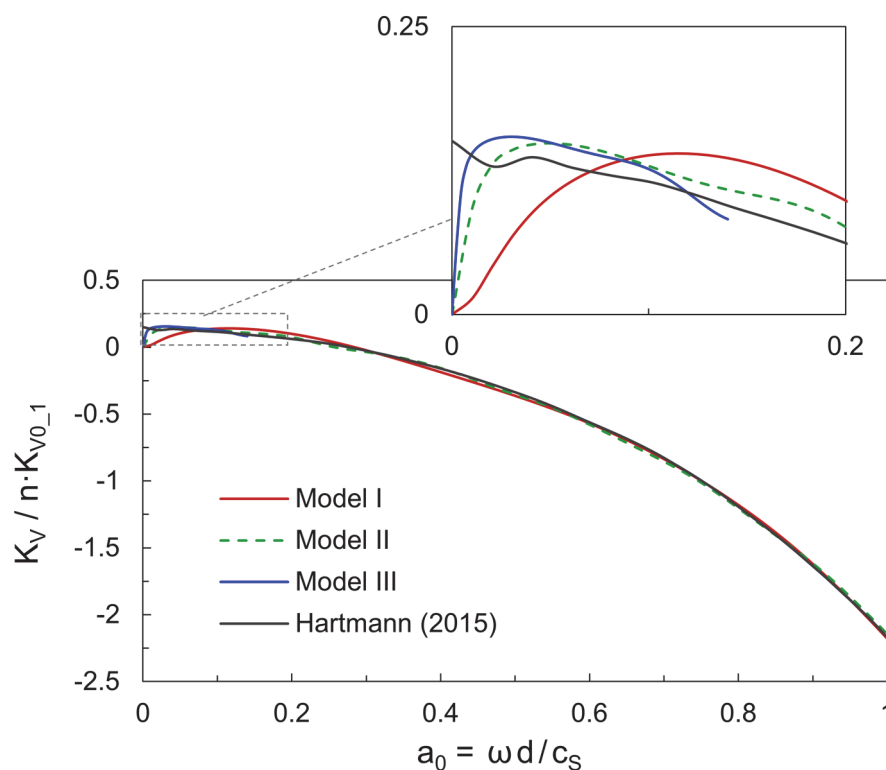


Figure 3.9: Influence of the model size on the vertical dynamic stiffness of a 4x4 pile group; $E_p/E = 1000$, $l/d = 15$, $\nu = 0.4$.

3.2 Dynamic impedances of an embedded footing

3.2.1 Problem statement and finite-element modelling

In the present section, an extensive parametric study on the dynamic impedances of an embedded footing in a soil stratum is presented in detail. The SUPELM code (Kausel, 1999) based on the thin-layer method is employed for verification. On this basis, the finite-element model is optimized in order to achieve the highest possible accuracy.

The problem involves a cylindrical footing with a diameter $d = 2 \cdot R = 1$ m, being equal to that of the piles in Section 3.1. The massless, rigid footing has an embedment depth $l = 2 \cdot d = 4 \cdot R$. The foundation is embedded in a soil stratum with a thickness $H = 2 \cdot l$, and is in perfect contact with the supporting soil.

In order to save computational time, the optimization of basic characteristics such as the model size and mesh fineness is performed with respect to the vertical mode of oscillation, so that an axisymmetric finite-element model can be employed. The initial model is portrayed in Figure 3.10. The radius of the finite-element region of the model, L_f , as well as the finite-element size L_{FE} , are the model parameters to be varied.

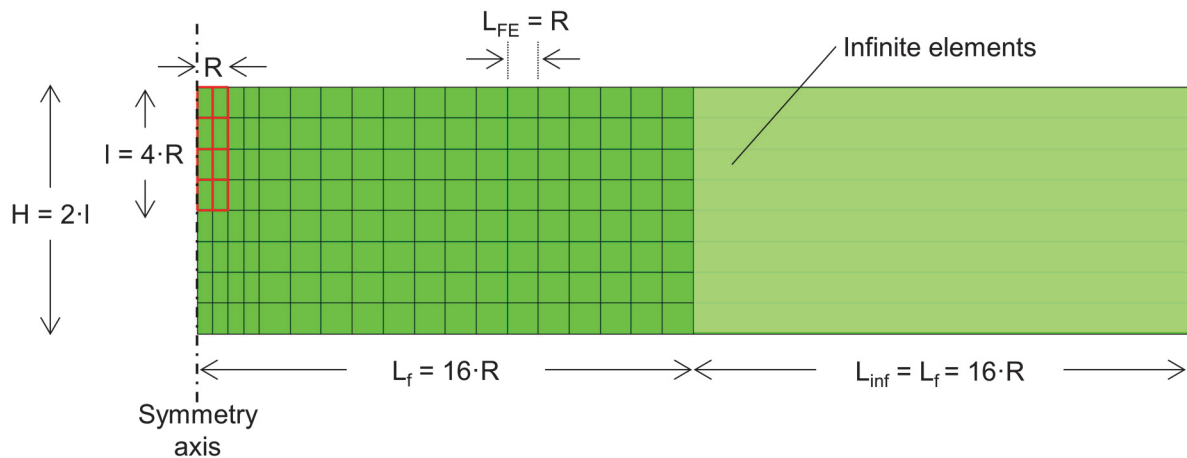


Figure 3.10: Axisymmetric finite-element model of a cylindrical foundation with $l/d = 2$ embedded in a soil stratum with thickness $H = 2 \cdot l$.

For the modelling of the soil and the embedded footing, 4-node axisymmetric elements CAX4 are used. These are expanded into C3D8 in three-dimensional models. The base of the model is fixed in all three directions to account for the rigid substratum. Infinite elements (CINAX4) are placed peripherally at a

distance $L_f = 16 \cdot R$ to minimize wave reflections. In accordance with the documentation of Abaqus (2019), the length of the infinite elements L_{inf} is taken equal to L_f . Since, in a sense, the examined footing is a very short pile, the radius of the axisymmetric model was chosen on the basis of Model I (Figure 3.1(b)). Appropriate boundary conditions are applied on the axis of symmetry. A unit uniform vertical displacement is imposed on all points of the bottom surface of the footing, with the load reference point being located at the center-point on the symmetry axis.

The fineness of the mesh is characterized by the finite-element size L_{FE} prevailing at the largest part of the model. A refined region in the vicinity of the foundation can be distinguished in Figure 3.10, with a two times finer discretization (in the horizontal direction) in comparison with the rest of the mesh with L_{FE} . This refined region includes the footing as well, and is extended from its edge by a distance equal to R . In the initial model, the finite-element size is taken as $L_{FE} = 0.5$ m, while in the refined region this value is half. This 2:1 mesh ratio between the main part of the model and the refined region is kept constant for all cases considered herein. For example, in analyses with $L_{FE} = 0.25$ m, the finite-element size in the refined region is equal to 0.125 m.

The soil properties are kept the same as in Section 3.1.1. Accordingly, the initial highest excitation frequency applied is $f = 13$ Hz. However, since in the frame of the current parametric study, the mesh is varied too, analyses involving finer discretized models consider frequencies up to $f = 26$ Hz, as shown in the sequel.

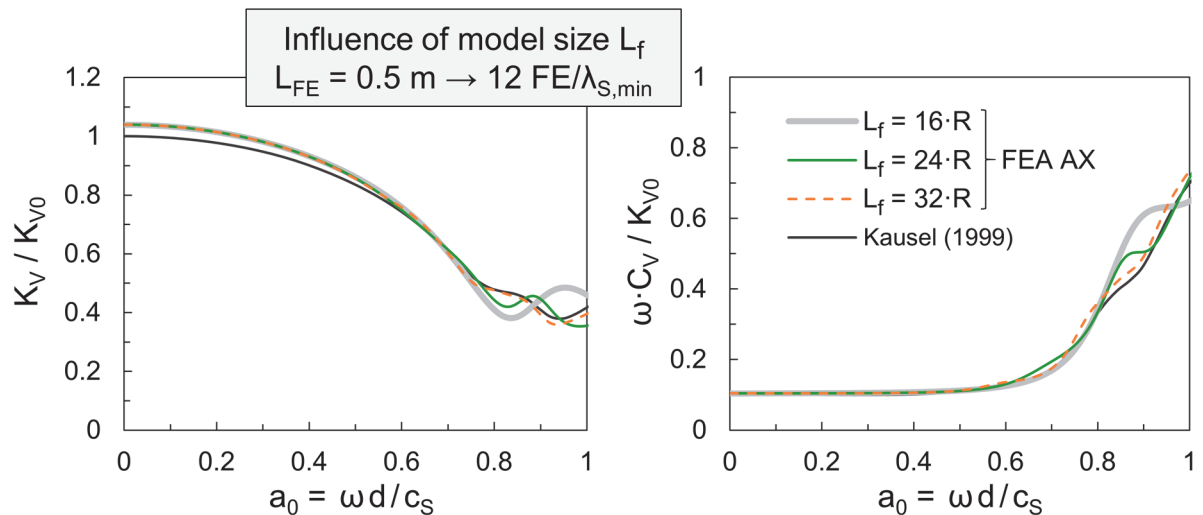


Figure 3.11: Influence of the model size on the vertical dynamic impedance of a footing with $l/d = 2$ embedded in a soil stratum with thickness $H = 2 \cdot l$; $\nu = 0.4$.

3.2.2 Results

Figure 3.11 depicts the vertical dynamic impedance of the embedded footing derived from axisymmetric models with varying model size, but with a constant mesh discretization ($L_{FE} = 0.5$ m) corresponding to approximately 12 finite elements per S-wavelength λ_S at the highest excitation frequency $f = 13$ Hz ($a_0 = 1$). The FEA results are compared to the rigorous solution obtained with the code SUPELM (Kausel, 1999), which requires discretization only in the vertical direction, while accounting for a perfect wave attenuation in the lateral direction. All dynamic stiffnesses are normalized by the vertical static stiffness from Kausel (1999) denoted as K_{V0} .

The response up to $a_0 = 0.6$ is almost independent from the model radius L_f . The small deviation from the rigorous solution detected at quasi-static conditions tends to disappear as the excitation frequency increases. As expected, at higher frequencies, the model with the smallest radius $L_f = 16 \cdot R$ yields the least accurate results. By increasing the model size, the agreement with the rigorous solution improves. In fact, in the case of $L_f = 32 \cdot R$ an almost perfect match is accomplished.

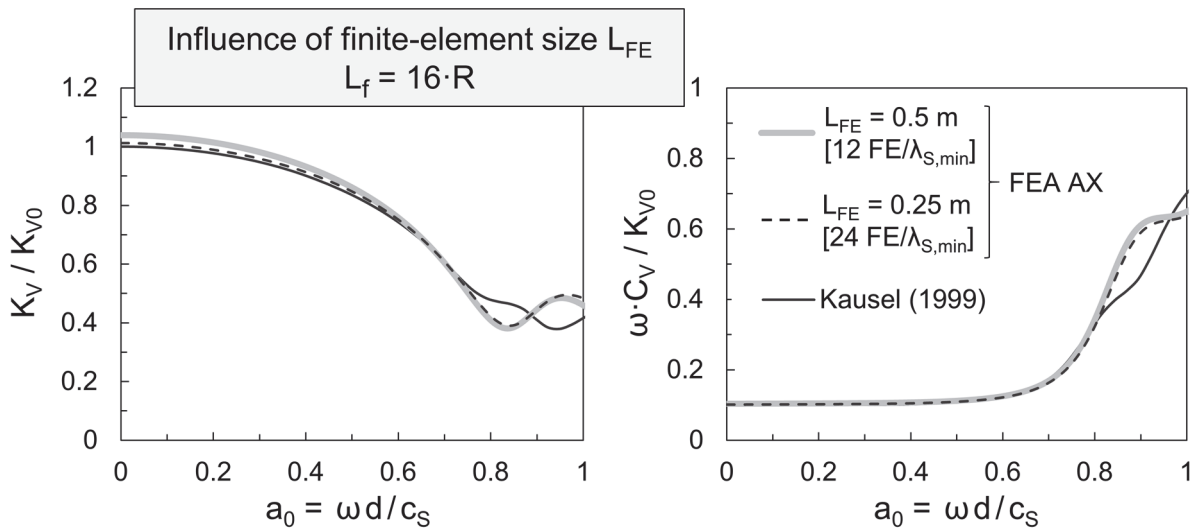


Figure 3.12: Influence of the mesh fineness on the vertical dynamic impedance of a footing with $l/d = 2$ embedded in a soil stratum with thickness $H = 2 \cdot l$; $\nu = 0.4$.

To examine whether the mesh fineness could be the culprit behind the discrepancies in the range $a_0 = 0.75 - 1$ in the case of the axisymmetric model with $L_f = 16 \cdot R$, a mesh twice as fine as the initial one is implemented. As shown

in Figure 3.12, the results at these high frequencies are practically insensitive to the mesh fineness. Nevertheless, the finer mesh has a positive influence on the accuracy at low frequencies. In specific, the system becomes “softer”, which leads to a slightly reduced stiffness at quasi-static conditions.

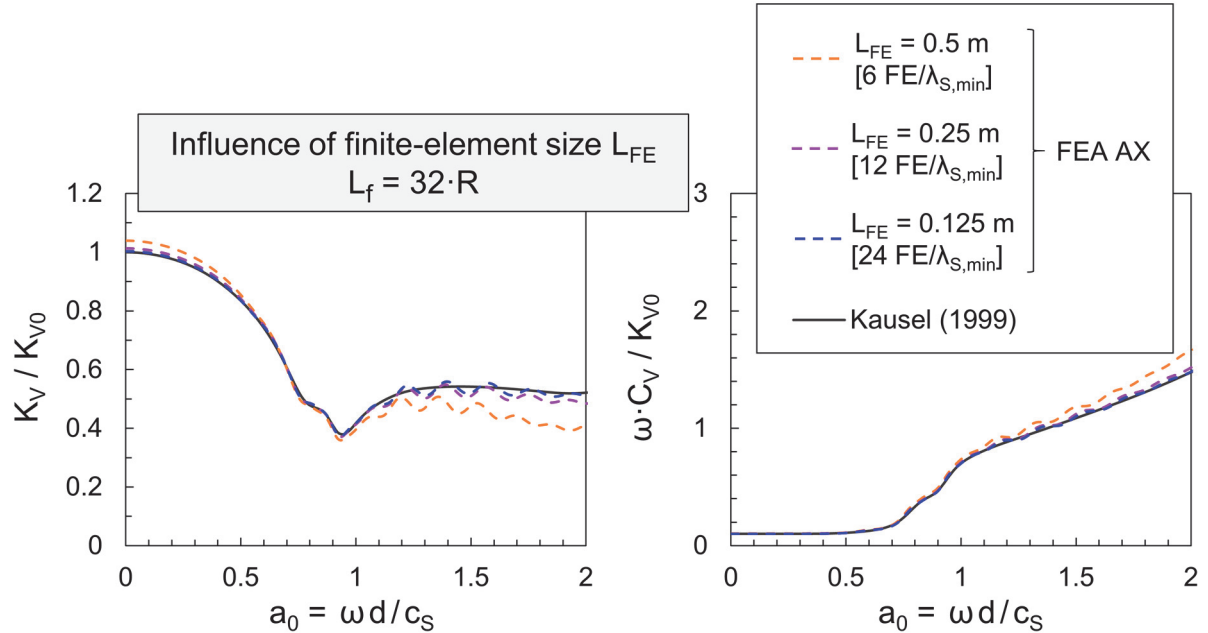


Figure 3.13: Influence of the mesh fineness on the vertical dynamic impedance of a footing with $l/d = 2$ embedded in a soil stratum with thickness $H = 2 \cdot l$; $\nu = 0.4$.

Based on the above observations, the optimal model is the one with $L_f = 32 \cdot R$. The next step is to explore the influence of the mesh discretization in the specific model. Starting from a mesh with $L_{FE} = 0.5 \text{ m}$, two additional refinement schemes are implemented by respectively halving the initial finite-element size. Note that since a finer mesh is applied, the new systems can support higher excitation frequencies by reproducing the associated smaller wavelengths. Consequently, the highest excitation frequency applied is increased from $f = 13$ to 26 Hz , with the latter yielding $a_0 = \omega d / c_S = 2$. Figure 3.13 compares the results for the three discretization degrees. As already shown in the previous case of $L_f = 16 \cdot R$ in Figure 3.12, with finer mesh, the match with the rigorous solution improves further at low frequencies. Up to $a_0 = 1$, which was the initial target, all three configurations yield similar results achieving a very good match with Kausel (1999). Beyond this point, however, the agreement deteriorates considerably with coarser mesh. Indicatively, the deviation of the curve obtained with the model with $L_{FE} = 0.5 \text{ m}$ from the rigorous solution reaches

approximately 20 % at $a_0 = 2$. For this specific combination of mesh and excitation frequency, an S-wavelength can be captured by about 6 finite elements, which is apparently an insufficient number. The other two finer discretization schemes yield considerably improved results; yet, in both cases a fluctuation is observed in the response, mostly in the dynamic stiffness component.

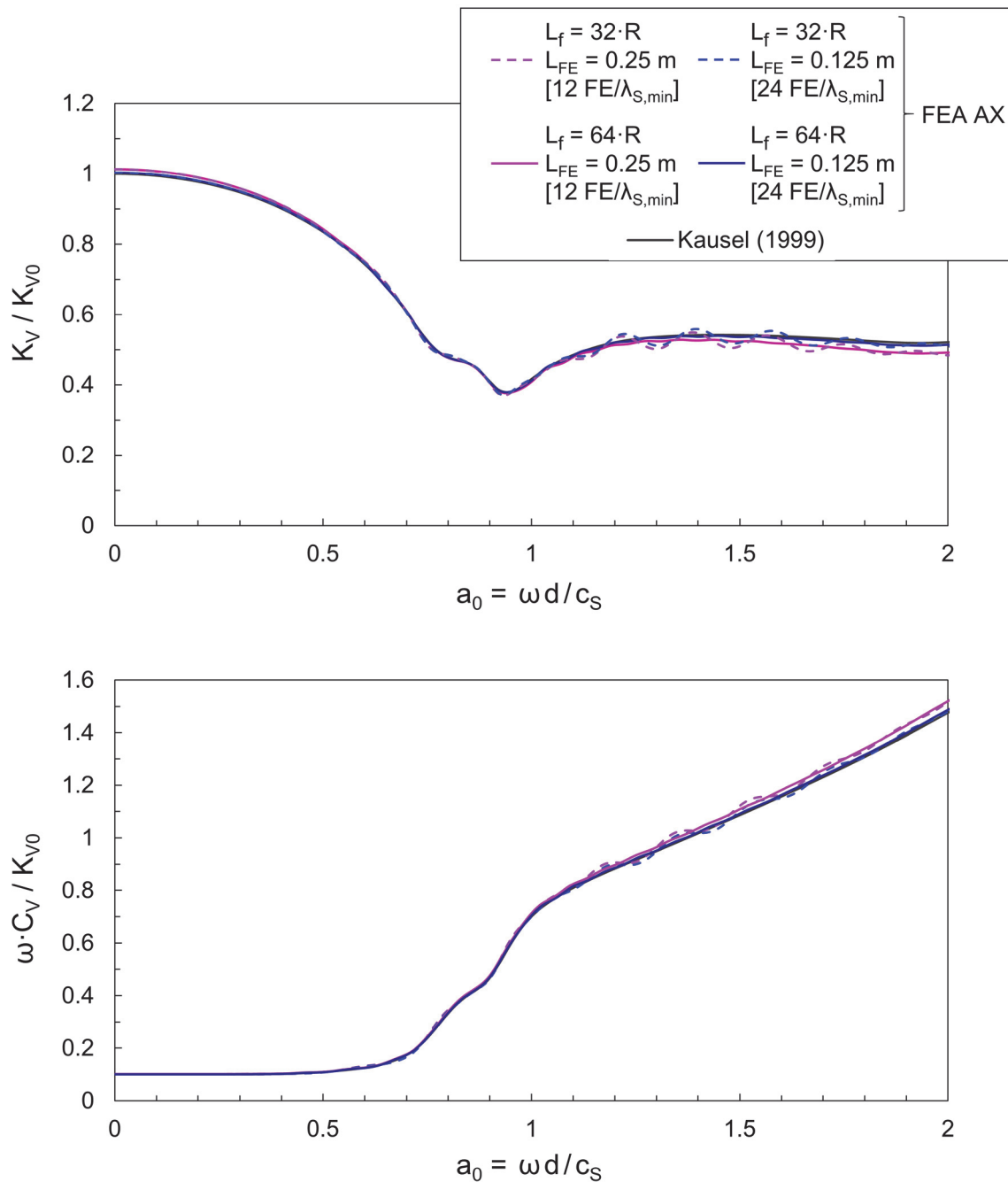


Figure 3.14: Influence of model size/mesh fineness on the vertical dynamic impedance of a footing with $l/d = 2$ embedded in a soil stratum with thickness $H = 2 \cdot l$; $\nu = 0.4$.

Obviously, having considered a very fine mesh with $L_{FE} = 0.125$ m excludes the possibility of the fluctuation in the curves being an outcome of inadequate mesh discretization. To examine whether the model size affects in that way the response at high frequencies, a further axisymmetric model was created with $L_f = 64 \cdot R$, twice as large as the optimal model in the longitudinal direction. The two finer discretization schemes ($L_{FE} = 0.25$ m and 0.125 m) as in the case of the optimal model are considered. Indeed, as Figure 3.14 reveals, the largest models eliminate the fluctuations, yielding smooth curves in the complete frequency range. The model with $L_f = 64 \cdot R$ and $L_{FE} = 0.125$ m exhibits practically no differences from Kausel (1999). Note that analyses with a 3D model with these characteristics are computationally challenging.

Moreover, attention is drawn to the valley in the vertical dynamic stiffness curves, which can be distinguished at $a_0 \approx 0.95$. To shed light into the physical meaning behind this, the one-dimensional amplification theory is employed for the calculation of the eigenfrequencies of a soil stratum with thickness H excited by vertically propagating P- or S-waves, which are given by the following formula:

$$f_n = (2 \cdot n - 1) \frac{c}{4 \cdot H}, n = 1, 2, 3, \dots \quad (3.1)$$

where the velocity c is equal to c_P or c_S for P- or S-wave excitation, respectively.

Note that the above expression refers to systems with zero hysteretic damping. Moreover, the soil stratum considered herein involves a massless, rigid footing being a local excitation source. Nevertheless, Equation (3.1) can be useful for roughly determining the eigenfrequencies of the actual system.

In the examined configuration, the soil stratum has a thickness $H = 2 \cdot l = 4$ m, and a P-wave velocity $c_P = 194.46$ m/s. Subsequently, its first eigenfrequency ($n = 1$) under P-wave excitation is $f_1 = 12.15$ Hz corresponding to $a_0 = 0.96$, which almost coincides with the frequency at which the valley appears. Practically, this suggests that the inertial loading at this frequency activates the first eigenmode of system for P-wave excitation. Due to resonance, the footing follows the soil movement. As a result, the force required for the embedded footing to resist the imposed displacement drops significantly.

In the extended frequency range up to $a_0 = 2$ considered herein (Figures 3.13 and 3.14), solely a single valley manifests itself in the response. Indeed, the second

eigenfrequency according to Equation (3.1) is $f_2 = 36.46$ Hz, which lies above the upper limit in the present study defined by $f = 26$ Hz.

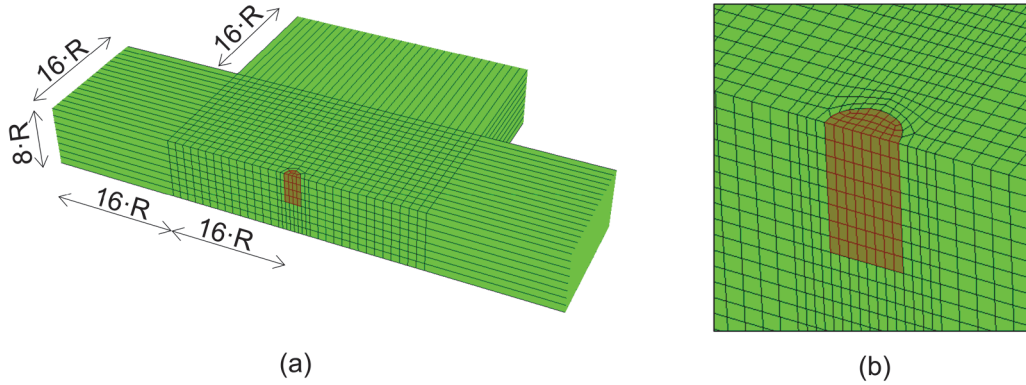


Figure 3.15: (a) 3D Finite-element model with $L_f = 16 \cdot R$ and $L_{FE} = 0.5$ m; (b) Details of the 3D FE model with $L_f = 32 \cdot R$ and $L_{FE} = 0.25$ m.

Finally, the effect of three-dimensionality on the results is explored. Even though the axisymmetric analyses reflect the actual problem of the vertical inertial loading considered herein, axisymmetric elements are based on a formulation different from the one for typical brick elements in 3D models. For this purpose, two 3D finite-element models with $L_f = 16 \cdot R$ and $L_f = 32 \cdot R$ were created with $L_{FE} = 0.5$ m and $L_{FE} = 0.25$ m, respectively. The first model, as well as details of the second one are portrayed in Figure 3.15. The vertical impedances derived from the corresponding axisymmetric and 3D models are presented in Figures 3.16 and 3.17. Interestingly, the curves from the 3D models are smooth. In the case of $L_f = 32 \cdot R$, the fluctuation detected in the response calculated with the axisymmetric model is eliminated when conducting 3D analyses.

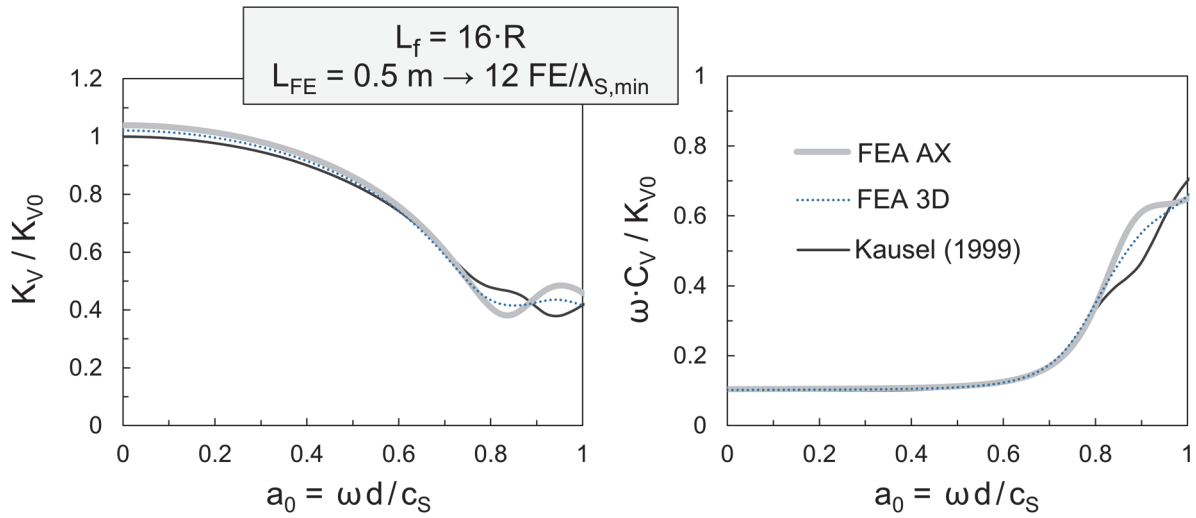


Figure 3.16: 3D vs. AX conditions: Vertical dynamic impedance of a footing with $l/d = 2$ embedded in a soil stratum with thickness $H = 2 \cdot l$; $\nu = 0.4$.

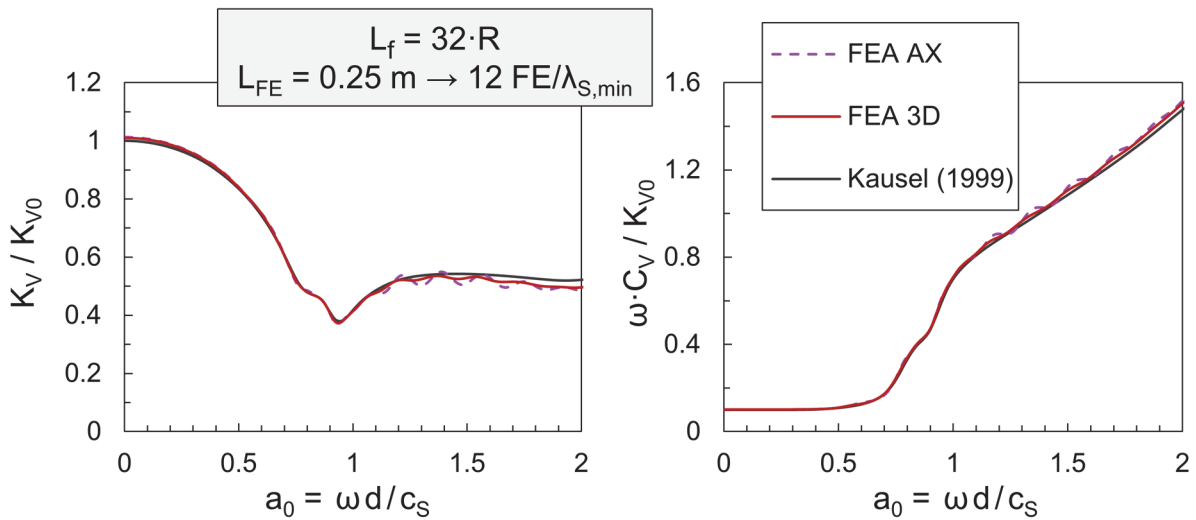


Figure 3.17: 3D vs. AX conditions: Vertical dynamic impedance of a footing with $l/d = 2$ embedded in a soil stratum with thickness $H = 2 \cdot l$; $\nu = 0.4$.

It is deduced that the 3D model with a finite-element region size of $L_f = 32 \cdot R$ and a finite-element size $L_{FE} = 0.25 \text{ m}$ (12 finite elements per λ_S for the highest excitation frequency $f = 26 \text{ Hz}$) is ideal for the calculation of dynamic impedances of the deeply embedded footing with respect to both accuracy and computational time. With it, further analyses are conducted to derive the horizontal as well as the rocking impedance.

Figure 3.18 shows the results for the horizontal dynamic impedance of the footing compared to those from Kausel (1999). Both the real and imaginary part are normalized by the horizontal static stiffness K_{H0} from Kausel (1999). Overall, the FEA results match the rigorous solution quite well. Discrepancies become more pronounced as the excitation frequency increases. The dynamic stiffness derived from the FEA exhibits a local peak at $a_0 \approx 0.55$, while the dashpot coefficient curve is also locally slightly unstable.

To elucidate the presence of the valley in the dynamic stiffness, Equation (3.1) is once again employed, yet, by introducing the S-wave velocity in the soil c_s . This is because the horizontal inertial loading of the footing excites the soil stratum in a similar manner as vertically propagating S-waves during a seismic event. As a first eigenfrequency under S-wave excitation, Equation (3.1) yields $f_1 = 4.96$ Hz. The valley in the numerical results for the soil stratum including the embedded footing is present at $a_0 \approx 0.43$, which corresponds to $f \approx 5.49$ Hz. The deviation from the analytical solution is equal to approximately 10 %, confirming that the valley is an outcome of resonance.

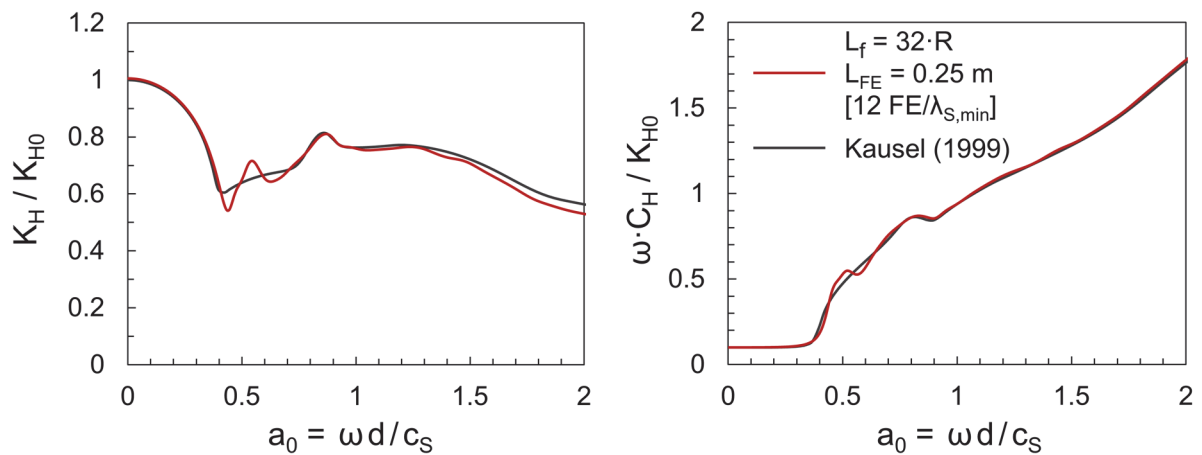


Figure 3.18: Horizontal dynamic impedance of a footing with $l/d = 2$ embedded in a soil stratum with thickness $H = 2 \cdot l$; $\nu = 0.4$.

Similarly, the rocking impedance is shown in Figure 3.19. A slightly unstable response can be noticed in the range $a_0 \approx 0.4 - 0.7$; nevertheless, the finite-element results match very well the solution from Kausel (1999). Negligible differences in the dynamic stiffness are also evident at higher frequencies, with the maximum being equal to 6 %.

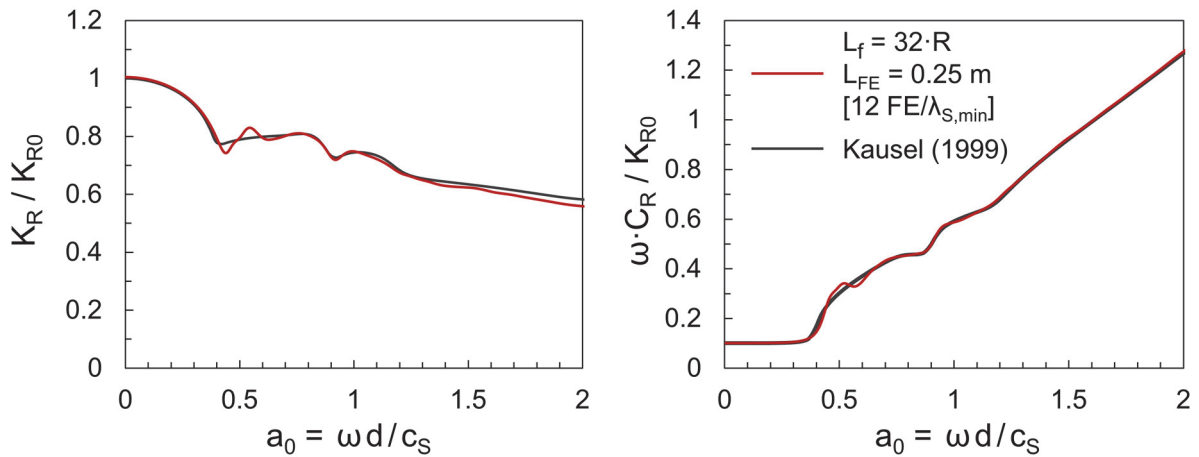


Figure 3.19: Rocking dynamic impedance of a footing with $l/d = 2$ embedded in a soil stratum with thickness $H = 2 \cdot l$; $\nu = 0.4$.

Lastly, it is pointed out that the dynamic stiffnesses of the embedded footing derived from the FEA are in remarkable agreement with the rigorous results at low frequencies. Recall, on the other hand, in Section 3.1.2, the significant deviations of the dynamic stiffnesses of the pile groups as static conditions are approached. Despite the fact that the two foundation systems are different, a key aspect in the modelling is that the footing is embedded in a soil stratum, while the piled foundations in a half-space. The assumption of a soil stratum resting on a rigid substratum suggests a straightforward boundary condition at the base of the model in contrast with the absorbing boundaries (e.g. infinite elements) used in the case of a half-space, the actual contribution of which is impossible to quantify. Apparently, it is the boundary condition at the base that is of critical importance for all modes of oscillation. Even though the models for the embedded footing include infinite elements peripherally, these do not seem to have an influence on the lateral response at low frequencies.

3.3 Conclusions

To gain insight into the mechanics of the problem of inertial loading of piled foundations, direct-solution steady-state dynamic analyses were performed in the frequency domain using the finite-element code Abaqus. Dynamic impedances were calculated for all vibration modes (vertical, horizontal and rocking). Furthermore, to elucidate details in modelling, a parametric study on the inertial response of a deeply embedded footing was also presented with respect to the

optimization of the finite-element model. In both examples, rigorous solutions were employed to verify the results.

The inertial response of a 4x4 pile group is contrasted to that of a corresponding piled raft in which the raft is in perfect contact with the underlying soil. A close as well as a wider pile spacing is considered. Both pile foundations are embedded in a half-space, whereas the deeply embedded footing is in a soil stratum. The following conclusions are drawn:

- In the case of closely spaced piles, the dynamic impedances of the pile group are practically equal to those of the piled raft for all vibration modes. The cause of this similarity lies on the overlap of the influence zones of the piles, prohibiting the raft in the case of the latter to participate in the load sharing.
- Even in the case of the wide pile spacing, the inertial response of both systems exhibits remarkable similarities up to $a_0 \approx 0.4$ for all modes of oscillation. While at higher frequencies this is not the case, as static conditions are approached, the influence zones of the piles expand due to the associated large wavelengths, and overlap despite the wider pile-to-pile distance.
- When simulating a half-space, the use of infinite elements as absorbing boundaries at the base of the model can be problematic in dynamic analyses at low frequencies or static analyses. It is possible to overcome this issue by increasing the distance of the boundary from the region of interest.
- With respect to the point above, when performing dynamic analyses for a half-space over a wide frequency range, it is suggested to employ at least two finite-element models, each properly adapted (model size, mesh fineness) to the requirements of the corresponding frequency range. Hence, not only the accuracy of the results is improved, but also computational costs can be significantly reduced.
- In models for static analyses, it is recommended to completely avoid the use of infinite elements to simulate a half-space. Instead, conventional boundaries can be used at a sufficient distance from the region of interest without compromising accuracy.
- The analyses considering a soil stratum resting on a rigid substratum, yield accurate results even at very low frequencies, in contrast to those assuming a half-space as explained above. The key difference between

the pertinent models lies on their base, which, in the case of the soil stratum, is fixed in all directions – a straightforward boundary condition. It is then deduced that the less accurate response at low frequencies detected in the case of the half-space is due to the infinite elements used at the base of the model, and not due to those placed peripherally, since the latter are also present in the soil stratum models.

4 Single piles and pile groups in the wave field of a moving load

In this chapter, the focus is placed on the kinematic response of single piles and pile groups to a wave field emanating from a distant vertical harmonic point load travelling with a constant speed on the surface of the soil. Moreover, the problem of a stationary harmonic point load is also considered as a lower-bound scenario corresponding to a travelling speed equal to zero. The finite-element analyses are carried out in the time domain targeting a range of high frequencies relevant for the vibration protection practice. Finally, a comparison is presented with a simple analytical solution on the pile response to a Rayleigh wave field. The main idea behind these analyses is to answer the following questions:

- Can a *stationary* harmonic load be a rational approximation of a *moving* harmonic load?
- At which distance from a vertical harmonic point load is the assumption of far-field conditions valid?
- For which cases of practical interest can the existing solution for piles under Rayleigh wave excitation be implemented?

Thus, not only useful solutions for the engineering practice are provided, but also valuable insight is gained into the problem of indirect harmonic loading of piled foundations.

4.1 Single pile in a Rayleigh wave field – Winkler model

To date, little attention has been paid to the dynamic response of a single pile in a Rayleigh wave field. An exception is the study of Makris (1994), who presented a simple analytical method based on a Winkler model with frequency-dependent springs (k_z) and dashpots (c_z) to account for the soil–pile interaction. The key points of the method are summarized in the present section.

A floating pile with length l , diameter d , density ρ_p and Young's modulus E_p , harmonically excited through a Rayleigh wave field, is assumed. The excitation frequency is denoted as f , with the circular frequency being $\omega = 2 \cdot \pi \cdot f$. Only the vertical component of the oscillation is presented, since it is of greater importance for the practice of vibration protection. The pile is embedded in a homogeneous half-space characterized by a density ρ and a shear-wave (S-wave)

velocity c_s or, alternatively, by a shear modulus G and a Poisson ratio ν . The Young's modulus of the soil is $E = 2 \cdot G \cdot (1 + \nu)$.

According to the wave propagation theory (Achenbach, 1973; Graff, 1975), the variation of the vertical displacement w of the free-field due to the passage of Rayleigh waves can be expressed as:

$$w(z) = w_1 e^{-\alpha_1 z} + w_2 e^{-\alpha_2 z} \quad (4.1)$$

where

$$w_1 = -\sqrt{1 - \psi_P^2}, \quad w_2 = \gamma \quad (4.2)$$

$$\alpha_1 = \frac{\omega}{c_R} \sqrt{1 - \psi_P^2}, \quad \alpha_2 = \frac{\omega}{c_R} \sqrt{1 - \psi_S^2} \quad (4.3)$$

$$\psi_S = \frac{c_R}{c_S}, \quad \psi_P = \frac{c_R}{c_P} = \psi_S \sqrt{\frac{1 - 2\nu}{2(1 - \nu)}} \quad (4.4)$$

$$\gamma = \frac{2 - \psi_S^2}{2\sqrt{1 - \psi_S^2}} \quad (4.5)$$

with c_R being the Rayleigh wave velocity, and c_p the dilatational wave (P-wave) velocity in the soil, respectively.

The interaction between pile and soil is taken into account by means of a series of Winkler springs and dashpots, as portrayed in Figure 4.1. The method from Makris (1994) utilizes the following algebraic expressions for the spring and dashpot coefficients, which were developed by matching the dynamic head displacement from Winkler and finite-element analyses for a Poisson's ratio of $\nu = 0.4$ (Gazetas & Makris, 1991):

$$k_z = 0.6 \cdot E \cdot (1 + 0.5 a_0^{0.5}) \quad (4.6)$$

$$c_z = c_{z\text{radiation}} + c_{z\text{hysteresis}} = 1.2 \cdot \pi \cdot a_0^{0.25} \cdot \rho \cdot c_s \cdot d + 2 \cdot \xi \cdot \frac{k_z}{\omega} \quad (4.7)$$

where a_0 is the dimensionless frequency defined as:

$$a_0 = \frac{\omega \cdot d}{c_s} \quad (4.8)$$

and ξ is the hysteretic damping ratio in the soil. Note that one of the approximations in the derivation of the Equations (4.6) and (4.7) for the spring

and dashpot coefficient, respectively, is to neglect the pile slenderness and flexibility reflected by the terms l/d and E_p/E , respectively.

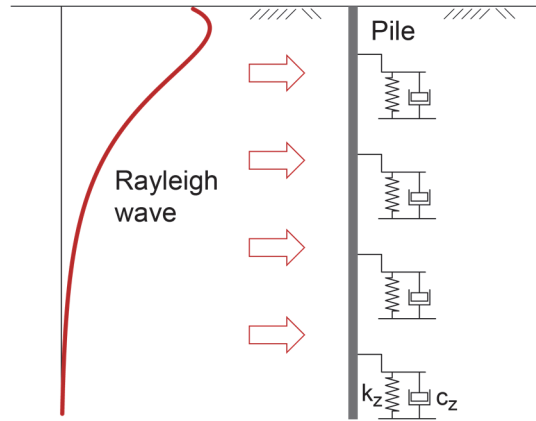


Figure 4.1: Single pile in a Rayleigh wave field.

From the differential equation from Makris (1994) for the vertical displacement at the pile head, and with appropriate boundary conditions (no stresses at pile head and pile tip), an expression in explicit form for the vertical displacement amplitude $w_p(0)$ at the pile head is derived:

$$w_p(0) = \frac{\varepsilon_z}{\delta \cdot \sinh(\delta \cdot l)} [(h_1 + h_2) \cosh(\delta \cdot l) - (h_1 \cdot \exp(-a_1 \cdot l) + h_2 \cdot \exp(-a_2 \cdot l))] - \varepsilon_z \left(\frac{h_1}{a_1} + \frac{h_2}{a_2} \right) \quad (4.9)$$

where

$$h_1 = \frac{w_1 \cdot a_1}{a_1^2 - \delta^2}, \quad h_2 = \frac{w_2 \cdot a_2}{a_2^2 - \delta^2} \quad (4.10)$$

$$\varepsilon_z = \frac{k_z + i \cdot \omega \cdot c_z}{E_p \cdot A_p} \quad (4.11)$$

$$\delta^2 = \frac{k_z + i \cdot \omega \cdot c_z - m_p \cdot \omega^2}{E_p \cdot A_p} \quad (4.12)$$

with i being the imaginary unit, m_p the mass of the pile, and A_p the cross-sectional area of the pile ($A_p = \pi \cdot d^2/4$).

Representative results in terms of transfer functions relating herein the vertical displacement amplitude at the center of the pile head $|w_p(0)|$ to that of the free-field $|w_{ff}(0)|$ at the same location, are provided in Figure 4.2. First, one can notice the strong dependency of the transfer function on frequency. Apart from this, though, the pile slenderness l/d and flexibility E_p/E also play a major role. For the vibration protection practice, these conclusions are of particular importance.

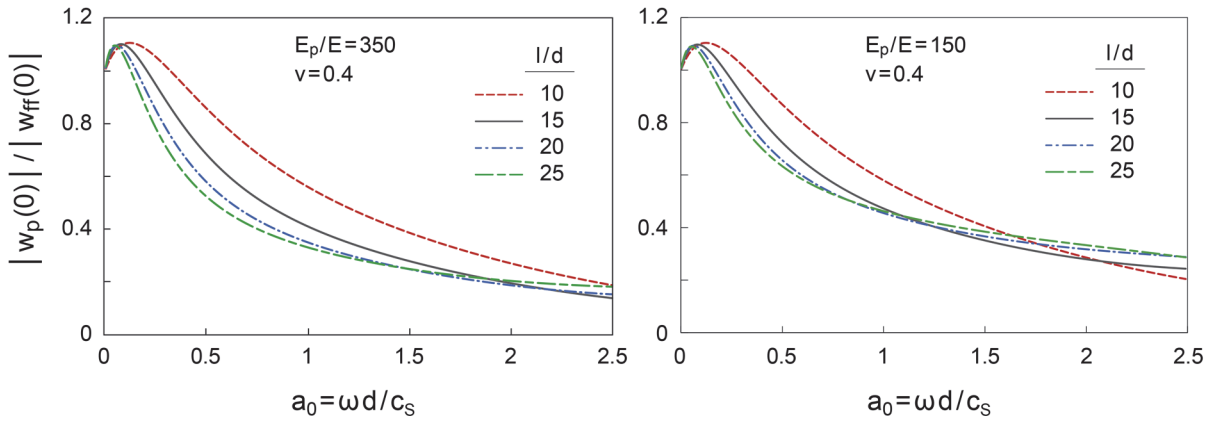


Figure 4.2: Vertical transfer function dependent on dimensionless frequency according to Equation (4.9).

4.2 Excitation due to a vertical harmonic point load – Finite-element method

4.2.1 Modelling of the near-field

The resulting wave field due to a dynamic excitation source, e.g. a vertical harmonic point load, acting on the surface of a half-space, involves *body waves* (P- and S-waves) as well as *Rayleigh waves*. As schematically illustrated in Figure 4.3 (redrawn from Woods (1968)), body waves travel into the soil along a hemispherical wave front, while Rayleigh waves spread out radially outward along a cylindrical wave front. At the surface of a half-space, the amplitude of body waves is proportional to $1/r^2$, with r being the distance from the source of excitation. The amplitude of Rayleigh waves, on the other hand, is proportional to $1/r^{0.5}$, which signifies that the attenuation of Rayleigh waves is slower. Essentially, this means that at a distance from the excitation source, while body waves will have completely dissipated, Rayleigh waves will still be further propagating. The area, where only Rayleigh waves are present, is defined as the far-field.

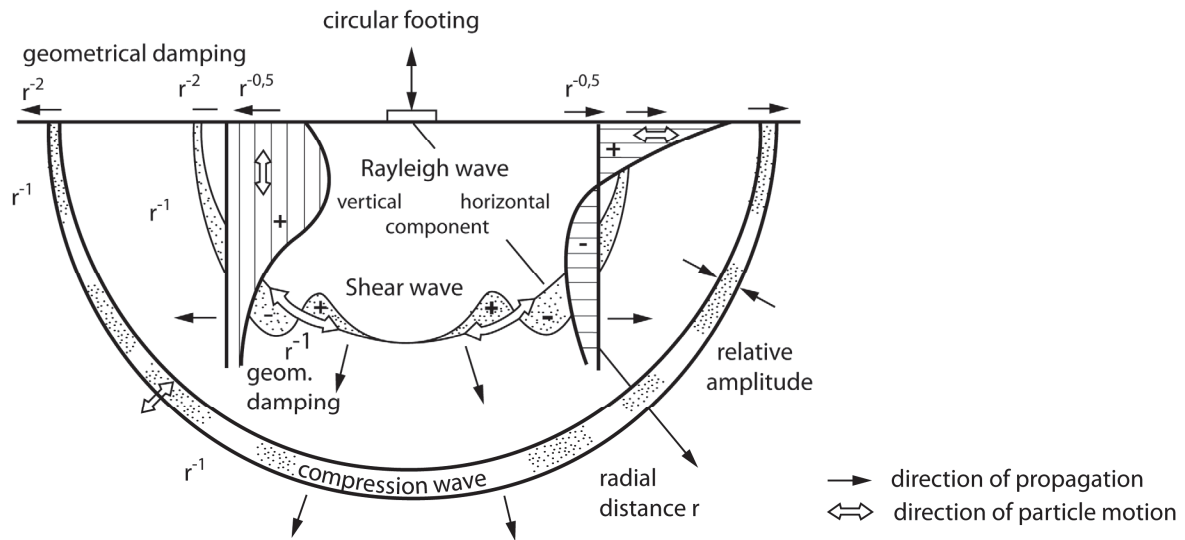


Figure 4.3: Distribution of waves from a circular footing (Woods, 1968).

Numerical limitations associated with the size of a 3D finite-element model do not allow the perfect simulation of far-field conditions with complete wave attenuation at large distances. Nevertheless, it is certainly useful for practical applications to (even roughly) determine a distance from the excitation source, up to which body waves will have dissipated to a significant extent, with Rayleigh waves dominating further on.

For this purpose, a finite-element model accounting for near-field conditions has been created with the software Plaxis 3D (2021). With this model, the dynamic response of: (a) the free-field, (b) a pile group and (c) a single pile in the wave field emanating from a distant vertical harmonic point load is investigated. The numerical analyses are conducted in the time domain. Taking advantage of symmetry, only half of the problem is simulated. The model including the 3x3 pile group (in absence of a pile cap), as well as aspects of the finite-element discretization are depicted in Figure 4.4. By simply replacing in the model all piles with soil, the free-field response is obtained. In a similar manner, to calculate the single pile response, only the pile of interest located at the face of symmetry remains active, while the rest of the piles are substituted by soil.

A top view of the 3x3 pile group geometry is given in Figure 4.5. Furthermore, the highlighted in grey front and furthest-back central piles, referred to as P3 and P1, respectively, serve as reference piles for which transfer functions are derived. The distance between the point load and a reference pile in the group or a single

pile is denoted as x_0 . More specifically, a single pile is considered at a varying distance $x_0 = 4, 8, 12, 16$ m from the load.

An optimized model size is selected, with the vertical harmonic point load placed asymmetrically. Since the focus lies on the response of the pile group and free-field next to the load, only the respective side of the model needed to be sufficiently extended to ensure minimum reflections at the boundary. Boundary conditions preventing the out-of-plane movement of the vertical plane of symmetry are implemented. The model has a depth of 20 m. To simulate a half-space, viscous boundaries have been placed peripherally and at the base. These special boundaries, promising to absorb incident waves, are based on the theory of Lysmer & Kuhlemeyer (1969). For the simulation of a soil stratum on a rigid substratum, the base of the model is “fixed” in all three coordinate directions.

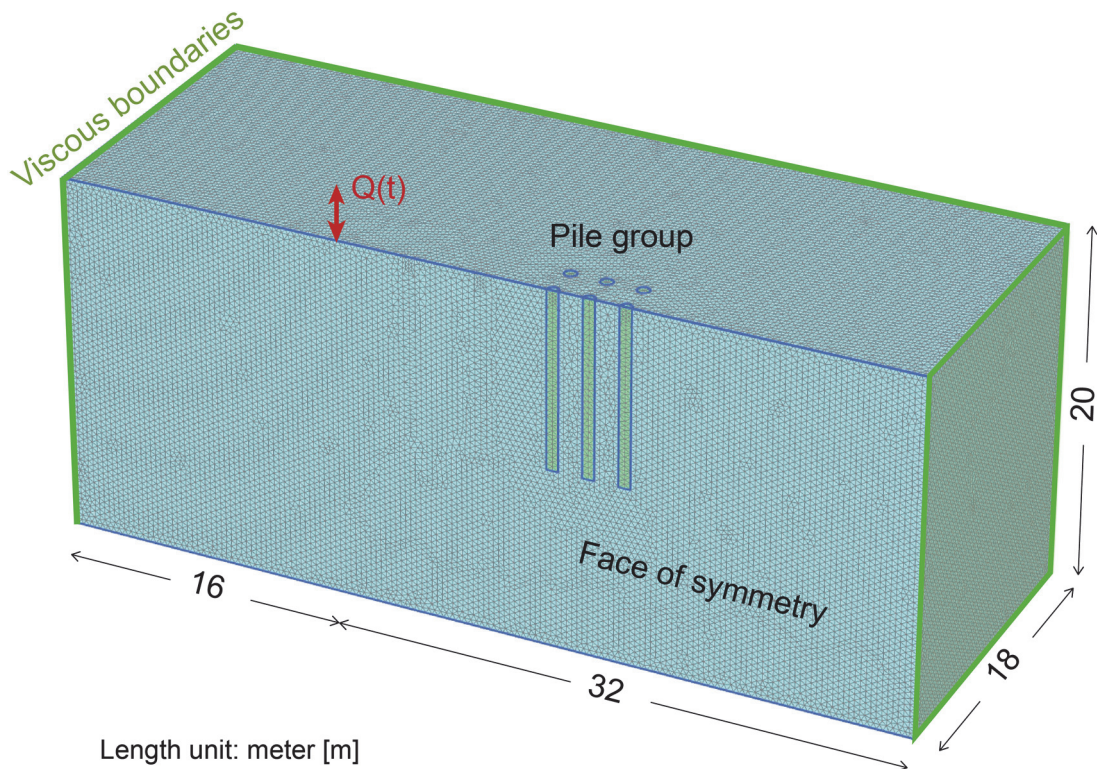


Figure 4.4: Three-dimensional finite-element model with a 3x3 pile group (in absence of a pile cap).

The soil is modelled as a linear-elastic continuum with a shear modulus $G = 30.5$ MPa, a density $\rho = 1.89$ Mg/m³ and a Poisson’s ratio $\nu = 0.4$, resulting in a shear wave velocity in the soil $c_s = 127$ m/s and a Rayleigh wave velocity $c_R = 120$ m/s. Furthermore, a Rayleigh-type damping is introduced in the soil.

Since this type of damping is frequency-dependent, it was suitably selected to correspond to a hysteretic damping of approximately $\xi = 1\%$ for the frequencies of interest lying between 15 and 45 Hz. The pertinent Rayleigh damping parameters (α and β) inherent to time-domain computation (Kausel, 2017) attain the values $\alpha = 1.555$ and $\beta = 0.05836 \cdot 10^{-3}$. The Poisson's ratio $\nu = 0.4$ is chosen to be in accordance with the assumed value in the spring and dashpot coefficients (Equations (4.6) and (4.7)) in the method from Makris (1994), with which a comparison is presented in the sequel.

For the piles, which consist of volume elements, a length equal to $l = 10$ m and a diameter $d = 0.67$ m are selected, resulting in a ratio $l/d = 15$. A linear-elastic material is assigned to the piles with a Young's modulus $E_p = 30$ GPa, a Poisson's ratio $\nu_p = 0.2$ and a unit weight $\gamma_p = 25$ kN/m³ corresponding to concrete. For the main configuration examined herein, this yields $E_p/E = 350$ and $\rho_p/\rho = 1.35$. The piles are in a fully bonded contact with the surrounding soil, allowing no slippage or detachment.

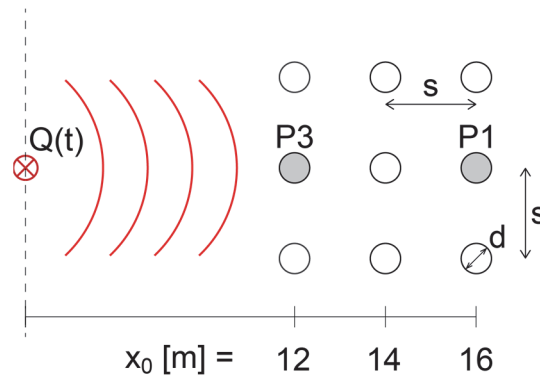


Figure 4.5: Top view of the problem of indirect loading of a 3x3 pile group.

Both soil and piles are modelled with 10-node tetrahedral elements providing a second-order interpolation of displacements.

The basic configuration targets an excitation frequency equal to $f = 30$ Hz. Additional frequencies between 20 and 40 Hz are also considered. Dynamic analyses require an adequate degree of mesh discretization that depends on the applied frequency of excitation. As a rule of thumb, a minimum number of 5 finite elements is required in order to reproduce a wavelength. Herein, the finest possible mesh was created with an approximate element size equal to 0.35 m, which at $f = 30$ Hz corresponds to about 11 finite elements per Rayleigh wavelength λ_R .

The total duration of each dynamic analysis was set equal to 0.67 s, which involves 20 cycles of dynamic loading at $f = 30$ Hz. The time-step is equal to 0.001675 s. Consequently, at $f = 30$ Hz, approximately 20 data points reproduce one dynamic cycle. Since the time-step is kept constant for all dynamic analyses, at higher frequencies the number of data points for one dynamic cycle drops (e.g. about 15 data points correspond to a dynamic cycle at $f = 40$ Hz), which slightly impairs accuracy. Accordingly, this is reversed at lower frequencies.

When conducting an analysis in the time domain, the system requires a certain number of cycles to reach a steady-state. In our case, for example, at $f = 30$ Hz this is accomplished after approximately 15 cycles of dynamic loading at the source. The displacement amplitude is determined as the average of the maximum and absolute minimum value of the response after the steady-state response has been reached. The deviation is yet negligible.

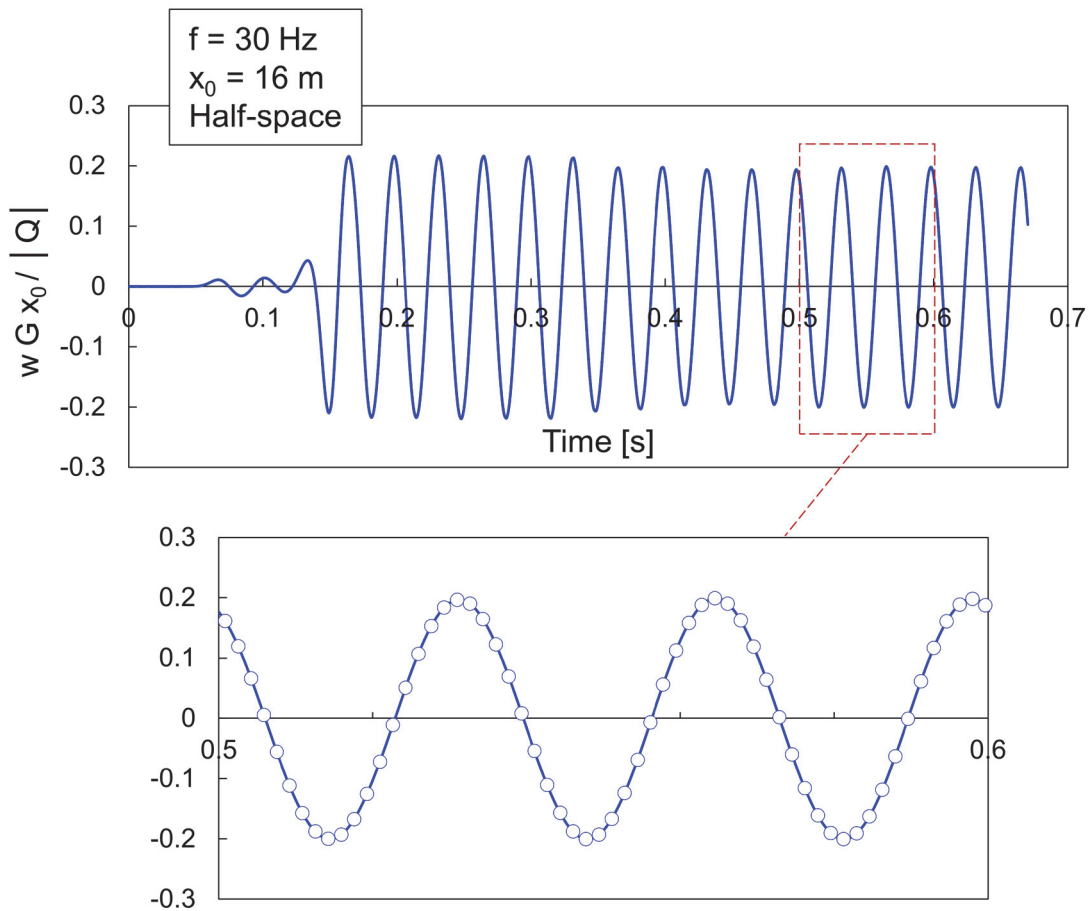


Figure 4.6: Vertical displacement time-history at a distance of $x_0 = 16$ m from the load with an excitation frequency $f = 30$ Hz. 3D FE model; half-space.

Indicatively, Figure 4.6 shows the displacement time-history at a distance of $x_0 = 16$ m from the load at a frequency $f = 30$ Hz, as derived from the 3D model for half-space. Although the oscillation of the load starts at the beginning of the dynamic analysis, the emanating waves do not instantly reach the observation point. Subsequently, there is practically no motion at $x_0 = 16$ m at the first part of the time-history, with the number of recorded cycles being understandably less than 20, which, as stated earlier, is the applied input for the excitation source. Furthermore, the displacement amplitude begins to stabilize after 0.35 s, indicating that the particular system requires at least this amount of time in order to reach a steady-state. Finally, in the enlarged selected time-window one can identify the data points obtained from the analysis.

Any displacement profiles with depth shown herein are obtained at a time-step during the steady-state response, at which the displacement at the surface attains its maximum value.

4.2.2 Modelling of the far-field

Apart from the 3D finite-element model previously described, an axisymmetric model was created in Plaxis 2D (2021) in order to calculate the response of the free-field under Rayleigh wave excitation. Due to the symmetry of the problem, this type of simulation of the free-field leads to considerable computational savings in comparison with a respective 3D analysis. In this axisymmetric model, the peripheral viscous boundary is placed at a sufficiently large distance from the excitation source, since the goal is to determine the distance from the harmonic point load, at which far-field conditions can be assumed as an acceptable approximation. For this purpose, a comparison with the analytical solution for the far-field is presented.

The same depth as in the 3D model, namely $H = 20$ m, is selected. Since the analytical solution for Rayleigh wave excitation refers to a half-space, viscous boundaries are implemented at the base of the model. Two model radii are tested. Apart from the model with a radius of 50 m chosen in order to account for far-field conditions, a model with a radius of 32 m, which coincides with the distance between load and furthest boundary in the previously presented 3D model, was also created for comparison in terms of the free-field response at the surface. For both cases, the finite-element discretization is kept constant, being almost twice as fine as for the case of the 3D model. In specific, for the single applied excitation frequency $f = 30$ Hz, 20 finite elements correspond to a Rayleigh

wavelength λ_R . The finite-element model for the far-field is depicted in Figure 4.7.

The duration of the dynamic analysis had to be sufficient for the waves emanating from the harmonic point load to reach the far-field, so that steady-state conditions at these large distances can be established. A total duration of 2 s is applied, which involves 30 dynamic cycles of excitation. The time-step is constant and equal to 0.00125 s; this practically means that one dynamic cycle is described by approximately 26 data points.

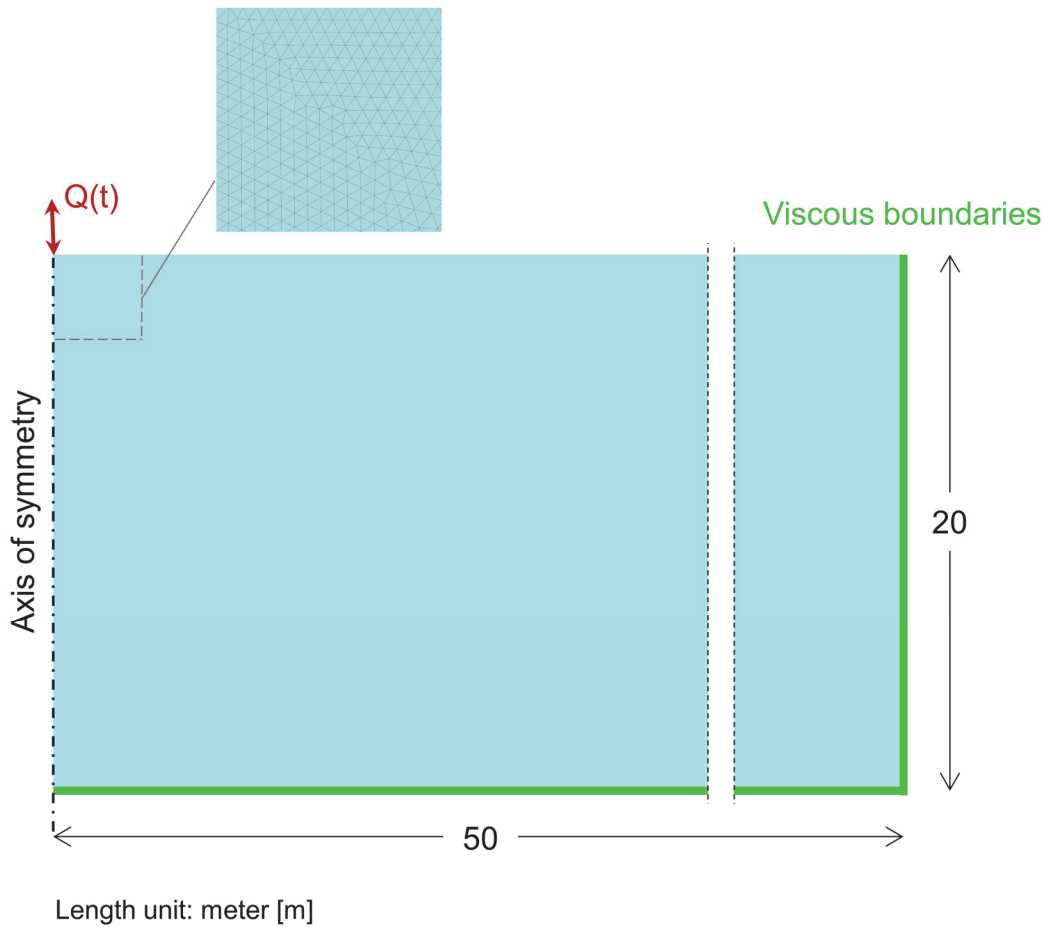


Figure 4.7: Axisymmetric finite-element model for the far-field.

4.2.3 Identification of the far-field

The first step is to obtain vertical displacement depth profiles at a varying distance r from the point load at the near- and far-field. The goal is to determine the distance at which the far-field can be assumed with a good approximation. Each displacement depth profile is basically a numerical snapshot after steady-

state conditions have been reached at a time-step, at which the vertical displacement at the surface attains its maximum value.

With these displacement depth profiles, which are obtained with the larger axisymmetric model (20 m x 50 m) and shown in Figure 4.8, it is possible to identify the far-field. It is reminded that at the far-field, P- and S-waves have dissipated, so the wave field is dominated by Rayleigh waves. The analytical solution for the far-field (Equation (4.1)) is also depicted. As can be seen, a relatively good agreement with the analytical solution is established at a distance from the source between $7.5 \cdot \lambda_R$ and $10 \cdot \lambda_R$. It is underlined, that for practical applications, the analytical solution for the far-field can be considered for the response of the surface even at close distances of $2 \cdot 3 \cdot \lambda_R$ (Rücker, 1989; Vrettos, 1991; Meek & Wolf, 1993). This is in good accord with the findings herein, and as Figure 4.8 reveals, the numerical results match the analytical solution quite well even up to a depth of $z = \lambda_R$.

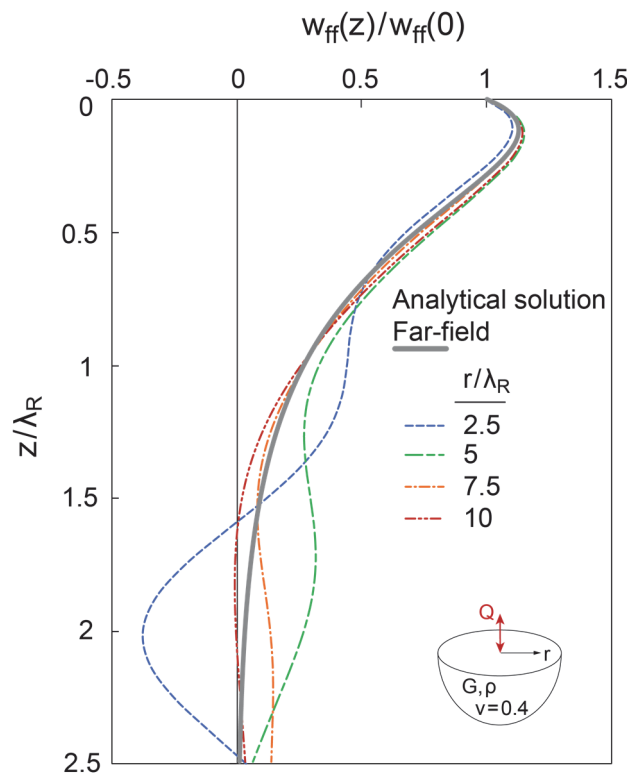


Figure 4.8: Depth profiles of vertical displacements at different distances from the harmonic point load; axisymmetric FE model.

At the far-field all points with depth should move in-phase. Certainly, the phase difference in the motion of the free-field depth profile in the close vicinity of the harmonic load ($r/\lambda_R = 2.5$) is a direct consequence of the interference of P- and

S-waves. By moving further away from the excitation source, this effect becomes, as expected, weaker and finally vanishes.

4.2.4 Verification of the free-field response

To verify the accuracy of the numerical results herein, the theoretical solution for the free-field response at the surface of a half-space to a harmonic point load, which is usually presented as a function of the dimensionless frequency $\omega \cdot r / c_s$ (see Rucker, 1989; Vrettos, 1991, Meek & Wolf, 1993, etc.) is employed. This normalization allows the use of the analytical solution for various combinations of frequency and distance from the load. Herein, the analytical solution derived from Vrettos (1991) is used. The hysteretic damping of $\zeta = 1\%$ considered in the finite-element analyses is incorporated in the theoretical solution by means of the Mintrop approximation (Vrettos, 2009; DGGT, 2019), according to which, the linear-elastic response is multiplied with the factor $\exp(-2 \cdot \pi \cdot \zeta \cdot r / \lambda_R)$.

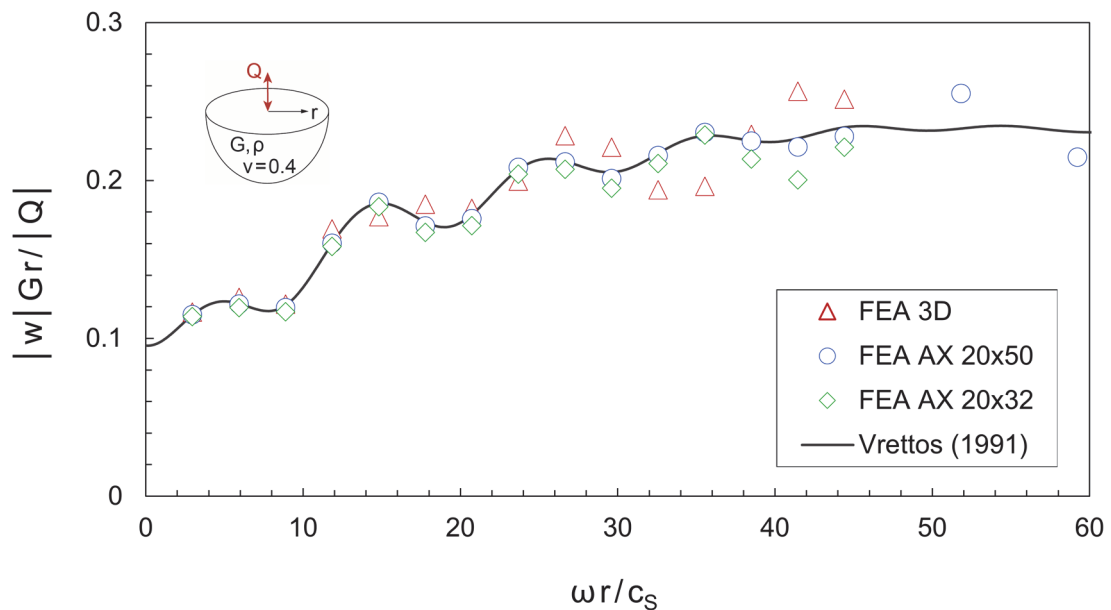


Figure 4.9: Normalized vertical displacement amplitudes at the half-space surface due to a vertical harmonic point load versus dimensionless frequency; $\nu = 0.4$

The vertical displacement amplitudes at the surface of a half-space obtained from finite-element analyses are presented in Figure 4.9, where they are also compared with the analytical solution from Vrettos (1991). By applying a single excitation

frequency ($f = 30$ Hz), the response is monitored at various distances from the harmonic point load. Since the solution is normalized, one could alternatively vary the excitation frequency and monitor the response at a specific distance. As will be shown in Chapter 5, this can be an advantage, when performing frequency-domain analyses, but in the time domain this is a time consuming approach.

The numerical results from the axisymmetric models are in excellent accord with the analytical solution up to $\omega \cdot r / c_s \approx 40$ ($r = 25$ m). The results from the model with the largest radius of 50 m (FEA AX 20x50) match overall better the solution from Vrettos (1991). It is reasonable to compare the results from the axisymmetric model with the smaller radius (FEA AX 20x32) with those from the 3D FE model, since the distance of the viscous boundary from the excitation source is in both cases the same. The mesh of the 3D model is, however, almost half as fine as that of the axisymmetric model, which explains the larger deviations from the analytical solution beyond $\omega \cdot r / c_s \approx 30$. The following conclusions are drawn:

- The distance of the viscous boundary from the area of interest plays an important role in the accuracy of the results.
- The mesh discretization plays an important in the accuracy. In this case, an acceptable agreement with the analytical solution is achieved with circa 11 finite elements per Rayleigh wavelength λ_R . Even with a twice as fine mesh though, deviations at distances close to the viscous boundary are not eliminated.
- With increasing distance from the source, the numerical accuracy deteriorates.

4.2.5 Results for single piles

In the 3D model described in Section 4.2.1, a solitary pile with a length over diameter ratio $l/d = 15$ ($l = 10$ m, $d = 0.67$ m) is activated at a distance x_0 from the point load. The kinematic interaction is expressed by transfer functions, which, herein, are ratios of the vertical displacement amplitude at the center-point of the pile head $|w_p(0)|$ over that of the free-field $|w_{ff}(0)|$ at the same location.

Firstly, the response of a single pile at the distances $x_0 = 12$ m and $x_0 = 16$ m is calculated for a range of frequencies $f = 20 - 40$ Hz. The pile is embedded either in a half-space or a soil stratum with a thickness twice its length ($H = 2 \cdot l = 20$ m).

The results are presented in Figure 4.10. A comparison with the method from Makris (1994) for a single pile in a Rayleigh wave field is also shown. Overall, the agreement with the analytical solution is quite satisfactory despite the neglect of the slenderness l/d and flexibility E_p/E of the pile in Equations (4.6) and (4.7) for the spring and dashpot coefficients that are employed in the method. As expected, the match with Makris (1994) improves as the distance from the point load increases. Due to the finite size of the model, it is impossible to completely avoid the interference of body waves; however, for increasing distance from the excitation source, the influence of P- and S-waves diminishes significantly, and Rayleigh waves start to dominate. Between half-space and soil stratum the differences are not particularly important. Finally, the decreasing trend in the curves suggests that the pile becomes more resistant against the free-field motion as the excitation frequency increases, which is a typical phenomenon in the kinematic response of embedded foundations.

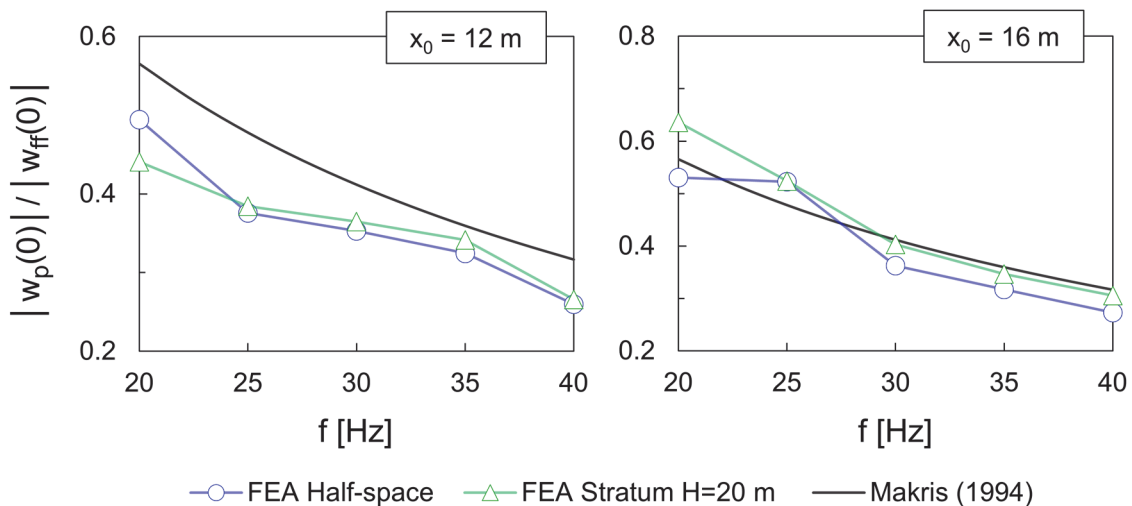


Figure 4.10: Vertical transfer functions at the pile head for two distances of the pile to the load; $l/d = 15$, $E_p/E = 350$, $\nu = 0.4$.

The values for the free-field response are given in normalized form in Table 4.1. They are verified against the analytical solution from Vrettos (1991) for half-space and the numerical solution from the thin-layer method from Kausel (1995) for a soil stratum. For all cases, the results from the finite-element analyses are in good accord with the aforementioned solutions.

Table 4.1: Normalized free-field response at distance x_0 at various frequencies; the first row number is the result from FEA, the second row number in cursive is from Vrettos (1991) for half-space or Kausel (1995) for a soil stratum.

		$ w_{ff}(0) \cdot G \cdot x_0 / Q $				
		f [Hz]				
	x_0 [m]	20	25	30	35	40
Half-space	12	0.169	0.201	0.185	0.185	0.211
		<i>0.160</i>	<i>0.185</i>	<i>0.174</i>	<i>0.178</i>	<i>0.207</i>
	16	0.181	0.158	0.200	0.213	0.204
		<i>0.184</i>	<i>0.172</i>	<i>0.207</i>	<i>0.209</i>	<i>0.211</i>
Soil stratum $H = 2 \cdot l$	12	0.185	0.201	0.186	0.174	0.207
		<i>0.177</i>	<i>0.186</i>	<i>0.165</i>	<i>0.162</i>	<i>0.207</i>
	16	0.164	0.156	0.184	0.191	0.182
		<i>0.154</i>	<i>0.167</i>	<i>0.193</i>	<i>0.196</i>	<i>0.200</i>

Next, depth profiles of the vertical dynamic interaction factor at $f = 30$ Hz have been calculated for a single pile at the distances $x_0 = 4, 8, 12, 16$ m corresponding to $x_0/\lambda_R = 1, 2, 3, 4$. The pile is embedded either in a half-space or a soil stratum of thickness $H = 2 \cdot l = 20$ m ($= 5 \cdot \lambda_R$ at this particular excitation frequency). Each depth profile is a numerical snapshot at a time-step, at which the vertical displacement at the pile head attains its maximum value. The depth profile is then normalized by the vertical displacement amplitude of the free-field at the surface ($z = 0$). In Figure 4.11, one can observe how, with increasing distance from the load, the single pile depth profile derived from the FEA tends to that from the analytical solution from Makris (1994) for the far-field. The fact that the dynamic

interaction factor attains smaller values in the vicinity of the excitation source, is a direct consequence of the interference of P- and S-waves, leading to a higher resistance of the pile against the induced displacements.

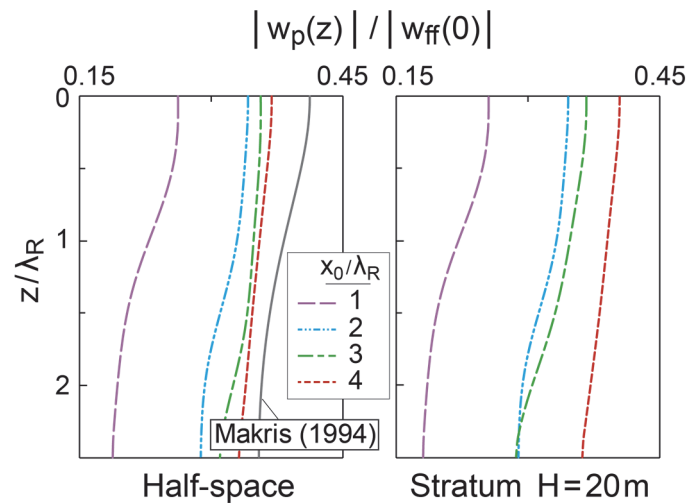


Figure 4.11: Depth profiles of the vertical dynamic interaction factor of a single pile embedded in a half-space or a soil stratum at a varying distance x_0 from the harmonic point load with $f = 30$ Hz; $\nu = 0.4$.

The distortion of the free-field motion through the presence of the pile for the excitation frequency $f = 30$ Hz is portrayed in Figure 4.12 for $x_0 = 16$ m ($= 4 \cdot \lambda_R$) in the case of a half-space. The vertical displacement depth profile of the free-field matches really well the one derived from Kausel (1995). The profile along the pile is reminiscent of that of a thin, deep wall. As explained by Haupt (1986), the shielding efficiency of a single pile is based on the re-direction of energy from Rayleigh waves that are linked with the surface towards greater depths. Apart from this, the wave propagation near the surface is hindered due to this stiff inclusion in the soil, and the waves are partially reflected.

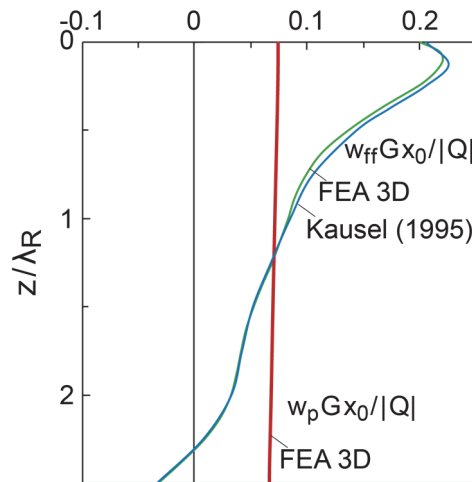


Figure 4.12: Comparison of the vertical displacement depth profiles of the free-field and a single pile at a distance of $x_0 = 16 \text{ m} (= 4 \cdot \lambda_R)$ from the harmonic point load with $f = 30 \text{ Hz}$; $\nu = 0.4$.

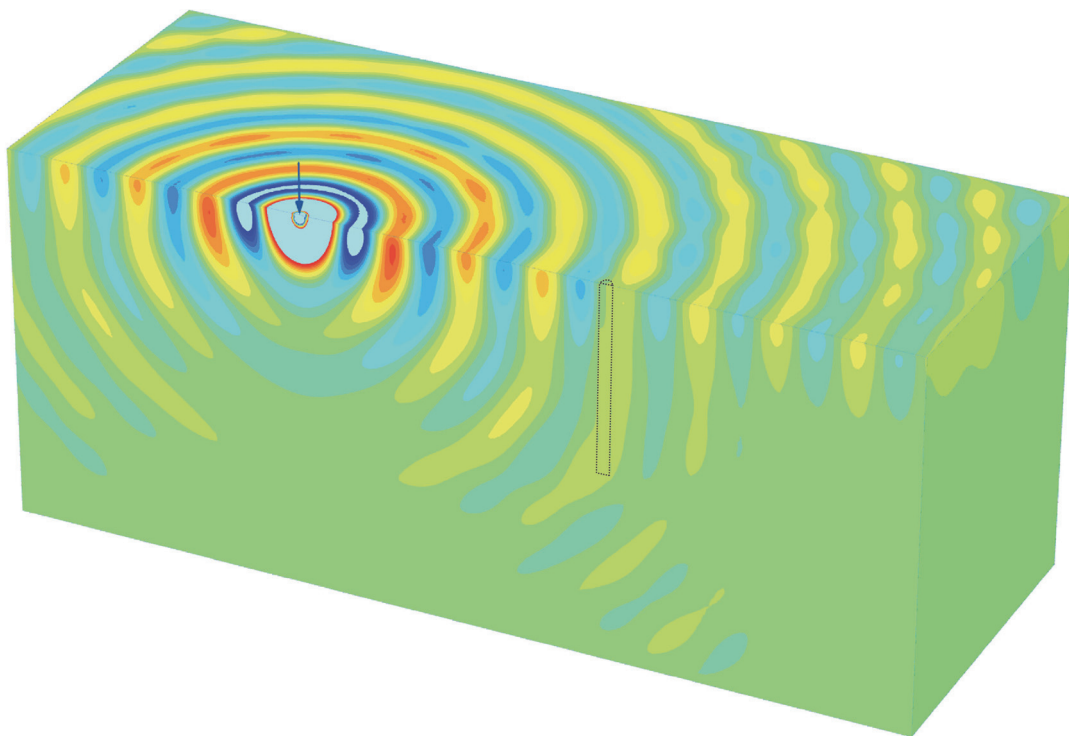


Figure 4.13: Snapshot of the vertical displacement field induced by a harmonic point load at a distance of $x_0 = 16 \text{ m} (= 4 \cdot \lambda_R)$ from a single pile in half-space.

A snapshot of the model from the analysis for the single pile embedded in half-space at $x_0 = 16 \text{ m}$ from the harmonic point load with $f = 30 \text{ Hz}$ is portrayed in Figure 4.13. The wave propagation is visualized through contours of vertical

displacements. In the vicinity of the load, body waves can be distinguished by their propagation along a hemispherical wave front. The attenuation with distance is also visible. In addition, the formation of a localized shadow zone just behind the pile indicates that it serves as a barrier against the propagating waves.

Finally, the influence of the stiffness ratio E_p/E on the response of a single pile at $x_0 = 16$ m from the load is examined at $f = 30$ Hz. The analyses were performed by varying the Young's modulus of the pile, while that of the soil was kept constant. The resulting vertical transfer functions are depicted in Figure 4.14. Between $E_p/E = 350$ and 10000 there is practically no difference in the response. When the pile becomes less stiff in relation to the surrounding soil ($E_p/E = 100$), the value of the transfer function increases, as expected, indicating that the pile follows the free-field motion in a more compliant manner.

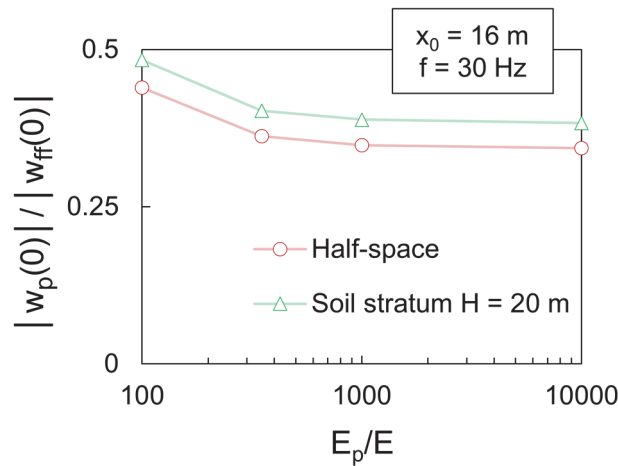


Figure 4.14: Vertical dynamic interaction factor for a single pile at $x_0 = 16$ m from the load with $f = 30$ Hz versus stiffness ratio E_p/E ; $\nu = 0.4$.

4.2.6 Results for pile groups

Next, the shielding efficiency of a 3x3 pile group, as presented in Figure 4.5, is investigated in half-space. The pile geometry is identical to that of the single pile examined in the previous section. The centre-to-centre pile distance (or pile spacing) is taken as $s = 3 \cdot d$, which is common in engineering practice. Consequently, for the examined frequency range 20 - 40 Hz at $c_R = 120$ m/s the ratio of pile spacing over Rayleigh wavelength s/λ_R varies between 1/3 and 2/3. Three scenarios are examined regarding the connection of the piles in the group:

- Free-head: The piles are free-standing; there is namely no connection between them, and they are in position to move freely.
- Fixed-head 1: The piles are connected via a rigid, massless cap.
- Fixed-head 2: The piles are connected via a rigid, concrete cap ($\gamma = 25 \text{ kN/m}^3$).

Although the third case is not relevant for kinematic interaction problems, it has been considered merely in order to assess the influence of the cap mass on the pertinent results.

The central pile located at the front pile row (P3), as well as the one at the furthest-back row (P1) at the distances $x_0 = 12 \text{ m}$ and $x_0 = 16 \text{ m}$, respectively, are chosen as reference piles for evaluation of the results. The response of the reference piles is presented in terms of vertical transfer functions in Figure 4.15, where it is also contrasted to their response as solitary piles.

In the frame of the free-head pile group, depending on the excitation frequency, the transfer function of pile P3 may attain values greater than those obtained for the single pile case. On the contrary, when connecting all piles via the rigid cap, the amplitudes experienced by pile P3 remain below the level of those in the single pile case, at least in the examined frequency range.

The attenuation of motion calculated for P1 at the furthest-back pile row in comparison with that as a single pile is much more significant, especially at higher frequencies. In this case, the vibration level is mainly reduced due to diffraction of waves through the two front pile rows, which in this frequency range serve protectively for pile P1. This is probably the reason behind the reduced amplitudes also in the case of a free-head group, with exception the frequency of 40 Hz, where a similar vibration level as in the single pile case is monitored.

In both cases, the effect of the cap mass on the results manifests itself practically only beyond $f = 35 \text{ Hz}$, resulting in a considerable increase of the transfer function, even up to 100 %.

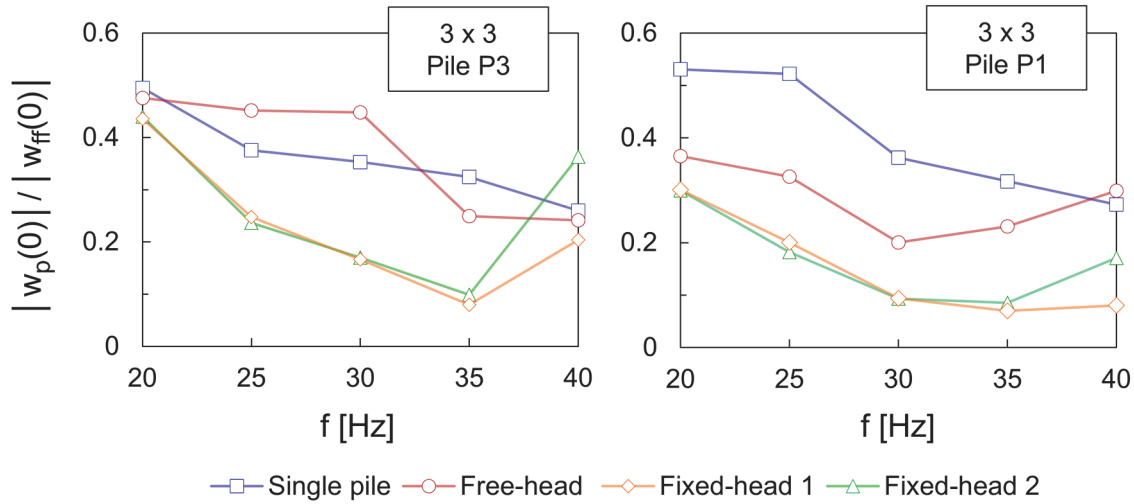


Figure 4.15: Vertical transfer functions of piles P3 and P1 as parts of the 3x3 pile group with $s/d = 3$ or as single piles; $E_p/E = 350$, $l/d = 15$, $\nu = 0.4$.

The shielding efficiency of a pile group is, among others, dependent on the relation of the Rayleigh wavelength λ_R to characteristic sizes in the pile group. It is underlined, though, that due to the interplay of the numerous parameters in this particular problem, a generalization on the vibration reduction as a function of the ratio s/λ_R was not possible.

4.3 Excitation due to a moving point load

4.3.1 Barber's analytical solution

The next step is to analyse the response of piles in the wave field induced by a moving point load of constant or time-harmonic magnitude. The closed-form expression derived from Barber (1996) is presented in the frame of validation. This analytical solution gives the vertical displacement at an observation point at the soil surface due to a vertical point load of constant magnitude Q , which is travelling on the surface of a half-space with a constant speed v_0 . A schematic illustration is given in Figure 4.16, along with basic parameters of the problem.

For the sub-Rayleigh case with $v_0 < c_R$, which is common in the engineering practice, the analytical solution from Barber (1996) is:

$$w(r, \theta) = -\frac{Q}{2 \cdot \pi \cdot G \cdot r} \frac{M_S^2 \sqrt{1 - M_P^2}}{(2 - M_S^2)^2 - 4 \sqrt{1 - M_P^2} \sqrt{1 - M_S^2}} \quad (4.13)$$

where

$$M_P = \frac{v_0 \cdot \sin\theta}{c_P}, M_S = \frac{v_0 \cdot \sin\theta}{c_S} \quad (4.14)$$

with $0 < \theta < \pi$ being the angle between the travel axis and the line connecting the load and the observation point, and r the distance between the load and the observation point. The minimum distance of the observation point to the travel axis is denoted as $x_0 = r \cdot \sin(\theta)$, so that $\theta = \pi/2$ at $r = x_0$.

For the critical case where $v_0 > c_R$ the solution becomes complicated. This situation is, however, quite rare, since it corresponds to the special case of an extremely high travelling speed on a soft soil (Madshus & Kaynia, 2000).

For low travelling speeds ($v_0 \rightarrow 0$), Equation (4.13) converges to the solution from Boussinesq (1885) for a static point load:

$$w_{st}(r) = -\frac{Q}{2 \cdot \pi \cdot G \cdot r}$$

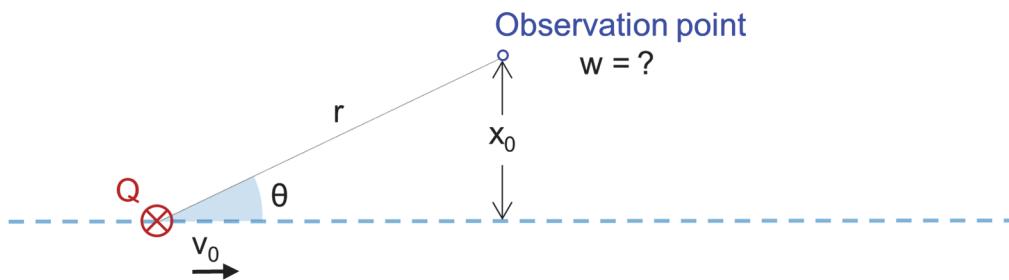


Figure 4.16: Definition of the moving load problem (plan view).

4.3.2 Finite-element modelling

First, the results for the free-field response to a moving load of constant magnitude are verified against the analytical solution from Barber (1996). The finite-element model for this purpose is portrayed in Figure 4.17 along with aspects of discretization. It is based on the model by Galavi & Bringreave (2014) for the computation of the free-field response. In the sequel, this initial model presented herein is appropriately modified according to the needs of the present study to account for the presence of piles.

Due to geometric and load symmetry only half of the system is simulated. The length of the model is equal to 104 m, while that of the load path 100 m. The latter is slightly shorter so that its starting and end point do not coincide with the lateral viscous boundaries. The width and depth of the model are taken equal to 50 m and 100 m, respectively. Appropriate boundary conditions preventing the out-of-plane movement are applied at the symmetry face of the finite-element model. To simulate a half-space, viscous boundaries are implemented peripherally as well as at the base of the model.

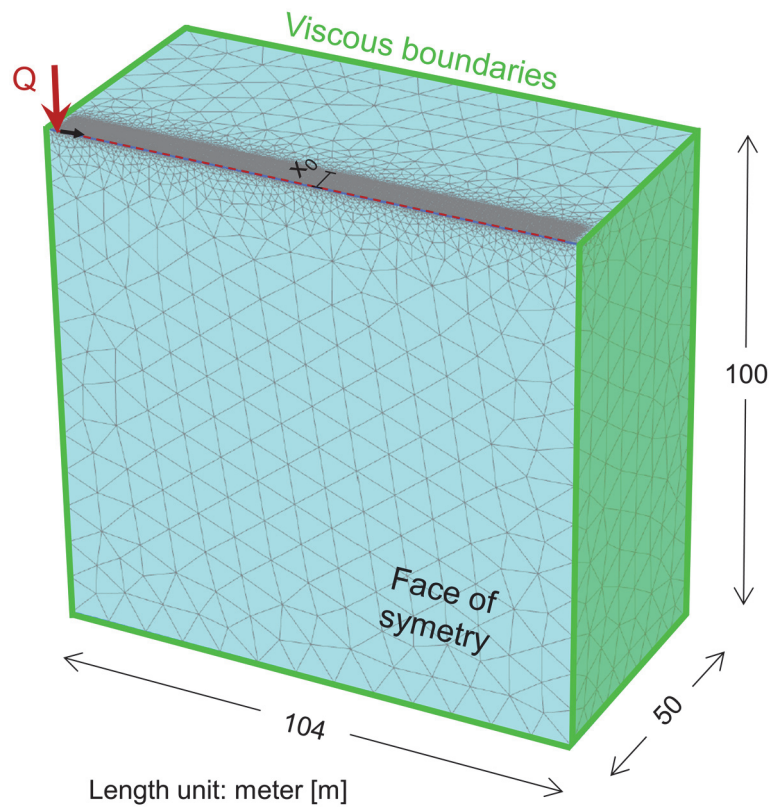


Figure 4.17: Finite-element model for the moving load of constant magnitude Q .

The vertical point load has a magnitude Q , which is constant (invariable with time). Regarding the speed of the load, v_0 , two values are selected: 50 m/s and 100 m/s, which correspond to 180 km/h and 360 km/h. These values are typical for high-speed trains.

The soil is linear-elastic with a shear modulus $G = 30.5$ MPa, a density $\rho = 1.89$ Mg/m³ and a Poisson's ratio $\nu = 0.3$, so that $c_s = 127$ m/s and $c_R = 118$ m/s. A very small value of Rayleigh-type damping is introduced in the soil to obtain a

smooth response. The free-field response at the surface is monitored at a distance $x_0 = 6$ m from the travel axis.

Under this type of loading, the vertical displacement time-history at the surface attains a maximum value as soon as the load arrives at the distance x_0 from the observation point. Barber (1996) assumes that the point load is travelling from infinity. However, the simulation by means of the FEM of a load that is travelling even from a very far distance requires an extremely long model, which is computationally not feasible. As a result, the activation of the load at the beginning of the analysis unavoidably leads to a transient procedure, the effects of which appear in the response as a disturbance that ideally should be eliminated. For this purpose, different scenarios for the load application are compared:

- The total magnitude of the load is directly applied by means of a “*step-function*”.
- The magnitude of the load increases linearly from zero up to its maximum value for a fraction of the total analysis time by employing a “*ramp-function*” of constant gradient. A total time for the ramp function between 20 % and 30 % of the time needed for the load to reach the end of the load path was proven optimal.

The above cases are also depicted in Figures 4.18 and 4.19 along with the verified free-field response. It is clarified that the total analysis time is the ratio of the load path length (100 m) over the travelling speed of the load (v_0).

4.3.3 Verification of the free-field response

First, the results for the highest load speed $v_0 = 100$ m/s (corresponding to a ratio $v_0/c_R = 0.847$) are presented in Figure 4.18. The response at the observation point at $x_0 = 6$ m is shown in terms of normalized vertical displacements. For the cases “Ramp (i)” and “Ramp (ii)” presented herein, the time for the ramp function was set as 20 % and 30 %, respectively, of the total analysis time. Despite the long load path, after about 0.4 s, a significant disturbance is monitored in the response, which reaches the observation point with the S-wave velocity c_s . The disturbance becomes less intense when the load is gradually applied by means of the ramp-function; yet, it does not completely vanish. The system requires a considerable time to reach a steady-state condition. Despite the disturbance, though, the vertical displacement peak, which appears as soon as the load arrives at the

shortest distance from the observation point x_0 , is reproduced with high accuracy. From this point on (and even for a certain amount of time before this) a very good agreement with the analytical solution from Barber (1996) is established. In fact, by taking into account time-symmetry, one can reproduce the complete solution by mirroring the response obtained after the settlement peak (Galvín & Domínguez, 2007). The vertical displacement derived from the Boussinesq solution, which corresponds to the static case ($v_0 = 0$) is also depicted in Figure 4.18, being equal to 43 % of the maximum displacement due to the moving load.

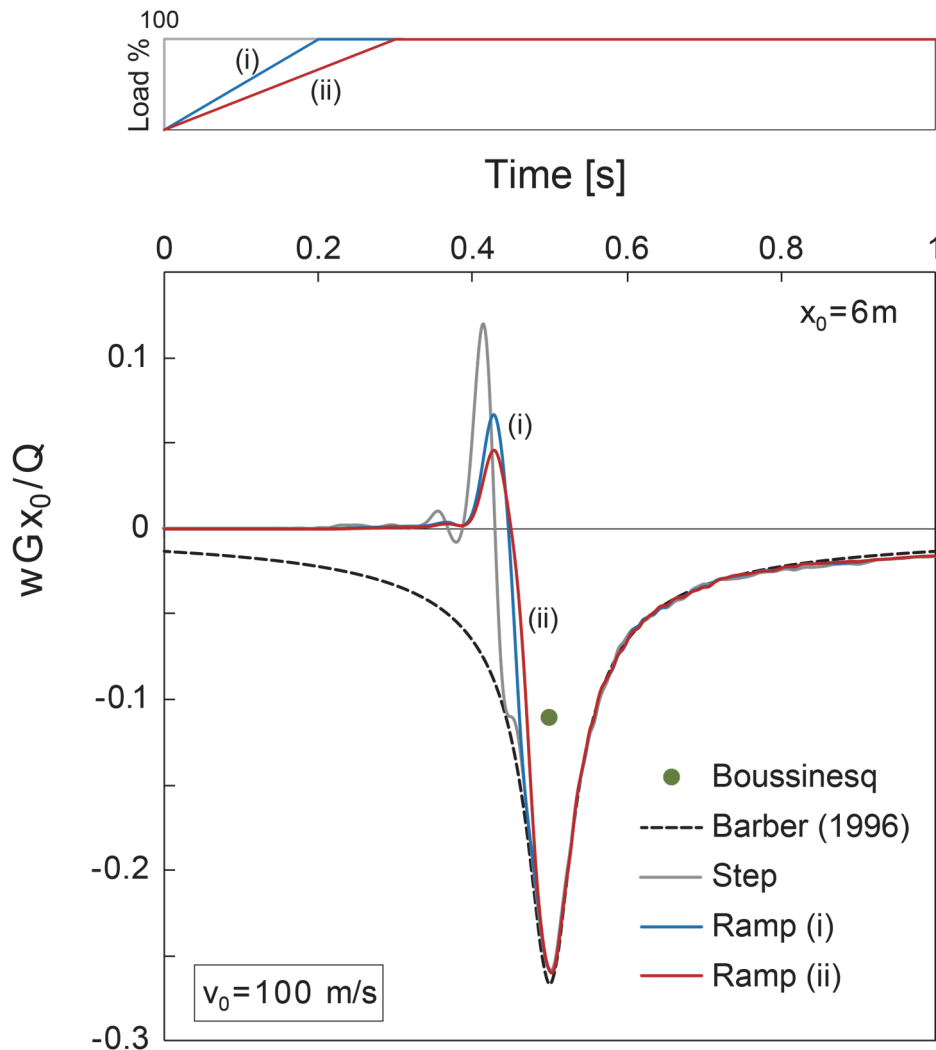


Figure 4.18: Vertical displacement time-history at a distance of $x_0 = 6$ m from the load path due to a vertical point load moving with $v_0 = 100$ m/s at the surface of a half-space; $\nu = 0.3$.

The results for $v_0 = 50$ m/s ($v_0/c_R = 0.423$) are depicted in Figure 4.19. The ramp-function is applied up to 20 % of the total analysis time, which was sufficient for

this case. First of all, the negligible deviation from the Boussinesq solution reveals the static character of this type of loading in the case of a relatively low ratio of travelling speed over Rayleigh wave velocity in the soil v_0/c_R .

Generally, the absence of an excitation frequency signifies that there is no wave propagation in the soil. This conclusion also justifies why the accuracy of the results is practically insensitive to mesh fineness, which was also observed in additional analyses not shown herein, including the higher travelling speed of $v_0 = 100$ m/s. Nevertheless, the nature of the problem is certainly dynamic, but, in the essence, it is a single “disturbance” that propagates.

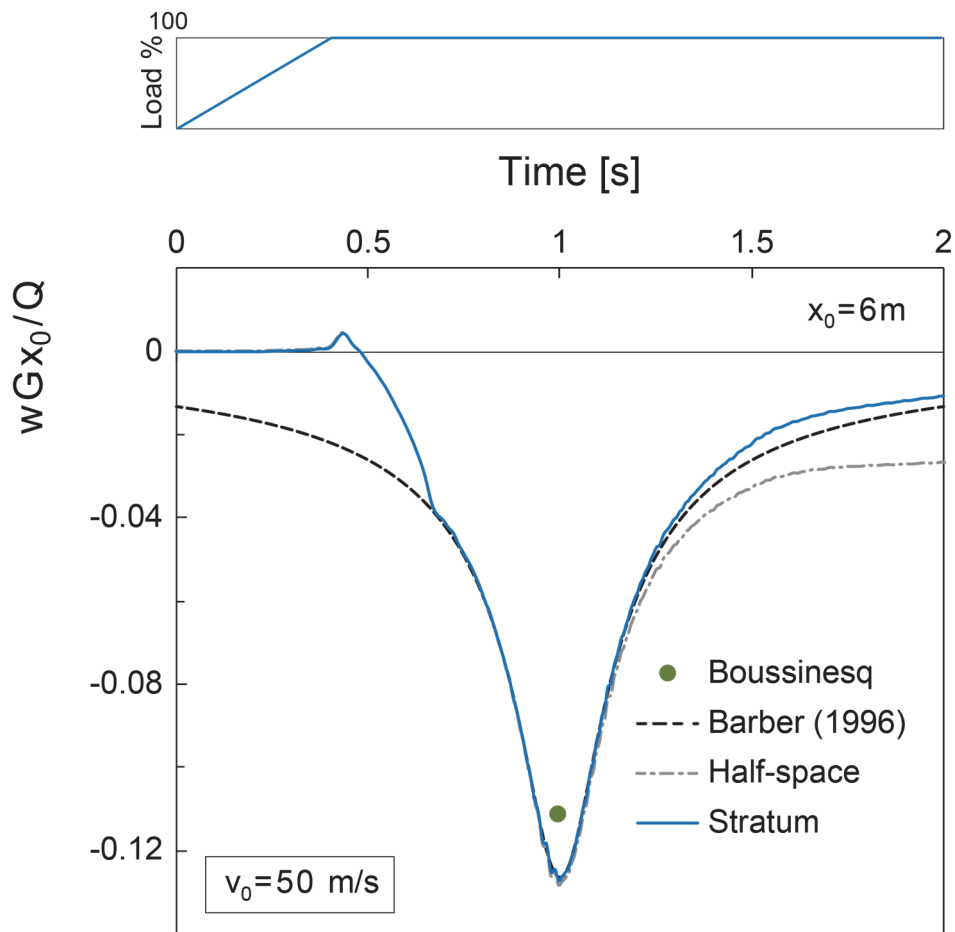


Figure 4.19: Vertical displacement time-history at a distance of $x_0 = 6$ m from the load path due to a vertical point load moving with $v_0 = 50$ m/s at the surface of a half-space; $\nu = 0.3$.

However, in Figure 4.19 is shown that shortly after the displacement peak is reached, significant deviations from the analytical solution from Barber (1996)

arise (half-space case). Since this problem does not occur in the case of the higher travelling speed, these differences are attributed to the insufficient accuracy of the bottom viscous boundary for the case of low values of the ratio v_0/c_R ; in other words, as the static case is approached. The improved accuracy after the replacement of the bottom viscous boundary by a rigid base (stratum case) confirms the above assumption. Considering a rigid substratum at this great depth of 100 m has a minor effect on the targeted simulation of the half-space response. Yet, for cases where a fine mesh discretization is required (i.e. oscillating moving load), a large model depth is not computationally feasible, at least in the vast majority of the cases of interest for the engineering practice. Understandably, the simulation of a half-space in these cases constitutes an important limitation of the FEM. Subsequently, for the following investigations of a single pile or a pile group under excitation by the wave field from a moving load of time-harmonic magnitude, a soil stratum of thickness equal to $H = 2 \cdot l = 20$ m was considered, being associated to a straightforward boundary condition at the base of the model.

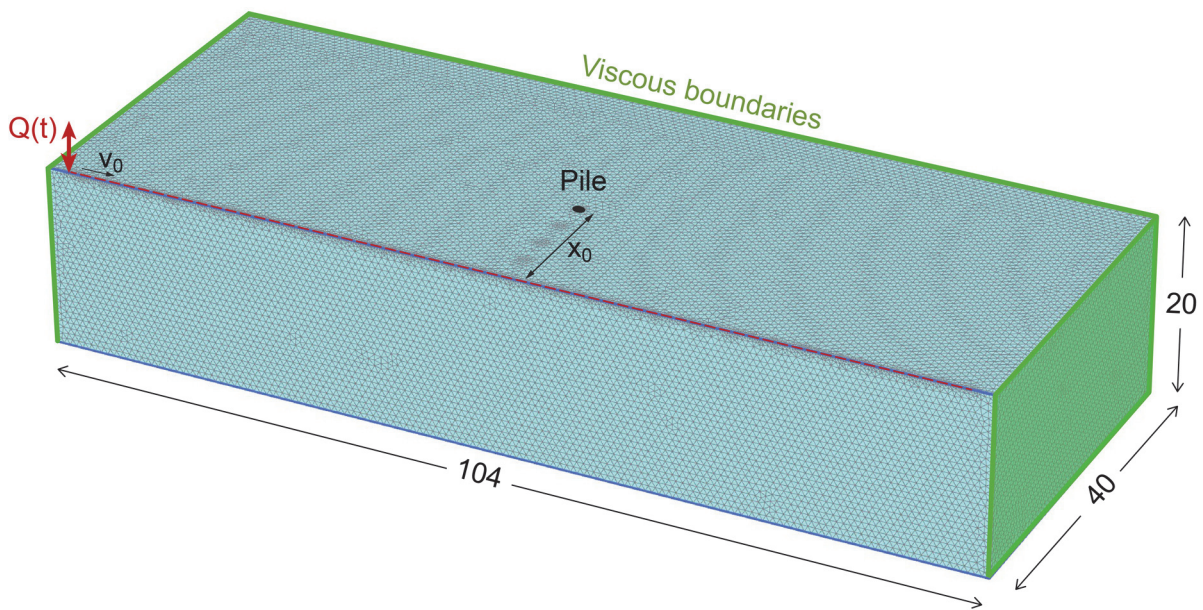


Figure 4.20: Finite-element model for a moving oscillating load on a soil stratum.

4.3.4 Soil stratum: FE modelling

A new finite-element model was created by shortening the width and depth of the previous model with the rigid base to 40 m and 20 m, respectively. The idea behind this configuration was to simulate a soil stratum of a thickness twice as large as the considered pile length $l = 10$ m; in that way, correspondence to the previous examined case of a stationary harmonic load on a soil stratum is accomplished. Besides, this shorter model enables the required finer discretization in order to perform analyses with a moving harmonic load. Regarding the aspect of mesh discretization, two schemes are tested:

- A non-homogeneous finite-element mesh being fine in the vicinity of the load path, while gradually becoming coarser farther away.
- A uniform fine mesh with approximately 5 finite elements per Rayleigh wavelength λ_R (yet, still finer along the load path)

The first scheme is used for the analyses with a moving load of constant magnitude Q , while the second one for the analyses with an oscillating moving load $Q(t) = |Q| e^{i\omega t}$. In the last case, the magnitude of the load varies harmonically with time at a frequency of $f = 30$ Hz. The FE model with the uniform fine mesh is shown in Figure 4.20. Assuming a common sleeper distance of 0.60 m, the above excitation frequency leads to a travelling speed of $v_0 = 18$ m/s (= 64.8 km/h), which is representative of medium-speed trains. A schematic illustration of the concept is presented in Figure 4.21. This simplified concept serves mainly the assessment of the effect of frequency in case of a moving excitation source. To realistically examine railway problems additional aspects are required, such as the simulation of the railway sleepers, the consideration of the weight of the wagons etc. However, it is the dynamic component of moving loads that is relevant for the vibration protection practice, since this mostly affects the response.

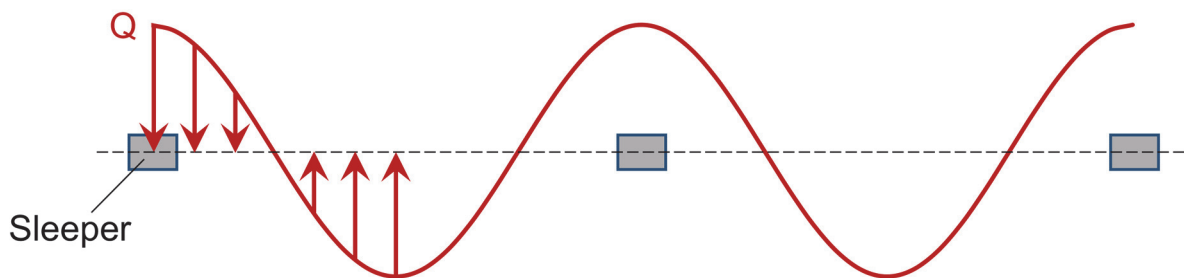


Figure 4.21: Schematic illustration of the variation of the oscillating load magnitude.

The same soil properties as in the case of the stationary harmonic load are considered: $G = 30.5$ MPa, $\rho = 1.89$ Mg/m³ and $\nu = 0.4$, see Section 4.2.1. A Rayleigh-type damping corresponding to a hysteretic damping ratio of $\zeta = 1\%$ is introduced in the soil.

The moving load is applied by means of a ramp-function, the duration of which is equal to 1.1 s (corresponding to 20 % of the total analysis time). After this point, the oscillation of the load starts.

It is underlined that the use of symmetry in the model (see Figure 4.20) implies the existence of an identical, mirror pile group/single pile on the other half of the stratum that is not modelled. This could have a small influence on the results. An analysis with a full model without use of symmetry was at this point of the study computationally not possible. Indicatively, the computation on an Intel i9-10900K, 3.70 GHz processor with 64 GB RAM (which was, however, employed at a later point of the study and enabled analyses with a full 3D model without use of symmetry, presented in Section 4.3.7) lasted 15 hours.

4.3.5 Results for single piles

First, the influence of a moving load of constant magnitude on the free-field response is considered. To derive the free-field response, soil properties are assigned to all pile parts in the model. Figure 4.22 presents the time-histories of the normalized vertical displacements at four observation points located at the distances $x_0 = 4, 8, 12, 16$ m from the load path. Note that due to the specific normalization of the results, the farther the distance x_0 , the more scaled up the curves appear. Due to the relatively low travelling speed, the long load path and the ramp-function, no considerable disturbance appears in the response.

As already explained, the displacement peaks in the response at the observation points lying on the centreline at the surface of the soil stratum model appear as soon as the load passes by at a distance x_0 from the observation point. This occurs at approximately 2.78 s, which is half of the total analysis time. In the frame of verification, these maximum values are compared in Figure 4.23 to those derived from the algorithm provided by Kausel (2018) using the thin-layer method. An additional comparison is shown with results obtained from an axisymmetric model of the respective soil stratum including a static load acting at a distance x_0 from the observation point. The differences are negligible. The applied travelling speed $v_0 = 18$ m/s (≈ 65 km/h) in combination with the selected soil parameters

leads to a response, which is quite close to the static solution. Greater deviations from the static case are expected at higher travelling speeds.

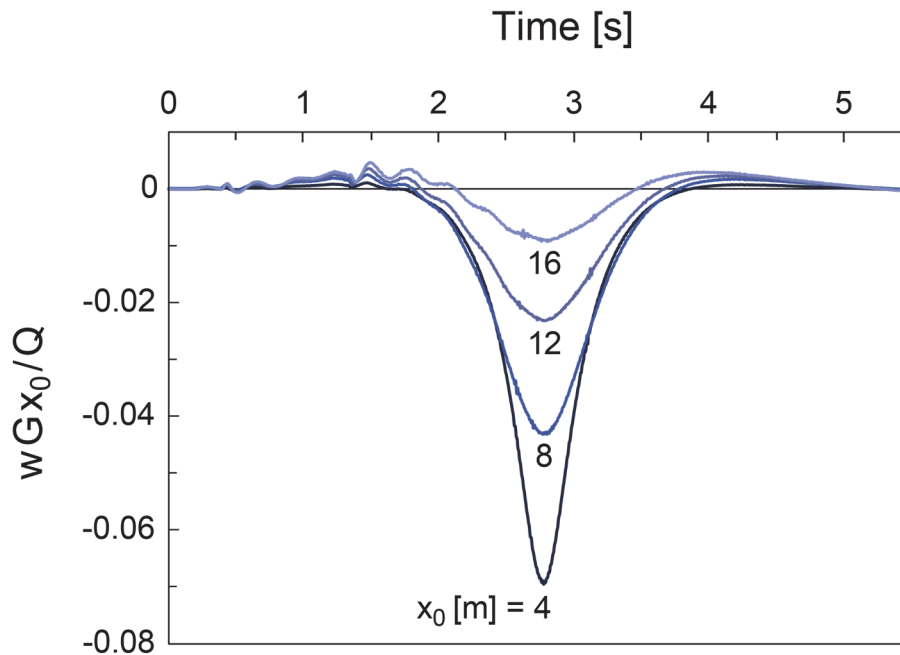


Figure 4.22: Vertical displacement time-histories at the surface of a soil stratum of thickness $H = 20$ m during the passage of a moving constant load at $v_0 = 18$ m/s; $\nu = 0.4$.

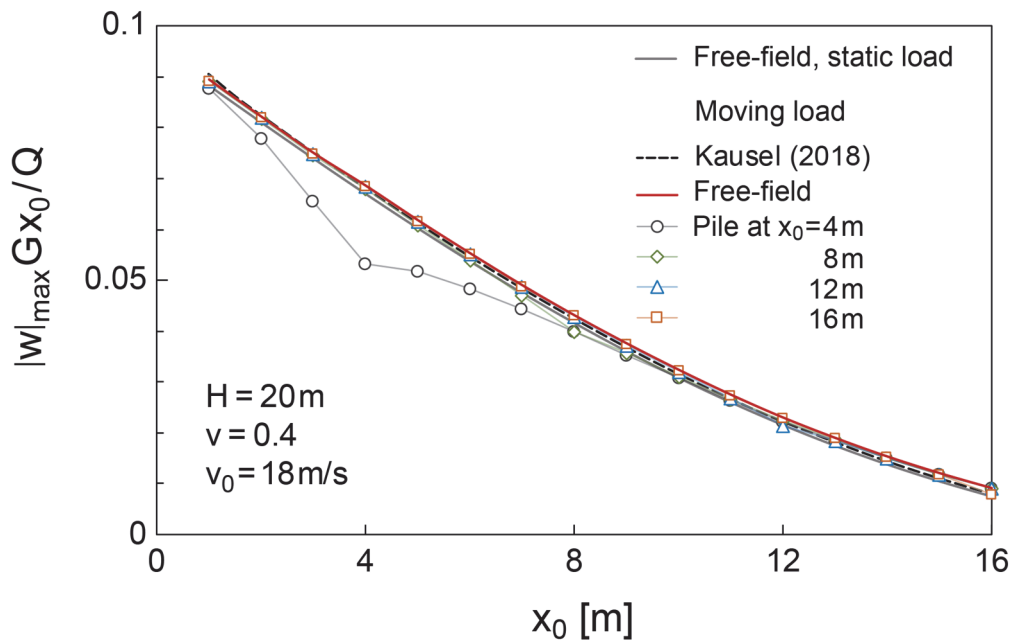


Figure 4.23: Maximum vertical displacement time-histories at the surface of a soil stratum without/with an embedded pile due to a moving load of constant magnitude.

Subsequently, a single pile with the properties defined in Section 4.2.1 is considered at a varying distance x_0 from the load path. Apart from the free-field response to the moving load of constant magnitude, Figure 4.23 also shows the alternation of the vertical displacement field on the centreline of the model at the surface through the presence of the pile. Only in the near-field a considerable influence is noticed in the case of the single pile at the distance of $x_0 = 4$ m. In particular, its presence reduces the free-field motion by 23 %. The explanation is straightforward, and lies on the static character of a moving load with constant magnitude. Since there is no influence of excitation frequency on the response, and no Rayleigh waves are developed, considerable displacement amplitudes are monitored only up to a relatively short distance from the load path. The latter was also observed by Auersch (2010). As an additional confirmation, an analysis was performed with the refined model, which yielded practically no differences, since static analyses are relatively insensitive to mesh discretization.

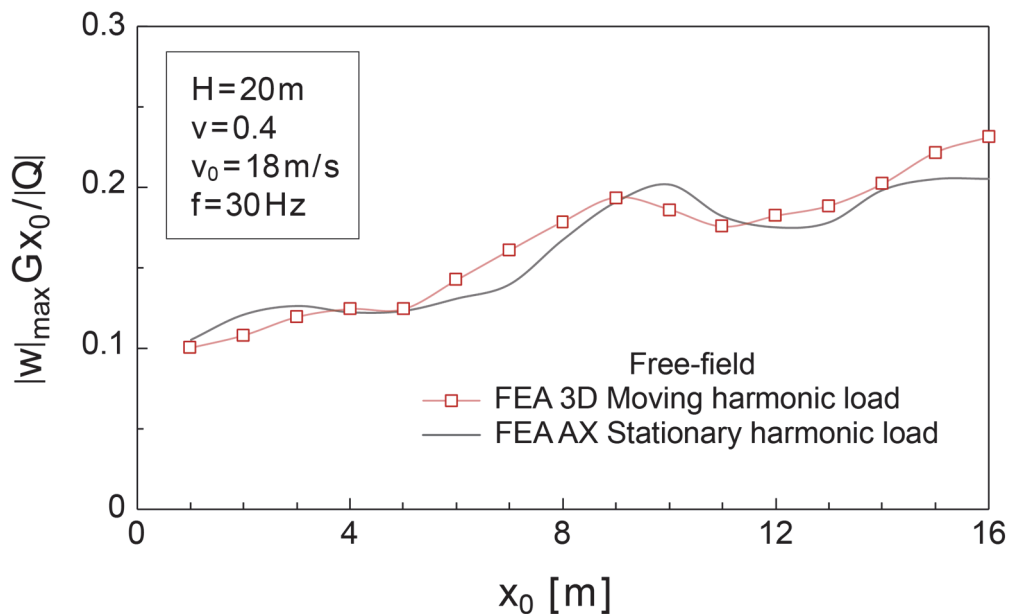


Figure 4.24: Maximum vertical displacement amplitude at the surface of a soil stratum due to a moving load of time-harmonic magnitude.

A moving load of time-harmonic magnitude leads to a peak in the free-field response as soon as the load reaches the minimum distance x_0 from the observation point located at the near-field. For farther distances this peak in the response appears earlier. In Figure 4.24, a comparison is presented between the maximum vertical displacements induced by a moving or a stationary harmonic

load acting at a distance x_0 from the observation point (the latter results were obtained from an axisymmetric model). It is obvious that at a relatively low travelling speed in relation to the Rayleigh wave velocity in the soil, the stationary harmonic load is a good approximation of the moving load scenario.

The curves in Figure 4.25 demonstrate how the vertical displacement field along the centreline normal to the load path changes due to the presence of a solitary pile at a varying distance x_0 . In the 3D finite-element model portrayed in Figure 4.20, for each analysis, the corresponding pile of interest is activated. It is observed that especially in the vicinity of the load path, the level of attenuation of motion through the pile is particularly high. Overall, the effect of the pile on the free-field motion is rather localized, since the influence range of the pile is equal to approximately 1 - 2 m, mostly developing at the back with respect to the wave propagation direction. For the examined configuration the vertical transfer function $|w_p|/|w_{ff}|$ varies between 0.26 at $x_0 = 4$ m and 0.38 at $x_0 = 16$ m. This reduction is quite similar to the one for the case of a stationary harmonic load, as can be seen in Table 4.2 summarizing the results. The vertical transfer function for a single pile located at the far-field, as calculated from the analytical solution for Makris (1994), is also depicted. As expected, the agreement with the analytical solution for the far-field is improved as the distance from the load path increases. But, interestingly, even from at $x_0 = 12$ m, the deviation from the far-field solution is less than 10 %.

The above observation suggests that as long as the considered pile is not located too close to the excitation source, even if it is not located at the far-field, the analytical solution from Makris (1994) can be used as a good approximation. As already implied by the corresponding comparison, this is valid not only for a stationary harmonic load, but also for a moving harmonic load with a speed v_0 relatively low in comparison with the Rayleigh wave velocity c_R in the soil.

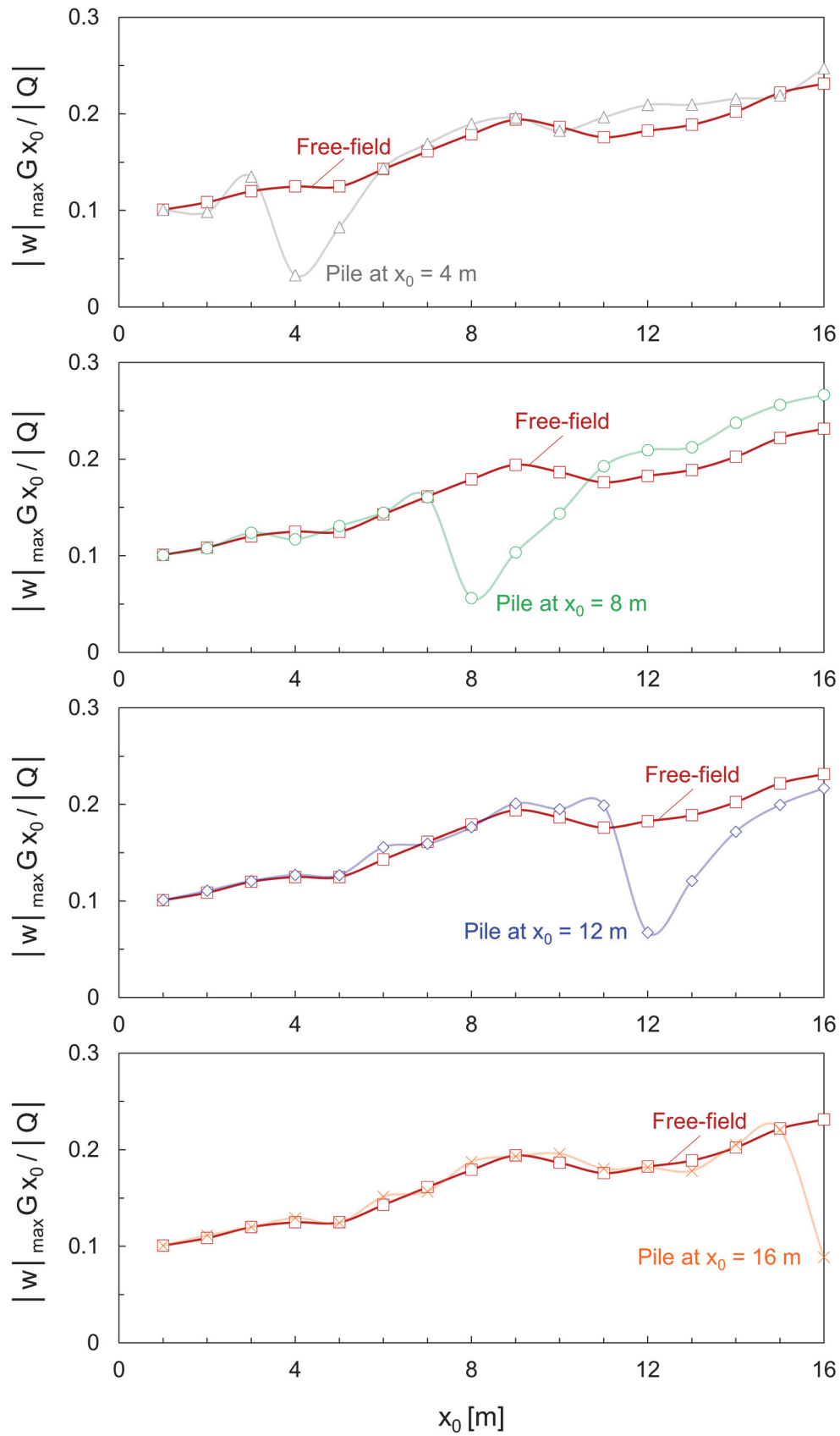


Figure 4.25: Maximum vertical displacement amplitude at the surface of a soil stratum with a single pile due to a moving load of time-harmonic magnitude.

Table 4.2: Vertical transfer function of pile over free-field response $|w_p|/|w_{ff}|$: Comparison between FEA (moving load versus stationary load) and analytical solution from Makris (1994). $f = 30$ Hz, $E_p/E = 350$, $l/d = 15$, Soil stratum $H = 2 \cdot l$, $c_s = 127$ m/s, $\nu = 0.4$.

		$ w_p / w_{ff} $				
		x_0 [m]	4	8	12	16
FEA	Moving harmonic load ($\nu_0/c_s = 0.14$)		0.26	0.31	0.37	0.38
	Stationary harmonic load ($\nu_0/c_s = 0$)		0.26	0.35	0.37	0.40
Makris (1994)	Rayleigh wave field		0.41			

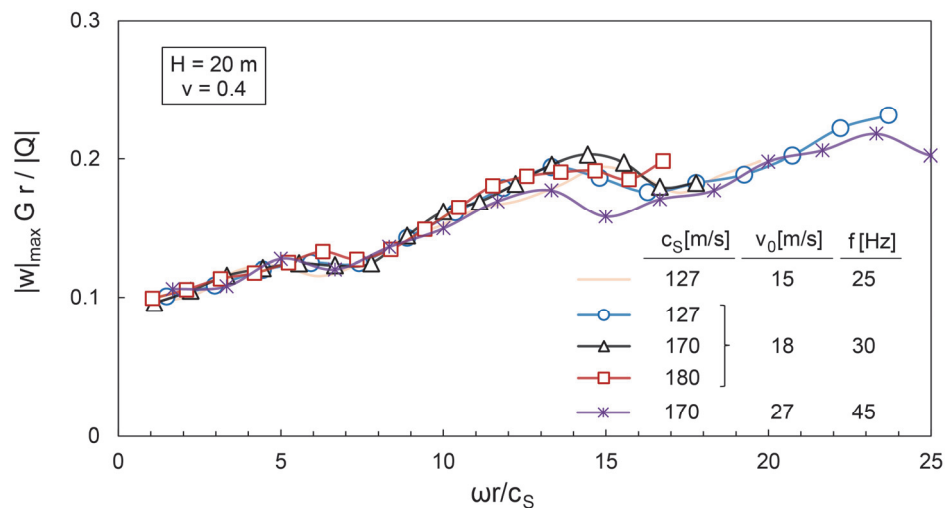


Figure 4.26: Influence of c_s and ν_0 (or f) on the maximum vertical displacement amplitude at the surface of a soil stratum due to a moving load of time-harmonic magnitude.

Furthermore, the influence of the S-wave velocity in the soil c_s and the travelling speed ν_0 (the latter linked with the excitation frequency f , due to the assumed

railway sleeper distance) is parametrically investigated. The vertical displacement amplitudes of the free-field along the centreline of the model are presented in Figure 4.26 in dimensionless form, so the curves overlap to a great extent. However, this dimensionless representation, which is typically employed for the free-field response to a stationary harmonic load (recall Figure 4.9) is not expected to be valid at larger values of the ratio v_0/c_s , since a higher travelling speed of the load certainly leads to greater deviations from the stationary response.

Respective analyses were carried out with the model including a single pile at $x_0 = 16$ m. The resulting dynamic interaction factors are presented in Table 4.3, where they are also compared to the corresponding values derived from the analytical solution from Makris (1994). The agreement is quite satisfying, with a sole exception at $v_0 = 27$ m/s or, alternatively, at $f = 45$ Hz, where, a larger deviation of 17 % appears. This is unsurprising at this higher travelling speed. It is reminded at this point that the solution from Makris (1994) refers to a half-space, while the finite-element model employed for these analyses includes a rigid base. Nevertheless, as the distance from the excitation source increases, with surface waves starting to dominate the wave field, it is expected that the presence of a rigid base will not have a significant effect on the response at the surface.

Table 4.3: Dynamic interaction factor $|w_p|/|w_{ff}|$ for a single pile at $x_0 = 16$ m from the load path: Comparison between FEA and the analytical solution from Makris (1994); $l/d = 15$, Soil stratum $H = 2 \cdot l$, $\nu = 0.4$.

v_0 [m/s]	c_s [m/s]	E_p/E	f [Hz]	$ w_p / w_{ff} $	
				FEA	Makris (1994)
15	127	350	25	0.44	0.48
18	127	350	30	0.38	0.41
	170	200		0.58	0.55
	180	175		0.56	0.58
27	170	200	45	0.34	0.41

Indicatively, a numerical snapshot from the analysis with the pile at $x_0 = 16$ m embedded in the soil stratum with $c_s = 170$ m/s and subjected to the wave field emanating from a moving harmonic load with speed $v_0 = 27$ m/s and frequency $f = 45$ Hz is shown in Figure 4.27. The wave propagation is visualized with contours of vertical displacements. At the particular time-step ($t = 1.85$ s), the load is located at the shortest distance (x_0) from the pile. The shielding efficiency of the pile can be visualized through the formation of a shadow zone behind the pile (in relation to the wave propagation direction), where the displacement amplitudes are considerably reduced. In the case of a moving excitation source, the location of the shadow zone obviously changes depending on the position of the load.

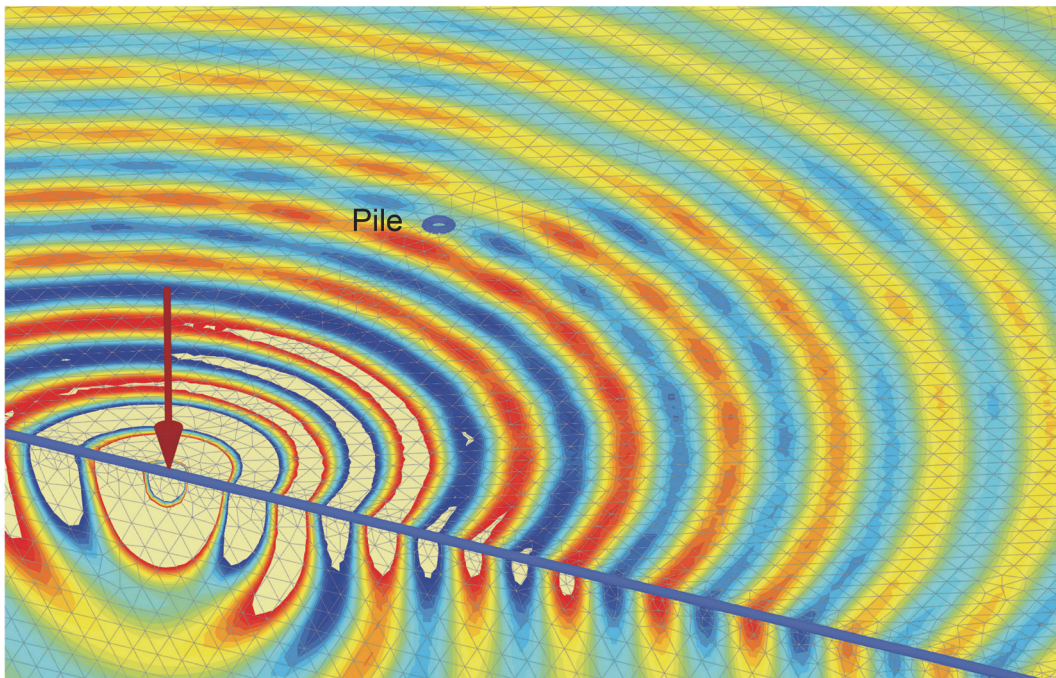


Figure 4.27: Snapshot of the vertical displacement field in the soil stratum ($c_s = 170$ m/s) as soon as the moving harmonic load ($v_0 = 27$ m/s and $f = 45$ Hz) reaches the shortest distance from the pile at $x_0 = 16$ m.

4.3.6 Results for pile groups

The response of the 3x3 pile group with $s/d = 3$ (recall Figure 4.5) is investigated under the excitation due to a moving harmonic point load. The load path axis is parallel to the three pile rows, which are located at distances $x_0 = 12, 14$ and

16 m. Initially, the pile group is free-standing; there is namely no cap connecting the piles. A further system of 2x3 free-head piles is also considered by replacing in the finite-element model the front pile row of the 3x3 configuration by soil. The recorded vertical displacement time-histories as well as the dynamic interaction factors $|w_p(0)|/|w_{ff}(0)|$ are presented with respect to the central pile P1 at the furthest-back row, which is chosen as the reference pile.

Vertical displacement time-histories during the passage of the point load are depicted in Figure 4.28 for the free-field, as well as for the reference pile which is either a solitary pile or part of a free-head 2x3 or 3x3 pile group. Moreover, for the case of the 3x3 group, the influence of the pile connection to a rigid, massless cap is additionally investigated. At selected time-steps during the passage of the load, corresponding snapshots from the analysis of the 3x3 pile group without cap are also shown.

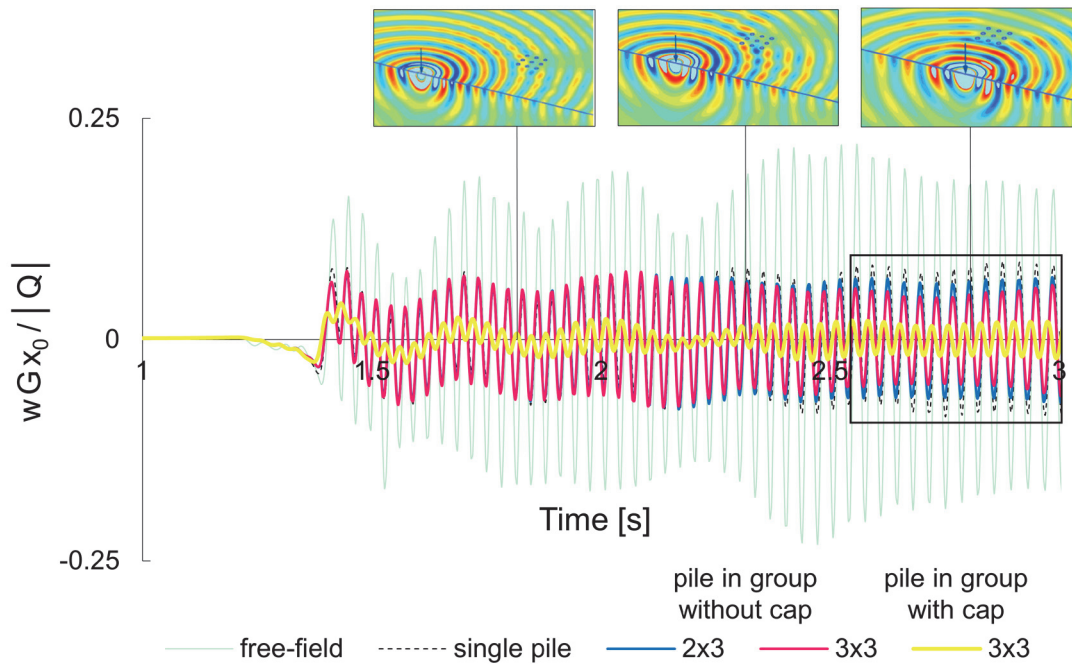


Figure 4.28: Vertical displacements of the free-field and of pile P1 at distance $x_0 = 16$ m as single pile or as part of a pile group for an excitation by a moving harmonic load of $f = 30$ Hz and $v_0 = 18$ m/s; soil stratum with $H = 20$ m and $\nu = 0.4$.

Apparently, even the presence of a single pile leads to an important reduction of the free-field motion. The shielding efficiency of the pile group becomes stronger when the load is nearby (see highlighted time-window in Figure 4.28). The

corresponding dynamic interaction factor $|w_p(0)|/|w_{ff}(0)|$ (calculated here between 2.75 and 2.8 s) attains the following values: 0.46 for the single pile, 0.34 for the pile in the 2x3 pile group and 0.27 for the pile in the 3x3 pile group. The addition of a rigid cap to the last scheme reduces dramatically the ratio to 0.09. However, when the kinematic interaction is calculated by taking into account the complete time-history, the following values are obtained: 0.38/0.34/0.34/0.18 for the four cases distinguished above.

Figure 4.29 portrays a snapshot with the load at the minimum distance from the 3x3 pile group without a cap. It is obvious that the pile group acts as a barrier to the propagating waves that are visualised with contours of vertical displacements. As already shown by previous examples, the vibration reduction due to the pile group manifests itself with the formation of a shadow zone at the back of the pile group, where the displacement amplitudes are significantly reduced.

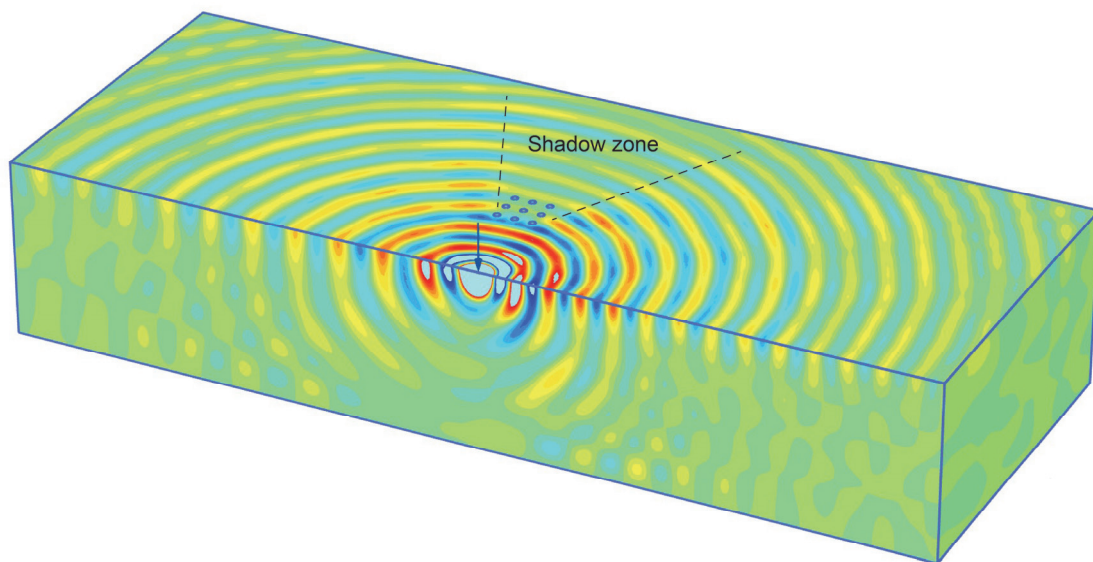


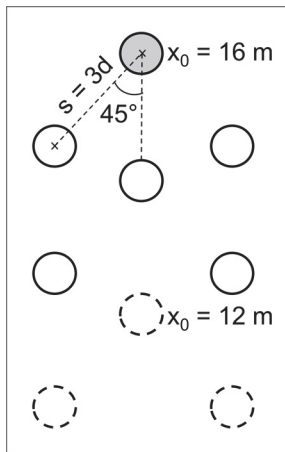
Figure 4.29: Snapshot of the vertical displacement field induced by a harmonic moving load ($f = 30$ Hz, $v_0 = 18$ m/s) at the shortest distance from a 3x3 pile group without cap; soil stratum with $H = 20$ m and $\nu = 0.4$.

Motivated by a possible application under the scope of metamaterials, a “zig-zag” pile group layout, depicted in Figure 4.30, was also examined in terms of vibration reduction. In specific, a free-head 2x3 and a 3x3 configuration are considered. The position of reference pile P1 at $x_0 = 16$ m from the load axis remains unchanged. The obtained time-histories of its response are contrasted in Figure 4.30 to the free-field motion at the same location. The ratio $|w_p(0)|/|w_{ff}(0)|$

derived from the entire time-history is equal to 0.32 for the reference pile in both groups and thus, approximately identical to the respective values observed in the rectangular grid configuration. The additional attenuation offered by the pile group appears in the time-history shortly after the load passes by the pile group. In the corresponding time-window (2.98 - 3.13 s), the kinematic interaction factor attains the values 0.46, 0.38 and 0.31 for the pile as single pile, as part of the 2x3, and as part of the 3x3 “zig-zag” pile group, respectively.

In comparison with the regular pile group layout, the “zig-zag” scheme is proven similarly effective in reducing the vibrations from the moving load. For the cases investigated herein, the addition of a further pile row, i.e. 2x3 pile group becoming a 3x3 one, led to an additional attenuation of the vibration level experienced by pile P1. The reduction level depends on the time-window selected for the derivation of amplitudes.

As already shown, the travelling speed of $v_0 = 18$ m/s (64.8 km/h) in combination with the selected soil properties leads to a response similar to that under stationary conditions. It would be therefore meaningful to consider a higher travelling speed. For the sake of computation consistency, and in order to keep the same mesh discretization, the stiffness of the soil was increased. The shear wave velocity of the soil was set equal to $c_s = 170$ m/s. This allows an analysis with a 50 % higher travelling speed, namely $v_0 = 27$ m/s (97.2 km/h) linked with a frequency $f = 45$ Hz. The free-head 2x3 and 3x3 pile groups with a rectangular grid layout are examined, and the respective time-histories are presented in Figure 4.31. The ratio $|w_p(0)|/|w_{ff}(0)|$ obtained from the entire time-history is equal to 0.34, 0.32, and 0.30 for the reference pile ($x_0 = 16$ m) as single pile, and as part of the 2x3 and the 3x3 pile group, respectively. In the time-window from 1.94 to 1.99 s, in which an additional attenuation offered by the 3x3 pile group is manifested, the transfer function for the above cases becomes equal to 0.39, 0.36 and 0.27.



“Zig-zag” layout

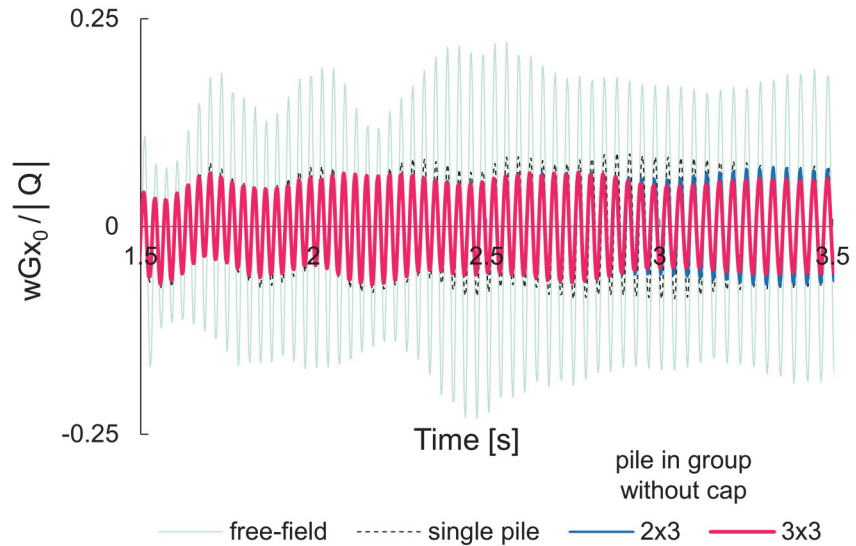


Figure 4.30: “Zig-zag” layout for a 2x3 pile group (solid lines) and a 3x3 pile group (solid plus dashed lines). Vertical displacements of the free-field and of the reference pile P1 at distance $x_0 = 16$ m as single pile or as part of a pile group without cap for an excitation by a harmonic moving load with $f = 30$ Hz and $v_0 = 18$ m/s; soil stratum with $H = 20$ m and $\nu = 0.4$.

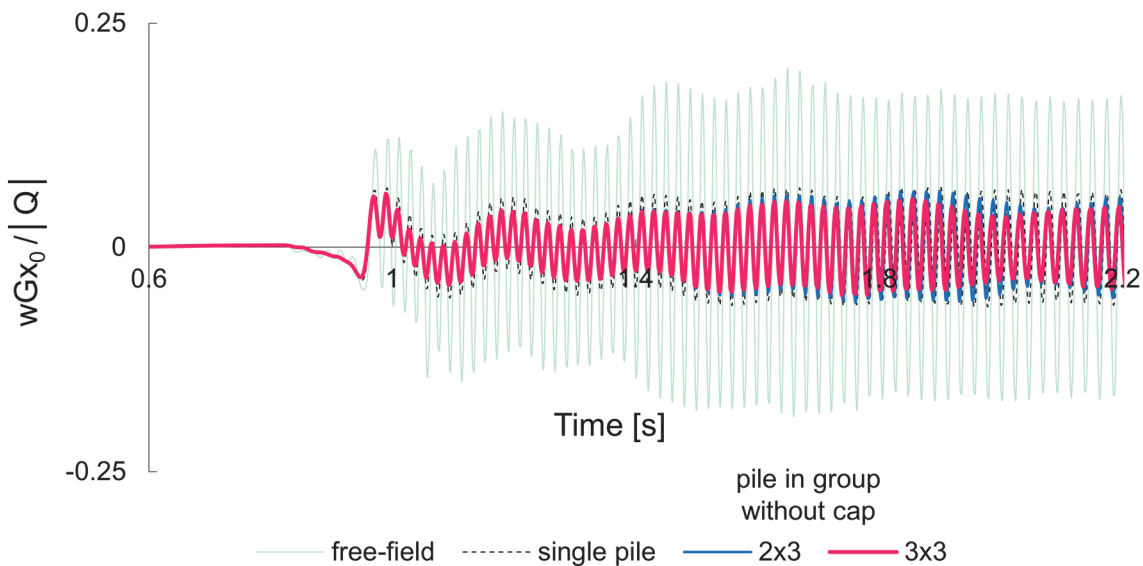


Figure 4.31: Vertical displacements of the free-field and of reference pile P1 at distance $x_0 = 16$ m as single pile or as part of a pile group without cap for an excitation due to a harmonic moving load with $f = 45$ Hz and $v_0 = 27$ m/s; soil stratum with $H = 20$ m and $\nu = 0.4$.

4.3.7 Full 3D FE-model

As already underlined, the presence of an unwanted mirror pile/pile group in the half of the system that is not modelled is implied due to the use of symmetry in the respective models for the moving load. In order to overcome this issue, which may admittedly have a rather minor effect on the results, an updated finite-element model comprising viscous boundaries over its complete periphery was created. In that way, the problem of indirect loading of a single pile group/pile is properly reproduced. The model is depicted in Figure 4.32 along with details of the mesh discretization. It accounts for a 3x3 rigidly capped pile group with $s/d = 3$, as considered previously. However, in this particular section, the material properties differ, since a comparison is presented with results from analyses in the frequency domain considering a stationary harmonic load (this problem is analysed in Chapter 5). Details are given in Section 5.2 (with the most important properties being: $E = 172368$ kPa, $\rho = 1.9$ Mg/m³, $c_s = 180$ m/s, $\nu = 0.4$ $\xi = 2.5$ %, $E_p/E = 150$, $l/d = 15$). The mesh discretization with a uniform finite-element size equal to approximately 0.7 m (becoming very fine in the vicinity of the load path) in combination with the soil parameters and the excitation frequency of $f = 30$ Hz can reproduce one S-wavelength with circa 8 finite elements.

Viscous boundaries are placed peripherally, while the base of the model is fixed, representing thus a soil stratum resting on bedrock. The length of the model is equal to 102 m, and that of the load path 100 m. The load path is placed asymmetrically at a distance of 16 m from the one viscous boundary parallel to it and at 32 m from the other. The pile group under investigation is located centrally between the latter boundary and the load path. The philosophy behind the dimensions in the present design is the same as in the finite-element model for the analyses with the stationary harmonic load (Figure 4.4).

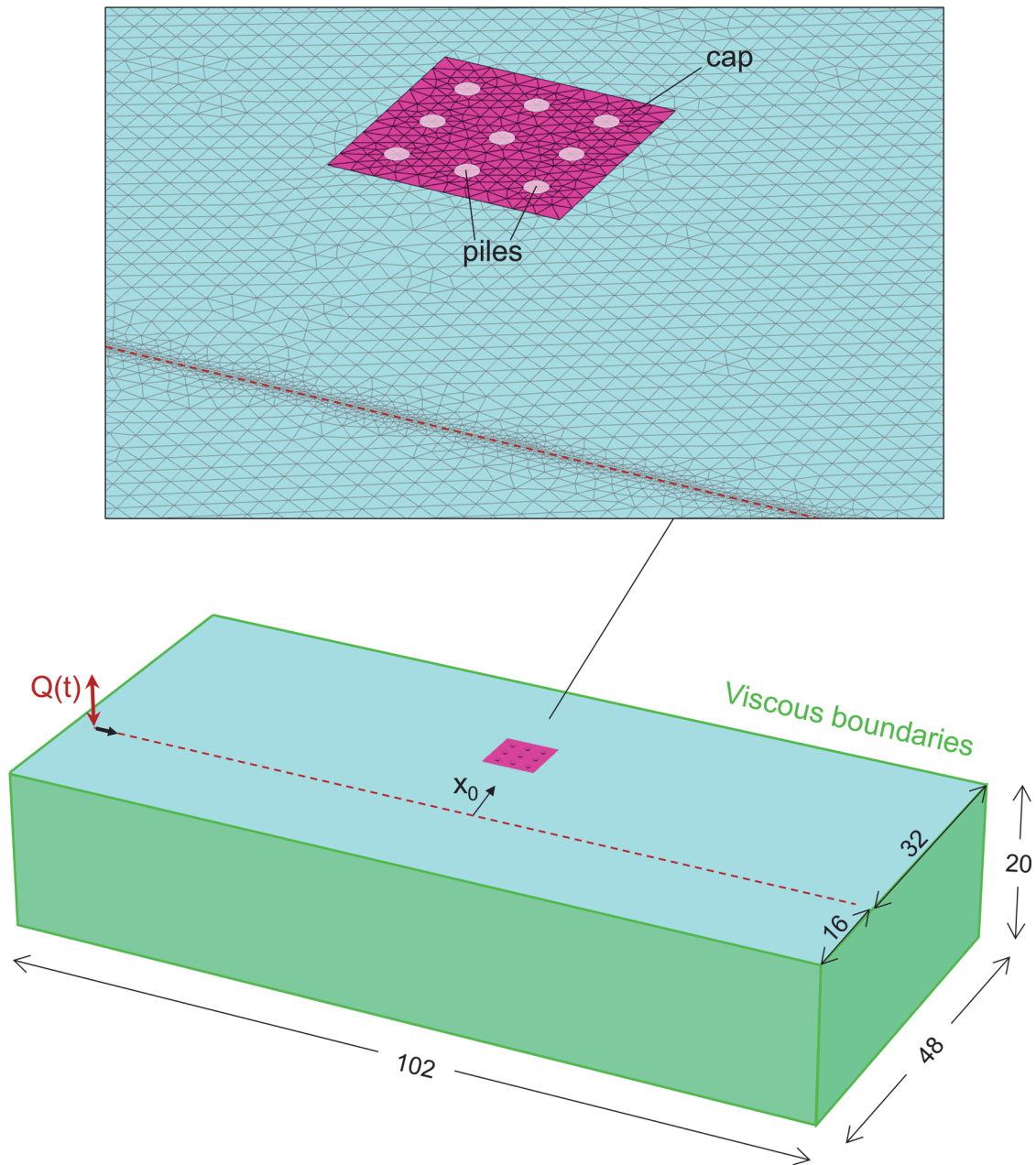


Figure 4.32: Full 3D FE-model for a moving oscillating load on a soil stratum.

The point load travels with a constant speed of $v_0 = 18 \text{ m/s}$ ($\approx 65 \text{ km/h}$). It is applied by means of a ramp-function with a duration equal to 20 % of the total time required for the load to pass by the complete load path ($= 100 \text{ m} / 18 \text{ m/s} = 5.56 \text{ s}$). The magnitude of the load is increased linearly from zero up to its maximum value ($|Q| = 1 \text{ kN}$), and then it starts varying harmonically at $f = 30 \text{ Hz}$. Figure 4.33 shows up to 2 s the load multiplier introduced in Plaxis 3D.

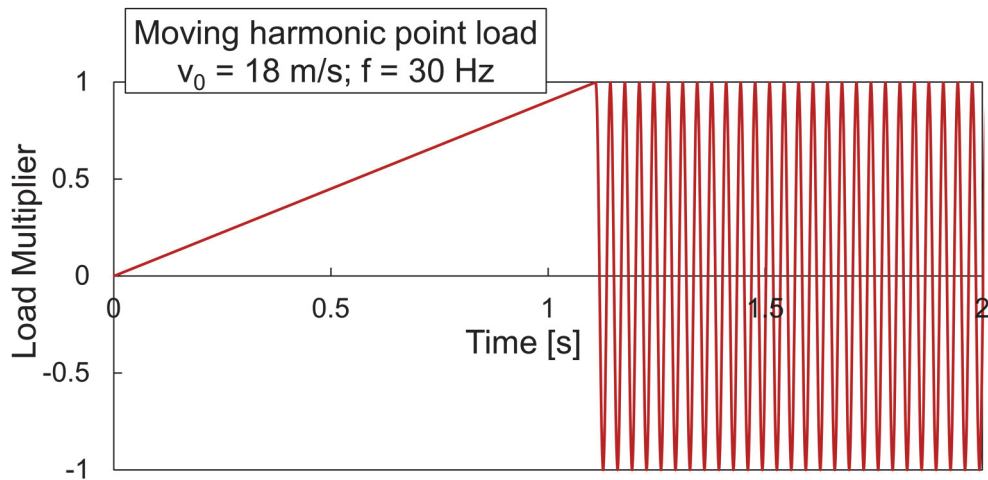


Figure 4.33: Load multiplier for a moving load with $v_0 = 18$ m/s and $f = 30$ Hz.

The comparison with the results from the finite-element analyses with the stationary load in the frequency domain with Abaqus is presented in terms of absolute values of vertical displacement amplitudes in Table 4.4. An additional analysis for pile P1 as a single pile was also performed. The agreement between the two cases is quite satisfactory. The small deviations occur to a great extent due to the different boundary conditions at the base of the models, since the analyses with the moving load consider a soil stratum of thickness $H = 2 \cdot l$, while those with the stationary load a half-space. Nevertheless, the analyses with the updated model confirm that the stationary solution can be used as a good approximation for the moving load problem in many cases of practical interest for which the travelling speed of the excitation source is relatively low in comparison with the Rayleigh wave velocity in the soil.

Table 4.4: Vertical displacement amplitudes $|w_p|$ of piles P1, P2, P3 in a 3x3 pile group: Comparison with the FEA results from Abaqus in the frequency domain.

		$ w_p \cdot 10^{-8}$ [m]	
		Moving load Time domain	Stationary load Frequency domain
3x3 pile group	P1	3.51	3.94
	P2	2.90	2.33
	P3	7.16	8.26
single pile	P1	7.17	8.05

4.5 Conclusions

The kinematic response of single piles and pile groups to a wave field from a moving oscillating load was investigated by means of the finite-element method (FEM) in the time domain with the software Plaxis 3D. A stationary harmonic load was also considered as a lower-bound of a travelling speed equal to zero. First, the observations on the response to the latter are summarized:

- A good agreement of the free-field response to the wave field of a stationary harmonic load with the analytical solution for Rayleigh wave excitation is established at a distance from the load between $7.5 \cdot \lambda_R$ and $10 \cdot \lambda_R$ ($\nu = 0.4$). It is known that for practical applications, the analytical solution for the far-field can be considered for the response of the surface at close distances of $2-3 \cdot \lambda_R$; but even up to a depth of $z = \lambda_R$ according to the findings herein, the numerical results match the analytical solution quite well.
- The distance of the viscous boundary from the area of interest plays an important role in the accuracy of the results, and so does the mesh discretization. An overall good agreement with the analytical solution can be established with circa 10 finite elements per Rayleigh wavelength λ_R .
- Even with a twice as fine mesh though, the accuracy of the FEA results at farther distances in the vicinity of the lateral viscous boundary deteriorates.
- Dynamic interaction factors (or transfer functions) for a single pile attain smaller values as the distance from the excitation source decreases. This

is due to the interference of P- and S-waves leading to an enhanced resistance of the single pile to the induced motion.

- Increased transfer functions are obtained for piles less stiff in relation to the surrounding soil (e.g. $E_p/E = 100$), indicating that the pile follows the free-field motion in a more compliant manner.
- A connection of the piles within a group via a rigid cap results in significant vibration reduction.
- For the examined case herein, the effect of the pile cap mass on the response of the group manifests itself practically only beyond $f = 35$ Hz, resulting in a considerable increase of the transfer function, even up to 100 %.
- Both the single pile and the pile group can reduce the free-field vibrations mainly due to the redirection of the energy towards greater depths, but also as a result of the wave diffraction through front pile rows (against the wave propagation direction)
- At higher excitation frequencies the shielding efficiency of piles increases.
- A good agreement with the analytical solution from Makris (1994) for single piles in a Rayleigh wave field is established even at closer distances ($2-3 \cdot \lambda_R$) to the point load as the ones considered herein.

The analyses with a moving load of constant magnitude showed that:

- The gradual application of the load by means of a ramp-function increasing linearly its magnitude reduces a distortion in the response, which appears due to the finite load path.
- A ramp-function over a time equal to 20 - 30 % of the total analysis time was proven to be optimal.
- A sufficiently long load path (and thus, model length) in combination with a ramp-function for the load application, and a travelling speed v_0 relatively low in comparison with the Rayleigh wave speed in the soil c_R can significantly reduce the aforementioned distortion in the response.
- The absence of excitation frequency signifies that there is no wave propagation in the soil. The point load yields a vertical displacement, which can be perceived as a single “disturbance” that propagates.
- Due to its quasi-static character, the moving constant load has a rather limited influence zone. This confirms the static nature of this loading type.
- When the travelling speed v_0 is relatively low in comparison with the Rayleigh wave velocity in the soil c_R (indicatively under 50 %), which is quite common in engineering practice, the maximum vertical

displacement due to the moving load exhibits a negligible deviation from the static solution.

- At low values of the ratio v_0/c_R , the use of a viscous boundary at the base of the model in order to simulate a half-space leads to lower accuracy. Replacing it with a rigid base may be a solution in cases where the model depth is sufficiently large so that the rigid base does not have practically any influence on the response. This is a limitation of the FEM.

Finally, from the investigations on the moving oscillating load, the following conclusions are drawn:

- The influence zone of the moving load with a time-harmonic magnitude is larger in comparison with that of the moving constant load. Consequently, the former load type is of critical importance for the vibration protection practice.
- Overall, the effect of a single pile on the induced free-field motion is rather localized, since the influence range of the pile is equal to approximately 1-2 m, mostly developing at the back (with respect to the direction of wave propagation).
- The single pile response to a moving oscillating load matches the analytical solution from Makris (1994) for Rayleigh wave excitation very well, especially as the distance of the pile from the load path increases.
- Under the scope of metamaterials, a further pile row to the front of the 2x3 pile group without cap (turning it into 3x3) resulted in an additional attenuation of the vibration level experienced by the central pile at the back. This was observed in the cases of both a rectangular and a “zig-zag” layout, as well as of the higher travelling speed of 27 m/s ($f = 45$ Hz).
- For low values of the ratio v_0/c_R , the agreement of the free-field response to a moving oscillating load with the stationary solution is quite satisfactory.
- Of particular importance for the engineering practice, is that the stationary harmonic load can be a good approximation for the moving harmonic load for low values of the ratio v_0/c_R , not only in the case of the free-field, but also of solitary piles and pile groups.

5 Kinematic response of piles to a stationary harmonic load

5.1 Problem statement

The need for a detailed study over a wide frequency range was the motive to investigate the problem of kinematic interaction of piles in the frequency domain. For this purpose, the finite-element software Abaqus (version 2019) was employed. Direct-solution steady-state dynamic analyses were performed, with which the steady-state dynamic linearized response of a system to harmonic excitation is computed.

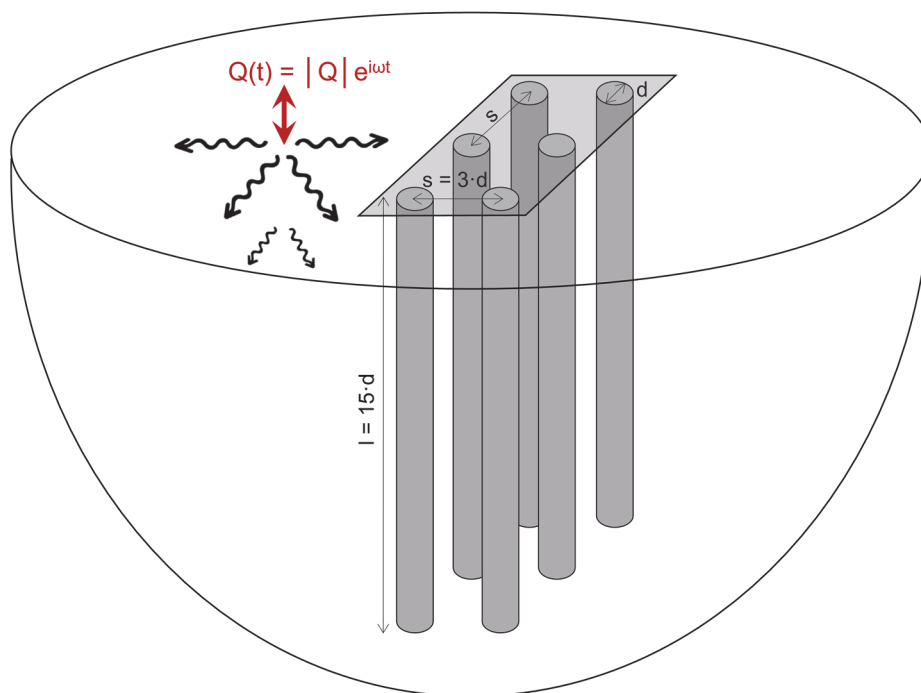


Figure 5.1: Schematic illustration of a pile group excited by the wave field emanating from a stationary harmonic point load.

A stationary vertical harmonic point load acting on the surface of a half-space is the source of excitation. The response of various pile group as well as piled raft configurations located at a distance from the load is examined. A sketch of the problem under investigation is given in Figure 5.1. The emanating waves lead to a complex foundation response including vertical, horizontal and rocking

components. Herein emphasis is placed on the vertical vibration mode, the output of which is given in terms of displacement amplitudes.

The present study was in part conducted under the scope of metamaterials, which are natural or artificial materials, or structures in periodic patterns, able to control wave propagation. Based on this definition, the piles embedded in the soil form a composite pile–soil system with potential in wave shielding. Consequently, the following question is raised: How does the periodicity of the piled foundation affect the resulting attenuation of motion?

In this direction, the pertinent finite-element analyses aim to explore how the number of pile rows and columns in a piled foundation influences the vibration reduction. Consequently, the following concept is implemented: By keeping the location of the furthest back pile row, as well as the center-to-center pile distance invariable, the piled foundation is extended to the front – opposite to the wave propagation direction – by additional pile rows. Their effect on the attenuation of motion is quantified through transfer functions with respect to the mid-pile at the furthest back row (referred to as reference pile P1), as well as to the free-field behind the pile group/piled raft (point B). In specific, these transfer functions are ratios of the vertical displacement amplitude of the reference pile as part of the corresponding configuration over the vertical displacement amplitude of the free-field at the location of the pile head center. Similarly, the transfer function at point B is defined as the ratio of vertical displacement amplitudes at this point with/without the presence of the piled foundation. The distance of each pile row from the point load is denoted as x_0 .

The examined configurations are summarized in Figures 5.2 and 5.3. In specific, a top view of the problem involving pile groups 2x3, 3x3, 4x3 and 5x3 is shown in Figure 5.2. Correspondingly, configurations 2x5, 3x5, 4x5 and 5x5 are portrayed in Figure 5.3. The piles P1-P5 located at the center of each row are monitored for the derivation of transfer functions. The center-points of these reference piles and the point load collinear. Pile rows are defined perpendicularly to the wave propagation direction with respect to the piled foundation, while pile columns are defined parallel to it. Evidently, the smallest system tested herein is a 2x3 pile group/piled raft consisting of 2 rows parallel to the wave propagation direction and 3 columns. The number of pile rows is increased up to 5. In a similar manner, each configuration is extended by two additional pile columns

(e.g. 2x3 to 2x5) to examine the effect from the extension of the piled foundation parallel to the wave propagation direction.

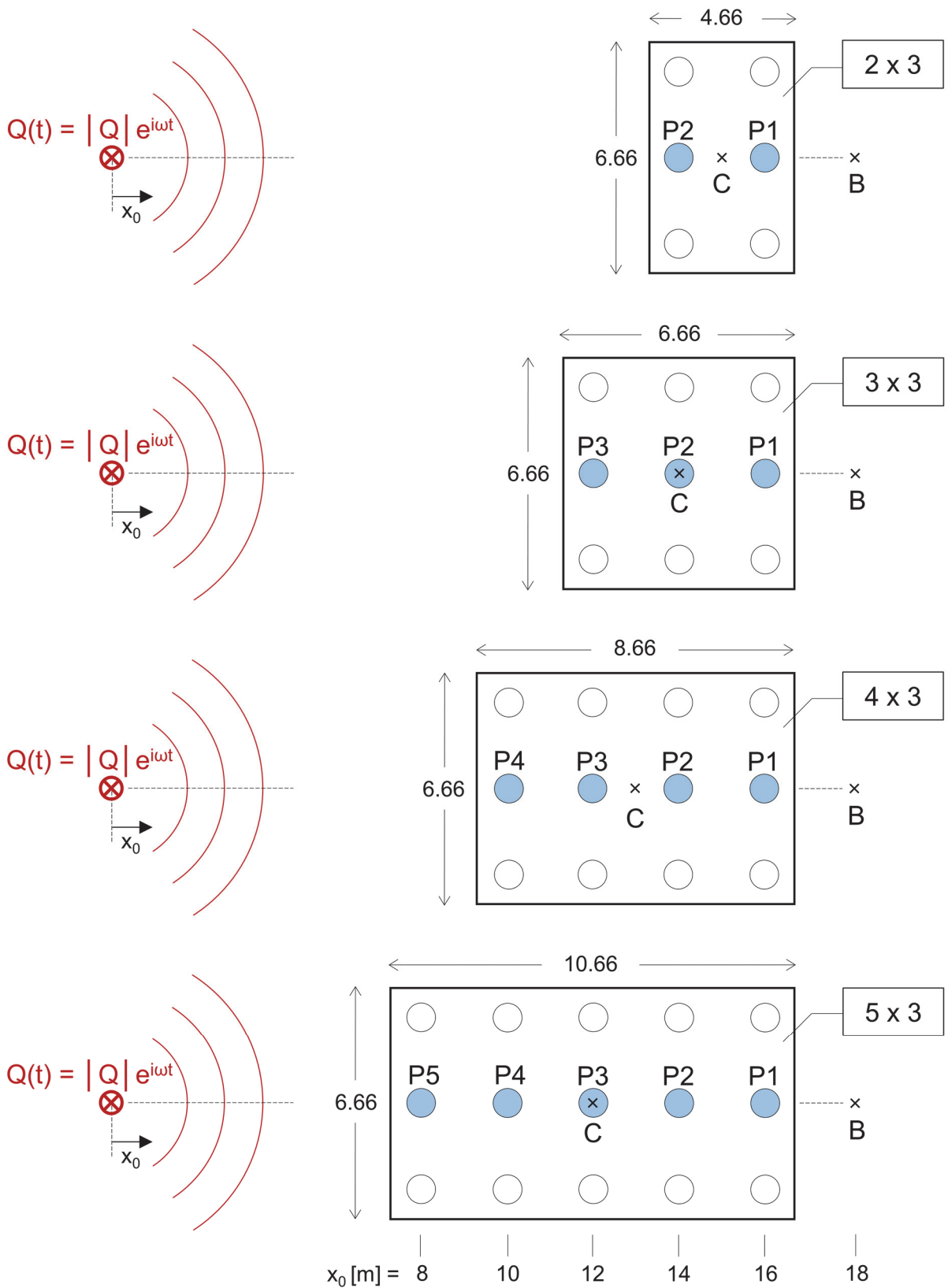


Figure 5.2: Top views of pile groups/piled rafts 2x3 - 5x3. $d = 0.67$ m.

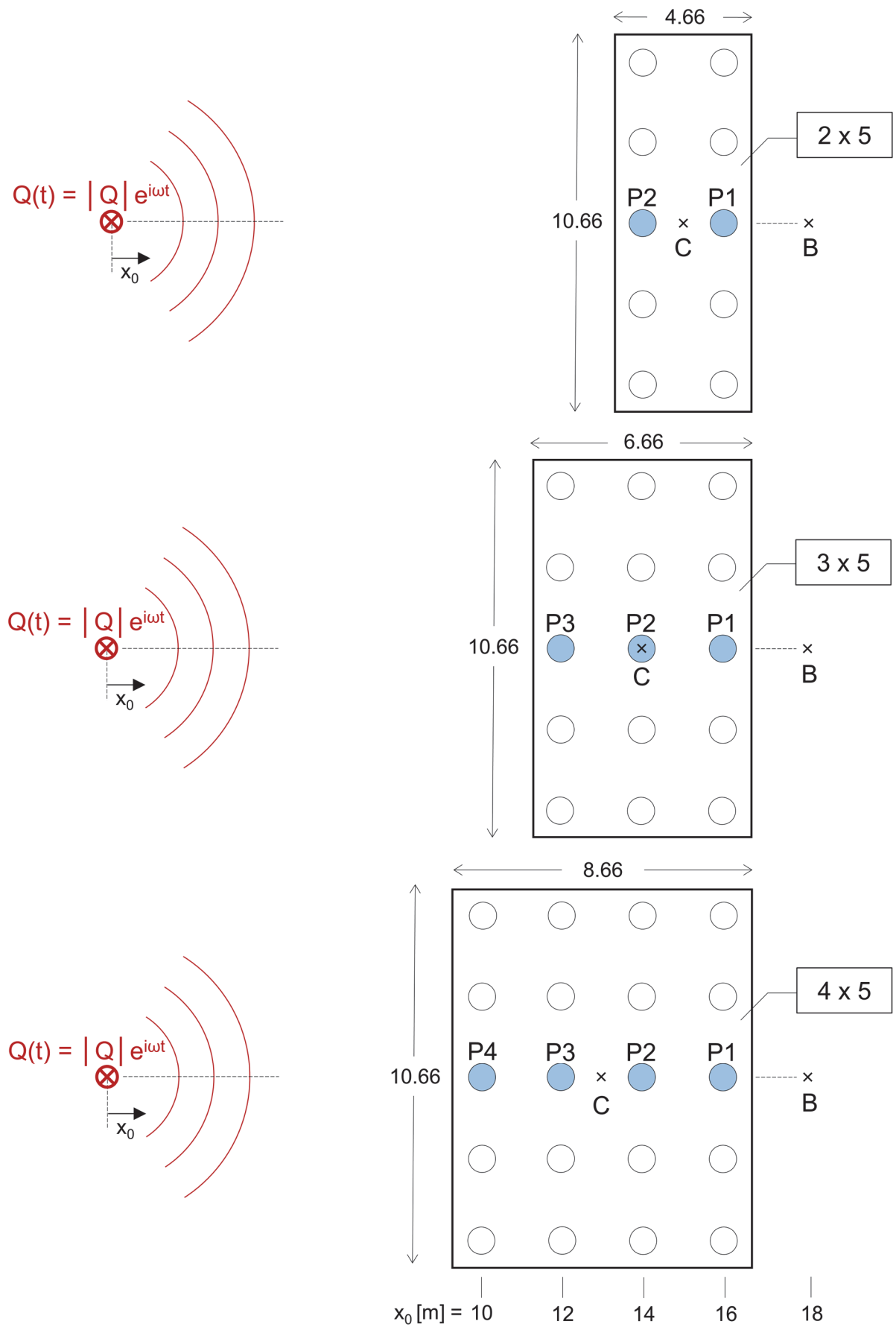


Figure 5.3: Top views of pile groups/piled rafts 2x5 - 5x5. $d = 0.67$ m.

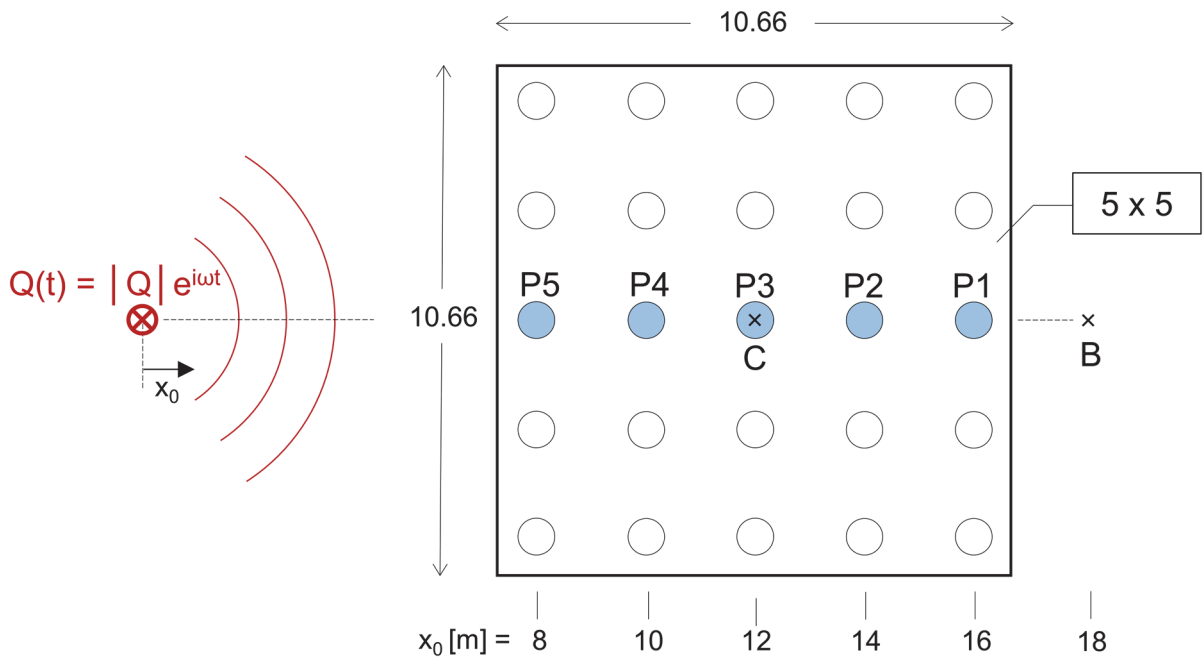


Figure 5.3 continued.

Fixed-head conditions (zero top rotation) are considered for the piles, which are connected via a rigid, massless cap. In the case of a pile group, the cap is not in contact with the soil. To examine the effect of the boundary condition enforced through a perfect contact between cap and soil, corresponding piled rafts as well as rafts acting alone were also analysed. All the above cases are schematically illustrated in Figure 5.4.

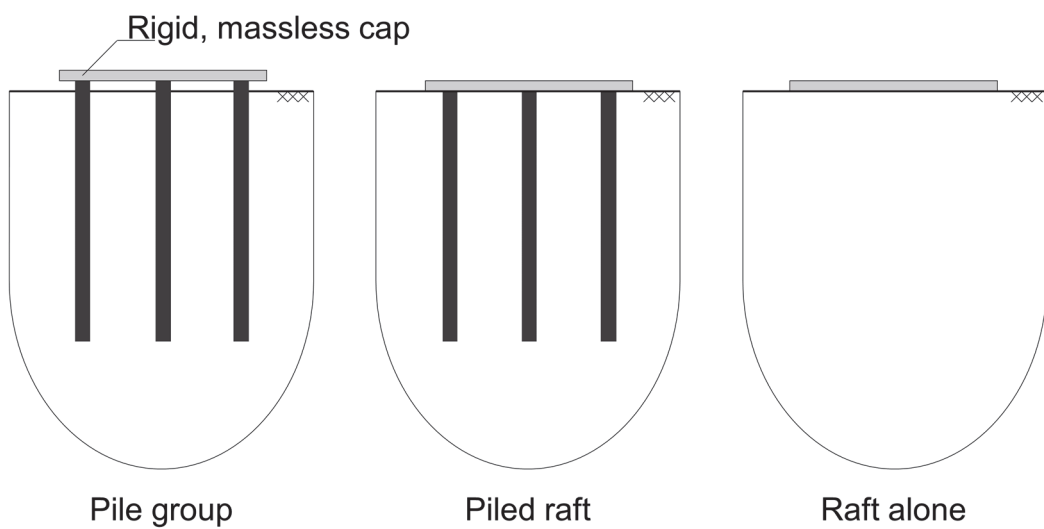


Figure 5.4: The different systems under investigation: pile group, piled raft, and raft alone.

5.2 Finite-element modelling

The finite-element model developed with Abaqus is depicted in Figure 5.5 along with aspects of mesh discretization. Taking advantage of symmetry, only half of the problem is simulated.

In conjunction with the standard finite elements used to model the region of interest (Figure 5.6), solid continuum infinite elements serving as absorbing boundaries are placed peripherally as well as at the base of the model to simulate a half-space. These special elements provided by Abaqus are, in the case of dynamic analyses, based on the theory of Lysmer & Kuhlemeyer (1969). Their response assumes plane body waves traveling orthogonally to the boundary. In this study first-order 8-node continuum infinite elements (CIN3D8) are used.

As shown in Figure 5.5, the distance of the point load from the peripheral absorbing boundaries varies. The interacting system load–piled foundation is placed at the center of the model, not the load. Unwanted reflections were not noticed in the response. The above distance was also chosen between the furthest back pile row and the closest absorbing boundary. A model with the load acting at its symmetry axis would have led to an unnecessarily large finite-element region, increasing thus the computational time by far. The length of the infinite elements is also based the documentation of Abaqus (2019). According to it, the second node along each edge of an infinite element in the direction of infinity must be positioned twice as far from the so-called “pole” of the far-field solution for the element edge as the node at the interface between finite- and infinite-element region on the same edge. For example, in the case of a point load applied on the surface of a half-space, the pole of the solution coincides with the point of application of the load.

The model is designed to account for pile group or piled raft configurations up to 5x5; when smaller configurations are examined, the “redundant” piles are replaced by soil. This is achieved by simply assigning soil properties to these unnecessary pile parts. The same philosophy is behind the pile geometry, which can be identified in Figure 5.5 at the location of the vertical point load: by activating solely this pile, and by applying a uniform displacement at its head, dynamic impedances and interaction factors were obtained in the frame of an additional validation. For the main core of the analyses, however, where the

focus is placed on the pile group, these particular solitary piles remain inactive and simply serve as soil.

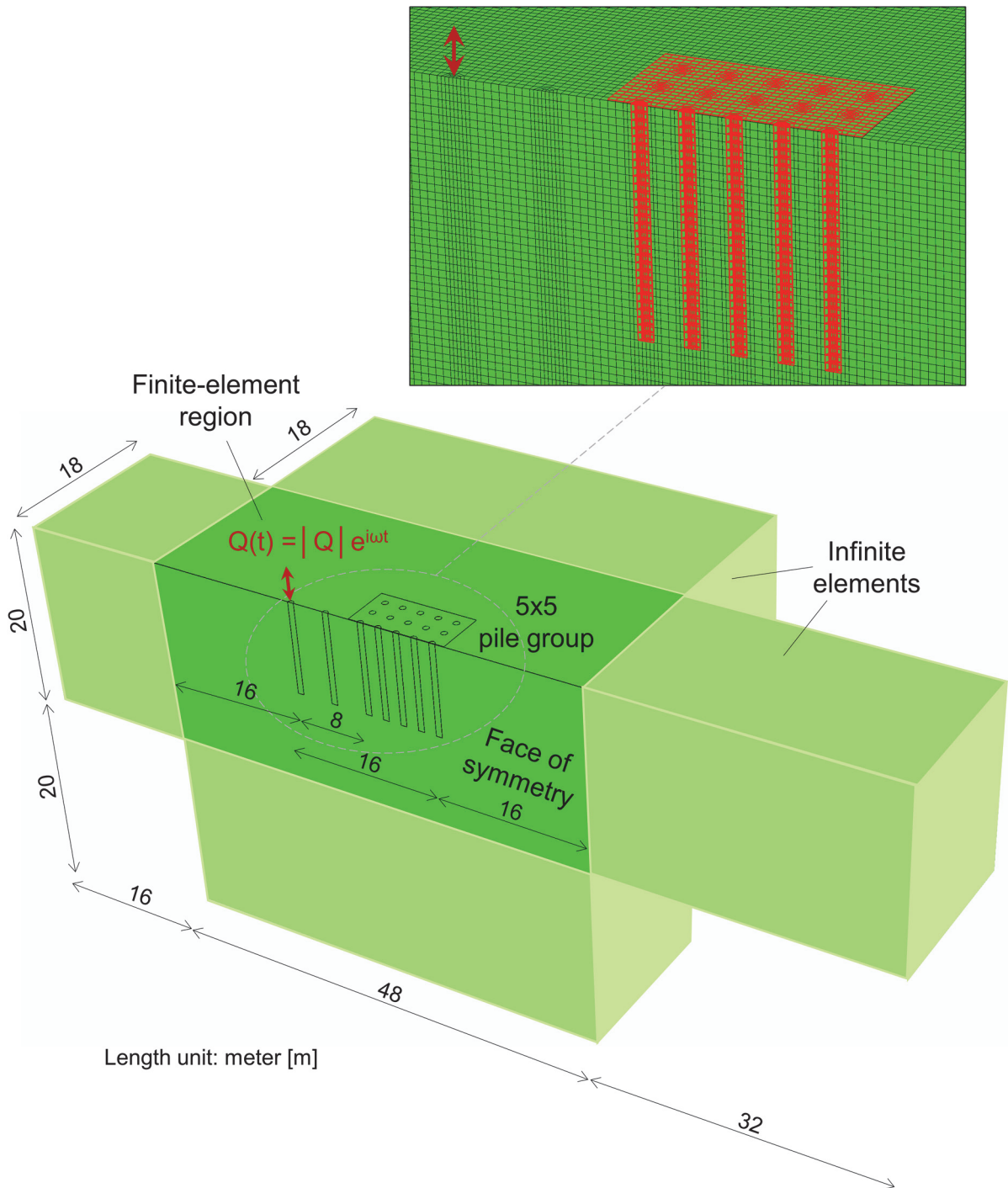


Figure 5.5: Finite-element model including the 5x5 pile group. (The part with pile geometry underneath the load, as well as the one between the load and the pile group, represent *soil* and not piles in pile group analyses.)

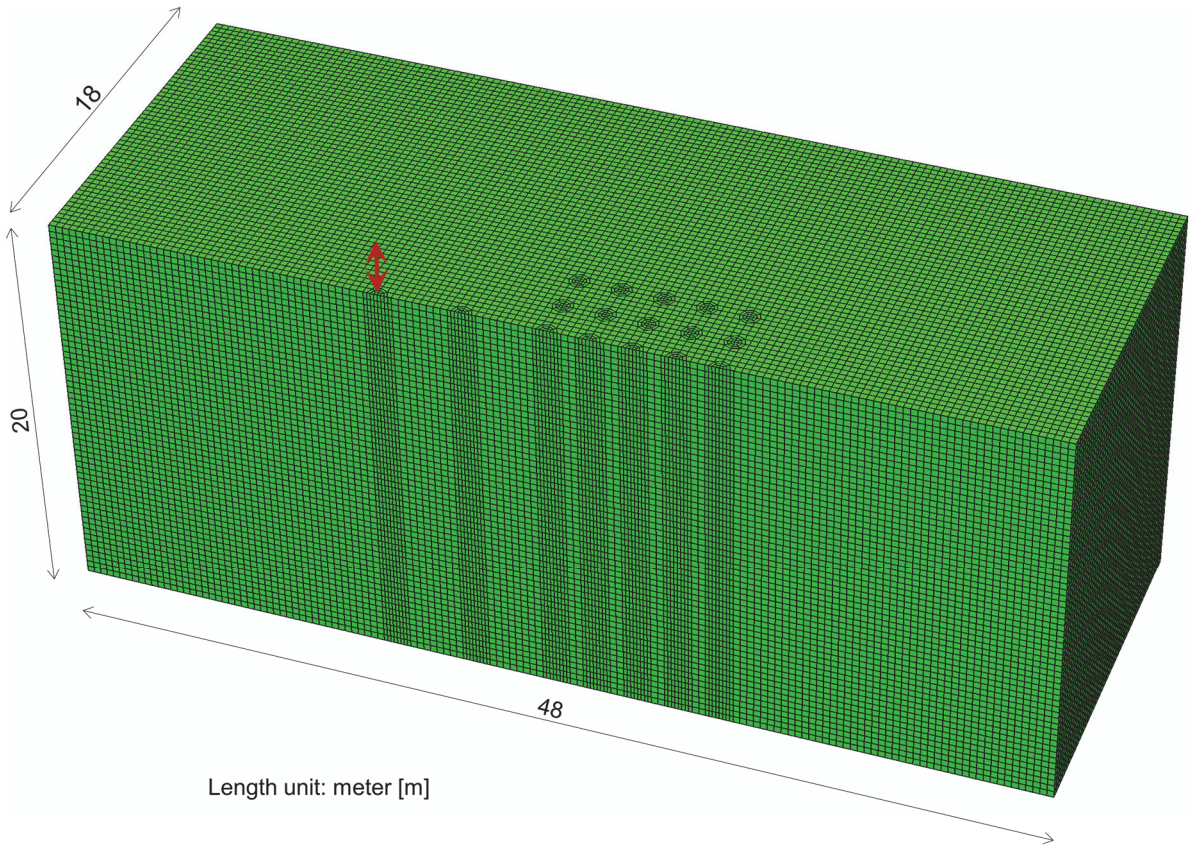


Figure 5.6: Finite-element region of the model.

For the core of the analyses investigating the response of various pile group configurations, the implemented parameters can be found below. Only for the comparison with the results obtained with the program Plaxis, presented next, the same parameters of Section 4.2.1 were applied.

The soil is modelled as a linear-elastic continuum with a Young's modulus $E = 172368$ kPa and a Poisson's ratio $\nu = 0.4$. The resulting shear modulus $G = 61560$ kPa in combination with the density $\rho = 1.9$ Mg/m³ yields a shear wave velocity $c_S = 180$ m/s. The Rayleigh wave velocity in the soil is $c_R \approx 170$ m/s. A hysteretic damping ratio of $\zeta = 2.5$ % is introduced.

A linear-elastic material with a Young's modulus E_p representing concrete is assigned to the piles. The resulting pile flexibility is $E_p/E = 150$, which is common in engineering practice. The Poisson's ratio is taken as $\nu_p = 0.2$, whereas the unit weight $\gamma_p = 25$ kN/m³. The mass density ratio is $\rho_p/\rho = 1.34$. The length $l = 10$ m is kept constant for all analyses, as well as the diameter $d = 0.67$ m

resulting in a pile slenderness $l/d = 15$. The center-to-center pile distance s normalized by the diameter d is equal to $s/d = 2.985$. For conciseness, $s/d = 3$ is used throughout the text.

The soil as well as the piles are modelled with first-order 8-node brick elements (C3D8). A fully bonded contact between the piles and the soil is assumed, so that no slippage or detachment occurs.

Table 5.1: Geometric characteristics of the examined pile group configurations.

Configuration [Pile rows x columns]	Distance of configuration center from load x_0 [m]	Dimensions of cap/raft	
		a [m]	b [m]
2 x 3	15	4.66	6.66
3 x 3	14	6.66	6.66
4 x 3	13	8.66	6.66
5 x 3	12	10.66	6.66
2 x 5	15	4.66	10.66
3 x 5	14	6.66	10.66
4 x 5	13	8.66	10.66
5 x 5	12	10.66	10.66

Geometric aspects of the examined systems are presented in Table 5.1, including the cap/raft dimensions. These are relevant only in the case of piled rafts, where the raft–soil contact is considered, and, consequently, the area of the raft has an effect on the results. The massless, rigid cap/raft is modelled with linear 4-node shell elements (S4). The thickness of the raft is taken as $d_{\text{cap}} = d = 0.67$ m, which, however, has no influence on the response. The distance between the pile- and raft-edge is equal to circa $1.5 \cdot d_{\text{cap}}$.

In the finite-element models including the pile groups, the piles are extended above the soil surface by 0.005 m. The cap is then placed atop them. The pile-head response of each pile is calculated at its central node at the level of the soil

surface. The geometric center of the cap is chosen as a characteristic point for the calculation of the pile group response, as indicatively shown in Figure 5.7 for the 3x3 pile group. In the depicted system, the response obtained at the head of the central pile is practically equal to the response calculated at the center-point of the cap. Obviously, when modelling a piled raft there is no gap between the raft and the soil, so the response of all elements is calculated at the respective nodes at the soil surface level.

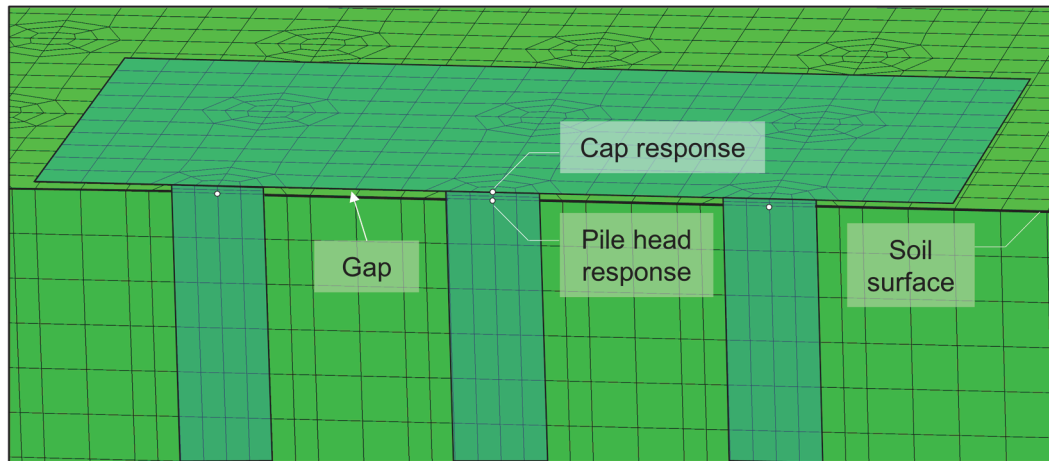


Figure 5.7: Modelling details of the 3x3 pile group. The white points highlight the nodes at which the response is calculated.

The excitation frequency f of the vertical harmonic point load $Q = |Q| \cdot e^{i\omega t}$ varies from 8 to 64 Hz with a step of 2 Hz.

The mesh is uniform with a finite-element size equal to approximately 0.333 m. For the highest frequency considered herein, this corresponds to approximately 8 finite elements per Rayleigh wavelength λ_R .

5.3 Frequency- vs. time-domain analysis

5.3.1 Verification of the free-field response

The efficiency of the analysis in the frequency domain (FD) in the frame of the present study was one the main motives for using the finite-element software Abaqus. The first step was to verify the free-field response to a stationary harmonic point load against the semi-analytical solution from Vrettos (1991). To

account for the presence of hysteretic damping in the soil, the linear-elastic response derived from Vrettos (1991) is multiplied with the factor $\exp(-2 \cdot \pi \cdot \xi \cdot r / \lambda_R)$. This is known as Mintrop approximation (Vrettos 2009, DGGT 2019). Moreover, a comparison is presented with the results in Chapter 4 from analyses in the time domain (TD) using the finite-element software Plaxis. It is underlined that the finite-element region of the model in Abaqus has not only the same dimensions as the model in Plaxis, but also *almost* the same discretization in order to allow a fair enough comparison between the two analysis tools. For this comparison, the same soil properties as in Section 4.2.1 are considered, which correspond to a relatively incompetent soil.

To calculate the free-field response to a vertical harmonic point load acting on the surface of a half-space, all parts in the finite-element model intended for piles are substituted by soil. With reference to Figure 5.5, the free-field response is monitored to the right of the load. The resulting vertical displacement amplitudes on the soil surface are normalized by the shear modulus of the soil G , the distance from the excitation source r and the load amplitude $|Q|$, and are presented in Figure 5.8 against the dimensionless frequency $\omega r / c_s$. The response in the different cases compared in Figure 5.8 is derived as follows:

- Plaxis [TD – r : variable, f : constant]: A single excitation frequency ($f = 30$ Hz) is applied, and the response is obtained at nodes at a varying distance r from the source. Note that with a single time-domain analysis, this is the only possible way to reproduce the pertinent curve.
- Abaqus [FD – r : variable, f : constant]: The response to a single excitation frequency ($f = 30$ Hz) is calculated at a varying distance from the load. The principle is the same as above, yet the analysis is conducted in the frequency domain.
- Abaqus [FD – r : constant, f : variable]: A range of frequencies ($f = 1 - 60$ Hz) is applied, with the response being monitored at a specific distance from the point load ($r = 16$ m, which corresponds to the location of the farthest pile from the excitation source).

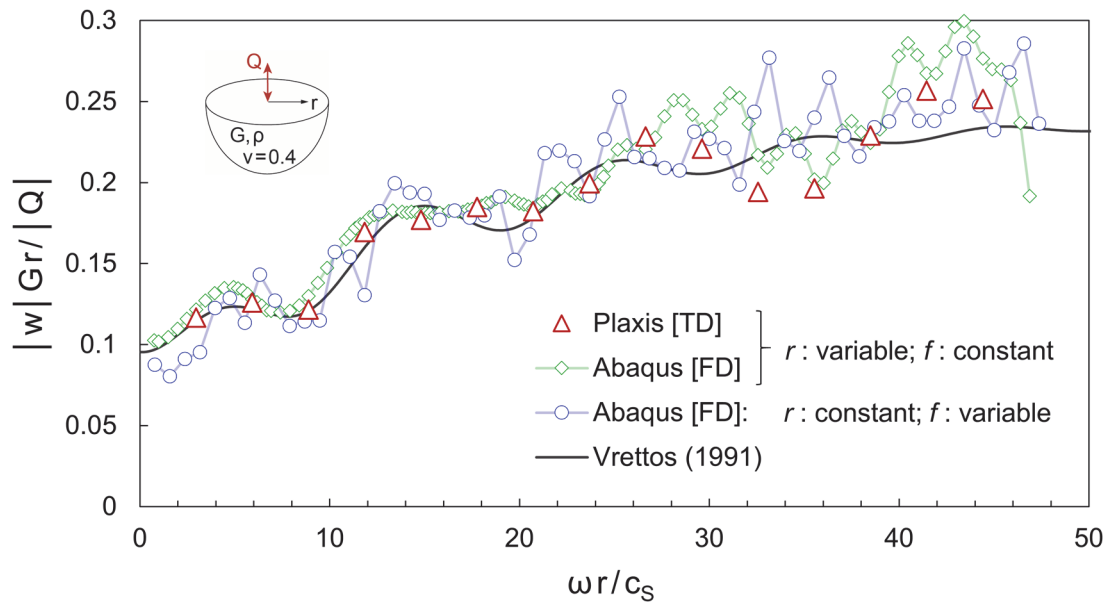


Figure 5.8: Frequency- vs. time-domain analysis: Normalized vertical displacement amplitudes at the surface of a homogeneous half-space due to a vertical harmonic surface point load versus the dimensionless frequency. $\xi = 1 \%$, $\nu = 0.4$.

As shown in Figure 5.8, the agreement between time- and frequency-domain analysis is satisfactory. In addition, the FEA results match reasonably the theoretical solution, with deviations becoming more pronounced as the excitation frequency or distance from the load increases. This is unsurprising though, since in the vicinity of the absorbing boundary unavoidable minor reflections have an effect on the response. In the case of increasing frequency, on the other hand, the number of finite elements corresponding to a single wavelength decreases, leading thus to an overall less accurate response. One can observe that the analyses with varying frequency in Abaqus yield some discrepancies from the analytical solution at low frequencies, which, due to the corresponding large wavelengths, are attributed to reflections by the infinite elements set as absorbing boundaries. A larger finite-element model would have improved these results, but for the main analyses further on, the focus lies on frequencies $f \geq 8$ Hz, which are not affected by this.

The frequency-domain analyses yield very similar results regardless of the approach employed (varying either the distance from the load or the frequency). Since the focus in the present study lies primarily on the effect of frequency on

the kinematic response, all results presented from this point on are derived from analyses with a varying frequency.

- Influence of hysteretic damping

It is reminded that a Rayleigh-type damping corresponding to a hysteretic damping ratio $\zeta = 1\%$ was introduced in the soil for the time-domain analyses performed with Plaxis. In Abaqus, the frequency-independent hysteretic damping ζ reflecting the internal energy dissipation characteristics of the soil can be directly implemented. To investigate whether the above low value could be the cause of the irregularities appearing in the free-field response curves (recall Figure 5.8), additional analyses were conducted in the frequency domain, with the hysteretic damping ratio being varied up to 4%.

The Mintrop approximation (Vrettos, 2009; DGGT, 2019) is employed in order to adjust the semi-analytical solution from Vrettos (1991) used for verification to the different hysteretic damping ratios. The resulting free-field response curves are presented in Figure 5.9. The graph is enlarged in the low-frequency range up to $\omega r/c_s = 16$. Indeed, even from a value of $\zeta = 2.5\%$, the curve becomes significantly smoother, and the deviations from Vrettos (1991) are substantially reduced. At high frequencies, the free-field response for $\zeta = 4\%$ exhibits some slightly increased differences from the theoretical curve, which are attributed to the approximation for the attenuation of motion with distance from the source.

Apparently, the hysteretic damping ratio $\zeta = 1\%$ does not offer adequate energy dissipation in the specific system, presumably leading to reflections when the waves reach the absorbing boundary. A higher value of material damping ensures a sufficient attenuation of vibrations before they arrive at the interface between the finite-element region and the infinite elements.

Therefore, a hysteretic damping ratio $\zeta = 2.5\%$, which is also relevant for the vibration protection practice, was selected for the analyses further on.

A final point to highlight is that the deviation from the analytical solution at low excitation frequencies due to wave reflection by the infinite elements is, as expected, independent from hysteretic damping, which is present in dynamic systems.

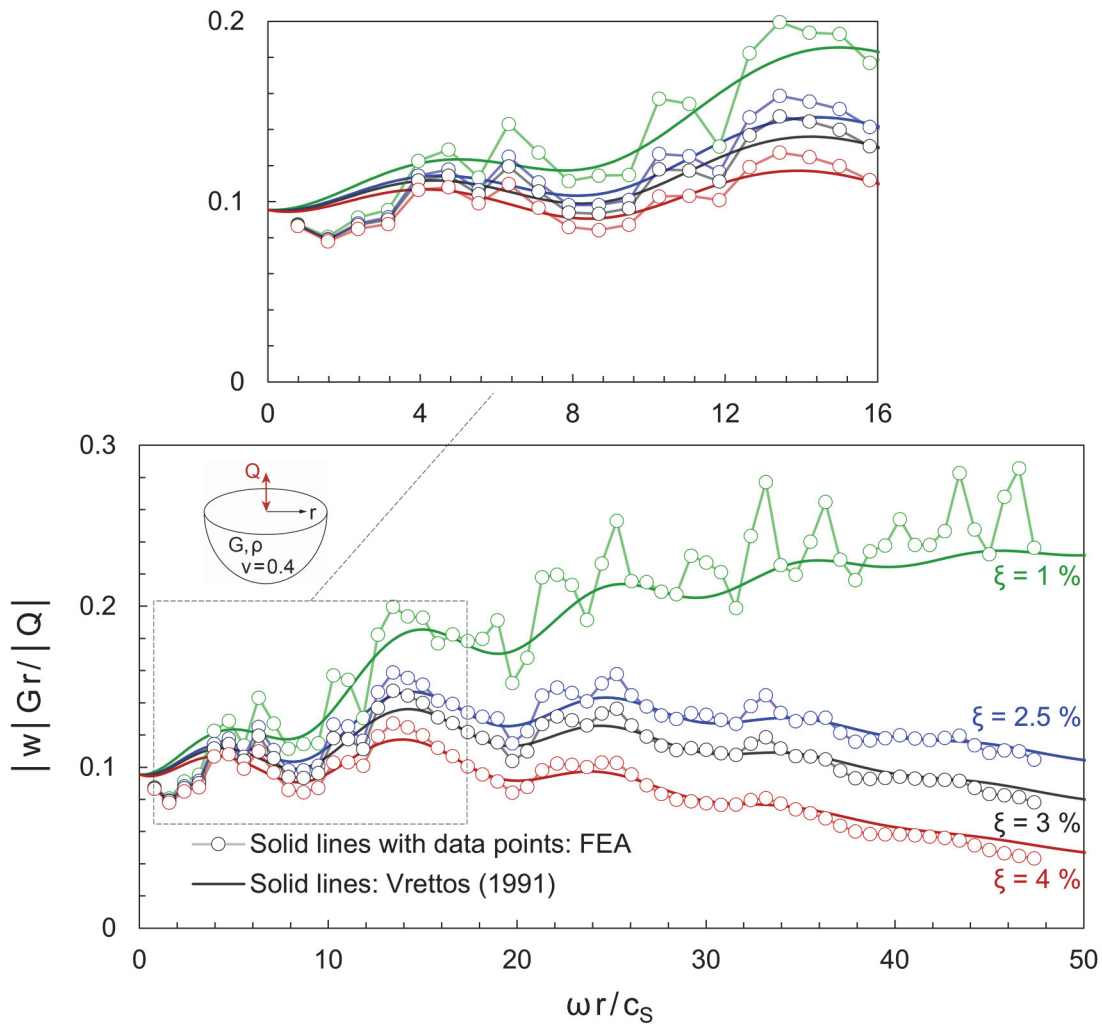


Figure 5.9: Influence of the hysteretic damping ratio ξ : Normalized vertical displacement amplitudes at the surface of a homogeneous half-space due to excitation with a vertical harmonic surface point load versus the dimensionless frequency. $\nu = 0.4$.

5.3.2 Results for a single pile and pile group

After the verification of the free-field response, as a next step, the kinematic response of the 3x3 pile group analysed in the time domain with Plaxis in Chapter 4, was recalculated with Abaqus in the frequency domain within a broader frequency range (10 - 60 Hz). Results are presented in terms of transfer functions, relating the vertical displacement amplitude at the pile head $|w_p|$ to that of the free-field at the same location $|w_{ff}|$. Piles P3 and P1 (see Figure 5.2) being the front and furthest-back central piles at the distances $x_0 = 12$ m and $x_0 = 16$ m, respectively, are monitored. First, the response of each one as a solitary pile is

presented in Figure 5.10 along with a comparison with the analytical solution from Makris (1994), which is thoroughly presented in Section 4.1. Interestingly, the results are in good accord with the analytical solution for the whole frequency range, despite the fact that the latter assumes excitation exclusively by Rayleigh waves. In our case, however, due to the vicinity to the excitation source, P- and S-waves interfere in the response, especially at low frequencies. Accordingly, one would expect the agreement to improve with increasing frequency, since the distance from the excitation source at which the far-field begins becomes shorter. Note also that the solution from Makris (1994) employs a Winkler model, while herein the piles modelled with volume elements are embedded in a continuum.

Figures 5.11 and 5.12 depict the response of piles P1 and P3 in the 3x3 group, which is either free-standing or rigidly capped, respectively.

In all cases, the match between the two analysis tools (frequency- and time-domain analysis) is excellent. Based on the needs of the present study, the analyses in the frequency domain are undoubtedly superior in terms of efficiency, since, compared to the time-domain analyses that require a large number of dynamic cycles to reach a steady-state response in order to derive displacement amplitudes with higher accuracy, they yield in a significantly reduced running time a plethora of data points. This is essential for a realistic representation of response characteristics. For example, notice Figure 5.12 for pile P1 in the rigidly capped group: With the frequency-domain analysis, a valley in the response is captured between the dimensionless frequencies 1.16 and 1.32 (corresponding to $f = 35$ and 40 Hz). On the other hand, the fewer available data points from the time-domain analyses create the (false) impression of a smoother response. To avoid misunderstanding: The issue addressed is the lower competence of time-domain analysis in the derivation of results for the type of problems examined herein, not the accuracy of the method.

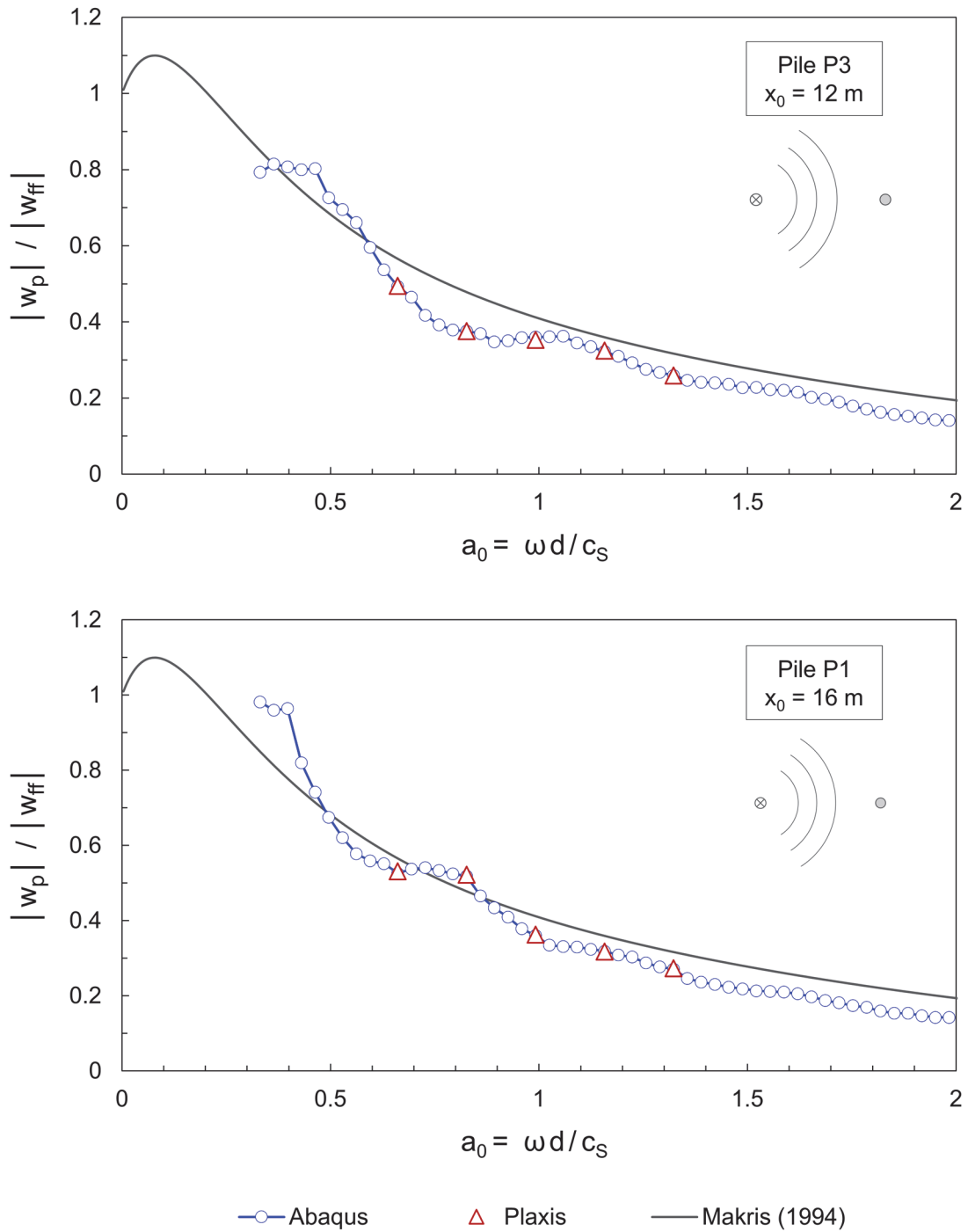


Figure 5.10: Comparison between time- and frequency- domain using Plaxis and Abaqus, respectively: Response of a single pile embedded in half-space at a distance x_0 from the vertical point load. The solution from Makris (1994) for Rayleigh wave excitation is also depicted for comparison.

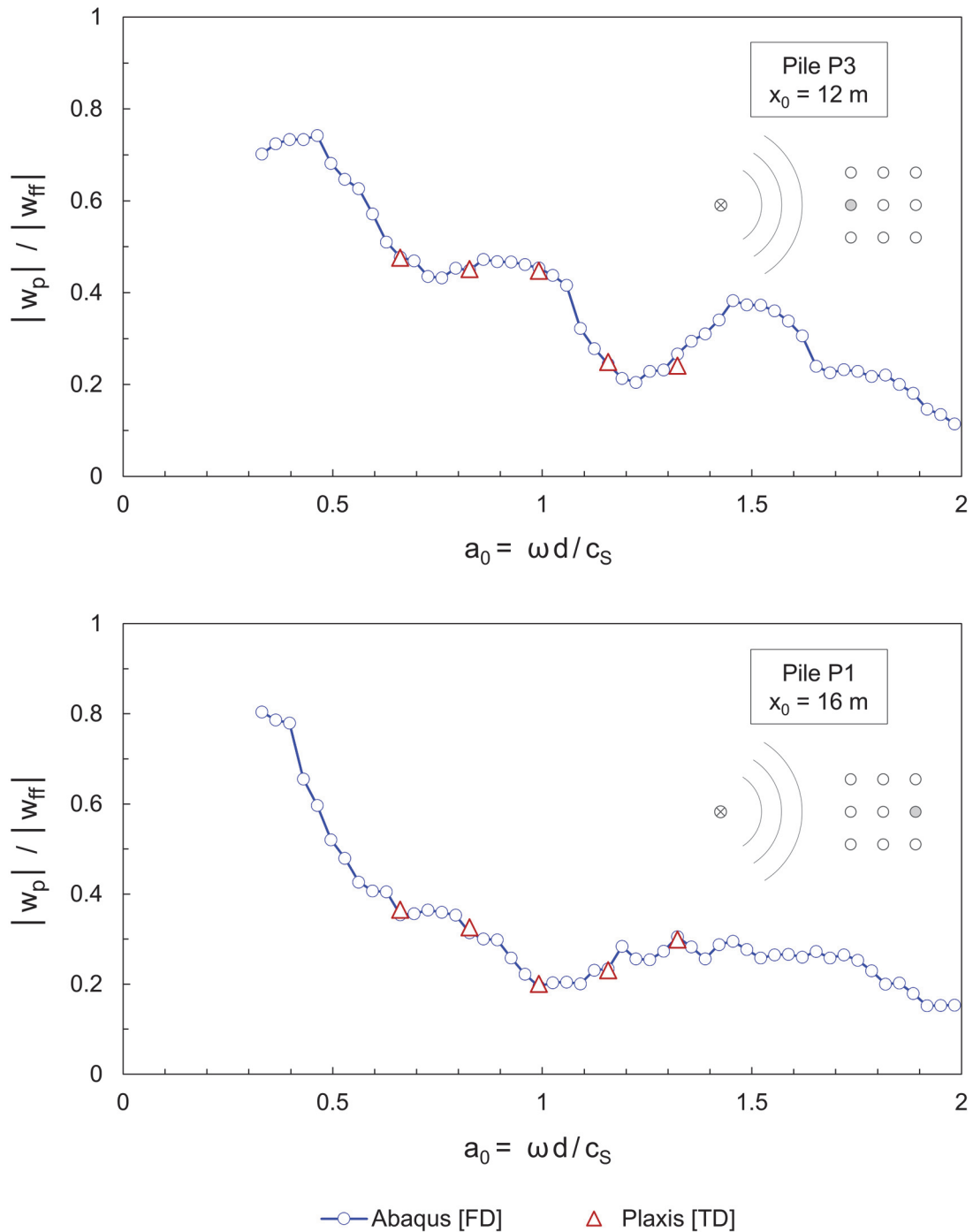


Figure 5.11: Comparison between time- and frequency- domain using Plaxis and Abaqus, respectively: Response of a reference pile at a distance x_0 from the vertical point load. The pile is part of a 3x3 free-standing pile group (without cap) with $s/d = 3$ embedded in half-space.

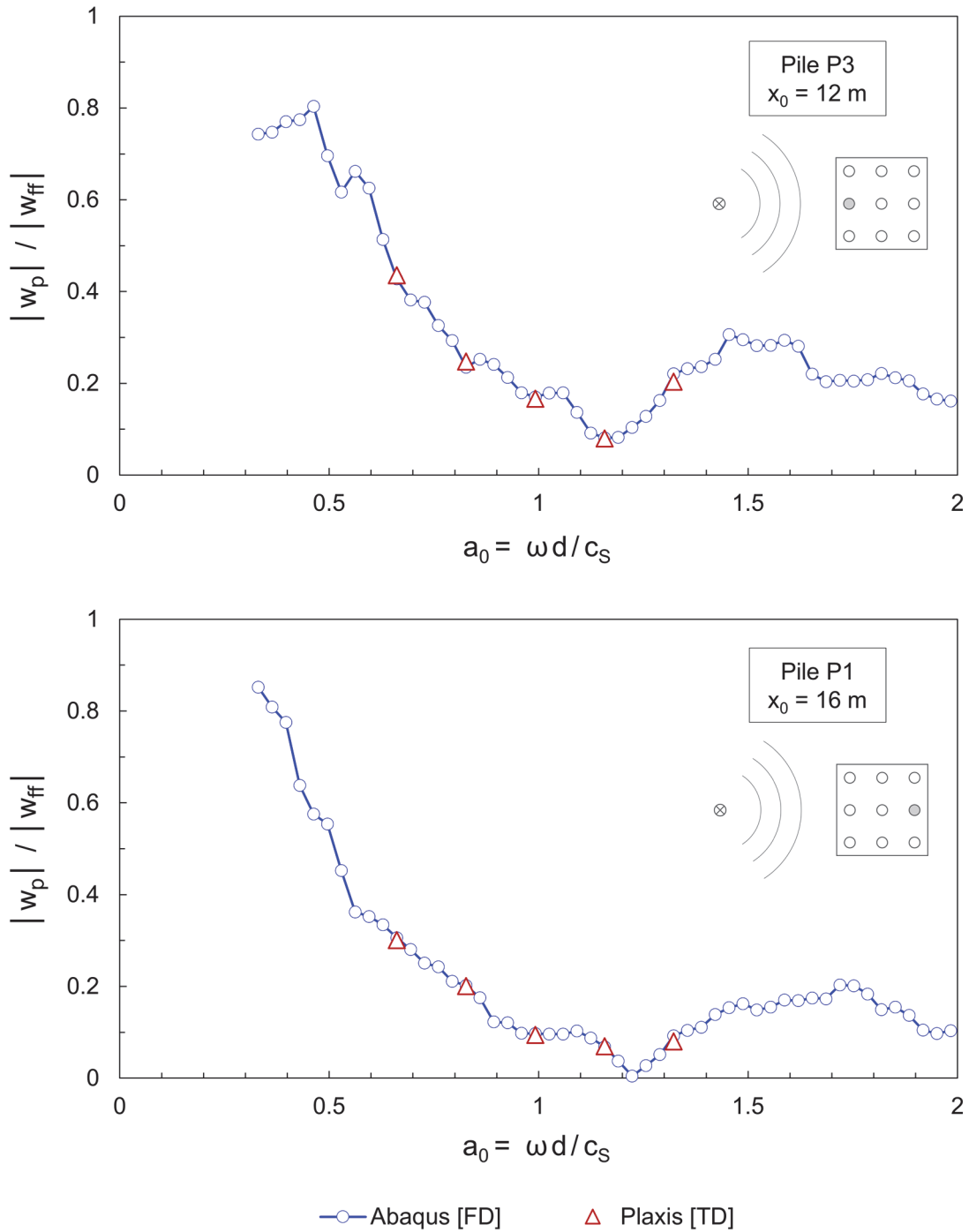


Figure 5.12: Comparison between time- and frequency- domain using Plaxis and Abaqus, respectively: Response of a reference pile at a distance x_0 from the vertical point load. The pile is part of a 3x3 rigidly capped pile group with $s/d = 3$ embedded in half-space.

5.4 Additional validation: inertial loading of a single pile

By solely activating the pile located at the point where the load is acting (see Figure 5.5), dynamic impedances, as well as interaction factors were derived and compared to existing solutions in the frame of an additional validation of the finite-element model. Figure 5.13 shows a snapshot of the deformed mesh at $f = 30$ Hz ($a_0 = 0.99$) along with contours of vertical displacements. Highlighted are the loaded pile as well as the nodes on the soil surface at a distance s/d from the center of the former; these nodes correspond to the receiver pile locations when deriving interaction factors.

The case of a stiff pile relatively to the supporting soil is examined ($E_p/E = 1000$), with the same soil properties as in Section 4.2.1.

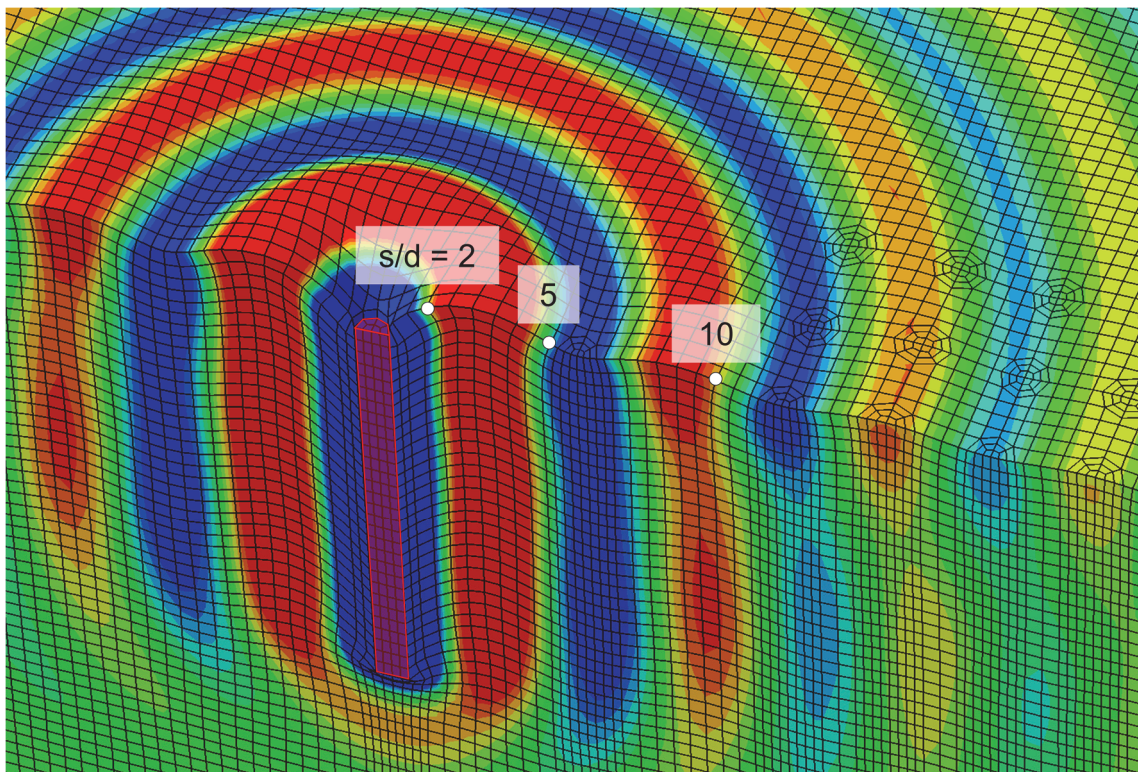


Figure 5.13: Deformed mesh with contours of vertical displacements (real part) due to inertial loading ($f = 30$ Hz; $a_0 = 0.99$) of a single pile with $l/d = 15$ and $E_p/E = 1000$ in half-space with $\zeta = 5$ %. The nodes highlighted at distances $s/d = 2, 5$ and 10 from the center of the loaded pile are monitored for the derivation of interaction factors.

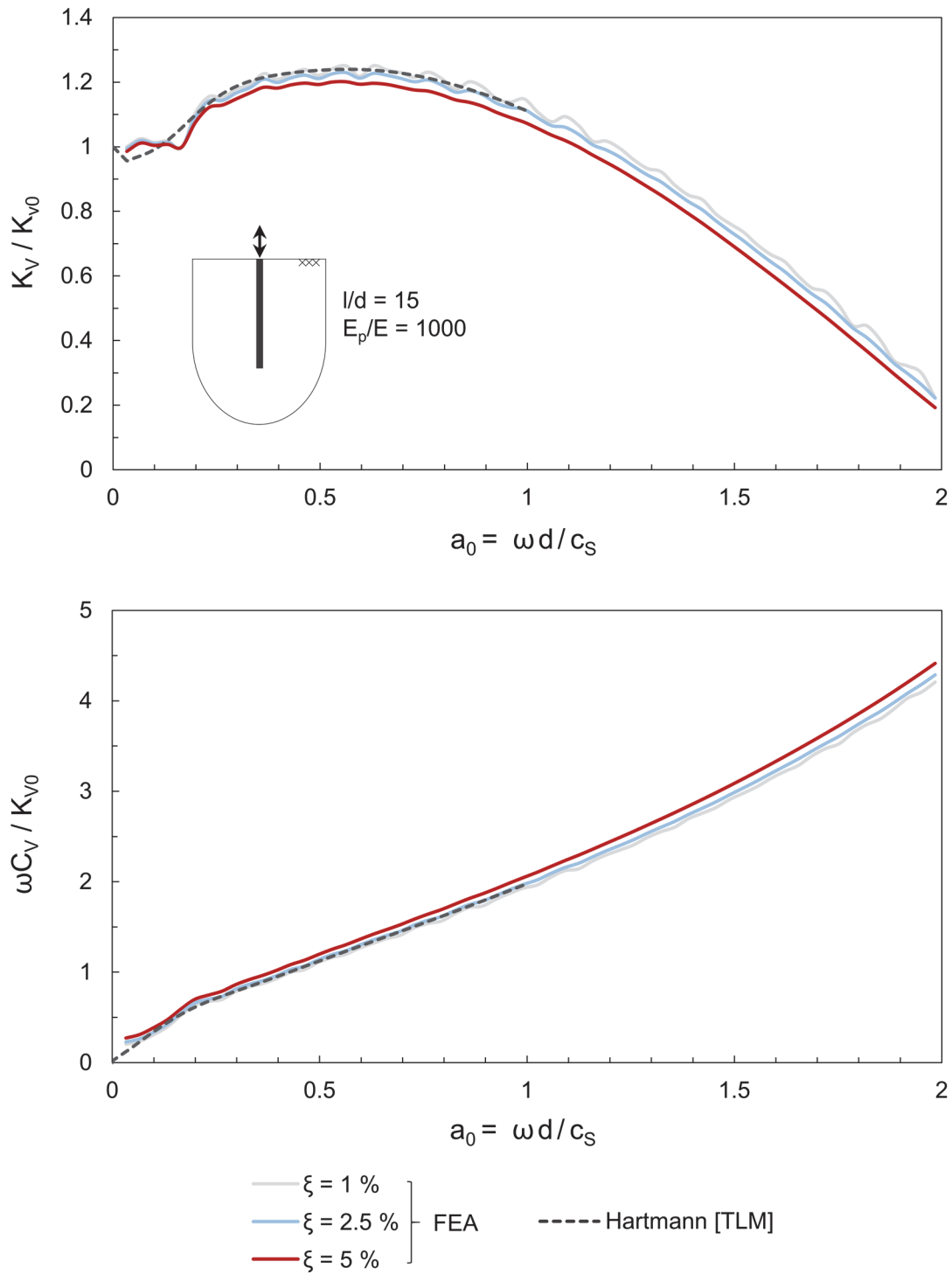


Figure 5.14: Vertical dynamic stiffness and damping coefficient of a single pile with $l/d = 15$ and $E_p/E = 1000$ in half-space for various values of hysteretic damping ratio ξ . The FEA results are compared to the results from Hartmann for $\xi = 1\%$ with the thin-layer method.

First, the vertical dynamic impedance of a single pile in half-space ($l/d = 15$, $E_p/E = 1000$) is compared with the rigorous solution from Hartmann (2015) with the thin-layer method (TLM), which is also published in DGGT (2019).

Figure 5.14 depicts the dynamic stiffness K_V and the dashpot coefficient $\omega \cdot C_V$, normalized by the vertical static stiffness K_{V0} . Due to the low value of hysteretic damping ratio $\zeta = 1\%$ chosen to match the one assumed in the solution from Hartmann (2015), a fluctuation is evident in the FEA results. By increasing the hysteretic damping ratio up to 5% a smoother response is obtained; though, unsurprisingly, this leads to a greater deviation from the rigorous solution.

Note also that the value of the dynamic stiffness for $f = 1$ Hz with $\zeta = 1\%$ is taken as static stiffness K_{V0} to normalize the FEA results. The ratio $K_{V0}/ER = 18.2$ exhibits a deviation of less than 1% from the static solution from the TLM (DGGT, 2019).

Subsequently, interaction factors have been derived and compared to the analytical approximation from Dobry & Gazetas (1988) given by Equation (2.9). For consistency, the numerical analyses assume $\zeta = 5\%$. The interaction factor a_v is defined in this case as the dynamic displacement of the free-field at a normalized distance s/d from the loaded pile, which corresponds to the location of a potential receiver pile, divided by the dynamic displacement of the loaded pile. The real and imaginary part of the interaction factors, $\text{Re}(a_v)$ and $\text{Im}(a_v)$, respectively, are depicted in Figure 5.15 versus the dimensionless frequency $a_0 = \omega \cdot d/c_s$ for three values of $s/d = 2, 5$ and 10 . Up to $a_0 = 1$, which is the upper limit of the frequency range considered by Dobry & Gazetas (1988), the FEA results are in overall good agreement with the approximation, especially as s/d increases.

One of the assumptions by Dobry & Gazetas (1988) is that cylindrical waves emanate simultaneously from all points along the pile periphery, then spreading radially outward. As can be observed in Figure 5.16, which shows three snapshots of the analyses at $f = 16, 32$ and 48 Hz corresponding to $a_0 = 0.53, 1.06$ and 1.59 , this assumption becomes invalid with increasing excitation frequency, which could clarify the above differences in the interaction factors. In addition, Equation (2.9) does not take into account neither the pile flexibility E_p/E or the pile slenderness l/d . However, for soft soils, as in the example presented herein, this is not expected to affect the results.

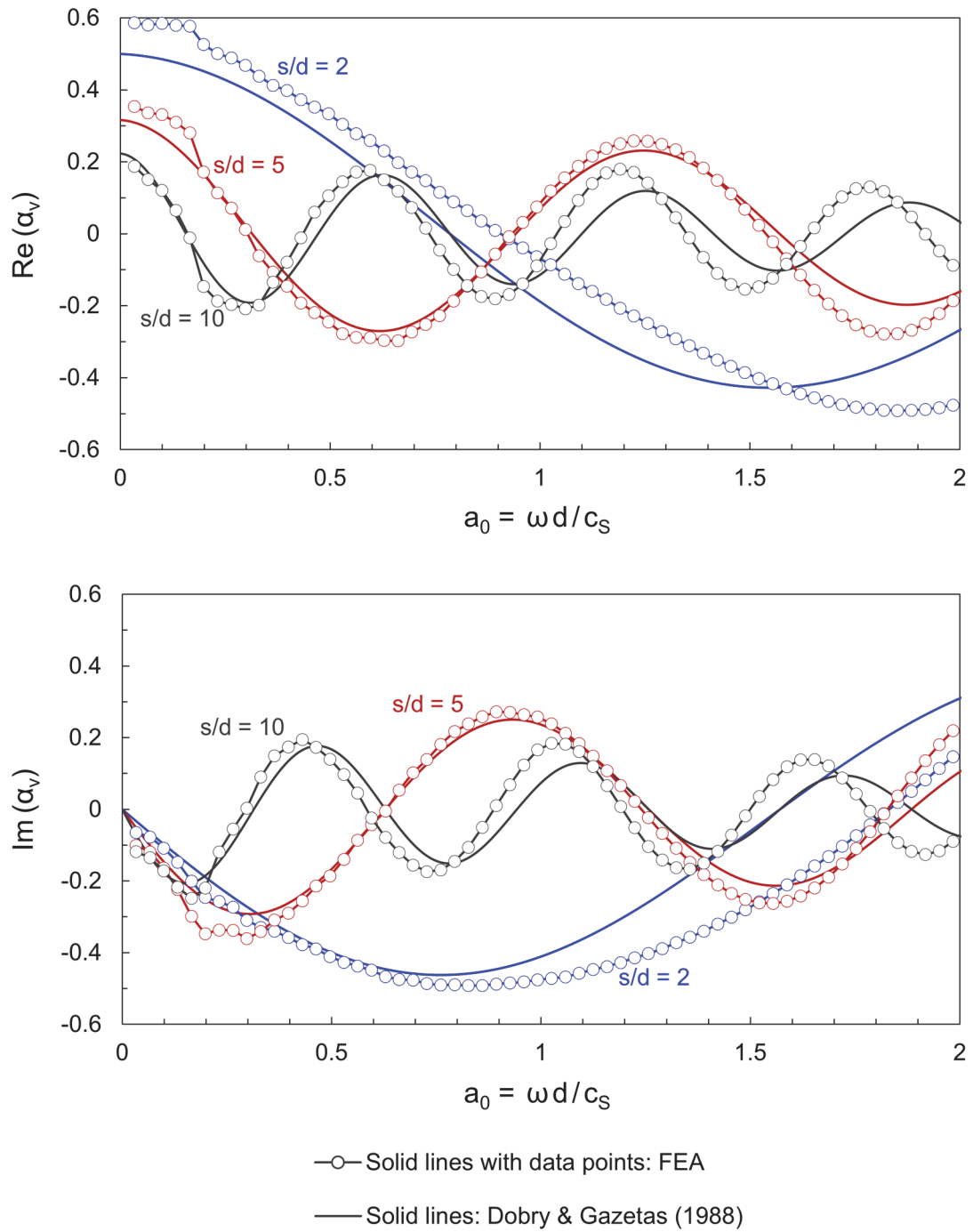


Figure 5.15: Comparison of the interaction factors derived from the FEA for $l/d = 15$ and $E_p/E = 1000$ with the analytical approximation from Dobry & Gazetas (1988) given by Equation (2.9).

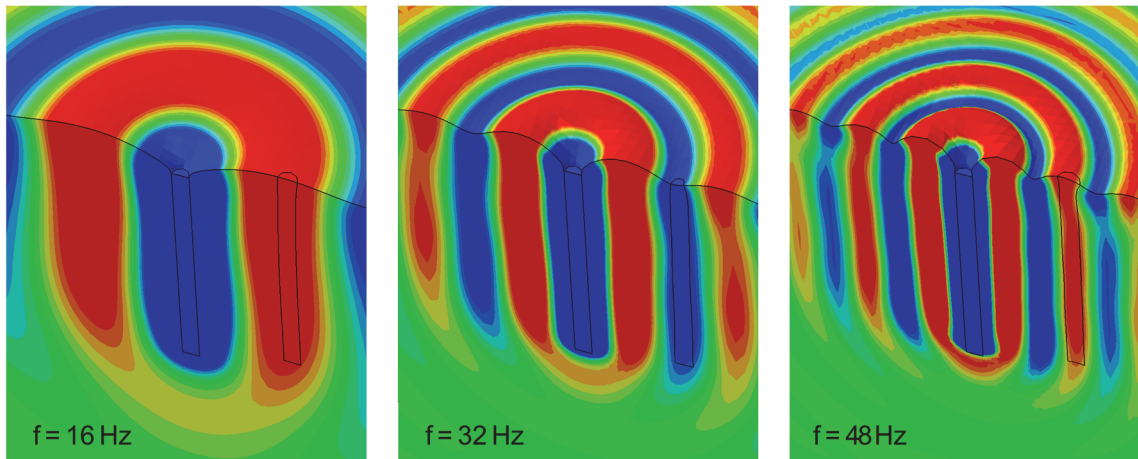


Figure 5.16: Contours of vertical displacements (real part) showing the wave propagation due to the inertial loading of a single pile in half-space.

Finally, the same results are compared to the rigorous solution from Kaynia & Kausel (1982), who presented interaction factors defined as ratios of the dynamic displacement of the receiver pile over the static displacement of the source pile under unit load. In our case, the static solution is assumed to appear at the lowest examined frequency of $f = 1$ Hz ($a_0 = 0.03$), and the results are presented in Figure 5.17 following the normalization by Kaynia & Kausel (1982).

The rigorous results are available up to $a_0 = 1$. Overall, the agreement is significantly improved compared to the approximation by Dobry & Gazetas (1988). The actual presence of a second pile (receiver pile) at the distance s/d from the harmonically loaded pile (source pile) is considered by Kaynia & Kausel (1982). It is reminded that in the FEA herein only the source pile is active. So, herein, to derive the interaction factor, the response of the free-field at the corresponding location is assessed. Obviously, this has an influence on the results.

This issue has been addressed in the recent study of Kanellopoulos & Gazetas (2020), where interaction factors derived by means of the FEM with and without the presence of a neighbouring pile are presented. In the first case, the rigidity of the receiver pile in axial deformation leads to smaller amplitudes of interaction factors, especially at higher frequencies and higher relative stiffness of the soil. This is described as a “reinforcing” effect of the neighbouring pile, a term originally introduced by Randolph (2003). This is, however, beyond the scope of the present study.

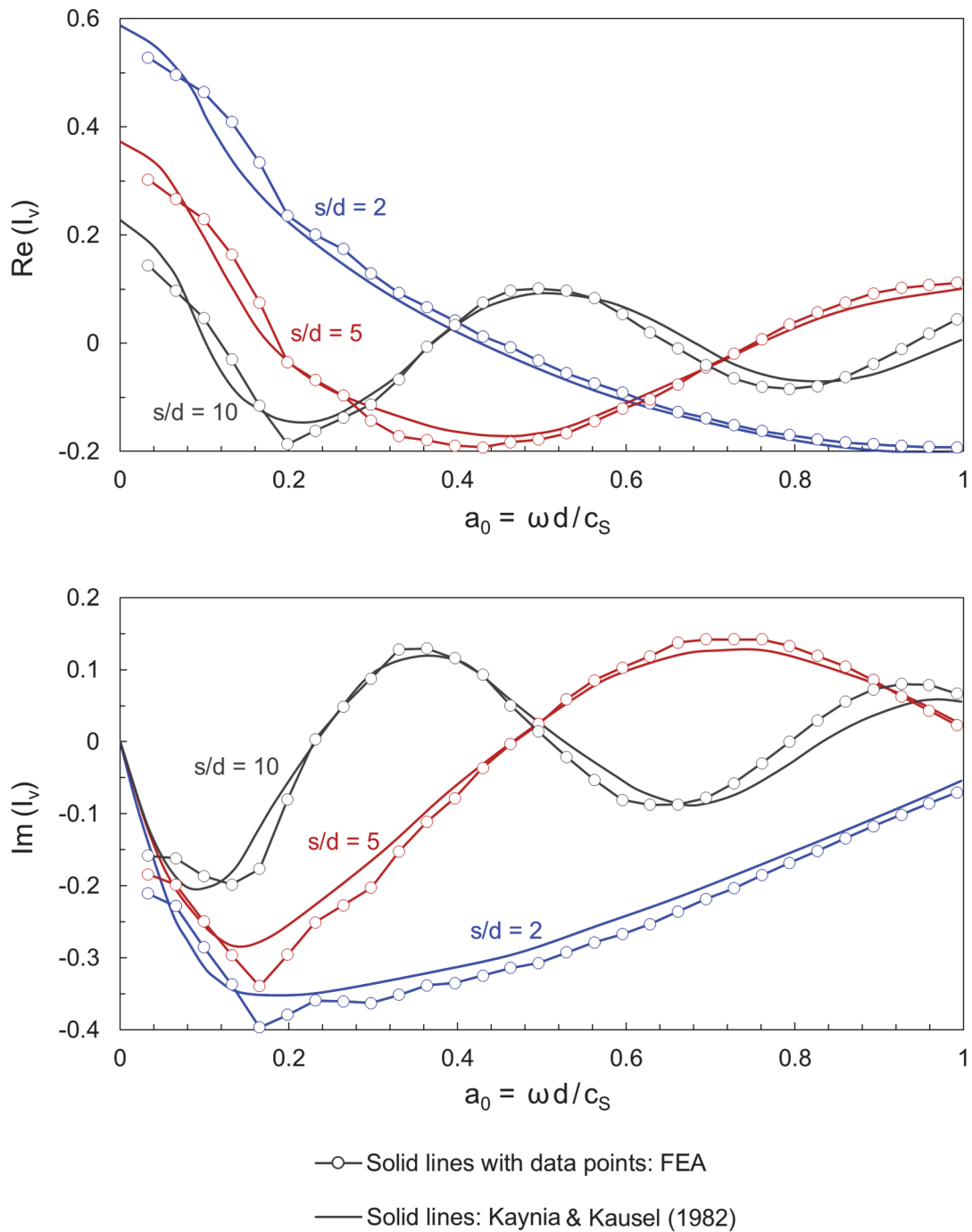


Figure 5.17: Comparison of the interaction factors derived from the FEA for $l/d = 15$ and $E_p/E = 1000$ with the rigorous solution from Kaynia & Kausel (1982).

The successful comparison confirms that the finite-element model is able to successfully reproduce wave propagation problems. Even though the inertial loading of the pile is not taking place at the center of the finite-element model, the good agreement with existing solutions confirms that the choice of asymmetry with respect to the application of the load might only have a minor effect on the results.

5.5 Pile group vs. piled raft – Frequency-domain analysis

5.5.1 Pile array 2x3

The vertical point load considered as an excitation source leads to a vertical, rocking and horizontal motion of the distant pile foundation. Due to the symmetry of the problem and to the rigid cap connection, all the piles at the same row move in an identical way.

Starting with the 2x3 pile group/piled raft (Figure 5.2), which is the smallest one examined, the response of the central piles at each row, P1 and P2, is presented in terms of vertical transfer functions in Figure 5.18, where it is also compared to their response as solitary piles. To derive the transfer functions, the vertical displacement amplitudes of the pile heads are normalized by those of the free-field at the exact location. In that way, it is revealed how the presence of each pile affects the free-field motion at a local level.

The first pile in the 2x3 system being struck by the waves, P2, as part of the pile group exhibits a behavior similar to that as if it were a solitary pile, especially for dimensionless frequencies higher than $a_0 = 0.5$. Being part of the piled raft, it experiences overall slightly reduced vibration amplitudes.

A quite different trend is observed for the reference pile P1 being located at the back of the system. As part of the 2x3 pile group, this pile is subjected to a significantly reduced vibration level in comparison with the single pile case. Apparently, the front pile row serves ‘protectively’ in the examined frequency range. The attenuation of motion is even more pronounced when P1 becomes a piled-raft component. In this case, as the dimensionless frequency increases, the vertical transfer function of the pile tends to zero.

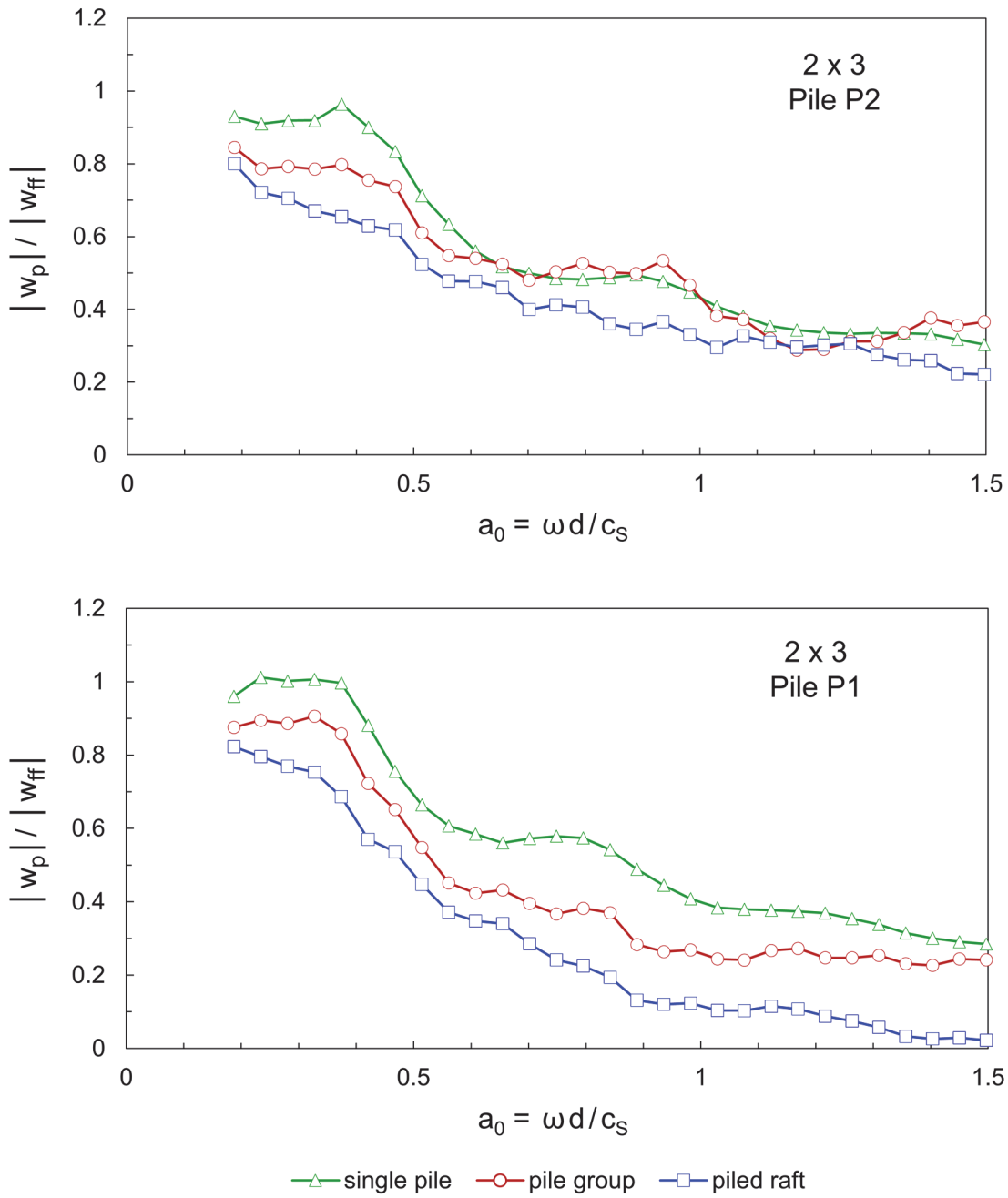


Figure 5.18: Vertical transfer functions of reference piles in the 2x3 configuration as single piles or parts of a pile group/piled raft.

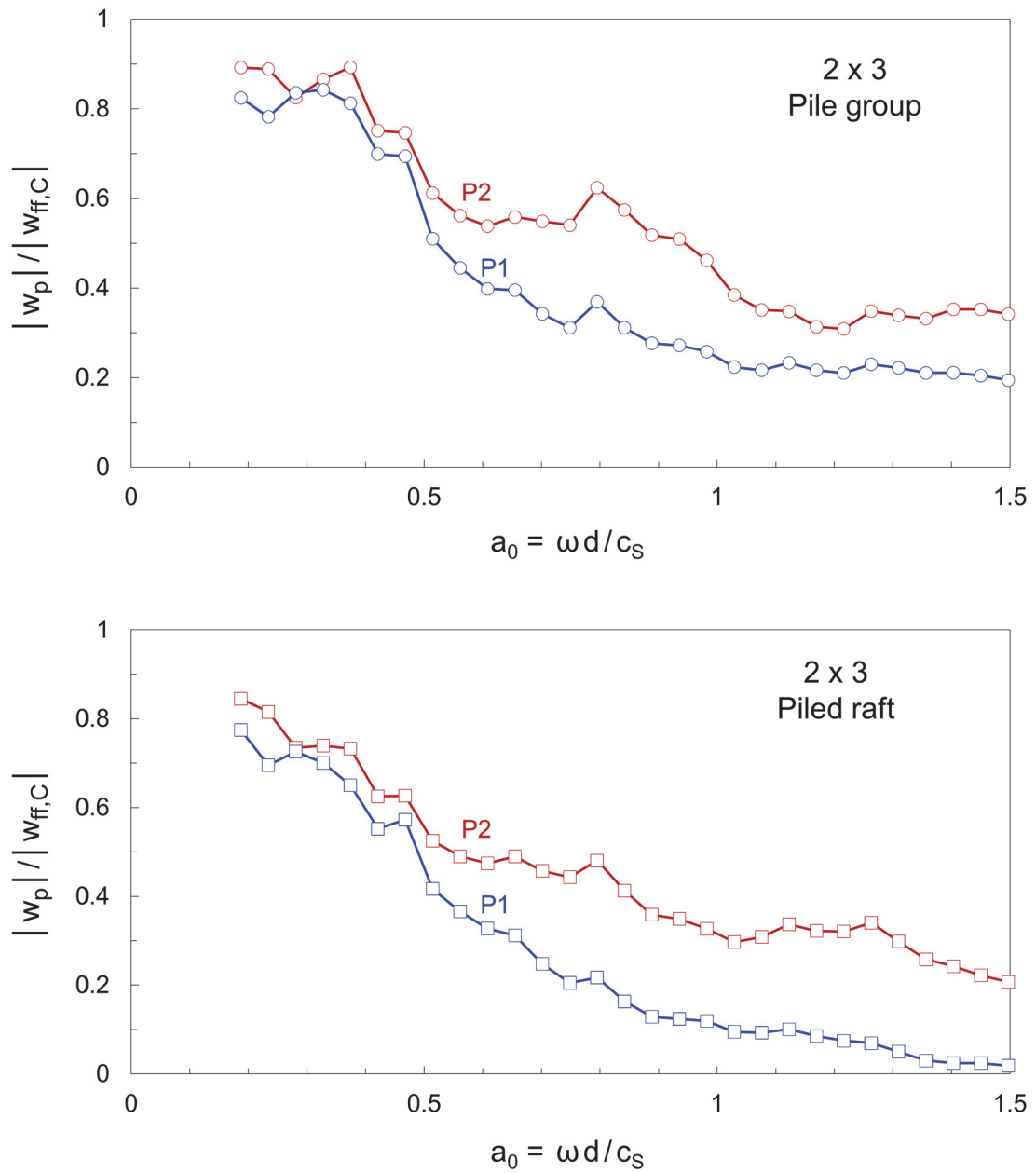


Figure 5.19: Vertical transfer functions of reference piles normalized by the free-field amplitude at the center-point of the 2x3 configuration.

Most importantly, at $a_0 = 0.5$ already, which herein corresponds to $f \approx 22$ Hz, both reference piles as components of the 2x3 configuration manage to reduce the free-field motion down to 60 %. In fact, with increasing frequency, the attenuation becomes even stronger.

In order to properly quantify the variation of the vibration level inside the same configuration, a common normalization is implemented in Figure 5.19, where the vertical displacement amplitudes of the reference piles P1 and P2 are divided by those of the free-field corresponding to the geometric center of the configuration denoted as $|w_{ff,C}|$. For both pile group and piled raft it can be seen, that up to approximately $a_0 = 0.5$, the two piles lying successively in the direction of wave propagation exhibit almost the same response. Furthermore, the nature of loading is quasi-static at these low frequencies, due to the corresponding large wavelengths in comparison with the dimensions of the examined configuration, so the piles move in-phase. By further increasing the frequency though, the vibration level of the furthest back pile P1 begins to deviate from that of the front pile P2. In fact, in the case of the piled raft, it drops dramatically. As previously mentioned, the applied excitation leads to a rocking motion of the pile group/piled raft; consequently, it is deduced that the furthest back pile serves practically as the center of oscillation at these high frequencies, since its vertical displacement amplitude tends to zero.

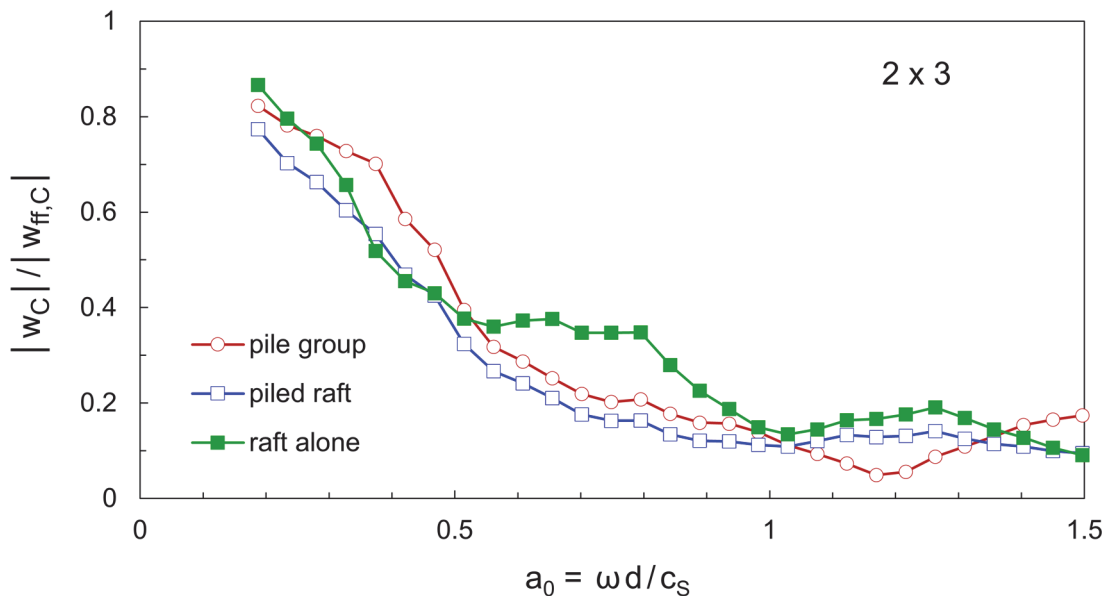


Figure 5.20: Vertical transfer function at the center-point of the 2x3 configuration.

Figure 5.20 shows the transfer function being the ratio of the vertical displacement at the geometric center of each configuration $|w_C|$ over that of the free-field $|w_{ff,C}|$ corresponding to the same location. In specific, for the pile group, the amplitude $|w_C|$ is calculated at the geometric center of the cap connecting the piles, and, accordingly, for the piled raft and the raft alone, this value is obtained at the geometric center of the raft.

Overall, the least reduction of the free-field motion is accomplished by the raft acting alone; an exception is noticed though within the frequency range $a_0 = 0.3 - 0.38$ as well as within $a_0 = 1.4 - 1.5$, where the transfer function of the pile group attains the highest values. On the other hand, the maximum drop of the vibration level is observed in the case of the piled raft; within the range $a_0 = 1.08 - 1.31$, however, it is the pile group, which leads to the maximum attenuation, with respect to the geometric center of the system.

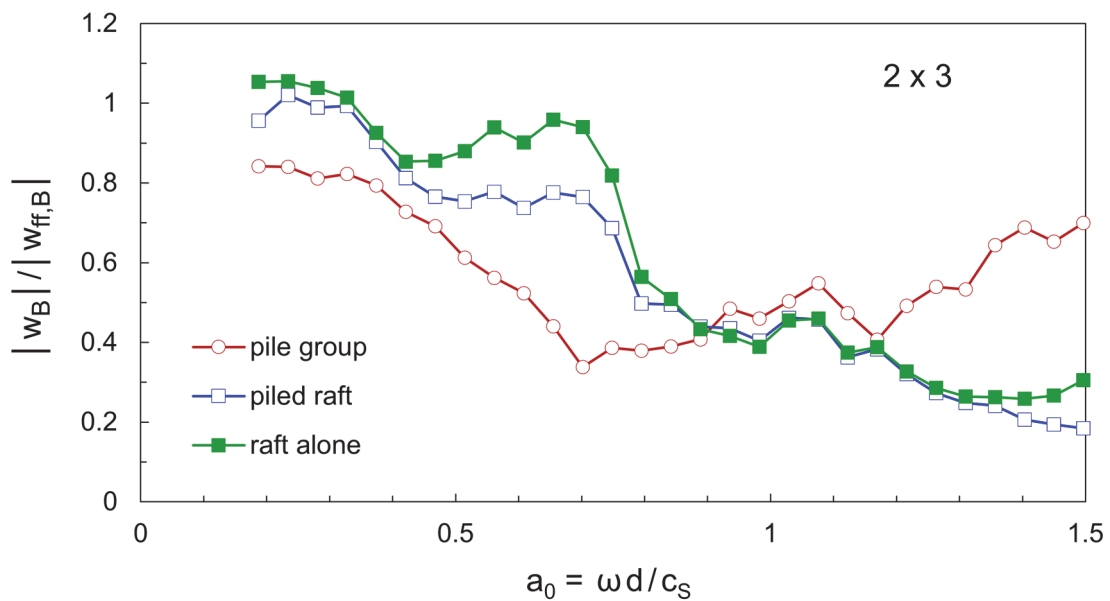


Figure 5.21: Vertical transfer function at point B behind the 2x3 configuration.

Finally, Figure 5.21 compares how the three investigated schemes influence the free-field response behind them – with respect to the wave propagation direction. The response is calculated at the observation point B located at $x_0 = 18$ m on the soil surface. The transfer function is defined as the ratio of the vertical

displacement amplitude of point B $|w_B|$ in presence of the pile group, the piled raft or the raft alone over the vertical displacement amplitude of point B considering merely the free-field $|w_{ff,B}|$. Up to $a_0 \approx 0.9$, the pile group has the most beneficial influence on point B by significantly reducing the original free-field motion. However, beyond this point, a reversal of the trend can be noticed, with the piled raft and the raft alone acting favorably in terms of vibration reduction. The piled raft and the raft alone lead to an overall similar response, and, surprisingly, from $a_0 = 0.85$ up to $a_0 = 1.3$, they have practically the same effect on point B. This agreement though was not observed inside the configuration.

5.5.2 Pile array 3x3

The extension of the previous 2x3 configuration by an additional pile row against the direction of wave propagation leads to a 3x3 pile array, as already explained in Section 5.1.

In Figure 5.22 the response of each central reference pile in the 3x3 system is portrayed as part of a pile group or piled raft, or as a solitary pile. Firstly, the response of pile P3, which is the first one to be struck by the propagating waves is discussed. Recall that in the respective case of the 2x3 configuration, pile P2, being the first-row central pile, exhibits essentially the behavior of a single pile. In the current case, however, this is valid for P3 only when being part of the pile group for low frequencies up to $a_0 \approx 0.6$. Beyond this point, the attenuation of motion is generally significantly stronger compared to the single pile case. This indicates that group effects dominate in larger configurations. Only at the highest examined frequencies, the transfer function of the pile in the group exceeds slightly that of the single pile. The greatest deviation from the corresponding single pile case can be observed for pile P2 at the mid-row of the 3x3 system. In addition, whether the piles are connected via a cap or a raft that is also in contact with the soil, does not have an influence on the response of the central row in the 3x3 pile array. Finally, the furthest-back pile P1 also shows a considerable deviation from the single pile case, with the type of the pile array (pile group or piled raft) having an effect only at higher frequencies.

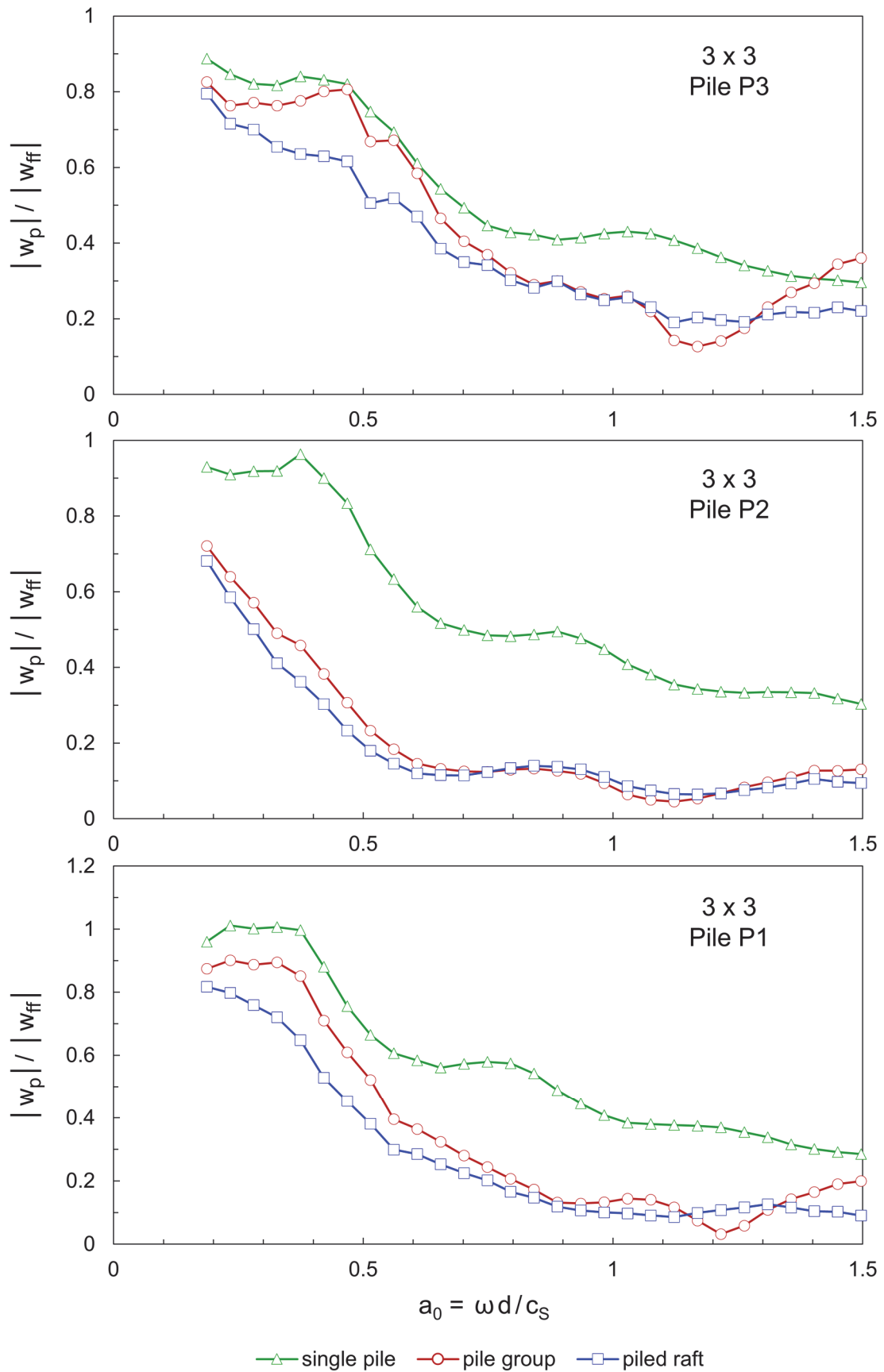


Figure 5.22: Vertical transfer functions of reference piles in the 3x3 configuration as single piles or parts of a pile group/piled raft.

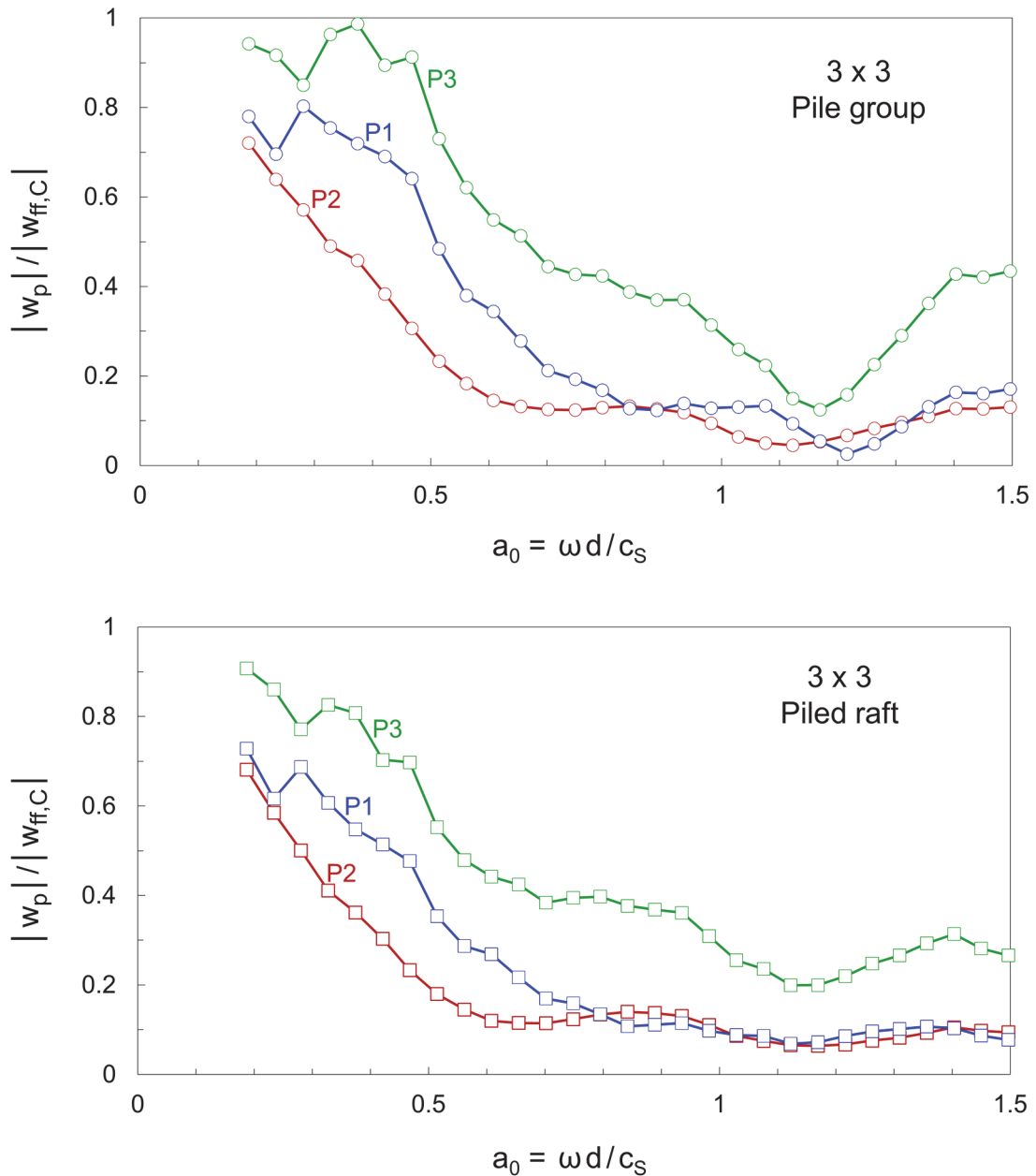


Figure 5.23: Vertical transfer functions of reference piles normalized by the free-field amplitude at the center-point of the 3x3 configuration.

The direct comparison in Figure 5.23 between the reference piles after a common normalization by the vertical displacement amplitude of the free-field at the center of the 3x3 configuration, shows that pile P2 at the mid-row experiences generally a lower vibration level. The motion of the pile group is quite complex. On the other hand, the curves for the piled raft reveal that between $a_0 = 0.8$ and $a_0 = 1.5$, the mid- and furthest back central pile are subjected to almost identical

displacement amplitudes. This could be an indication that the center of oscillation for the rocking motion is located about the mid-point between them.

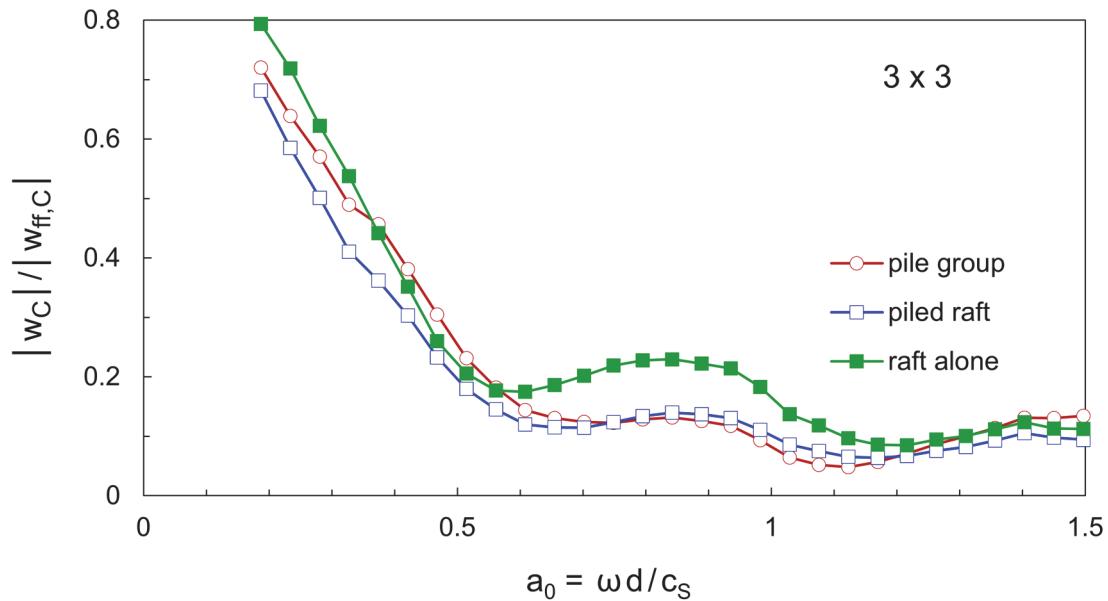


Figure 5.24: Vertical transfer function at the center-point of the 3x3 configuration.

The transfer functions with respect to the geometric center of the 3x3 configuration are presented in Figure 5.24. The transfer function of the raft acting alone exceeds those of the pile group and the piled raft in the dimensionless frequency range 0.5 - 1, but apart from that the results are similar for the three schemes. Especially the response at the center-point of the pile group matches quite well that of the piled raft. This last point was already revealed in Figure 5.22 for P2 though, since the location of the geometric center of the 3x3 system coincides with that of the central reference pile P2.

The response of point B at the free-field behind each scheme is portrayed in Figure 5.25. Except from the frequency range 0.9 - 1.3, the vibrations are reduced the most in the presence of the pile group. The response due to the piled raft is similar to that of the raft acting alone. The contact of the raft with the supporting soil in this case affects in a rather unfavorable manner the response at point B behind the foundation.

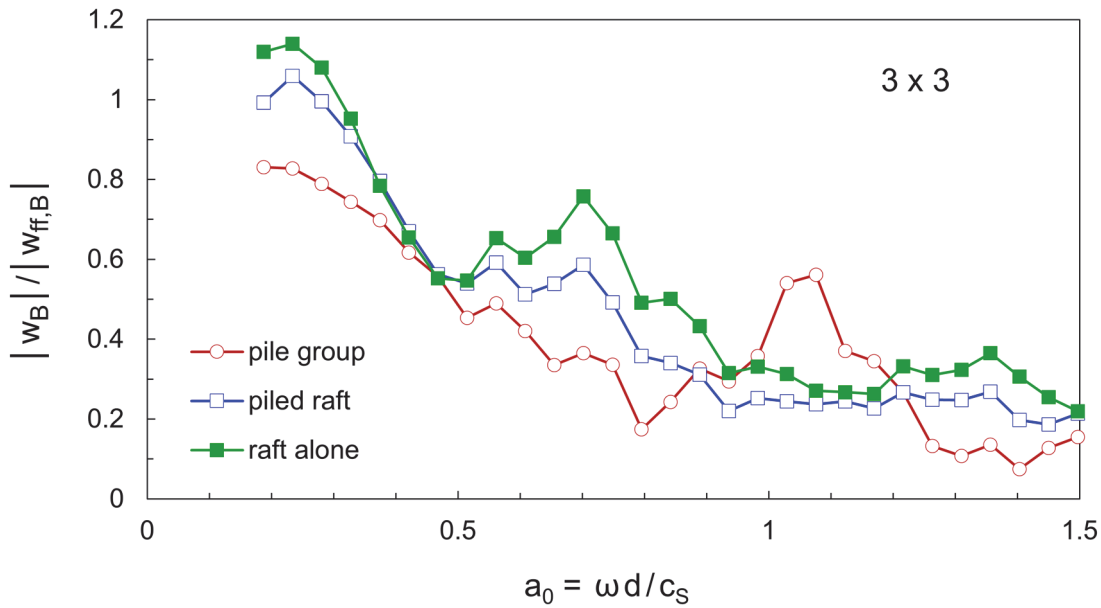


Figure 5.25: Vertical transfer function at point B behind the 3x3 configuration.

5.5.3 Pile array 4x3

In Figure 5.26, the response of the reference piles P4 - P1 being part of the 4x3 configuration, is contrasted to their response as single piles.

First, results are presented for pile P4 at the first row being hit by the waves generated by the point load. Compared to the other reference piles in the 4x3 pile array, the least deviation from the single pile case is documented throughout the total frequency range. Yet, the response of pile P4 differs by far from that of a solitary pile at the same location, with an exception at very low frequencies. As suggested previously in the case of the 3x3 system, this deviation is attributed to group effects prevailing in larger systems. By becoming part of a piled raft, the transfer function of pile P4, with the exception of the frequency range $a_0 \approx 0.85 - 1.25$, attains the lowest values. This last observation applies also to the following pile P3.

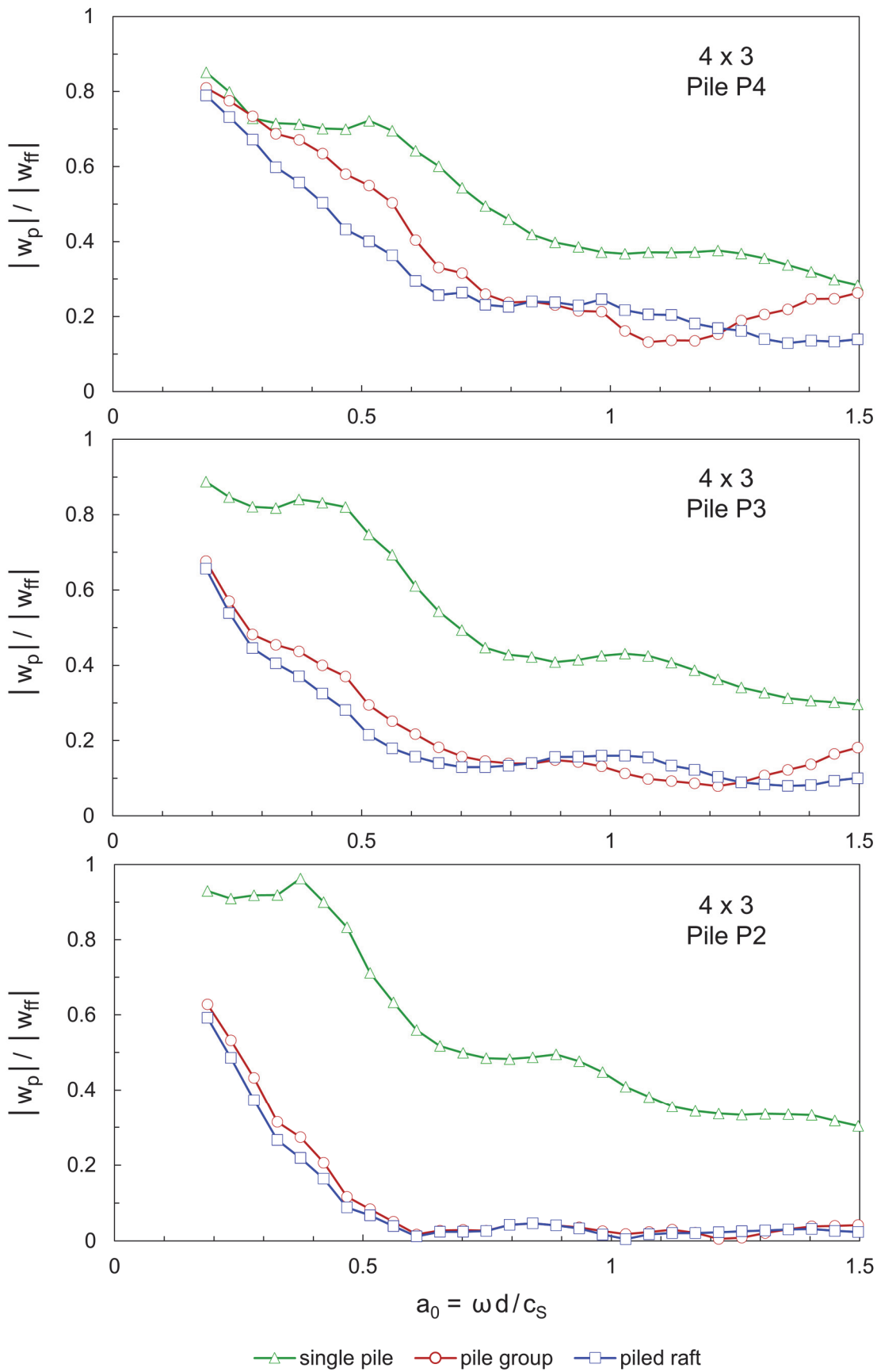


Figure 5.26: Vertical transfer functions of reference piles in the 4x3 configuration as single piles or parts of a pile group/piled raft.

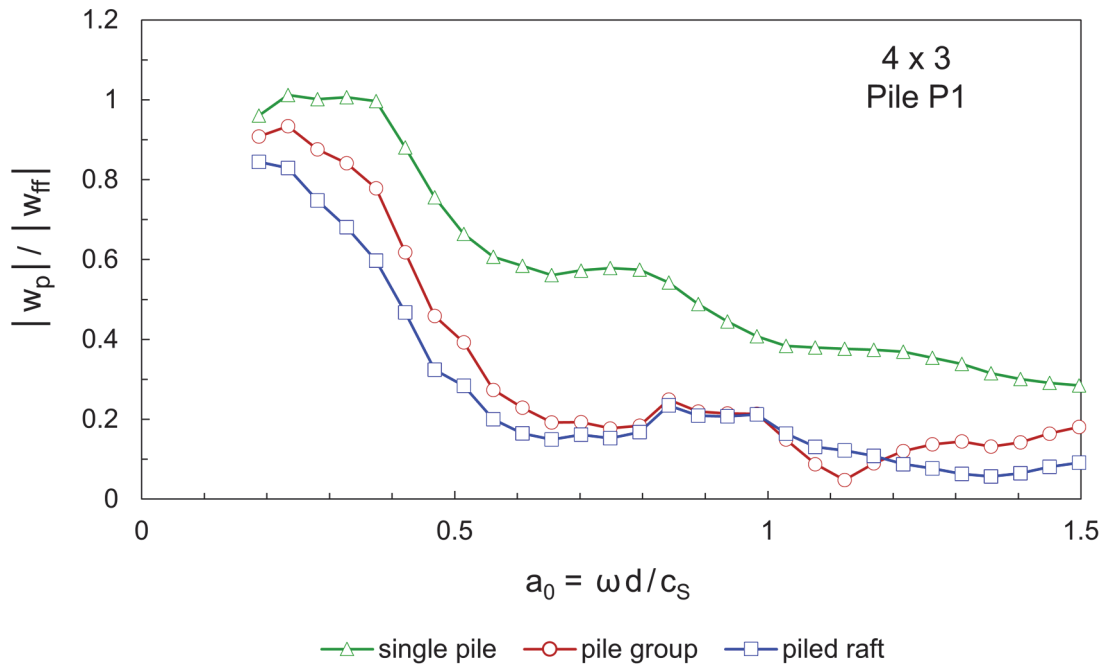


Figure 5.26 continued.

For the next pile, P2, the largest deviation from the corresponding single pile response can be noticed. Furthermore, there are practically no differences between pile group and piled raft. In fact, beyond the dimensionless frequency $a_0 = 0.6$, the transfer function is almost equal to zero, which indicates that for the largest part of the examined frequencies, there is nearly no motion of pile P2 in the vertical direction.

Finally, pile P1 at the furthest-back row reduces also significantly the free-field motion in comparison with the single pile scenario. Even though it mostly reduces the vibration level as part of the piled raft, in the range $a_0 = 0.80 - 1.03$, the agreement between the pile group and the piled raft is striking.

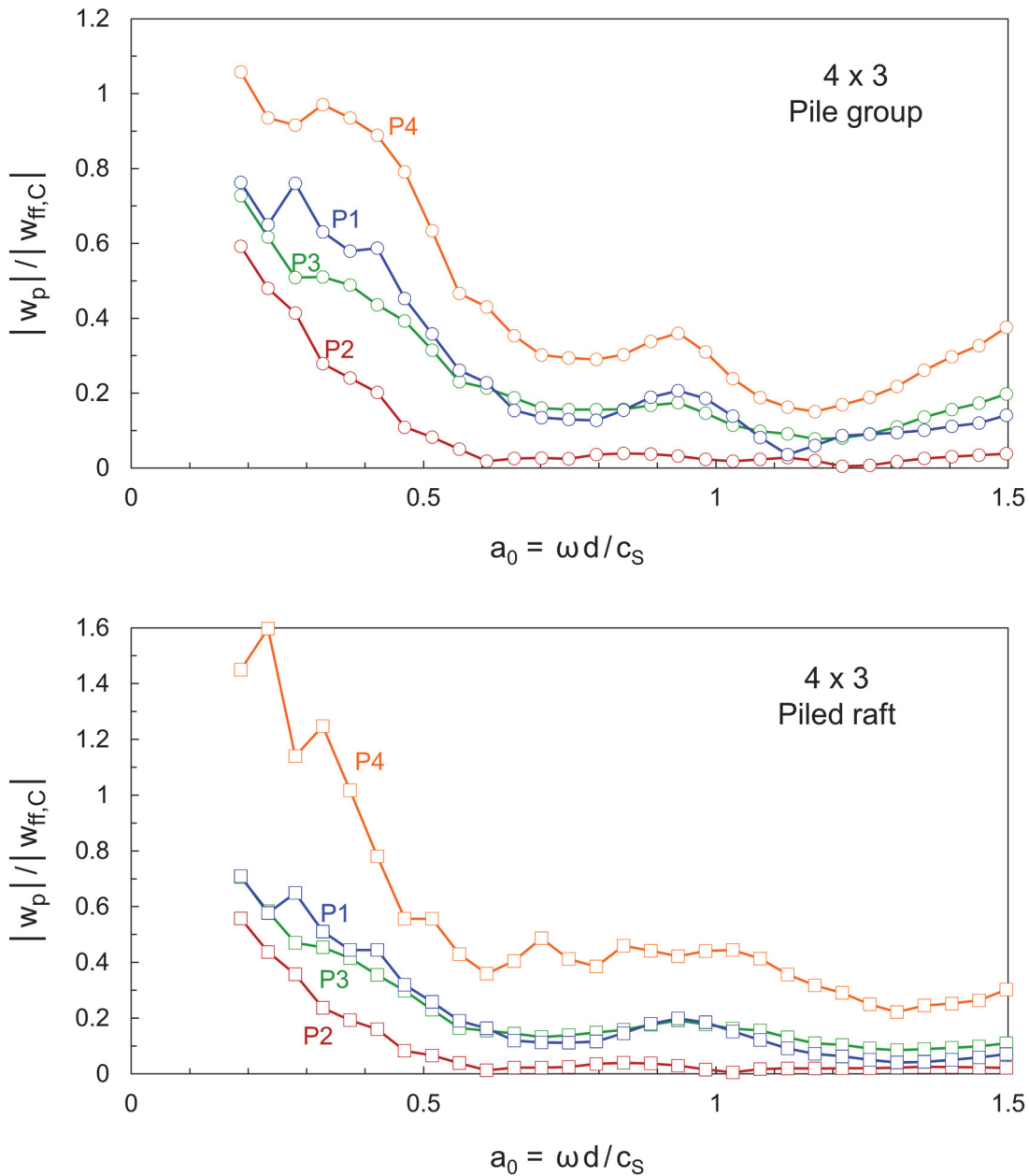


Figure 5.27: Vertical transfer functions of reference piles normalized by the free-field amplitude at the center-point of the 4x3 configuration.

A direct comparison of the piles in the pile group or the piled raft is portrayed in Figure 5.27. For both foundation types, pile P4 experiences the largest vertical displacement amplitudes. On the other side, the vibration level of pile P2 is the lowest, with the corresponding transfer function attaining in some cases values that are practically equal to zero. Indicatively, in the case of the pile group at $a_0 = 1.22$ (corresponding to $f = 52$ Hz), the vertical transfer function of P2 is

equal to zero. For P1 and P3, being the neighbour piles on either side of P2, the transfer function is equal to 0.09 and 0.08, respectively, while P4 experiences almost the double vibration level. Consequently, at this frequency, the location of pile P2 coincides with the center of oscillation for the rocking mode. Note however, that the system also has a horizontal component, which leads to a complicated motion. This practically means that multiple centers of oscillation may exist depending on the excitation frequency.

The results with respect to the geometric center of the three examined foundation types are shown in Figure 5.28, with the raft alone demonstrating the largest transfer functions up to approximately $a_0 = 1.3$. Overall, the pile group and the piled raft lead to a similar attenuation of motion as calculated at their center-point.

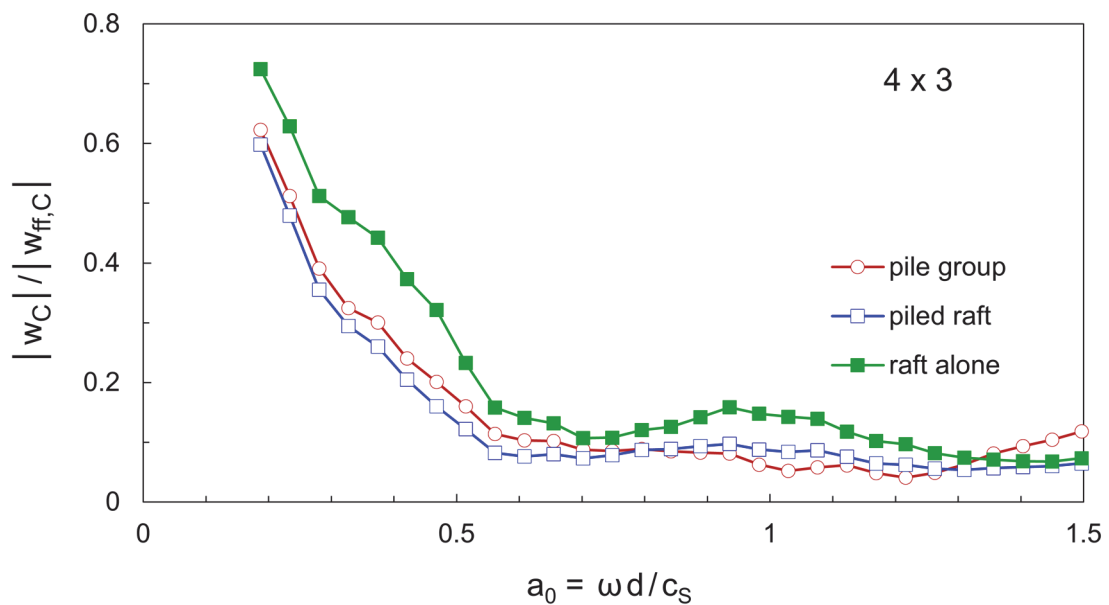


Figure 5.28: Vertical transfer function at the center-point of the 4x3 configuration.

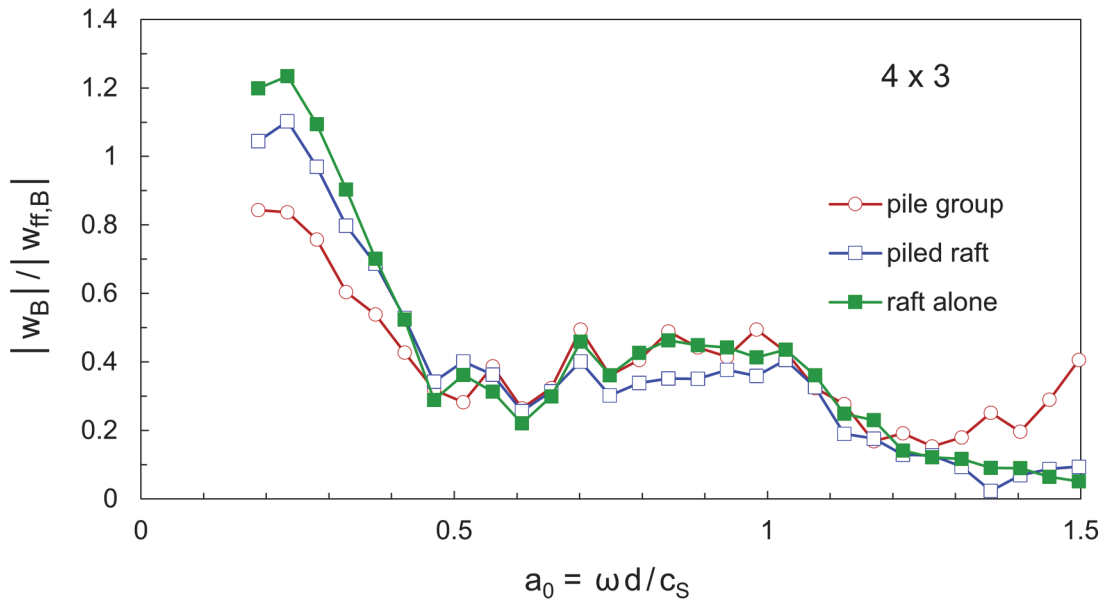


Figure 5.29: Vertical transfer function at point B behind the 4x3 configuration.

Regarding the free-field point B behind each investigated foundation type, an abrupt drop of the transfer function is observed up to $a_0 \approx 0.45$ for all cases in Figure 5.29. Beyond this point, the attenuation of motion is relatively similar; from $a_0 \approx 1.3$, however, the presence of the pile group results in the largest vertical displacement ratios, in fact exhibiting an increasing trend at high frequencies.

5.5.4 Pile array 5x3

The response of each reference pile in the 5x3 pile group as well as in the corresponding piled raft is contrasted to its response as a solitary pile in Figure 5.30. For low frequencies up to $a_0 \approx 0.3$, pile P5 at the first row to be struck by the propagating waves, exhibits roughly the same behavior regardless of scheme. After this point, an increasing deviation from the single pile response can be noticed, being, however, the smallest in comparison with the other reference piles. In addition, the differences between the pile group and the piled raft case are not particularly appreciable. At most frequencies, pile P5 as part of the piled raft exhibits the lowest vibration level; exception is the range $a_0 = 0.95 - 1.30$.

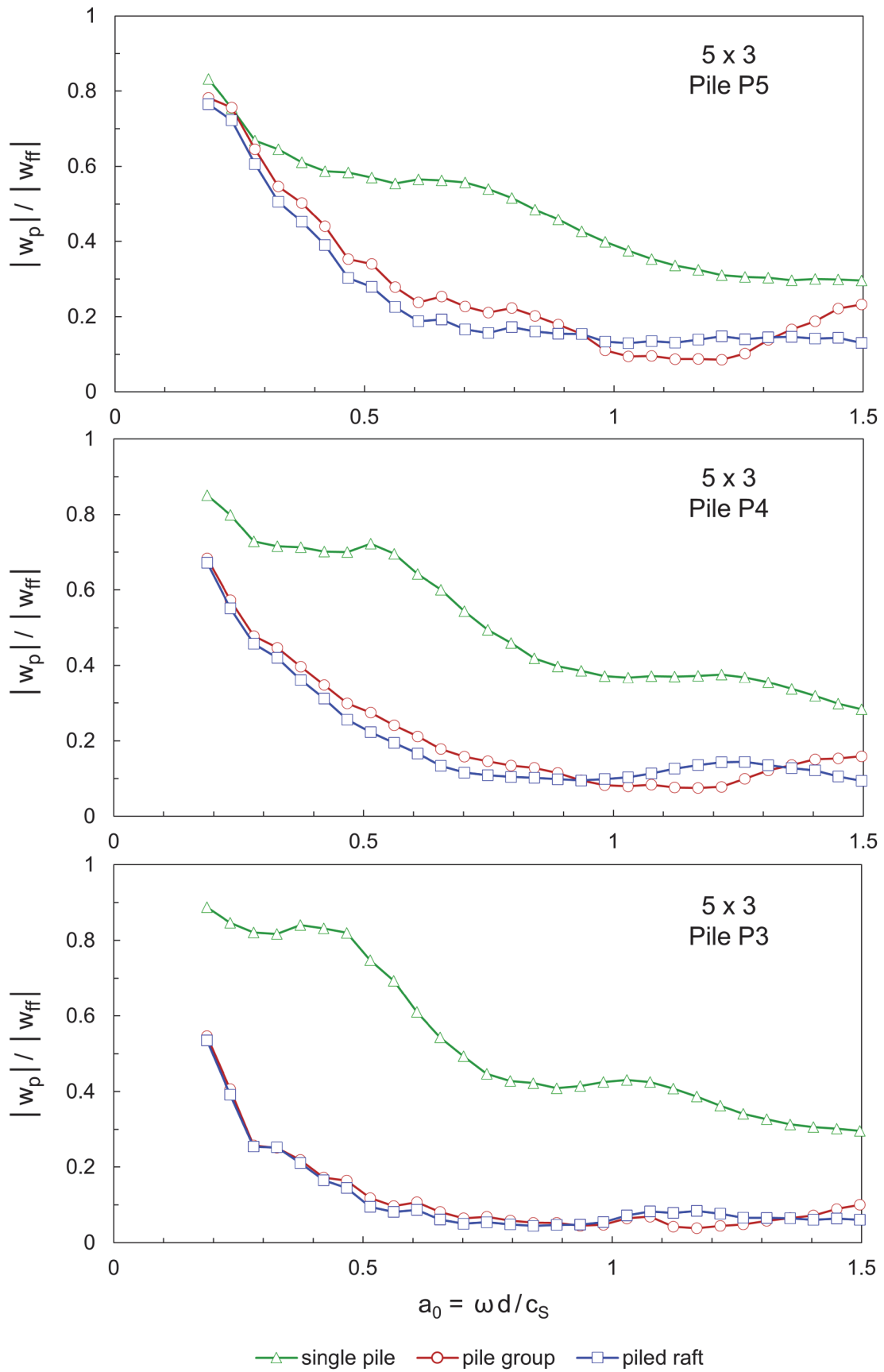


Figure 5.30: Vertical transfer functions of reference piles in the 5x3 configuration as single piles or parts of a pile group/piled raft.

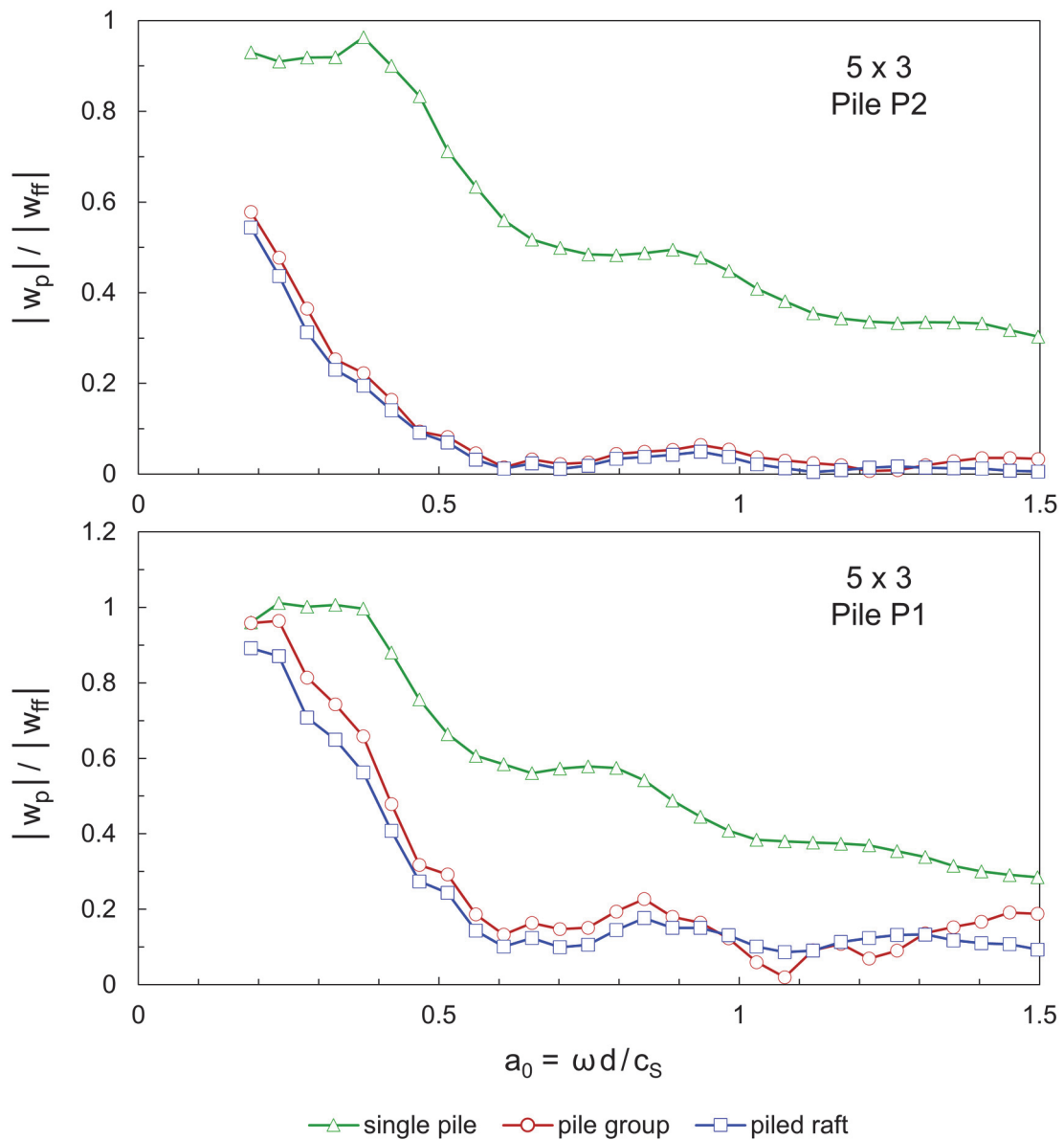


Figure 5.30 continued.

This trend is observed at the rest piles P4, P3 and P1 too. Pile P2 exhibits the greatest deviation from the single pile case, with its displacement amplitudes beyond $a_0 \approx 0.5$ being close to zero. Furthermore, the pile group and the piled raft case yield quite similar results.

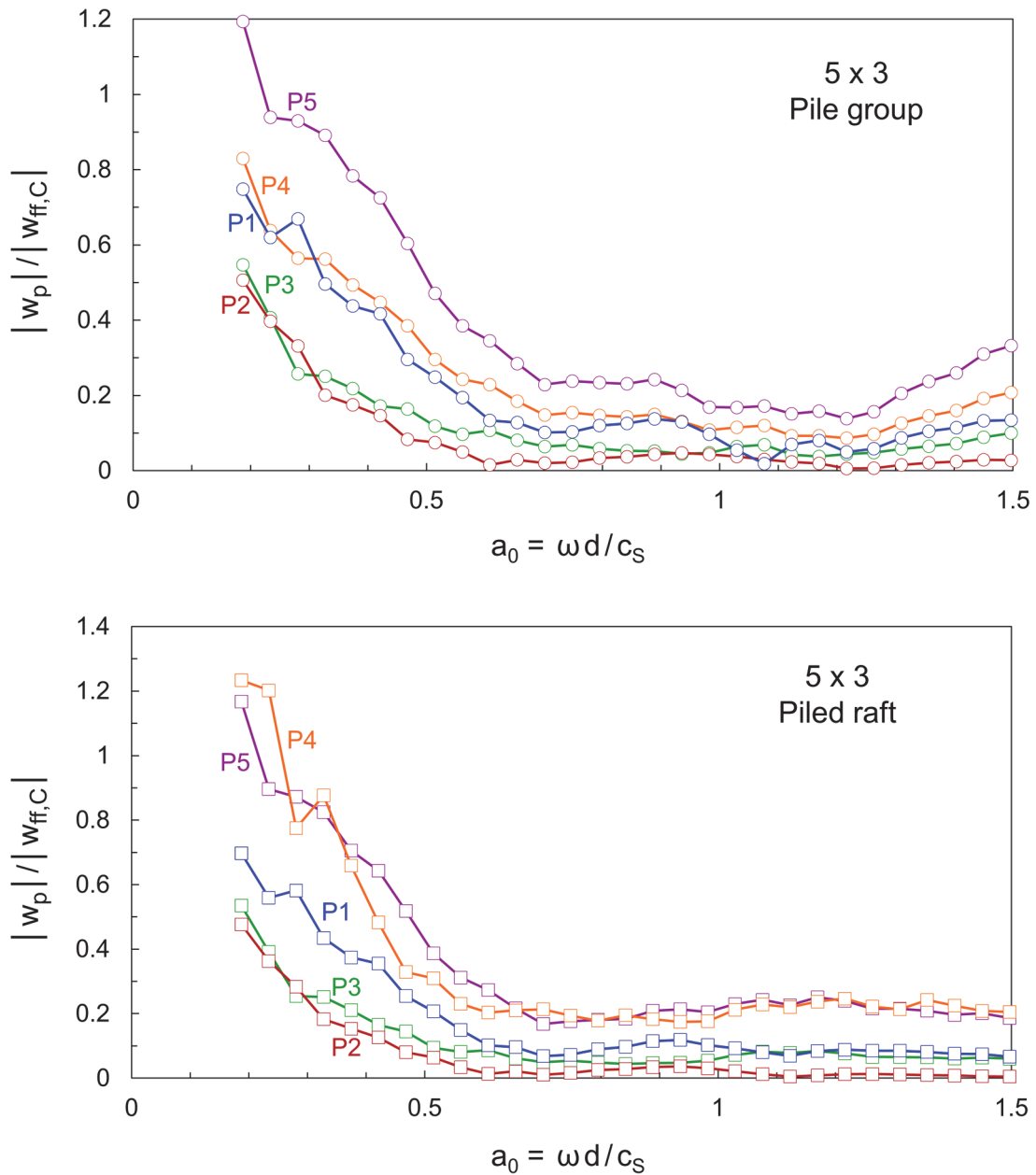


Figure 5.31: Vertical transfer functions of reference piles normalized by the free-field amplitude at the center-point of the 5x3 configuration.

The common normalization by the free-field motion corresponding to the geometric center of the 5x3 configuration in Figure 5.31 reveals that the front-row pile P5 demonstrates the greatest displacement amplitudes as part of the pile group; in the piled raft, its response is very close to that of pile P4. This indicates the complexity in the motion of the system. Similar to the 4x3 configuration, the transfer function of pile P2 attains overall the lowest values.

With respect to the geometric center of each investigated scheme, Figure 5.32 shows that the raft alone offers practically the least attenuation of the free-field motion, while the pile group and the piled raft are overall in good agreement.

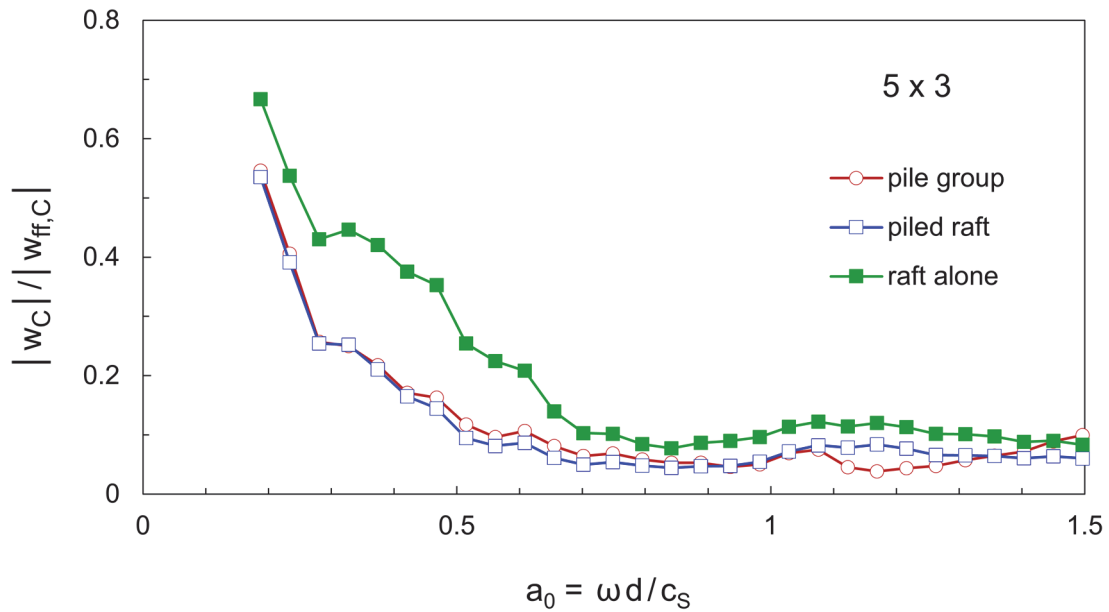


Figure 5.32: Vertical transfer function at the center-point of the 5x3 configuration.

Finally, the response at the observation point B behind each scheme is presented in Figure 5.33. Once again, it is shown that the piled raft and the raft alone modify the free-field behind them in a similar way. At $a_0 \approx 1.1$ the piled raft leads to a practically zero motion, but apart from this, the agreement is good, which implies that the boundary condition at the soil surface enforced by the raft mainly influences the free-field at the back. The effect of the pile group, on the other hand, in the frequency range $a_0 = 0.72 - 1.25$ is obviously unfavorable in comparison to that of the other schemes.

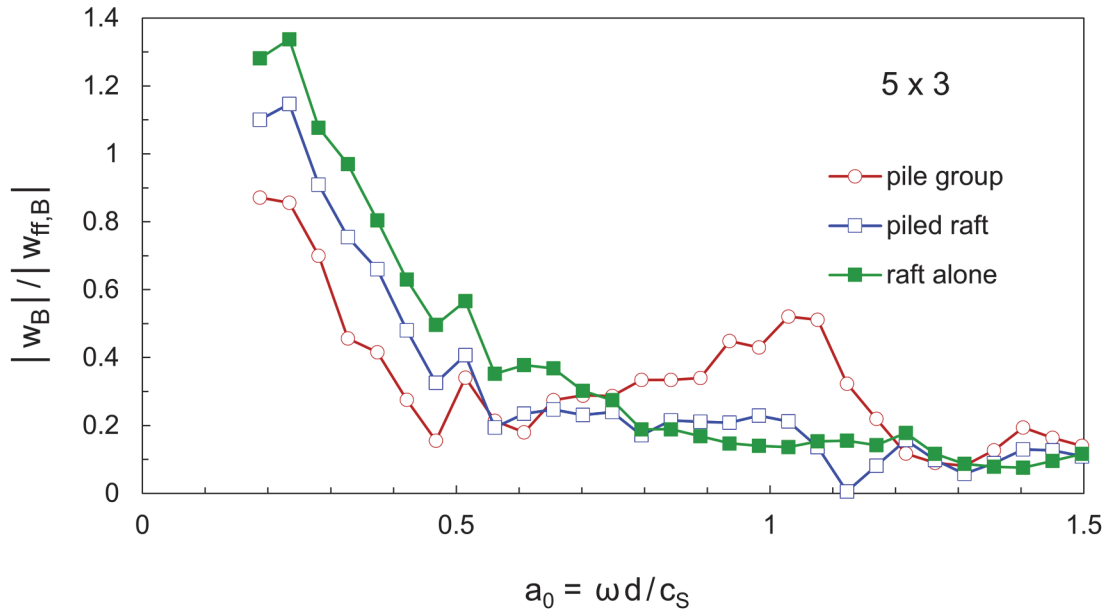


Figure 5.33: Vertical transfer function at point B behind the 5x3 configuration.

5.5.5 Comparison between 5x3 and 5x5 pile arrays

As a next step, a series of analyses including the configurations 2x5 - 5x5 presented in Figure 5.3 were performed. The motivation was to explore whether the addition of two columns (one column on either side) to each of the previous systems has a beneficial effect on vibration reduction.

In Figure 5.34, the response of each reference pile in the 5x3 pile group/piled raft is contrasted to its response as part of the corresponding 5x5 layout. It can be observed that the extension of the foundation system parallel to the wave propagation direction by additional piles does not significantly affect the response up to $a_0 \approx 1$. However, beyond this point, considerable differences appear, with the configuration including the additional columns reducing the vibration amplitudes the most in any case. In fact, with increasing excitation frequency, the attenuation of the free-field motion achieved by the largest configuration increases. These observations are similar for the rest configurations.

Detailed results for the rest pile arrays can be found in the Appendix.

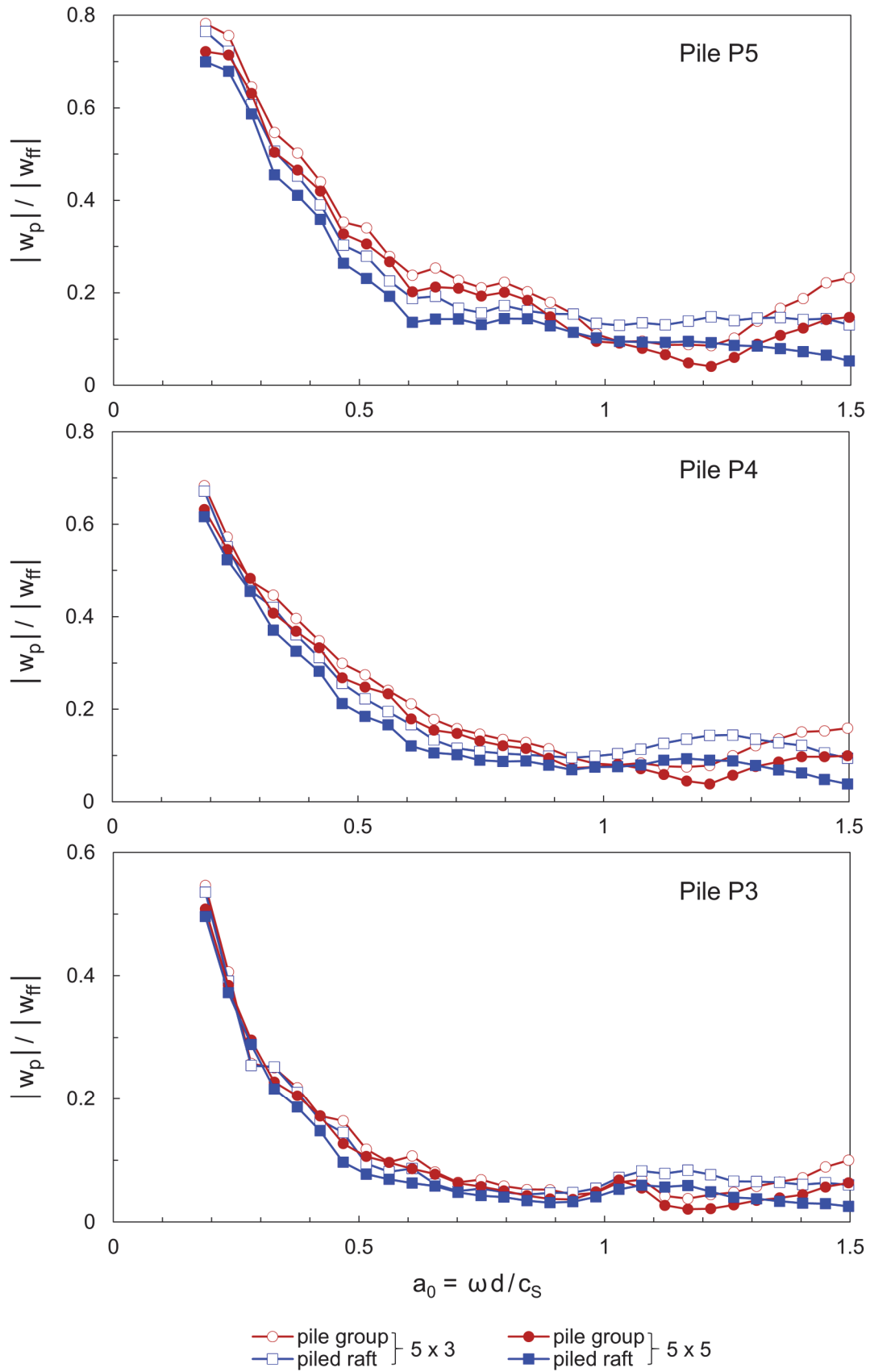


Figure 5.34: Vertical transfer functions of reference piles in the 5x3 or 5x5 piled foundation.

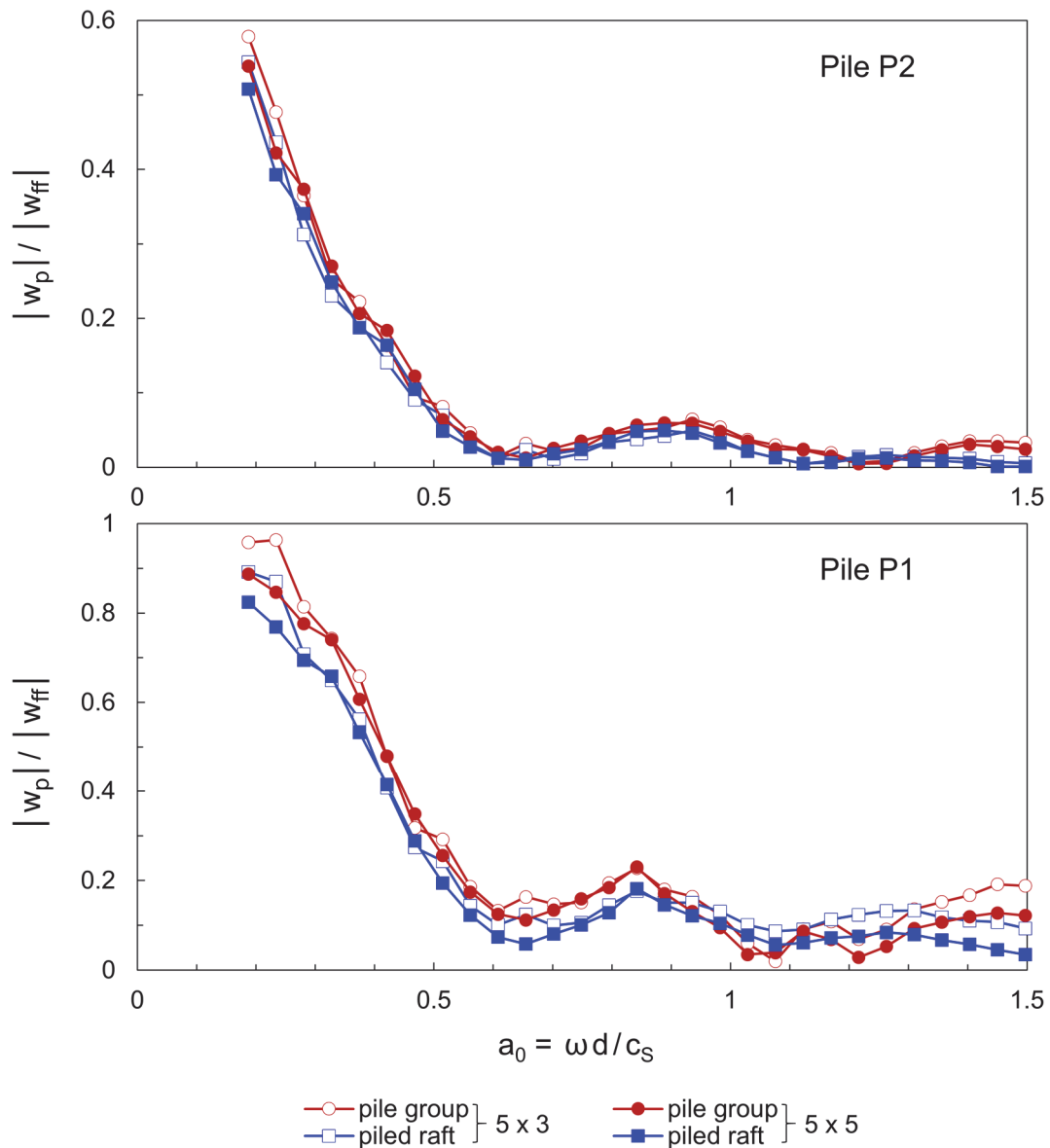


Figure 5.34 continued.

5.5.6 Comparison with a Winkler model solution

The results on the response of each pile group at the center-point are compared to the analytical solution from Makris & Badoni (1995) for pile groups under Rayleigh wave excitation. Being an extension of the work of Makris (1994) for the kinematic response of single piles to a Rayleigh wave field, the method is based on a dynamic Winkler model with frequency-dependent springs and dashpots to account for the pile–soil–pile interaction.

A Matlab code was written for the implementation of the method from Makris & Badoni (1995). From the review of the original paper, some minor typos were identified in the equations and corrected.

The vertical transfer functions for pile groups 2x3 - 5x3 are presented in Figure 5.35, and similarly, for 2x5 - 5x5 in Figure 5.36. First of all, two key differences between the analyses herein and the solution from Makris & Badoni (1995) need to be highlighted. It has been already mentioned that in finite-element analyses, the isolation of Rayleigh waves is practically impossible. With the harmonic point load being the source of excitation, in combination with the finite distance from the corresponding pile group, the presence of P- and S-waves in the vicinity of the pile group is inevitable. Furthermore, the analytical solution from Makris & Badoni (1995) utilizes a Winkler model, while in the present study the piles, which are modelled with volume elements, are embedded in a continuum.

Despite the above points, the FEA results are generally in very good accord with the analytical solution. Surprisingly, this is true even at low frequencies as well as for the largest configurations. Low frequencies are linked with large wavelengths, while in the present study, the size of the configuration increases towards the source of excitation, so the distance between the load and the pile group decreases. Both cases imply an enhanced influence of body waves.

The solution from Makris & Badoni (1995) can also be applied by neglecting the pile–soil–pile interaction. The corresponding curves reveal that this assumption is valid at rather lower frequencies. In addition, while the number of pile rows in the direction of wave propagation is a key point, the number of columns is irrelevant in the analytical solution when the interaction between the piles is ignored. As discussed in Section 5.5.6, although this is true at low frequencies, the interplay between the piles is more pronounced when the excitation frequency increases, and consequently, the number of columns plays an important role in the response in this case.

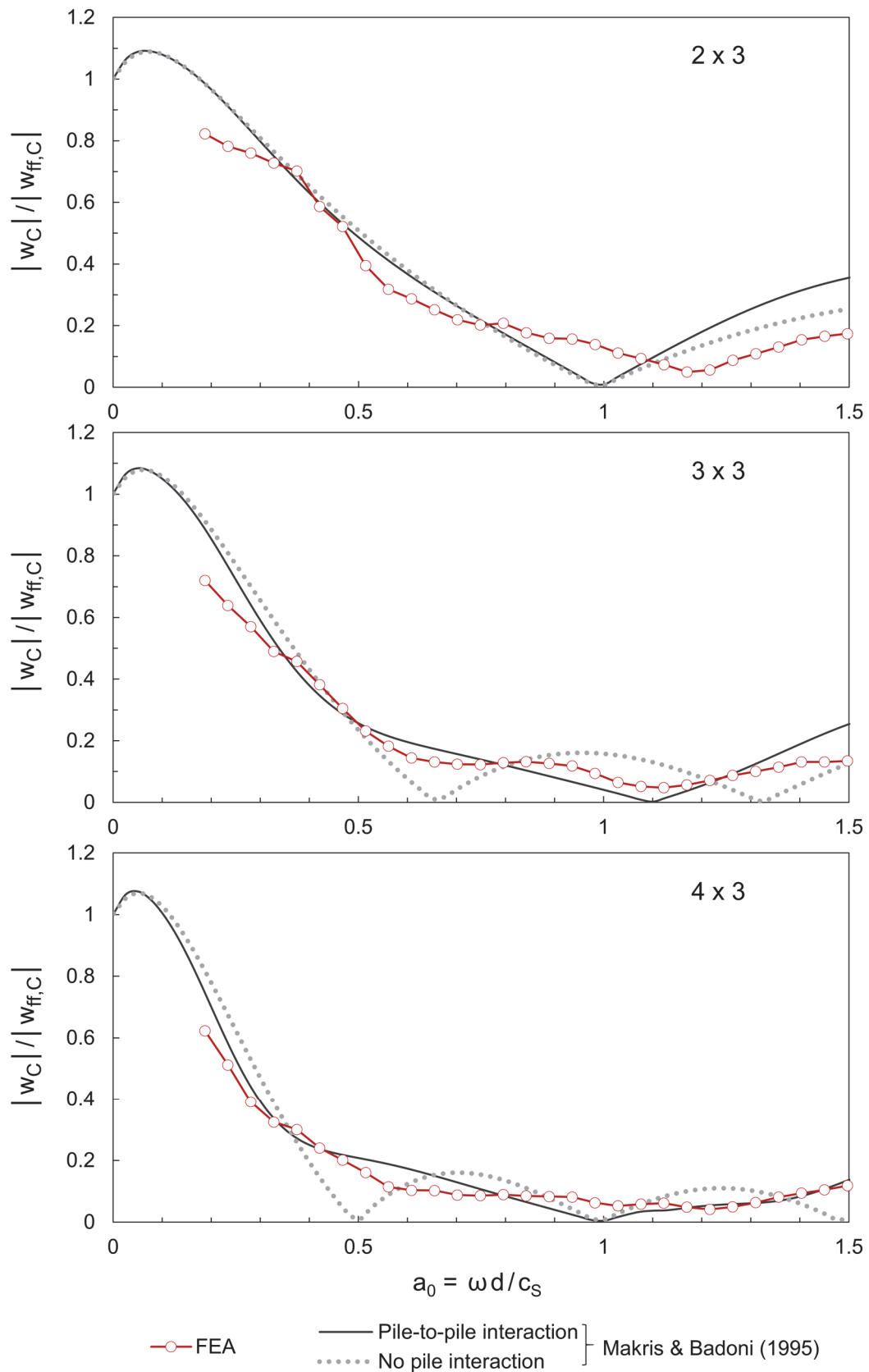


Figure 5.35: Vertical transfer functions at the center-point of configurations 2x3 - 5x3, compared to the analytical solution developed by Makris & Badoni (1995) for Rayleigh wave excitation.

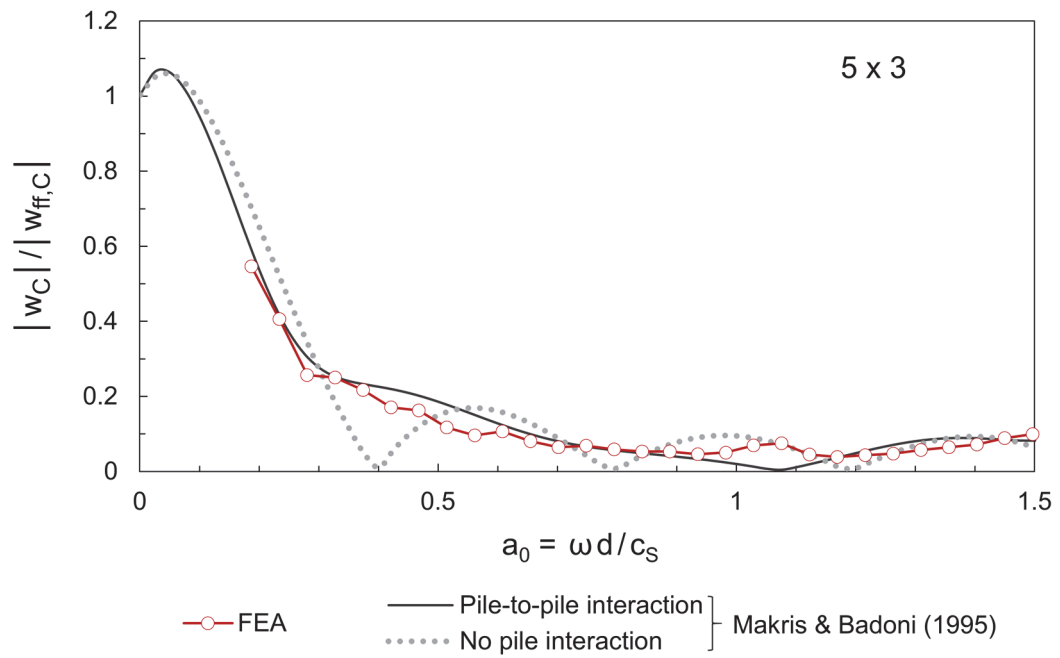


Figure 5.35 continued.

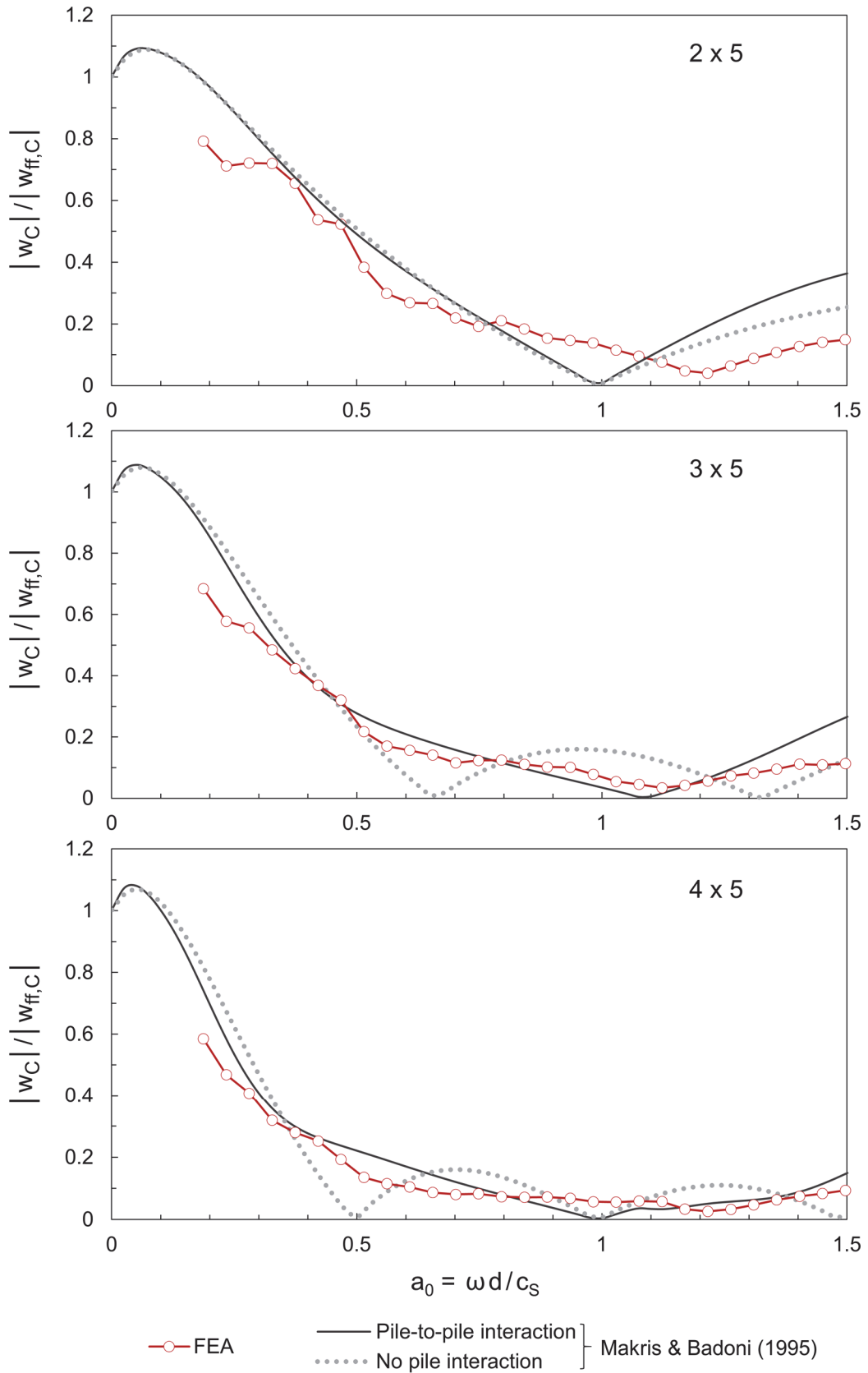


Figure 5.36: Vertical transfer functions at the center-point of configurations 2x5 - 5x5, compared to the analytical solution developed by Makris & Badoni (1995) for Rayleigh wave excitation.

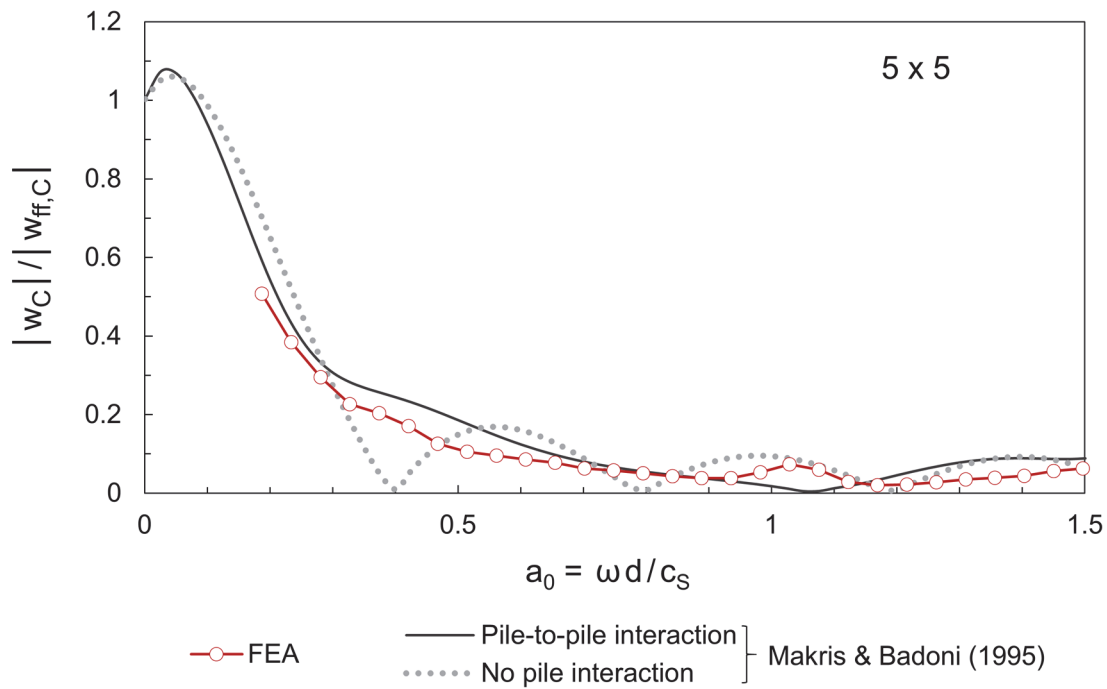


Figure 5.36 continued.

Finally, in Figure 5.37, the response of piles P1-P5 as solitary piles is compared to the solution from Makris (1994) for a single pile in a Rayleigh wave field. Overall, the agreement improves with increasing distance from the harmonic load, with the best match accomplished in the case of the most distant pile P1. The analytical solution could be employed in the frame of a preliminary design even for the near-field. Although it assumes Rayleigh wave excitation, the deviation of the FEA results for even the closest piles to the load is not dramatic.

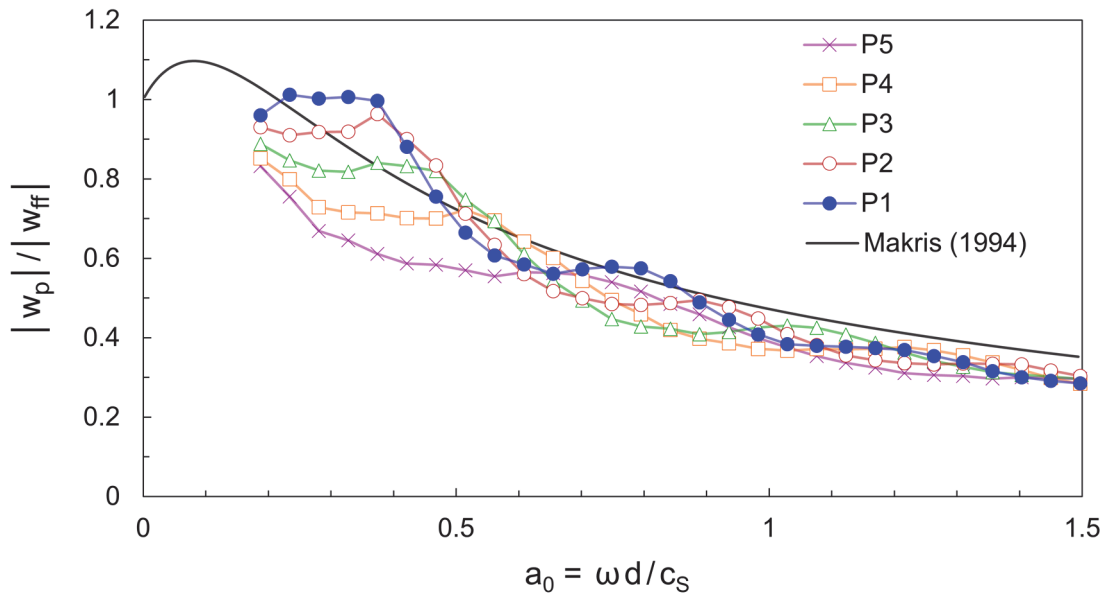


Figure 5.37: Vertical transfer functions for piles P1-P5 as solitary piles, compared to results from the analytical solution developed by Makris (1994) for Rayleigh wave excitation.

5.5.7 Influence of pile row number on vibration reduction

The influence of pile rows on the vibratory response of the furthest-back pile P1 as part of each configuration is summarized in Figure 5.38. Corresponding results for point B are given in Figure 5.39.

It is underlined that the distance of the pile array from the point load is an additional parameter that obviously affects the response. The overall good agreement with the analytical solution from Makris & Badoni (1995) implies that the finite distance of the examined pile arrays to the excitation source should not play a major role in the response.

Figure 5.38 shows that in the range $a_0 \approx 0.2 - 0.7$ additional pile rows reduce further the vibration level at the back of the pile array calculated at pile P1. This is also true for point B. Beyond $a_0 \approx 0.7$, due to the complexity of the dynamic problem, it is obvious that no clear pattern can be distinguished, and that the addition of pile rows against the wave propagation direction does not necessarily have a beneficial effect. This suggests that each problem needs to be analysed individually to obtain an optimal solution.

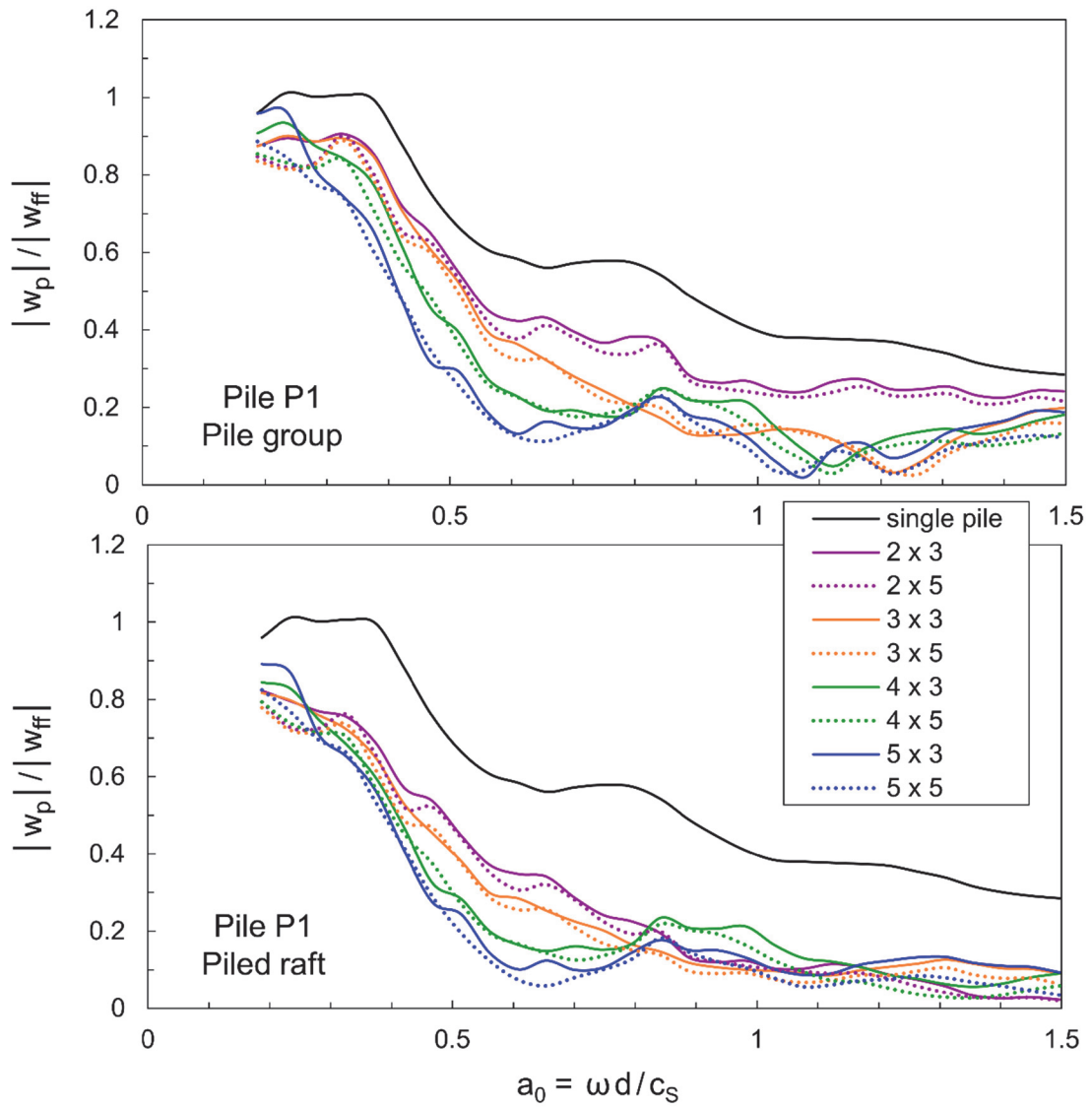


Figure 5.38: Vertical transfer functions of pile P1 as part of the various configurations or as solitary pile.

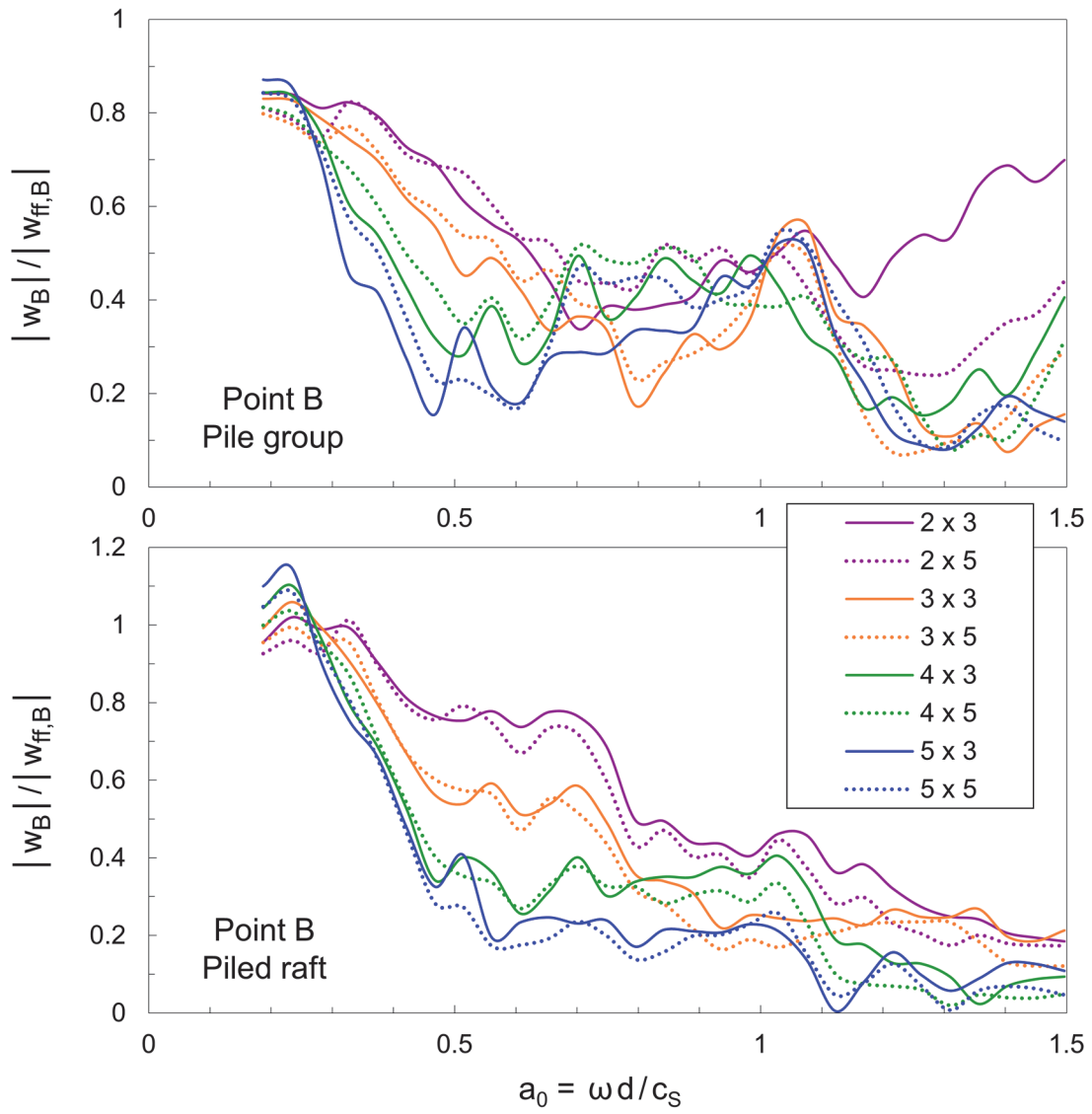


Figure 5.39: Vertical transfer functions at point B behind the various configurations.

Indicatively, Figure 5.40 provides a visualization of the wave propagation with contours of the induced vertical displacement field in presence of a 2x5 and a 5x5 pile group. At the selected excitation frequency of $a_0 = 0.5$ ($f = 22$ Hz), the addition of further pile rows has a favourable effect on the reduction of the vibration level, as revealed by the extended shadow zone forming at the back of the 5x5 pile group. Indeed, the transfer function of pile P1 $|w_p|/|w_{ff}| = 0.53$ in the 2x5 pile group drops at $|w_p|/|w_{ff}| = 0.26$, when the system is extended by three additional front pile rows.

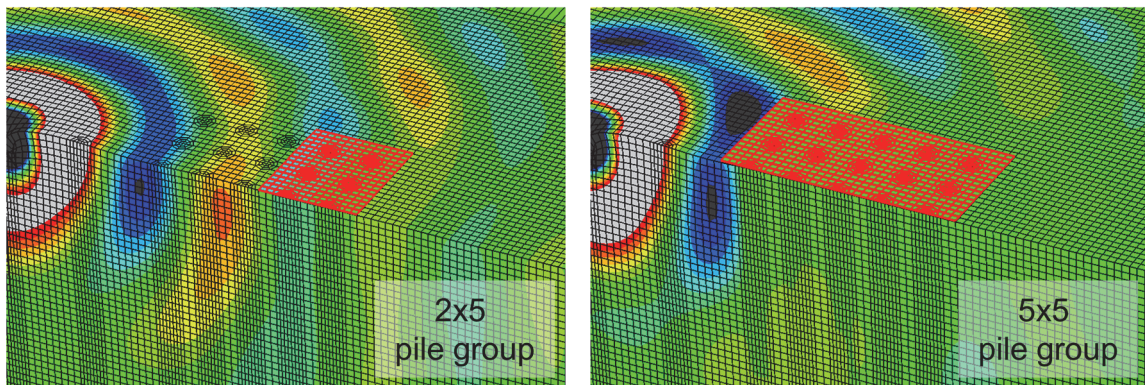


Figure 5.40: Vertical displacement contours at $a_0 = 0.5$ ($f = 22$ Hz) in the presence of a 2x5 (*left*) and a 5x5 pile group (*right*).

Finally, an interesting observation in Figure 5.39, is that for a large frequency range, the extended pile groups parallel to the wave propagation direction (2x5 - 5x5) reduce the vibration level at observation point B less compared to pile groups 2x3 - 5x3. This phenomenon could be attributed to increased reflections caused by the presence of additional piles that in combination with the ability of the soil about the piles to move freely, lead to higher displacement amplitudes at the free-field behind the pile group.

To enlighten this issue, Figure 5.41 portrays in top view contours of vertical displacement amplitudes in presence of the 5x3 and 5x5 pile group for an excitation frequency of $a_0 = 0.47$ corresponding to $f = 20$ Hz (load amplitude $|Q| = 1$ kN). The piles are highlighted in red. First of all, it can be seen that the each pile row exhibits the same vibration level, due to the symmetry of the problem and the connection of the pile heads via the rigid cap, which is not distinguished in the snapshots. Of particular interest is, however, that an extended influence zone as defined by the amplitude contours can be noticed about the

furthest back pile row, in which essentially the vibration level of the pile row dominates. Due to the additional pile columns in the case of the 5x5 pile group, the respective influence zone is larger. As a result, point B located at the soil surface behind the configuration, lies inside the influence zone in presence of the 5x5 pile group, demonstrating a higher vibration level as in the case of the 5x3 pile group.

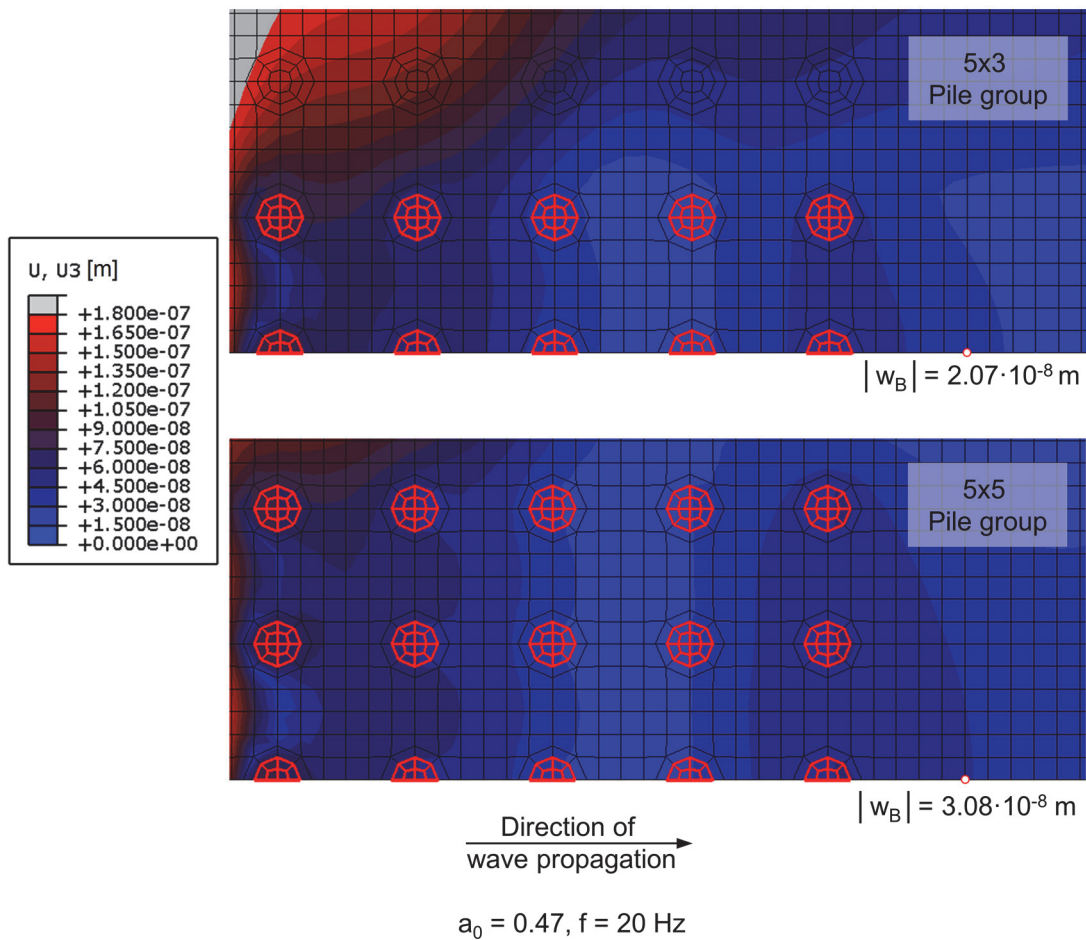


Figure 5.41: Top view of the models with contours of vertical displacement amplitudes in presence of pile groups 5x3 and 5x5 at the excitation frequency $a_0 = 0.47$.

5.6 Conclusions

The problem of kinematic response of pile foundations to a distant vertical surface harmonic point load was analyzed in the frequency domain with the finite-element software Abaqus. The examined foundations include pile groups and corresponding piled rafts for which a perfect contact is assumed between the raft and the underlying soil. In addition, to explore the contribution of the raft in the overall response, analyses with the raft acting alone were also performed. A wide frequency range was considered. The kinematic interaction is quantified through transfer functions being ratios of the vertical displacement amplitude at a characteristic location at the foundation (e.g. pile head) over that of the free-field corresponding to same location. Before proceeding to the main analyses, the model was validated by comparing the free-field response to that derived from a theoretical solution. A comparison between frequency-domain and time-domain analysis was also presented. The following conclusions are drawn:

- The accuracy of finite-element models for a half-space is lower as the excitation frequency decreases. This is attributed to reflections by the infinite elements set as absorbing boundaries, due to the large wavelengths associated with low frequencies.
- A low value of hysteretic damping ($\zeta = 1\%$) in the soil may cause fluctuation in the response. The propagating waves are not sufficiently attenuated before reaching the absorbing boundaries, and, consequently reflections occur.
- The results from frequency-domain analyses are in excellent agreement with those from time-domain analyses. With respect to the requirements of the present study, frequency-domain analysis is a superior tool reducing significantly the computational time.
- In the 2x3 and 2x5 pile groups/piled rafts, both pile rows in the direction of wave propagation exhibit almost the same vibration level up to $a_0 \approx 0.5$. The piles move in-phase due to the large wavelengths at low frequencies in comparison with the dimensions of the examined configuration.
- In the above small configurations, the response of the front pile row to be struck by the waves is comparable to the single pile response at this location. As more rows are added in the wave propagation direction, this is valid only at low frequencies, since group effects start to dominate in the dynamic response of larger pile arrays as the excitation frequency increases.

- The extension of the foundation system parallel to the wave propagation direction by additional piles columns does not significantly affect the response up to $a_0 \approx 1$. Beyond this point, an enhanced attenuation of the vibrations *inside* the pile array is accomplished by these larger systems.
- In the case of pile groups, this extension by additional pile columns increases the vibration level over a relatively wide frequency range as calculated at the free-field in the vicinity of the furthest-back pile row.
- The piled raft and the raft acting alone influence the response at the free-field behind them in a similar manner. This indicates that in this case the boundary condition enforced at the soil surface by the raft prevails against the piles. Beyond $a_0 \approx 0.9$, in comparison with a pile group, the presence of a piled raft or a raft alone results in a lower vibration level of the free-field at the back for all configurations. In fact, for the larger configurations (4x3, 5x3, 4x5 and 5x5), this is valid even from $a_0 \approx 0.7$.
- The results herein are compared with the methods from Makris (1994) as well as from Makris & Badoni (1995) for single piles and pile groups under Rayleigh wave excitation, respectively. The aforementioned solutions consider far-field conditions, which in the present study are not fulfilled due to the relatively close distance of the piles to the excitation source. Nevertheless, the agreement is generally good over the total frequency range. Consequently, these analytical solutions can be useful in the frame of a preliminary design of pile foundations located in the near-field of the excitation source.
- The extension of a pile array by additional pile rows against the direction of wave propagation has in the range $a_0 \approx 0.2 - 0.7$ a beneficial effect on the reduction of the vibration level calculated at the furthest-back pile row or at the free-field behind the foundation. This is, however, not true, as the excitation frequency increases further, and the interplay between the piles becomes more complex.
- The response of the pile group is similar to that of the piled raft for configurations including more than two pile rows against the wave propagation direction for $a_0 \leq 1$.

6 Summary & outlook

The problem of dynamic interaction of piled foundations was studied by means of the finite-element method with respect to vibration protection. The focus was placed on the kinematic response single piles, pile groups and piled rafts to a wave field emanating from a distant stationary or moving harmonic point load acting on the surface of the soil. In addition, dynamic impedances were derived for pile groups and piled rafts, as well as for an embedded footing. The finite-element programs Abaqus and Plaxis were employed for analyses in the frequency and time domain, respectively. Each of these tools was used with respect to the needs of the corresponding examined cases and to the optimization of the analyses. The results were verified against rigorous solutions. The importance of key aspects in finite-element modelling was also highlighted. The most significant conclusions are summarized as follows:

- For closely spaced piles, the dynamic impedances of a pile group are practically equal to those of a respective piled raft for all vibration modes (vertical, horizontal, rocking). This is due to the overlapping of the influence zones of the piles, while the raft remains practically inactive without participating in the load sharing.
- Even in the case of the wide pile spacing, the inertial response of both systems exhibits remarkable similarities up to $a_0 \approx 0.4$ for all modes of oscillation. At lower frequencies, the influence zones of the piles expand due to the associated large wavelengths, and overlap despite the wider pile-to-pile distance.
- The inertial response at low frequencies in the case of the half-space is less accurate due to the infinite elements used at the base of the model, and not due to those placed peripherally, since the latter are also present in the soil stratum models, which yield results in very good accord with rigorous solutions.
- In models for static analyses targeting a half-space response, it is recommended to use conventional boundaries at a sufficient distance from the region of interest, instead of infinite elements.
- In dynamic analyses for a half-space over a wide frequency range, it is suggested to employ at least two finite-element models, each accordingly adapted in terms of size and mesh fineness to the requirements of the corresponding frequency range. Hence, not only the accuracy of the results is improved, but also computational costs are significantly reduced.

- The free-field response with depth to a vertical harmonic point load acting on the soil surface is, from a distance between $7.5 \cdot \lambda_R - 10 \cdot \lambda_R$ from the load, in good agreement with the analytical solution for Rayleigh wave excitation. Even at closer distances, such as $2-3 \cdot \lambda_R$, the comparison is quite good up to a depth $z = \lambda_R$ from the soil surface.
- The fineness of the mesh is of critical importance in dynamic problems considering high frequencies. To reproduce the pertinent wave propagation phenomena with acceptable accuracy, the finite-element model needs to be uniformly discretized with a minimum number of finite elements corresponding to a Rayleigh wavelength. Ideally, this number needs to be determined with respect to the specific problem on the basis of a verification against rigorous results. As shown herein, circa 7 finite elements per Rayleigh wavelength can yield accurate results in many problems of practical interest.
- The distance of the infinite elements/viscous boundaries from the region of interest has an influence on the response. In the vicinity of these special boundaries, which are used to minimize wave reflections, the response is less accurate.
- A hysteretic damping ratio $\xi = 1\%$ leads to fluctuation in the response especially at farther distances close to the absorbing boundaries. Apparently, this low value does not offer adequate energy dissipation in the specific systems. The accuracy improves by increasing the hysteretic damping, which indicates that the waves are sufficiently attenuated before reaching the boundary, and consequently, wave reflections diminish.
- For a moving load speed v_0 , which is significantly smaller than the Rayleigh wave velocity in the soil c_R – a scenario quite common in the engineering practice – a static point load can be a good approximation for a moving load of constant magnitude. Analogously, this is true for a stationary harmonic point load and a moving oscillating load.
- At low values of the ratio v_0/c_R , the use of a viscous boundary at the base of the model in order to simulate a half-space results in lower accuracy. Applying a rigid base instead, may be a solution for models with a large depth, since the rigid base does not practically exert any influence on the response due to its large distance from the surface. When the need to shorten the model depth arises, e.g. in cases where a fine mesh discretization is required due to a moving harmonic load, a selection of a

rigid base will have a more pronounced effect on the response. This is a limitation of the FEM.

- The results herein are compared with the analytical solution from Makris (1994) as well as from Makris & Badoni (1995) for single piles and pile groups under Rayleigh wave excitation, respectively. The aforementioned solutions consider far-field conditions, which in the present study are not fulfilled due to the relatively close distance of the piles to the excitation source. Nevertheless, the agreement is generally good over the total frequency range examined, and even for piles located in the close vicinity of the excitation source (the accuracy improves obviously for piles at larger distances). Consequently, these analytical solutions can be useful in the frame of a preliminary design of piled foundations located at the near-field of the excitation source, whether it is a stationary or a moving harmonic load.
- An extensive parametric study on the kinematic response of 2x3 up to 5x5 piled foundations (pile rows x columns) to a stationary harmonic load was performed in the frequency domain. Results were in excellent agreement with those from time-domain analyses. With respect to the requirements of the present work, frequency-domain analysis is a superior tool reducing significantly the computational time. Yet, it is underlined that the time-domain analysis can be advantageous, since it can account for non-linearity.
- The extension of a pile group or piled raft by additional pile columns parallel to the wave propagation direction does not significantly affect the response up to $a_0 \approx 1$. Beyond this point, a further vibration reduction is monitored at characteristic points of these larger systems.
- The piled raft as well as its raft acting alone influence the response at the free-field behind them (with respect to the wave propagation direction) in a similar manner. This signifies that the boundary condition enforced at the soil surface by the raft prevails against the piles. In fact, beyond $a_0 \approx 0.9$, in comparison with a pile group, the presence of a piled raft or a raft alone results in a lower vibration level of the free-field at the back for all configurations. For the larger configurations 4x3, 5x3, 4x5 and 5x5, as the surface of the raft increases, this is valid even from a lower excitation frequency $a_0 \approx 0.7$.
- The extension of a pile array by additional pile rows against the direction of wave propagation has in the range $a_0 \approx 0.2 - 0.7$ a favourable effect on

the reduction of the vibration level calculated at the furthest-back pile row or at the free-field behind the foundation. This is, however, not true, as the excitation frequency increases further, with the interplay between the piles becoming more complicated.

- In terms of kinematic interaction, the pile group behaves in a similar manner as a corresponding piled raft in the cases of configurations including more than two pile rows in the wave propagation direction and up to a dimensionless frequency $a_0 = \omega \cdot d / c_s \approx 1$.

The main goal of this study was to gain valuable insight into the mechanics of the problem of kinematic interaction in the case of piled foundations. Additionally, the influence of key parameters of finite-element modelling on the accuracy of the results was investigated in detail. Simple solutions were suggested as good approximations for more complicated scenarios.

Further research needs to be conducted on the problem of kinematic interaction of piled foundations to stationary or moving harmonic loads. Key aspects that can be addressed in future studies include non-homogeneity as well as non-linearity of the soil, variation of the length in the frame of the pile group/piled raft and a varying speed of the moving load. Finally, the consideration of other structures in the vicinity of the examined foundation could also be of interest for the engineering practice.

Literature

Abaqus (2019): *Online documentation*, SIMULIA User Assistance, Dassault Systèmes.

Achenbach, J. D. (1973): *Wave propagation in elastic solids*. North-Holland, Amsterdam.

Appel, S., Vrettos, C., Hartmann, K. (2015) Messtechnische Bestimmung dynamischer Steifigkeiten eines Einzelpfahls sowie einer Pfahlgruppe für ein Maschinenfundament. *VDI-Berichte* Nr. 2244: 459–471.

Aubry, D., Clouteau, D., Bonnet, G. (1994): Modelling of wave propagation due to fixed or mobile dynamic sources. *Proceedings of Wave Propagation and Reduction of Vibrations*, Berg Verlag, Bochum, 109-121.

Auersch, L. (2005): The excitation of ground vibration by rail traffic: theory of vehicle–track–soil interaction and measurements on high-speed lines. *Journal of Sound and Vibration* 284: 103-132.

Auersch, L. (2006): Ground vibration due to railway traffic - The calculation of the effects of moving static loads and their experimental verification. *Journal of Sound and Vibration* 293: 599-610.

Auersch, L. (2008): The effect of critically moving loads on the vibrations of soft soils and isolated railway tracks. *Journal of Sound and Vibration* 310(3): 587-607.

Auersch, L. (2010). Wave propagation in the elastic half-space due to an interior load and its application to ground vibration problems and buildings on pile foundations. *Soil Dynamics and Earthquake Engineering* 30: 925-936.

Avilés, J.; Sánchez-Sesma, F. J. (1988): Foundation isolation from vibrations using piles as barriers. *Journal of Engineering Mechanics* 114(11): 1854-1870.

Barber J. R. (1996). Surface displacements due to a steadily moving point force. *Journal of Applied Mechanics* ASME 63: 245-251.

Boussinesq, J. (1885): *Application des potentiels à l'étude de l'équilibre et du mouvement des solides élastiques: principalement au calcul des déformations et des pressions que produisent, dans ces solides, des efforts quelconques exercés sur une petite partie de leur surface ou de leur intérieur:*

mémoire suivi de notes étendues sur divers points de physique, mathématique et d'analyse. Vol. 4. Gauthier-Villars.

Brûlé, S., Javelaud, E. H., Enoch, S., Guenneau, S. (2014): Experiments on seismic metamaterials: molding surface waves. *Physical Review Letters* 112(13), 133901.

Crispin, J., Mylonakis, G. (2022): Simplified models for axial static and dynamic analysis of pile foundations. *Analysis of pile foundations subject to static and dynamic loading*, CRC Press, 131-184.

De Barros, F. C. P., Luco, J. E. (1994): Response of a layered viscoelastic half-space to a moving point load. *Wave motion* 19(2): 189-210.

Deutsche Gesellschaft für Geotechnik e. V. (DGGT) (2019): *Empfehlungen des Arbeitskreises Baugrunddynamik*. Berlin: Ernst & Sohn.

Dobry, R., Gazetas, G. (1988): Simple method for dynamic stiffness and damping of floating pile groups. *Géotechnique* 38(4): 557-574.

Eason, G. (1965): The stresses produced in a semi-infinite solid by a moving surface force. *International Journal of Engineering Science* 2(6): 581-609.

Efthymiou, G., Vrettos, C. (2022a): Numerische Untersuchungen zur Abschirmwirkung von Einzelpfählen und Pfahlgruppen im Wellenfeld einer stationären oder bewegten harmonischen Last. *Bautechnik* 99(4): 249-261, doi:10.1002/bate.202100058

Efthymiou, G., Vrettos, C. (2022b): Pfahl unter Beanspruchung durch das Wellenfeld einer bewegten Last: Vergleich von FEM und Bettungsmodulverfahren, *VDI-Berichte* Nr. 2379, 631-641.

Efthymiou, G., Vrettos, C. (2022c): Vibration reduction effects of pile group foundations during the passage of nearby moving surface loads, *3rd International Conference on Natural Hazards and Infrastructure (ICONHIC)*, Athens.

Fan, K., Gazetas, G., Kaynia, A. M., Kausel, E., Ahmad, S. (1991): Kinematic seismic response of single piles and pile groups. *Journal of Geotechnical Engineering* 117(12): 1860-1879.

Fryba, L. (1972): *Vibration of solids and structures under moving loads*. Groningen, The Netherlands: Noordhoff International Publishing.

- Gakenheimer, D.C., Miklowitz, J. (1969): Transient excitation of an elastic half space by a point load traveling on the surface. *Journal of Applied Mechanics* ASME 36(3): 505-515.
- Galavi, V., Brinkgreve R. B. J. (2014): Finite element modelling of geotechnical structures subjected to moving loads. Hicks, M. A.; Brinkgreve R. B. J.; Rohe, A. (Eds.) *Numerical Methods in Geotechnical Engineering*. London: Taylor & Francis, 235-240.
- Galvín, P., Domínguez, J. (2007): Analysis of ground motion due to moving surface loads induced by high-speed trains. *Engineering Analysis with Boundary Elements* 31: 931-941.
- Gazetas, G. (1983): Analysis of machine foundation vibrations: state of the art. *International Journal of Soil Dynamics and Earthquake Engineering* 2(1): 2-42.
- Gazetas G., (1984): Seismic response of end-bearing single piles. *International Journal of Soil Dynamics and Earthquake Engineering* 3(2): 82-93.
- Gazetas G. (1987): Simple physical methods for foundation impedances. Banerjee, P.K., Butterfield, R. (Eds.), *Dynamic Behavior of Foundations and Buried Structures*. Elsevier Applied Science, 45-93.
- Gazetas G. (1991): Foundation vibrations. Fang, H.Y. (Ed.), *Foundation Engineering Handbook*. New York: Van Nostrand Reinhold, 553-593.
- Gazetas, G., Makris, N. (1991): Dynamic pile-soil-pile interaction. Part I: Analysis of axial vibration. *Earthquake Engineering and Structural Dynamics* 20(2): 115-132.
- Gazetas, G., Mylonakis, G. (1998): Seismic soil–structure interaction: new evidence and emerging issues. *Geotechnical Earthquake Engineering and Soil Dynamics III*, ASCE, Reston, 1119–1174.
- Graff, K. F. (1975): *Wave motion in elastic solids*. Ohio State University Press, The University Press, Belfast.
- Grundmann, H., Lieb, M., Trommer, E. (1999): The response of a layered half-space to traffic loads moving along its surface. *Archive of Applied Mechanics* 69: 55-67.

- Hartmann, H. G. (1986): *Pfahlgruppen in geschichtetem Boden unter horizontaler dynamischer Belastung*. Dissertation, Mitteilungen des Instituts für Grundbau, Boden- und Felsmechanik der TH Darmstadt, Heft 26.
- Hartmann, H. G. (2015): Dynamische Steifigkeiten von Gründungen aus Einzelpfählen oder Pfahlgruppen – Näherungsverfahren unter Ansatz vereinfachter Bodenmodelle. *VDI-Berichte* Nr. 2244: 39–55.
- Haupt, W. (1986): *Ausbreitung von Wellen im Boden*. Haupt, W. [Hrsg.], Bodendynamik. Braunschweig: Vieweg, 53-109.
- ISO 14837 (2005): Part 1, Mechanical vibration -- Ground-borne noise and vibration arising from rail systems, Part 1, General Guidance.
- Kanellopoulos, K., Gazetas, G. (2020): Vertical static and dynamic pile-to-pile interaction in non-linear soil. *Géotechnique* 70(5): 432-447.
- Karlström, A., Boström, A. (2006): An analytical model for train-induced ground vibrations from railways. *Journal of Sound and Vibration* 292(1-2): 221-241.
- Katou, M., Matsuoka, T., Yoshioka, O., Sanada, Y., Miyoshi, T. (2008): Numerical simulation study of ground vibrations using forces from wheels of a running high-speed train. *Journal of Sound and Vibration* 318(4-5): 830-849.
- Kattis, S. E., Polyzos, D., Beskos, D. E. (1999a): Vibration isolation by a row of piles using a 3-D frequency domain BEM. *International Journal for Numerical Methods in Engineering* 46: 713–728.
- Kattis, S. E., Polyzos, D., Beskos, D. E. (1999b): Modelling of pile wave barriers by effective trenches and their screening effectiveness. *Soil Dynamics and Earthquake Engineering* 18(1): 1-10.
- Kausel, E., Roesset, J. (1974): Soil–structure interaction for nuclear containment structures. *Proc. ASCE Power Division Specialty Conference*. Boulder, Colorado
- Kausel, E. (1995): PUNCH – Program for the dynamic analysis of layered media. Version W6.0
- Kausel, E. (1999): SUPELM: A computer program for dynamic stiffnesses of embedded footings on layered media, Version 4.0. Massachusetts Institute of Technology.

- Kausel, E. (2010): Early history of soil–structure interaction. *Soil Dynamics and Earthquake Engineering* 30 (9): 822-832.
- Kausel, E. (2017): *Advanced structural dynamics*. Cambridge University Press.
- Kausel E. (2018): Generalized stiffness matrix method for layered soils. *Soil Dynamics and Earthquake Engineering* 115: 663-672.
- Kaynia, A. M. (1982): *Dynamic stiffness and seismic response of pile groups*. PhD diss., Massachusetts Institute of Technology.
- Kaynia, A. M., Kausel, E. (1982): *Dynamic stiffness and seismic response of pile groups*. Research Report R82-03, Massachusetts Institute of Technology.
- Kaynia, A. M., Kausel, E. (1991): Dynamics of piles and pile groups in layered soil media. *Soil Dynamics and Earthquake Engineering* 10(8): 386-401.
- Kaynia, A. M., Novak, M. (1992): Response of pile foundations to Rayleigh waves and obliquely incident body waves. *Earthquake Engineering and Structural Dynamics* 21: 303-318.
- Kouroussis, G., Conti, C., Verlinden, O. (2013): Investigating the influence of soil properties on railway traffic vibration using a numerical model. *Vehicle System Dynamics* 51(3): 421-442.
- Lamb, H. (1904): On the propagation of tremors over the surface of an elastic solid. *Philosophical Transactions of the Royal Society of London. Series A, Containing Papers of a Mathematical or Physical Character* 203: 1-42.
- Lombaert, G., Degrande, G., Kogut, J., François, S. (2006): The experimental validation of a numerical model for the prediction of railway induced vibrations. *Journal of Sound and Vibration* 297: 512-535.
- Lu, J. F., Xu, B., Wang, J. H. (2009): Numerical analysis of isolation of the vibration due to moving loads using pile rows. *Journal of Sound and Vibration* 319: 940-962.
- Luco, J. E. (1982): Linear soil–structure interaction: a review. Datta, S.K. (Ed.), *Earthquake Ground Motion and its Effects on Structures*, ASME, AMD 53: 41-57.
- Lysmer, J., Kuhlemeyer, R. L. (1969): Finite dynamic model for infinite media. *Journal of the Engineering Mechanics Division, ASCE*, 95(4): 859-877.

- Madshus, C., Kaynia, A. M. (2000): High-speed railway lines on soft ground: dynamic behaviour at critical train speed. *Journal of Sound and Vibration* 231(3): 689-701.
- Makris, N. (1994): Soil-pile interaction during the passage of Rayleigh waves: An analytical solution. *Earthquake Engineering and Structural Dynamics* 23(2): 153-167.
- Makris, N., Badoni, D. (1995): Seismic response of pile groups under oblique-shear and Rayleigh waves. *Earthquake Engineering and Structural Dynamics* 24(4): 517-532.
- Makris, N., Gazetas, G. (1992): Dynamic pile-soil-pile interaction. Part II: Lateral and seismic response. *Earthquake Engineering and Structural Dynamics* 21(2): 145-162.
- Meek, J.W., Wolf, J.P. (1993): Approximate Green's function for surface foundations. *Journal of Geotechnical Engineering* 119(10): 1499-1514.
- Mylonakis, G., Nikolaou, A., Gazetas, G. (1997): Soil–pile–bridge seismic interaction: kinematic and inertial effects. Part I: soft soil. *Earthquake Engineering and Structural Dynamics* 26(3): 337-359.
- Mylonakis, G., Gazetas, G. (1999): Lateral vibration and internal forces of grouped piles in layered soil. *Journal of Geotechnical and Geoenvironmental Engineering* 125(1): 16-25.
- Mylonakis, G., Crispin, J. (2022): Simplified models for lateral static and dynamic analysis of pile foundations. *Analysis of pile foundations subject to static and dynamic loading*, CRC Press, 185-245.
- Nikolaou, S., Mylonakis, G., Gazetas, G., Tazoh, T. (2001): Kinematic pile bending during earthquakes: analysis and field measurements. *Géotechnique* 51(5): 425–440.
- Nogami, T. (1979): Dynamic group effect of multiple piles under vertical vibration. C. P. Johnson (Ed.), *Engineering mechanics*. ASCE, 750-754.
- Nogami, T. (1980): Dynamic stiffness and damping of pile groups in inhomogeneous soil. M. O'Neill, R. Dobry (Eds.), *Dynamic Response of Pile Foundations: Analytical Aspects*, ASCE Special Technical Publication, 31-52.

- Nogami, T. (1983): Dynamic group effect in axial responses of grouped piles. *Journal of Geotechnical Engineering ASCE* 109(2): 228-243.
- Padrón, L. A. (2008): *Numerical model for the dynamic analysis of pile foundations*. Doctoral diss., Universidad de las Palmas de Gran Canaria.
- Padrón, L. A., Aznárez, J. J., Maeso, O. (2008): Dynamic analysis of piled foundations in stratified soils by a BEM–FEM model. *Soil Dynamics and Earthquake Engineering* 28(5): 333-346.
- Palermo, A., Krödel, S., Marzani, A., Daraio, C. (2016): Engineered metabarrier as shield from seismic surface waves. *Scientific Reports*, 6(1):1-10.
- Payton, R.G. (1964): An application of the dynamic Betti-Rayleigh reciprocal theorem to moving-point loads in elastic media. *Quarterly of Applied Mathematics* 21(4): 299-313.
- Plaxis 3D (2021): Connect Edition V21.01, Plaxis bv, Bentley Systems, Incorporated.
- Plaxis 2D (2021): Connect Edition V21.01, Plaxis bv, Bentley Systems, Incorporated.
- Poulos, H. G. (1968): Analysis of the settlement of pile groups. *Geotechnique* 18(4): 449-471.
- Poulos, H. G. (1971): Behavior of laterally loaded piles: II-pile groups. *Journal of the Soil Mechanics and Foundations Division* 97(5): 733-751.
- Pu, X. & Shi, Z. (2018): Surface-wave attenuation by periodic pile barriers in layered soils. *Construction and Building Materials* 180: 177-187.
- Randolph, M.F. (2003): Science and empiricism in pile foundation design. *Géotechnique* 53(10): 847-875.
- Roesset, J. M. (1980): Stiffness and damping coefficients of foundations. O’Neil, M., Dobry, R. (Eds.), *Dynamic Response of Pile Foundations: Analytical Aspects*. ASCE, 1-30.
- Roesset, J. M. (1984): Dynamic stiffness of pile groups. *Pile foundations*. ASCE, New York.
- Rücker, W. (1989): Schwingungsausbreitung im Untergrund. *Bautechnik* 66(10): 343-350.

Sanchez-Salineró, I. (1983): *Dynamic stiffness of pile groups: approximate solutions*. Geotechnical Engineering Report GR83-5, University of Texas at Austin.

Satis, P.V. (2017): Railway induced vibration – State of the art report. International Union of Railways (UIC), Paris.

Sheng, X.Z., Jones, C.J.C., Petyt, M. (1999): Ground vibration generated by a load moving along a railway track. *Journal of Sound and Vibration*, 228(1): 129-156.

Takemiya, H. (2003): Simulation of track–ground vibrations due to a high-speed train: the case of X-2000 at Ledsgard. *Journal of Sound and Vibration* 261(3): 503-526.

Takemiya, H., Bian, X. (2005): Substructure simulation of inhomogeneous track and layered ground dynamic interaction under train passage. *Journal of Engineering Mechanics* 131(7): 699-711.

Tsai, P. H., Feng, Z. Y., Jen, T. L. (2008): Three-dimensional analysis of the screening effectiveness of hollow pile barriers for foundation-induced vertical vibration. *Computers and Geotechnics* 35(3): 489-499.

Vrettos, C. (1991): Time-harmonic Boussinesq problem for a continuously nonhomogeneous soil. *Earthquake Engineering and Structural Dynamics* 20(10): 961-977.

Vrettos, C. (2009): Erschütterungsschutz. Witt, K.-J. [Hrsg.] Grundbautaschenbuch – Teil 3: Gründungen und geotechnische Bauwerke, 7. Aufl. Berlin: Ernst & Sohn, 691-746.

Vrettos, C. (2014): Soil-Structure Interaction. *Encyclopedia of Earthquake Engineering*, Berlin: Springer, doi: 10.1007/978-3-642-36197-5_141-1

Vrettos, C. (2017): Bodendynamik. Witt, K.-J. [Hrsg.] Grundbautaschenbuch – Teil 1: Geotechnische Grundlagen, 8. Aufl. Berlin: Ernst & Sohn, 573-631.

Waas, G., Hartmann, H. G. (1981): Analysis of pile foundations under dynamic loads. *Conf. on Structural Mechanics in Reactor Technology*, Paris.

Waas, G., Hartmann, H. G. (1984): Seismic analysis of pile foundations including pile–soil–pile interaction. *Proc. 8th WCEE*, San Francisco, vol. v: 55-62.

Waas, G., Riggs, H. R., Werkle, H. (1985): Displacement solutions for dynamic loads in transversely-isotropic stratified media. *Earthquake Engineering and Structural Dynamics* (13): 173-193.

Wolf, J. P., Von Arx, G. A. (1978): Impedance function of a group of vertical piles. *Proc. of the Speciality Conference on Earthquake Engineering and Soil Dynamics*, ASCE, Pasadena, CA, USA, (2): 1024-1041.

Woods, R. D. (1968). Screening of surface wave in soils. *Journal of the Soil Mechanics and Foundations Division*, ASCE 94(4): 951-979.

Zhao, C., Zeng, C., Wang, Y., Bai, W., Dai, J. (2022): Theoretical and numerical study on the pile barrier in attenuating seismic surface waves. *Buildings* 12(10): 1488.

Zienkiewicz, O. C., Emson, C., Bettess, P. (1983): A novel boundary infinite element. *International Journal for Numerical Methods in Engineering* (19): 393-404.

Appendix

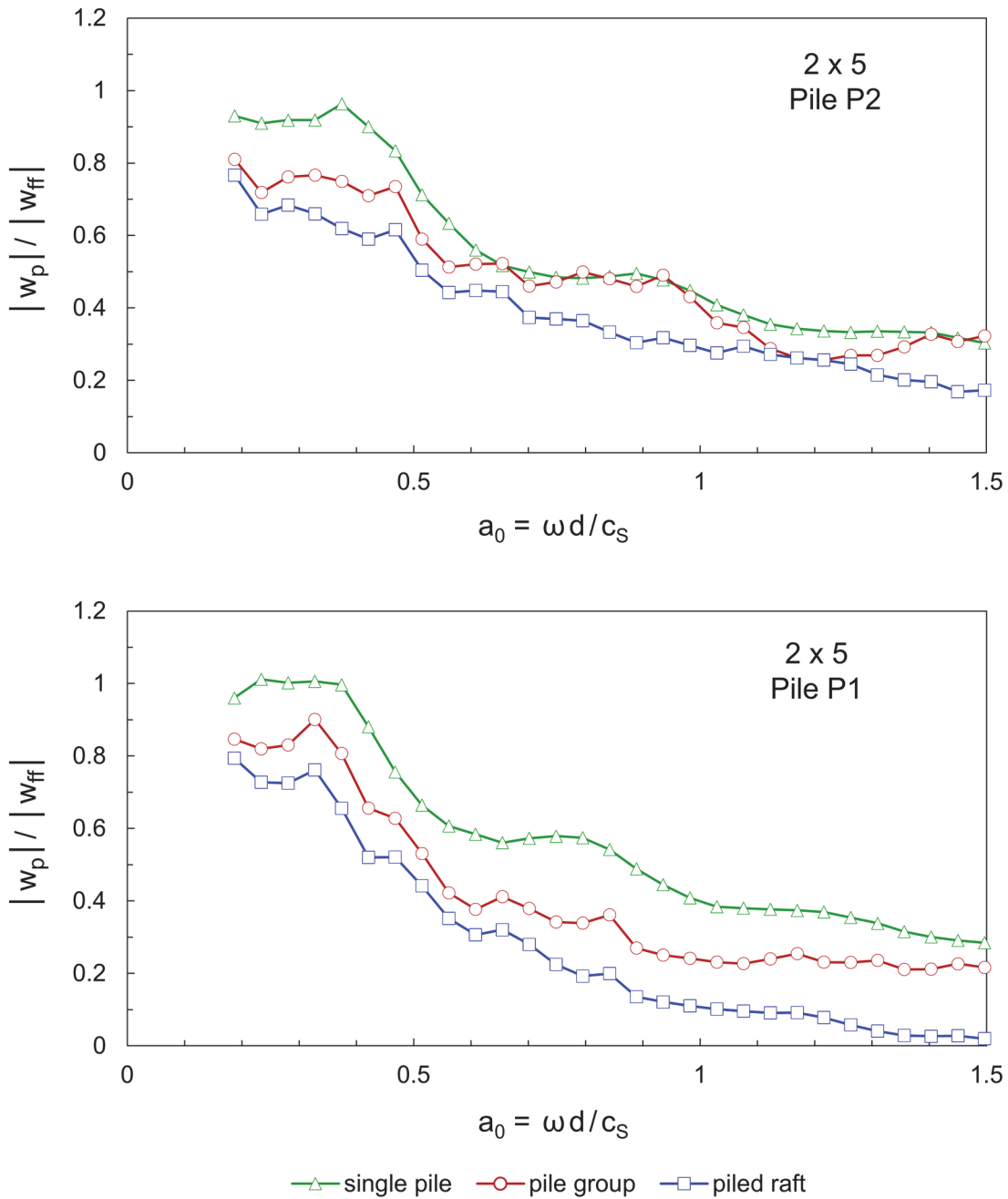


Figure A.1: Vertical transfer functions of reference piles in the 2x5 configuration as single piles or parts of a pile group/piled raft.

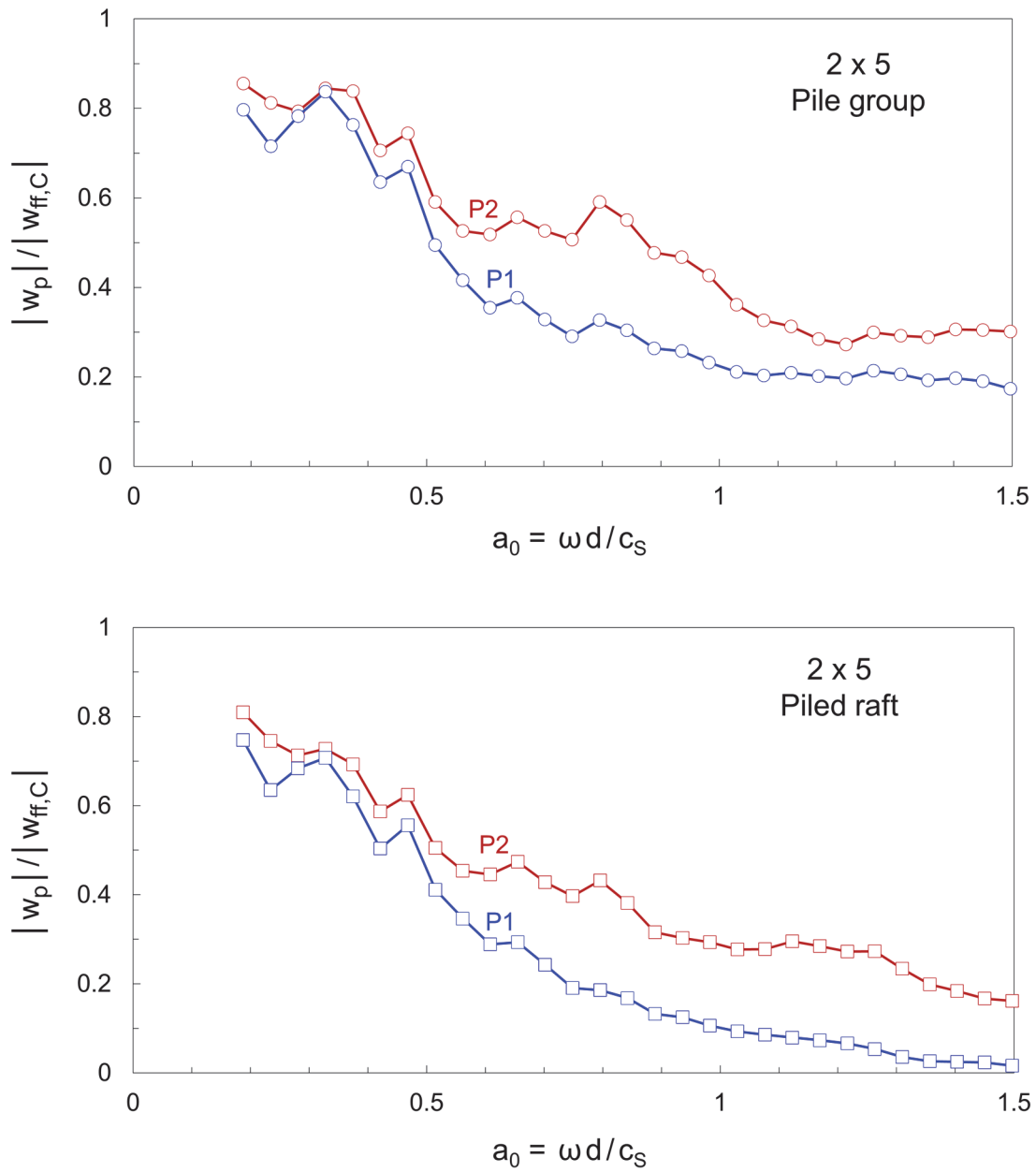


Figure A.2: Vertical transfer functions of reference piles normalized by the free-field amplitude at the center-point of the 2x5 configuration.

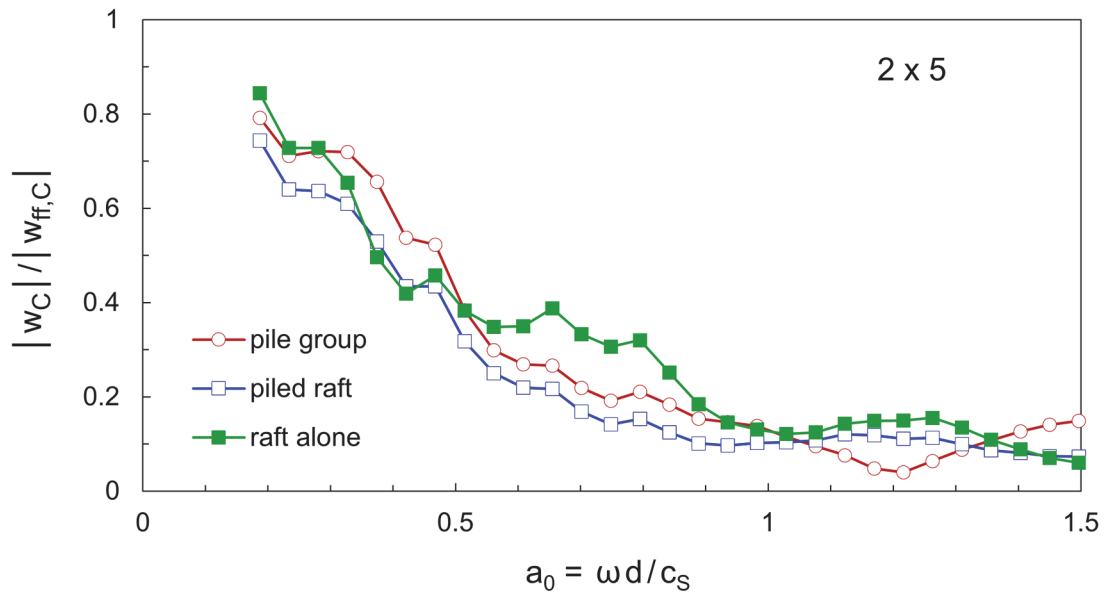


Figure A.3: Vertical transfer function at the center-point of the 2x5 configuration.

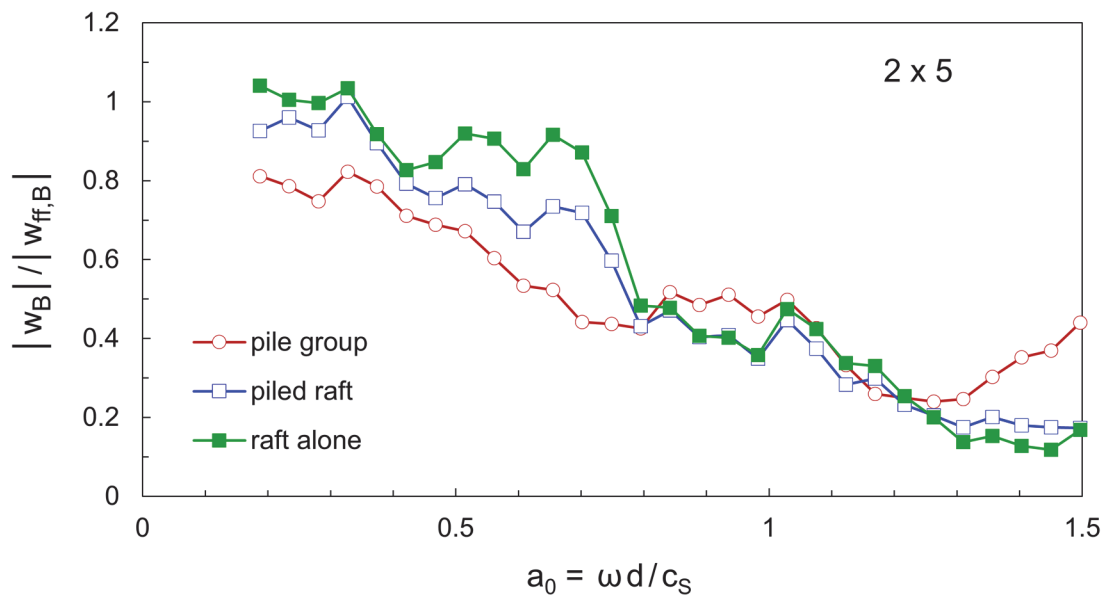


Figure A.4: Vertical transfer function at point B behind the 2x5 configuration.

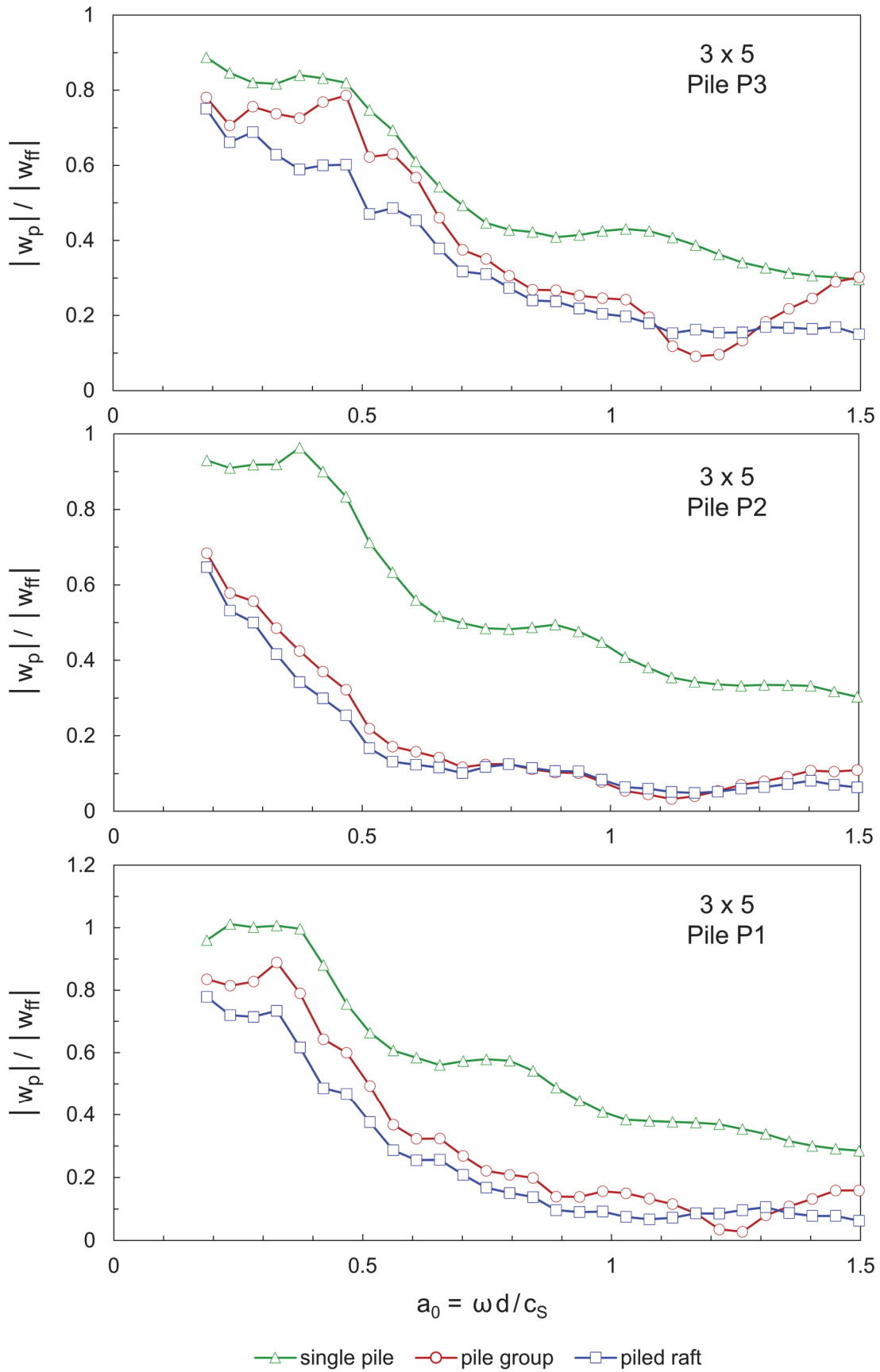


Figure A.5: Vertical transfer functions of reference piles in the 3x5 configuration as single piles or parts of a pile group/piled raft.

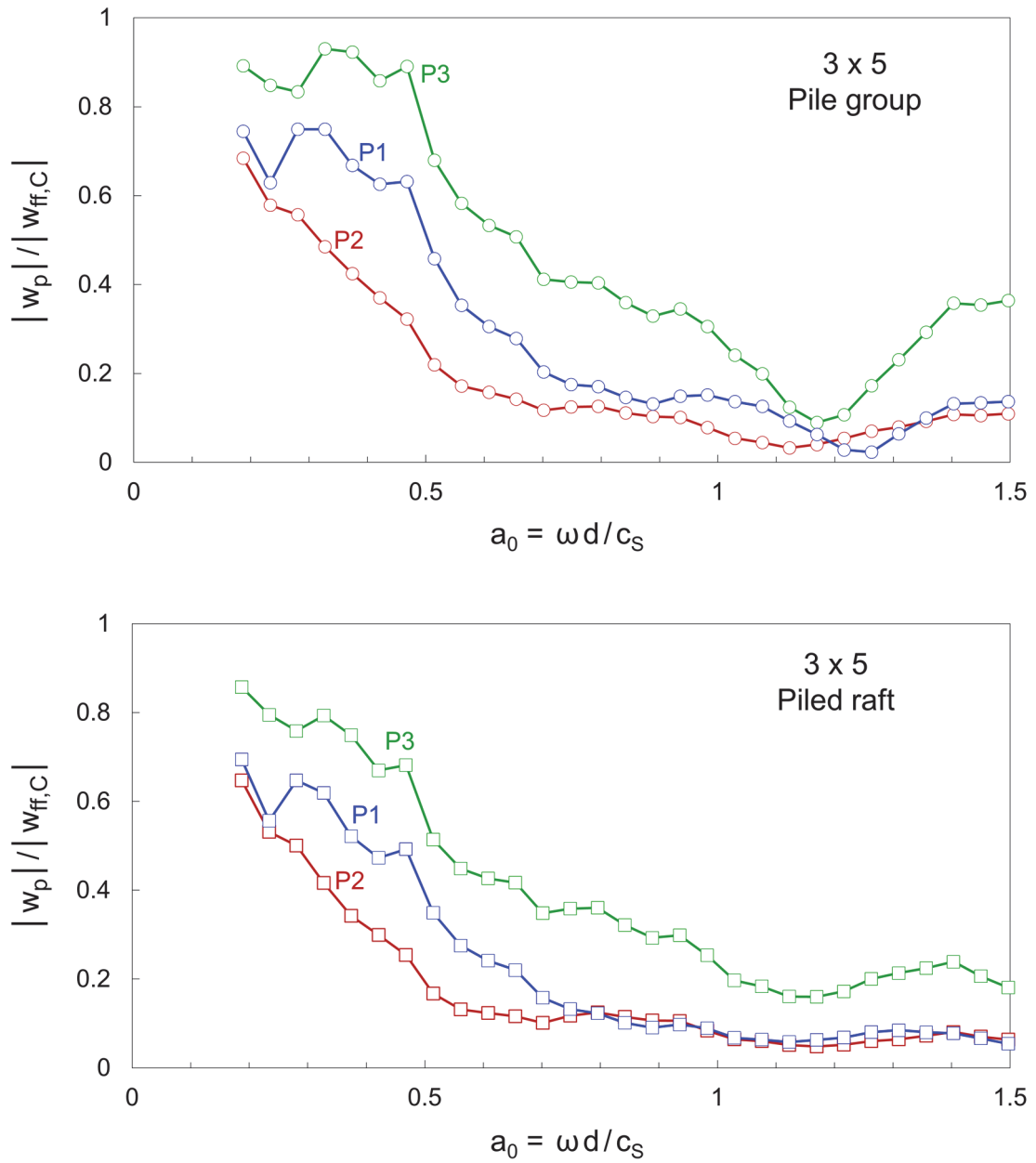


Figure A.6: Vertical transfer functions of reference piles normalized by the free-field amplitude at the center-point of the 3x5 configuration.

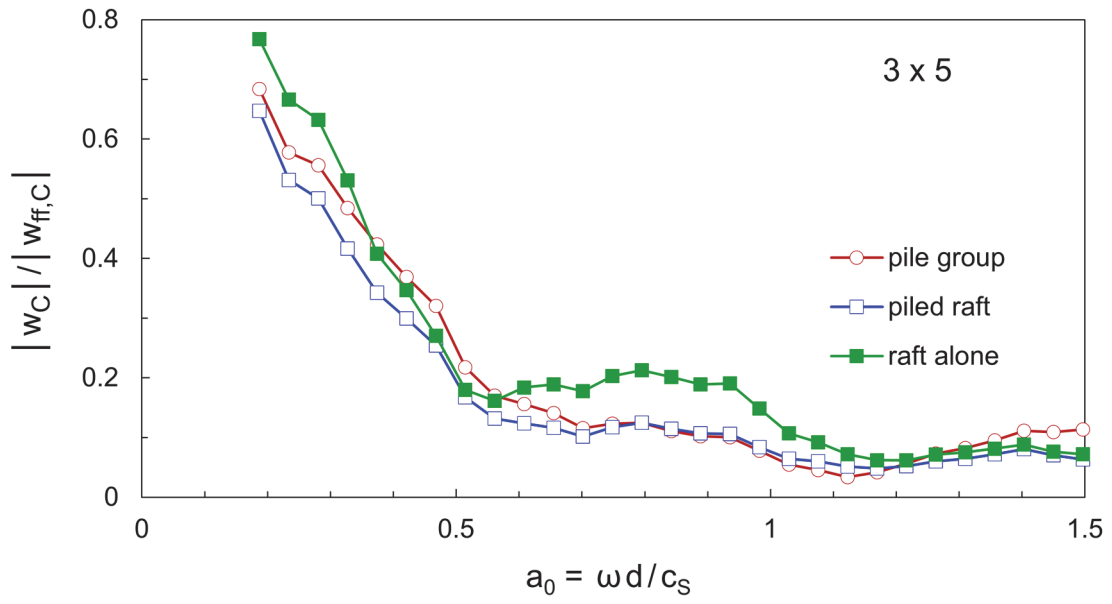


Figure A.7: Vertical transfer function at the center-point of the 3x5 configuration.

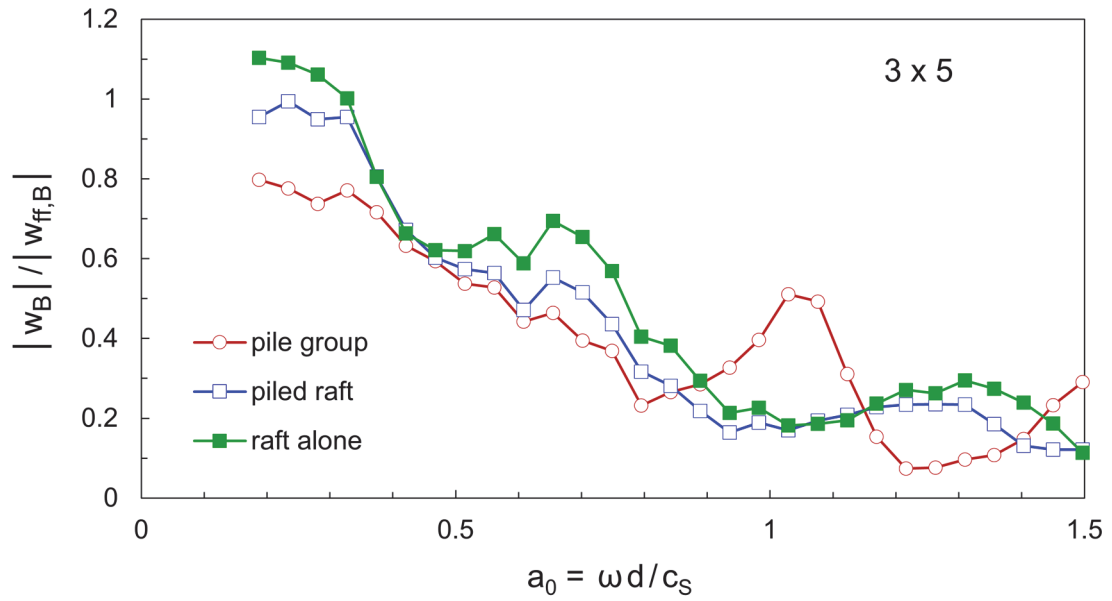


Figure A.8: Vertical transfer function at point B behind the 3x5 configuration.

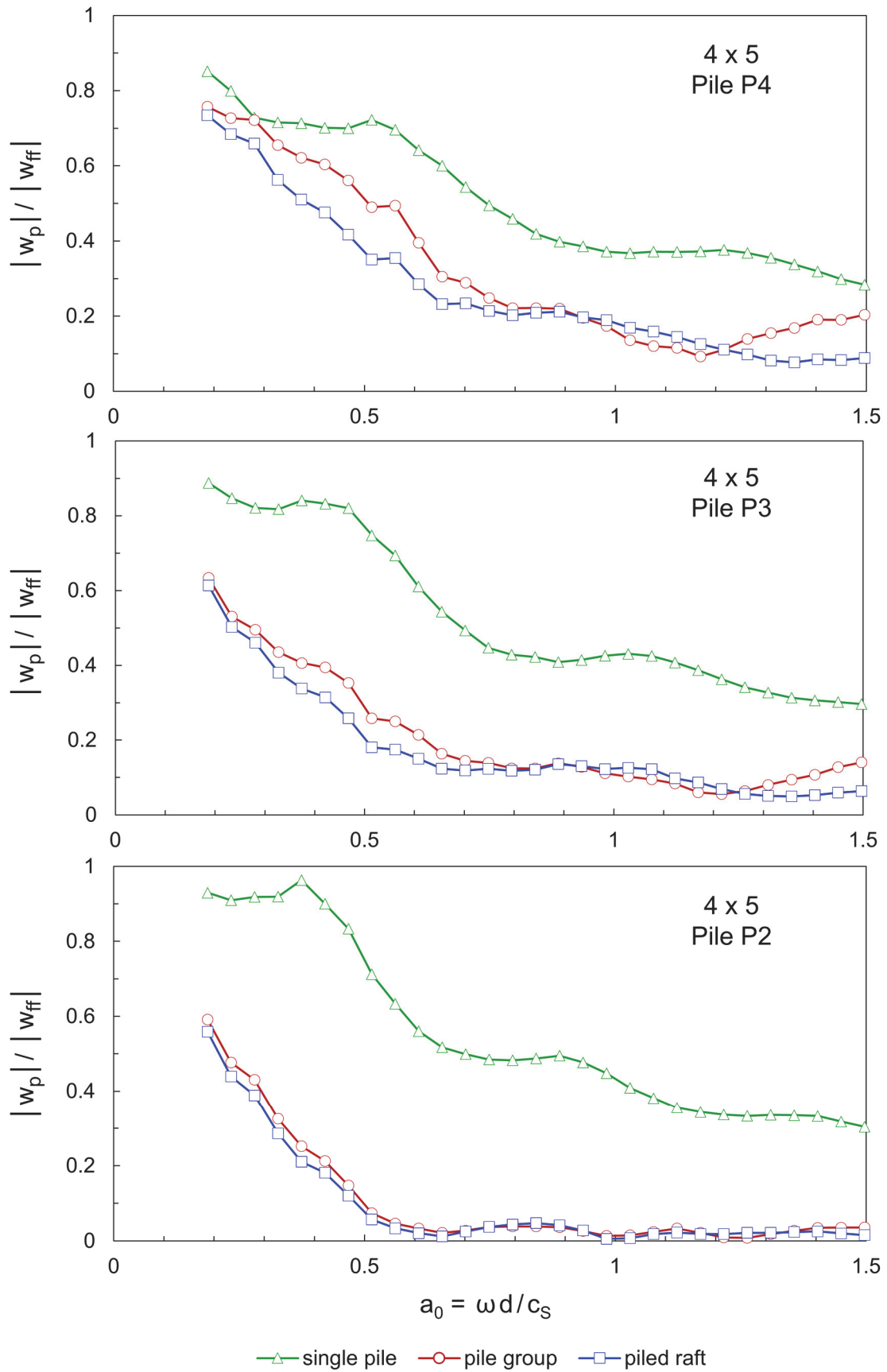


Figure A.9: Vertical transfer functions of reference piles in the 4x5 configuration as single piles or parts of a pile group/piled raft.

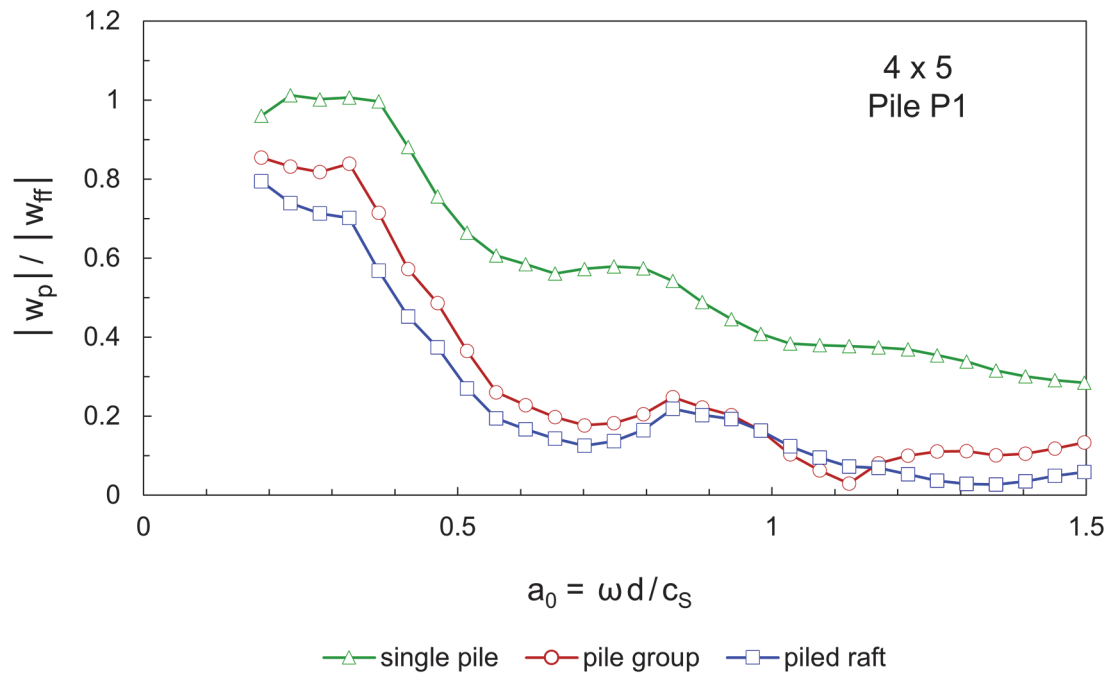


Figure A.9 continued.

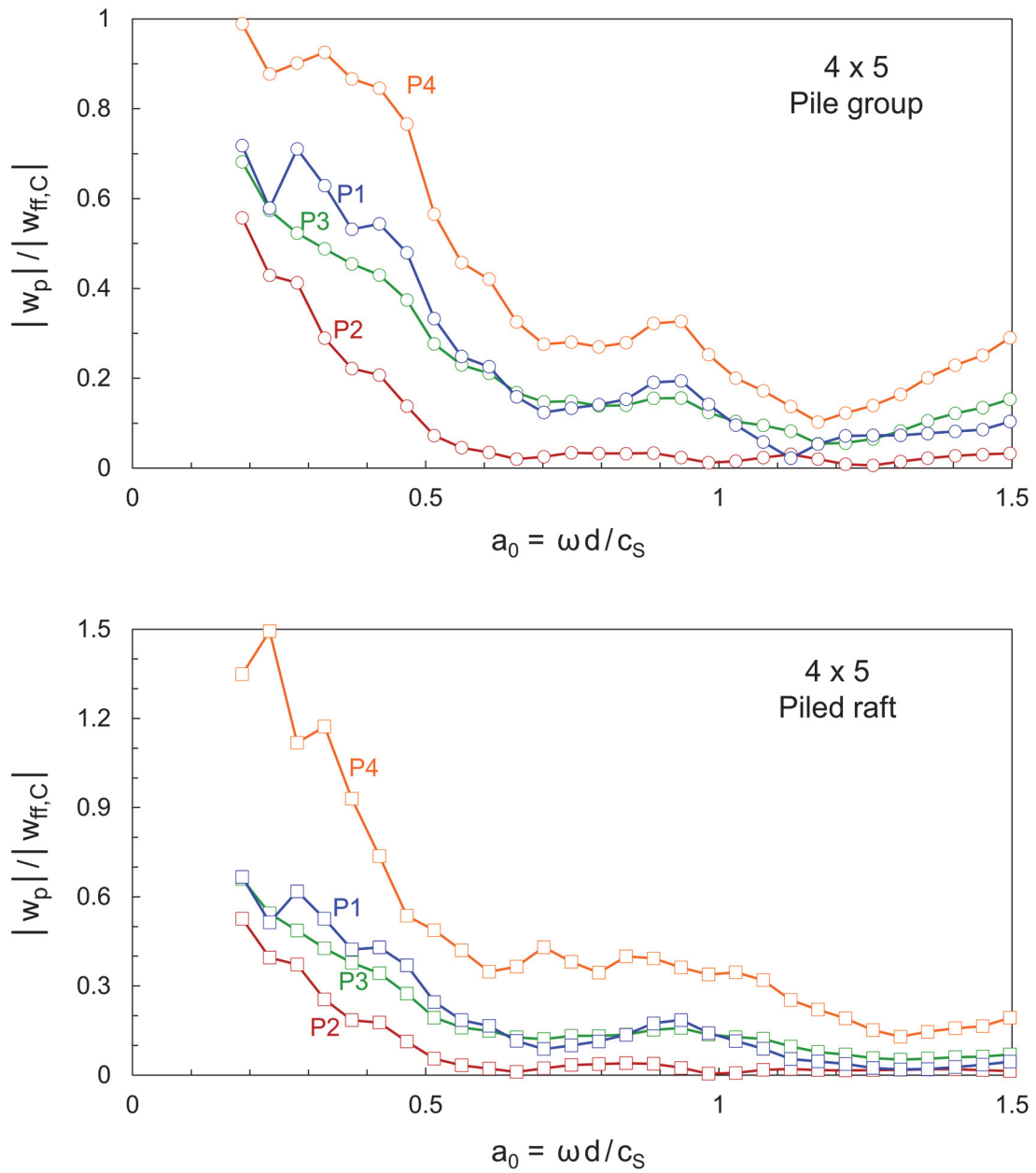


Figure A.10: Vertical transfer functions of reference piles normalized by the free-field amplitude at the center-point of the 4x5 configuration.

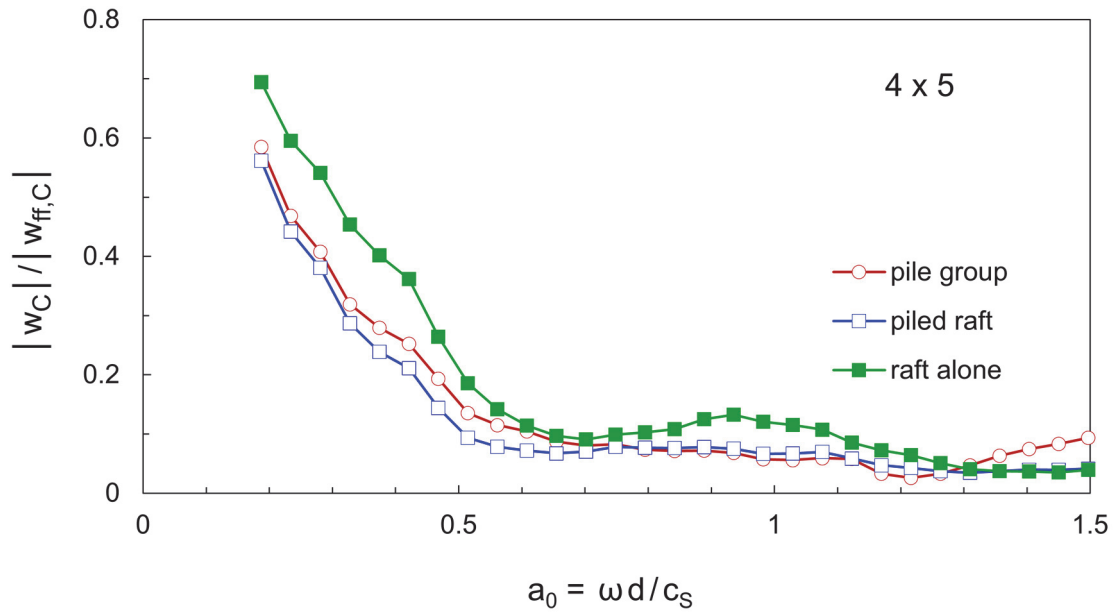


Figure A.11: Vertical transfer function at the center-point of the 4x5 configuration.

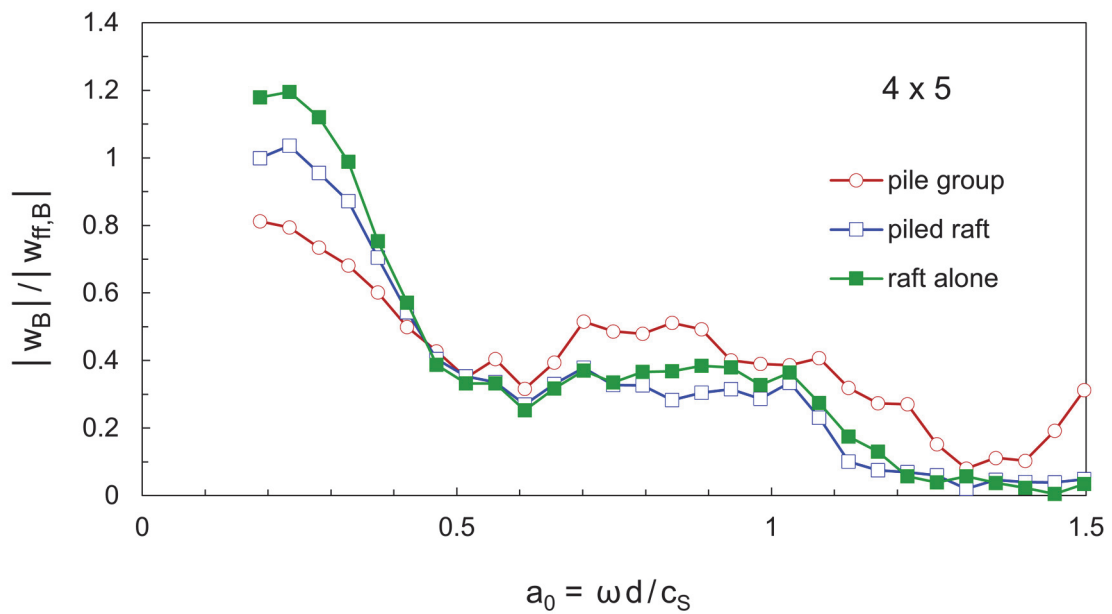


Figure A.12: Vertical transfer function at point B behind the 4x5 configuration.

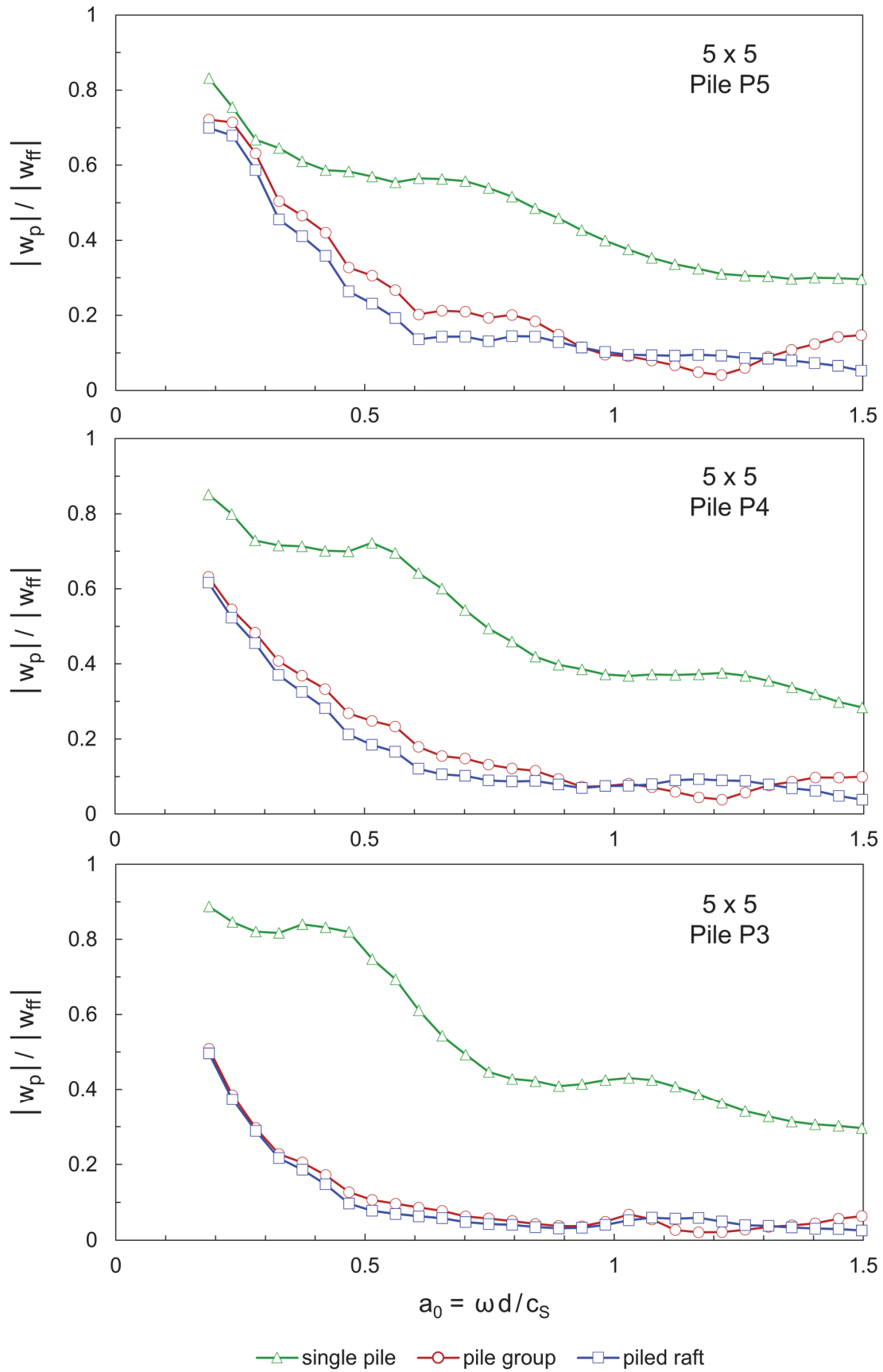


Figure A.13 Vertical transfer functions of reference piles in the 5x5 configuration as single piles or parts of a pile group/piled raft.

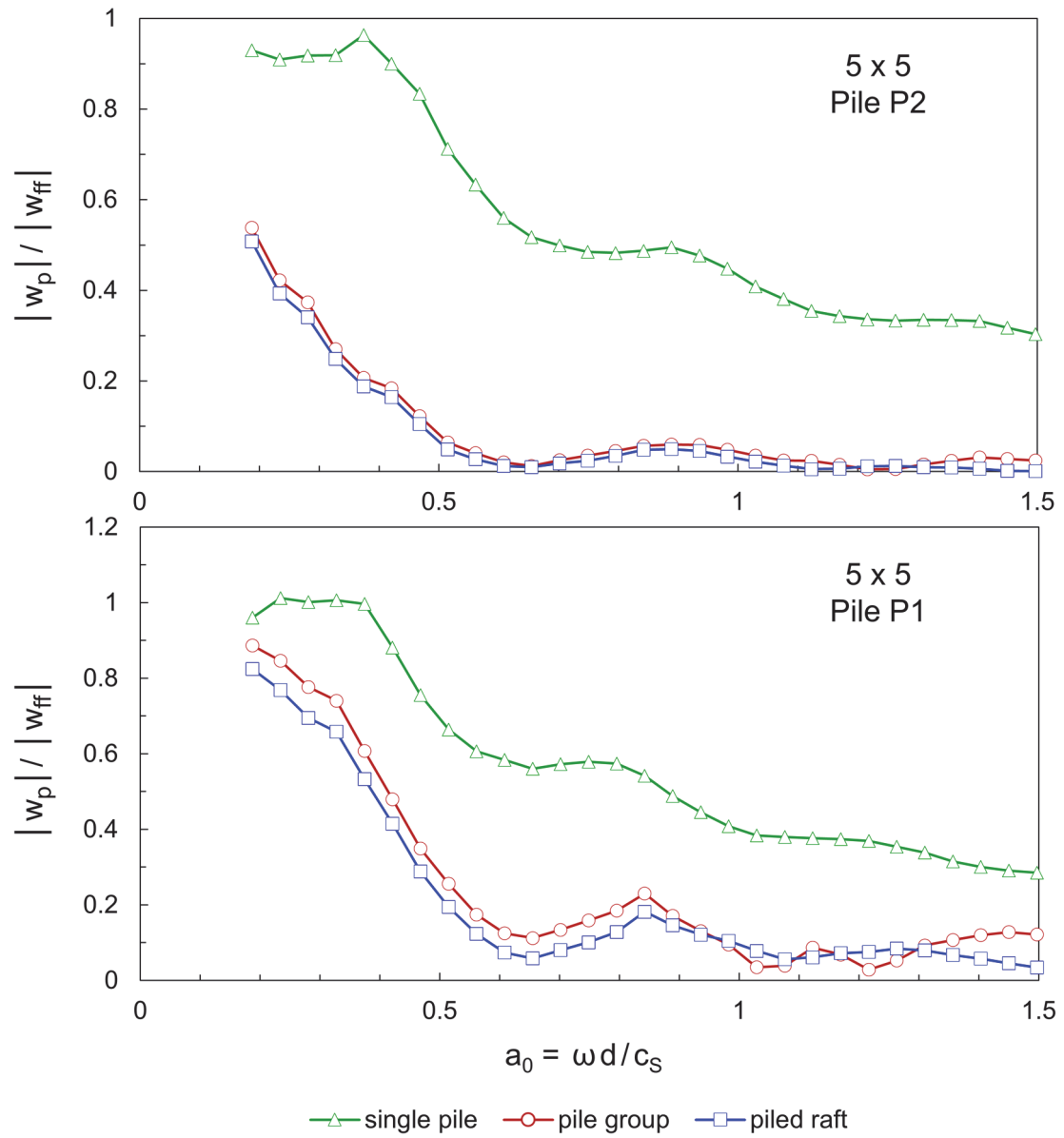


Figure A.13 continued.

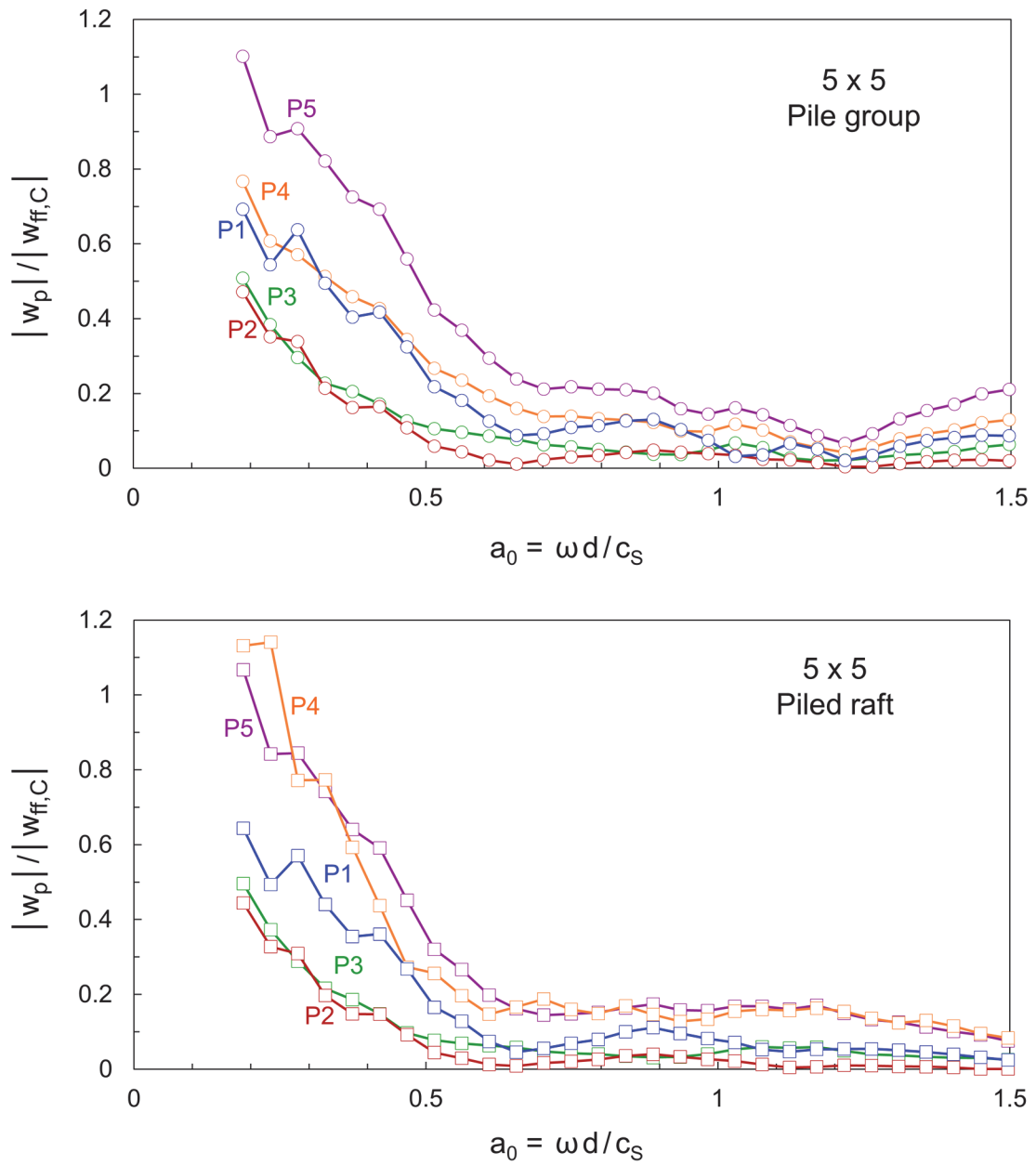


Figure A.14: Vertical transfer functions of reference piles normalized by the free-field amplitude at the center-point of the 5x5 configuration.

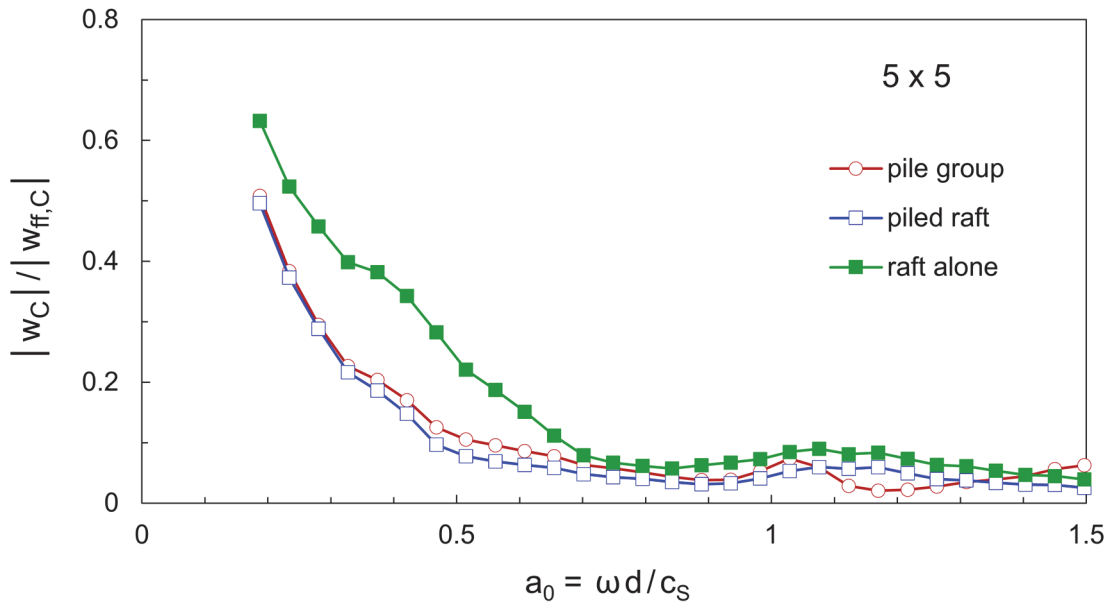


Figure A.15: Vertical transfer function at the center-point of the 5x5 configuration.

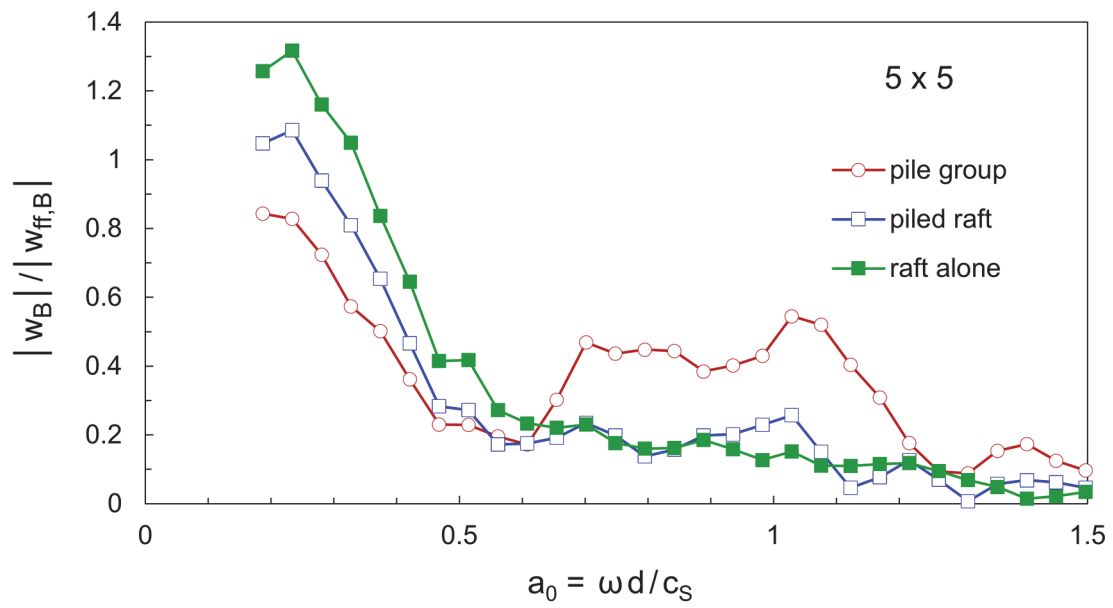


Figure A.16: Vertical transfer function at point B behind the 5x5 configuration.

Lebenslauf

Persönliche Angaben

Name Georgia Efthymiou
Geburtsort Athen, Griechenland

Ausbildung

09/2005 - 06/2011 Palladio Gymnasium in Agrinio, Griechenland; Abitur
09/2011 - 05/2017 Studium des Bauingenieurwesens an der Nationalen Technischen Universität Athen, Griechenland
05.05.2017 Diplom („Dipl.-Ing.“)
02/2018 - 01/2019 Doktorandin am Fachgebiet Bodenmechanik und Grundbau der Technischen Universität Kaiserslautern

Beruflicher Werdegang

05/2017 - 01/2018 Wissenschaftliche Mitarbeiterin in der Abteilung für Bodenmechanik der Nationalen Technischen Universität Athen, Griechenland
05/2019 - 02/2023 Wissenschaftliche Mitarbeiterin am Fachgebiet Bodenmechanik und Grundbau der Technischen Universität Kaiserslautern

Auszeichnungen

2011 - 2014 Evangelou Apergi Stipendium zum Studium des Bauingenieurwesens an der Nationalen Technischen Universität Athen, Griechenland
02/2018 - 01/2019 Promotionsstipendium des Fachgebietes Bodenmechanik und Grundbau der Technischen Universität Kaiserslautern
05/2019 - 05/2022 Stipendium der Marie Skłodowska-Curie-Maßnahme (MSCA) im Rahmen des europäischen Programms „Horizont 2020“

Veröffentlichungen des Fachgebietes Bodenmechanik und Grundbau der Technischen Universität Kaiserslautern

Herausgegeben von Prof. Dr.-Ing. habil. Helmut Meißner

- Nr. 1 Johannes Vogt (1992)
Tragverhalten von Schlitzwandelementen
- Nr. 2 Frank Rogmann (1992)
Untersuchungen zum Stoffverhalten von Kohle im Hinblick auf
Hohlraumstandsicherheiten
- Nr. 3 Wolfgang Weckbecker (1993)
Beitrag zur Berechnung oberflächennaher Tunnel
- Nr. 4 Egbert Adam (2001)
Untersuchungen zum temperaturabhängigen Materialverhalten kristalliner und
sedimentärer Gesteine
- Nr. 5 Andreas Becker (2002)
Stoffmodell und numerisches Modell für zyklisch beanspruchte, teilgesättigte
Sande
- Nr. 6 Katja Abel (2002)
Zugspannungen in Kunststoffdichtungsbahnen geneigter
Deponiebasisabdichtungen
- Nr. 7 Tao Li (2002)
Zweiflächen-Stoffmodell für wassergesättigte bindige Böden unter zyklischer
Beanspruchung
- Nr. 8 Solomon Taye Abebe (2002)
Foundation pits in saturated highly expansive soils
- Nr. 9 Festschrift anlässlich des 65. Geburtstages von Prof. Dr.-Ing. habil. Helmut
Meißner und dem 20-jährigen Bestehen des Fachgebietes Bodenmechanik und
Grundbau an der Technischen Universität Kaiserslautern (2003)

Herausgegeben von Prof. Dr.-Ing. habil. Christos Vrettos

Nr. 10 Sanaa Wendling (2004)

Untersuchungen zur Entstehung von Austrocknungsrisen in mineralischen Deponieabdichtungen

Nr. 11 Yi Lei Shen (2005)

Unterfangung belasteter Fundamente durch Bohrpfähle

Nr. 12 Stefan Jung (2007)

Nichtlinearer horizontaler Bettungsmodulansatz für Trägerbohlwände in mitteldicht gelagertem Sand

Nr. 13 Markus Dobrowolsky (2008)

Quellverhalten teilgesättigter bindiger Böden mit mittlerem Quellpotential

Nr. 14 Viktoria Schwarz (2011)

Mechanisches Verhalten eines teilgesättigten Tons: Experimentelle Untersuchungen, Stoffmodell und Implementierung

Nr. 15 Thomas Becker (2012)

Materialverhalten eines teilgesättigten bindigen Bodens unter zyklischer Belastung

Nr. 16 Dong Chen (2014)

Flachgründungen auf Böden mit tiefenabhängiger Steifigkeit unter vertikaler dynamischer Belastung: Ergebnisse von numerischen Berechnungen im Frequenz- und Zeitbereich

Nr. 17 Andreas Becker (2017)

Untersuchungen zu neuartigen und gängigen Methoden der Baugrundertüchtigung

Nr. 18 Salomi Papamichael (2019)

Experimental and numerical investigations on wheel-soil interactions in calibrated near-surface soil model

Nr. 19 Gerard Banzibaganye (2022)

Static and dynamic behaviour of sand-rubber chips mixtures

Veröffentlichungen des Fachgebietes Bodenmechanik und Grundbau der Rheinland-Pfälzischen Technischen Universität

Herausgegeben von Prof. Dr.-Ing. habil. Christos Vrettos

Nr. 20 Elisabeth Seibel (2023)

Erfassung von Grenzzuständen und Nachweisführung geotechnischer Bauwerke
mittels der Finite-Elemente-Methode

Nr. 21 Georgia Efthymiou (2023)

Numerical study on the kinematic response of piled foundations to a stationary or
moving load